Department of Mechanics, Mathematics and Management

MECHANICAL AND MANAGEMENT ENGINEERING

Ph.D. Program

SSD: ING-IND/16-TECHNOLOGIES AND MANUFACTURING SYSTEMS

Final Dissertation

Additive Manufacturing for soft robotics and sensors

---

by:

Gianni Stano

Supervisors:

Prof. Gianluca Percoco

Prof. Matteo Cianchetti

Coordinator of Ph.D Program:
Prof. Demelio

Course n°35, 01/11/2019-31/10/2022

Department of Mechanics, Mathematics and Management

MECHANICAL AND MANAGEMENT ENGINEERING
Ph.D. Program

SSD: ING-IND/16-TECHNOLOGIES AND MANUFACTURING SYSTEMS

Final Dissertation

Additive Manufacturing for soft robotics and sensors

---

by:

Gianni Stano

Referees

Prof. Alessio Merola

Prof Eric MacDonald

Supervisors:

Prof. Gianluca Percoco

Prof. Matteo Cianchetti

Coordinator of Ph.D Program:
Prof. Demelio

Course n°35, 01/11/2019-31/10/2022

Preface

The work shown in the present PhD thesis has been performed at the "Interdisciplinary Additive Manufacturing (IAM) Lab", Polytechnic of Bari, Italy (27 months) and at the "Humanoid Bio-Robotic and Smart materials (HBS) Lab", University of Texas at Dallas, USA (9 months).

The present PhD thesis refers to the following 10 papers, in which the candidate is first author and co-author, published in international journals.

- "Additive manufacturing and characterization of a load cell with embedded strain gauges"
  G Stano, A Di Nisio, A Lanzolla, G Percoco - Precision Engineering, 2020
- "Additive manufacturing for soft robotics: Design and fabrication of airtight, monolithic bending PneuNets with embedded air connectors"
  G Stano, L Arleo, G Percoco - Micromachines, 2020
- "Fused filament fabrication of commercial conductive filaments: experimental study on the process parameters aimed at the minimization, repeatability and thermal characterization of electrical resistance"
  G Stano, A Di Nisio, AM Lanzolla, M Ragolia, G.Percoco - The International Journal of Advanced Manufacturing Technologies, 2020
- "Additive manufacturing aimed to soft robots fabrication: A review"
  G Stano, G Percoco - Extreme Mechanics Letters, 2021
- "Analytical model to predict the extrusion force as a function of the layer height, in extrusion based 3D printing"
  G Percoco, L Arleo, **G Stano**, F Bottiglione - Additive Manufacturing, 2021
- "I-support soft arm for assistance tasks: a new manufacturing approach based on 3D printing and characterization"
  L Arleo, **G Stano**, G Percoco, M Cianchetti - Progress in Additive Manufacturing, 2021
- "Thermal characterization of new 3d-printed bendable, coplanar capacitive sensors"
  MA Ragolia, AML Lanzolla, G Percoco, **G Stano**, A. DiNisio- Sensors, 2021
- "Additive Manufacturing for Sensors: Piezoresistive Strain Gauge with Temperature Compensation"
  AML Lanzolla, F Attivissimo, G Percoco, MA Ragolia, **G.Stano**, A.DiNisio - Applied Sciences, 2022
- "Additive Manufacturing for bio-inspired structures: experimental study to improve the multi-material adhesion between soft and stiff materials"
  G Stano, S M Al I Ovy, G Percoco, R Zhang, H Lu, Y Tadesse – 3D Printing and Additive Manufacturing, 2022
- "One shot 3D printed soft device actuated using metal filled channels and sensed with embedded strain gauges"
  A Pavone, **G Stano**, G. Percoco- 3D Printing and Additive Manufacturing, 2022

AKNOWLEDGMENTS

November 2019- October 2022: what an amazing journey!
So many people to thank, to be grateful for their help and their patience during the last 3 years.
How can I not start from my advisor, Prof. Gianluca Percoco?
Grazie Gianluca, per tutto quello che hai fatto per me nel corso di questo viaggio. Ricordo ancora, quando bussai alla porta del tuo studio a Japigia nel Settembre 2018 per chiederti la tesi e tu mi proponesti un tema tanto strano quanto intrigante: stampa 3D di sensori. Ma come? Si possono stampare sensori in 3D? Da quel momento è cominciato un bellissimo rapporto durato, ad oggi 4 anni, nei quali mi hai insegnato veramente tantissimo: a pensare in maniera scientifica, a chiedermi sempre il perché dovessimo fare qualcosa, a chiedermi quali fossero i vantaggi ed a trasformare la mia passione da maker in passione scientifica. Come dimenticare i viaggi in macchina a Taranto nei quali facevamo veri e propri brainstorming interessantissimi sulla stampa 3D e la soft robotica. Grazie di tutto! Spero di diventare un ricercatore bravo almeno la metà di quanto lo sia tu.
Grazia a Matteo Cianchetti, mio co-advisor che mi ha fatto appassionare alla soft robotica: le nostre call le ho trovate sempre molto stimolanti e grazie per aver alzato sempre di più l'asticella della mia ricerca.
Grazie ad Attilio Di Nisio ed Annie Lanzolla, mi avete accolto nel vostro laboratorio e fatto sentire un "misurista", è stato veramente un piacere lavorare con voi!
Thanks to Dr Yonas Tadesse, you hosted me (and my very thick Italian accent) in your mythic HBS Lab in Dallas for 9 months making me feel home and teaching me day by day how to be a better scientist. Thanks for all the time we spent together out of work and thanks for the farewell party you set for me, I will never forget how kind you were.
Grazie ad i miei amici dottorandi: Antonio, Mojtaba, Marco e Mattia. Antonio e Mojtaba, è stato davvero stimolante e divertente lavorare fianco a fianco con voi, mi avete dato molto! Marco e Mattia, che dire…abbiamo condiviso tantissimi bei momenti e le mangiate di carne sono state sempre favolose.
Thanks to my friend and colleague Ovy, amazing person who helped me so much. It was a bless to get to work together, we had so much fun (never forget...you better watch out!), and we achieved great results in just 9 months. Bravo!
Grazie ad i miei amici di sempre Fabio, Annalisa, Giuseppe, Simone, Michelone. Il vostro supporto negli ultimi 3 anni è stato fondamentale, così come tutte le mangiate, tutti i caffe, tutte le vacanze le esperienze e soprattutto le risate fatte insieme.

Grazie alla mia famiglia, Rocco, Tonia e Simona, per avermi sostenuto quando ho scelto di intraprendere la strada del dottorato dopo la magistrale , per avermi sempre aiutato e per essere stati dalla mia parte qualsiasi decisione prendessi. Vi devo molto! Grazie di cuore.

TABLE OF CONTENTS

Summary

ABSTRACT

Additive Manufacturing (AM) is gaining tremendous interest in the soft robotics field because of the possibility to manufacture i) soft structures, ii) structures with embedded sensors and actuators, and iii) structures made up of several materials characterized by different degrees of stiffness.

All these advantages fit very well with soft robotic pillars such as bio-inspiration and design freedom. In the present work, Material Extrusion (MEX) technology, well known for being a low-cost AM technology, has been employed for the fabrication of soft robots with embedded sensors and actuators: a remarkable reduction in assembly tasks, manufacturing steps, manufacturing time, and cost has been achieved.

First, 3D printed sensors have been manufactured and characterized: sensors based on piezoresistive and capacitive principle were studied and 3D printed, proving that they can be easily integrated into soft structures. The sensors have been characterized for the force (sensitivity of 0.088 $\frac{\mathrm{mV}}{\mathrm{V}\cdot \mathrm{g}}$), temperature (sensitivity of 0.011 $\frac{\Omega}{^{\circ}C}$) and liquid sensing (sensitivity of 0.79 $\frac{pF}{mm}$) showing performances comparable with sensors manufactured in a traditional way.

Afterwards, several MEX-based soft robots have been proposed: three major actuation systems have been exploited (pneumatic, shape memory alloys, and electromagnetic) and several studies have been performed to correlate the final soft robot performance to MEX process parameters. A way to improve the adhesion between soft and stiff materials, analyzing several parameters, was discovered: an improvement of 48% in the adhesion (Young's modulus) was achieved compared to the best result found in scientific literature. Moreover, a custom-made MEX setup for the silicone extrusion was developed and used in conjunction with a custom-made cartesian pick and place robot (CPPR) for the fabrication of silicone skin with embedded SMA actuators.

Finally, a multi-material MEX machine was employed for the fabrication of a soft robotic finger equipped with a piezoresistive and capacitive sensors, fabricated in a monolithic way: the custom-made CPPR was used for the integration of the SMA actuator during the manufacturing process. In this way, a soft robot equipped with sensing units and actuation systems has been manufactured in a single-shot cycle, without recurring to any additional manual assembly tasks.

KEYWORDS: Additive Manufacturing, Material Extrusion, Soft Robots, 3D printed sensors, smart structures

1. CHAPTER 1: INTRODUCTION

1.1 INTRODUCTION

Additive Manufacturing (AM) technologies have started gaining a lot of interest in the soft robotics field [1], due to multiple intrinsic features such as the possibility to: i) employ soft materials, ii) easily create complex structures, iii) use more materials in the same manufacturing cycle, and iv) fabricate smart structures [2]–[6]. In accordance with ISO ASTM 52900 there are seven AM process groups, based on different physical and working principles: the Material Extrusion (MEX) process group seems to fit well with soft robotic requirements. The working principle underlying MEX technologies is based on the extrusion of materials through a calibrated nozzle: at the state of the art, three methods can be used to extrude materials in MEX technologies. The first method is called Fusion Filament Fabrication (FFF) and it is based on the extrusion of a solid thermoplastic materials by means of an heated nozzle where the material is completely melted and after deposited , the second method is named Direct Ink writing (DIW) and unlike the previous method the material (generally silicone or viscous inks) is not melted into the nozzle, the last method is called hybrid and it is a combination of FFF and DIW in which there are generally two nozzles, the first one used to meld and deposit thermoplastic material and the second one used to deposit liquid material without melting[7] [8].
One of the main pillars, soft robotics is based on the leverage of soft matters to mimic human beings and animals: the fabrication of soft structures is a key requirement to perform complex motions, adapt to unknown environments, to absorb huge amount of energy and to change stiffness.

The extrusion of extremely soft materials in MEX technologies is tough: these technologies were initially designed for the extrusion of thermoplastic materials such as polylactic acid (PLA) and Acrylonitrile butadiene styrene (ABS). Several researchers have been performed to allow the extrusion of soft materials: Yap et al[9] used FFF technology to extrude soft thermoplastic polyurethane (TPU) bending actuators, they also experimentally discovered TPU hyperelastic model parameters to reduce the gap between simulation and experiments. Holmes et al [10] extruded an extremely soft TPU (shore A hardness of 60A and elongation at break > 1000) using an FFF machine and some artefacts (filament pushing system modification) to fabricate gyroid-based structures characterized by a compression response comparable with polyurethane foams used for rehabilitation purposes. Hamidi and Tadesse [11] studied the problem of cavities when DIW technology is employed for the extrusion of silicone: sugar was extruded by means of an heated syringe to create supports which are dissolved in water, in this way pneumatic actuators having bending angle equal

to 70 ° were fabricated. Yirmibesoglu et al created a custom made DIW system using i) a mixing chamber to mix part A and part B of silicone on board of the 3D printer, and ii) heating elements to heat up the just extruded silicone in order to fabricate tall structures, overcoming the collapse of the structure[12].

Another feature making MEX technologies really appealing for the soft robotics domain is the possibility to extrude more materials in the same cycle. In this way, soft-stiff structures [13][14]can be fabricated: the fabrication of this kind of structure is the key enabler to mimic human beings and animal rigid parts connected by means of soft joints. The multi-material MEX methods allow another extremely vital feature for soft robotics (and many other fields): the fabrication of smart structures[15][16]. A smart structure is a structure with embedded sensing units capable to collect data and provide real-time feedbacks. The fabrication of soft robots with embedded sensing systems (by extruding conductive filaments) can really push the role of additive manufacturing towards a new perspective: many advantages such as i) the possibility to fabricate structures ready to be actuated in a single-step manufacturing cycle, ii) the possibility to reduce cost and time and iii) the possibility to fabricate complex geometries can be easily achieved using Multi-material MEX techniques.

1.2 Scope of the thesis

The purpose of the following thesis is the advancement of multi-material MEX technologies for the fabrication of soft robots with embedded sensing systems: the reduction (and elimination) of i) assembly tasks, ii) number of manufacturing technologies involved for the fabrication, and iii)cost and time, are the key points underlying the present work.

The main idea of the present work is the fabrication of soft robots ready to be activated and to provide feedbacks (thanks to the embedded sensing system) after the removal from the building stage of the 3D printer machine. **Fig.1.1** explains the ideal workflow from the CAD design to the soft robot actuation.

To achieve the present goal, three main aspects have been studied: i) MEX for the fabrication of sensors, ii) MEX for the fabrication of soft robots, iii) combination of point i) and ii) in order to fabricate smart soft structures.

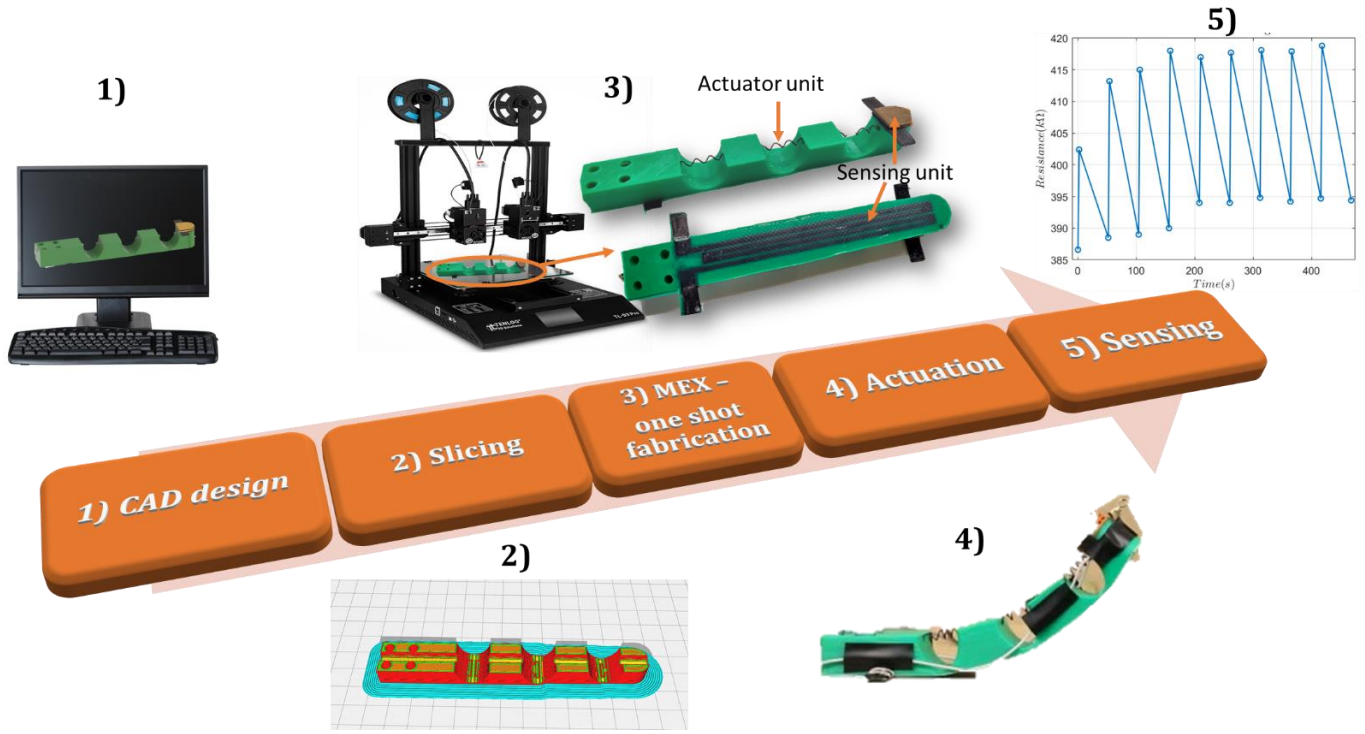

Fig. 1-1- Main idea underlying the present PhD thesis.

1.3 Structure of the thesis

The organization of the thesis is described in this section. There are four chapters and each chapter is written as a self-standing study that includes its own introduction, literature review, and conclusion. Based on that, the rest of the dissertation is organized as follows:

- Chapter 2 is named “MEX for sensors” and describes the studies performed for the fabrication and characterization of sensors based on two different working mechanisms (piezoresistive and capacitive).
- Chapter 3 is named “MEX for soft robots”: in this chapter, initially a focus on actuation systems used in soft robotics is provided and a study based on the Additive Manufacturing fabrication of soft robots based on different actuation systems are described.
- Chapter 4 named “Soft robots with embedded actuator and sensors” describes the one-shot fabrication and characterization of a soft robotic finger ready to use after the manufacturing and capable to provide real-time feedback when activated.
- Finally, in Chapter 5, a discussion is presented following the conducted research and the conclusions are summarized.

2. CHAPTER 2: MEX FOR SENSORS

2.1 Introduction of the chapter

Fused Filament Fabrication (FFF), well known for being one of the most widespread and inexpensive AM technologies, is recently gaining many popularity for the manufacturing of sensors and smart objects[17] .

FFF belongs to Material-extrusion (MEX) AM process group (ISO ASTM 52900: 2015), and is based on the extrusion of solid materials under form of filament through calibrated heated nozzles; due to the possibility to extrude more materials in the same printing cycle, the fabrication of sensors using conductive materials in conjunction with dielectric materials has become very appealing. As shown in [18], the FFF setup available on the market for the multi materials extrusion are divided into 4 categories: i) single extruder: a single extruder is used to extrude different materials, ii) multi nozzles-single print head: a single print head is equipped with different nozzles from which different materials are extruded, iii) multi nozzles- multi print heads: every nozzle is assembled on a different print head, and iv) single extruder equipped with filament selector.

Strain sensors, based on the piezoresistive principle is the most widespread group of sensors manufactured exploiting FFF technology; the working mechanism of this particular class of sensors is based on the change of the electrical resistance (R) when a force is applied due to the change in the ration $\frac{l}{A}$, as shown in Eq (1)

$$R = \rho \frac{l}{A} \qquad (1)$$

Where R is the electrical resistance of the sensor (Ω), ρ is the material resistivity ($\Omega\ cm$) while $\frac{l}{A}$ is the ratio between the piezoresistive material length and its transverse section surface ($\frac{1}{cm}$) .

Another important aspect correlated to the 3D printed strain sensors is the gauge factor (GF), a measure of the sensor sensitivity, defined as follows (eq (2)):

$$GF = \frac{\Delta R}{\varepsilon R_0} \qquad (2)$$

Where ΔR refers to the change of resistance, R_0refers to the initial resistance (Ω) and ε is the sensor stress defined as follow (eq (3)):

$$\varepsilon = \frac{\Delta l}{l_0} \qquad (3)$$

Where Δl is the change of the sensor length, and l_0 is the initial sensor length.

Two kinds of conductive materials are employed for the 3D printing of sensors through FFF technology: commercial and custom-made. All the conductive materials used for FFF are made up of a polymeric matrix doped with conductive filler making the whole material conductive. The percolation theory [19] describes the conductive polymer behavior, correlating the final material conductivity with the percentage of conductive filler, as shown in eq (4)

$$\sigma_m = \sigma_{filler}(p - p_t)^t \quad for\ p > p_t \quad (4)$$

Where σ_m is the conductivity of the whole material, σ_{filler} is the conductivity of the conductive filler, p is the filling content, p_t is the filling content threshold to obtain a conductive path and t is the electrical conductivity critical exponent.

Generally, researchers fabricate custom-made materials in order to obtain unique properties: i) Leigh et al used polycaprolactone (PCL), well known for having a low extrusion temperature (60°C), doped with 25%wt carbon nanotubes (CNs) in order to create a conductive material able to be extruder from common inexpensive 3D printing machines at 260 °C [20], ii) Christ et al [21] developed a flexible conductive filament mixing thermoplastic polyurethane (TPU) and multi-wallet carbon nanotubes (MWCNTs) varied from 2%wt to 5%wt obtaining a GF of 176 at 2%wt and a reduction of the Young modulus only of 14.4% compared to the pure TPU, and iii) Sezer et al [22] developed a filament made up of Acrylonitrile butadiene styrene (ABS) and 7%wt MWCNTs in order to improve the mechanical properties obtaining an Ultimate tensile strength (UTS) of 58 MPa and a maximum conductivity of 232 $e^{-2}\ \frac{S}{cm}$ employing 10%wt of MCWNTs.

From a 3D printing point of view, two major manufacturing approaches can be exploited for the manufacturing of sensors: monolithic method, and modular method. The first method implies the fabrication of smart objects (structures with embedded sensors) in a single additive manufacturing shot, while the second one implies the fabrication of the only sensor (more materials can be employed, i.e. conductive material for the sensors and dielectric materials for the substrate and/or coverage) which will be subsequently assembled to target object (i.e. glove, shoes).

The monolithic approach was used by the following researchers to create smart structures: Stano et al [23] manufactured a load cell with four embedded strain gauges employing TPU and conductive PLA, obtaining a load cell sensitivity of 0.008 $\frac{mV}{V\ g}$ connecting the four strain gauges in a full Weasthon

bridge configuration. Kim et al [24] fabricated a multiaxial sensor, made up of three beams using flexible TPU as dielectric material and a custom-made TPU/CNT as conductive material: every bean was very small (3 x 2.4 x 30 mm) and when a force along the z-axis of 4 N was applied the highest change in resistance along the z-axis of 2% was achieved. Leigh et al [20] manufactured a smart glove consisting of a conductive strip 3D printed using PLC doped with 25%CNTs over PLA, showing a change in resistance for every finger when activated. Georgopoulou et al [25] 3D printed a soft PneuNet (made up of a soft TPU with a shore A hardness of 25) equipped with a strain sensor made up of styrene-ethylene-butylenestyrene (SEBS) thermoplastic elastomers doped with CBs (50%wt) having shore A harness of 50, showing high linearity in the response change in resistance- Pneunet bending angle. Xiang et al [26] employed a conductive filament made up of TPU, CNTs and graphite nanosheet (GNs) to fabricate a small, lightweight (0.163 g) sensor for out of plane force detection, having a GF equal to 140 and a linearity of 0.93.

Li et al [27] fabricated an auxetic structure (negative Poisson ratio) using dielectric TPU and an ultrasonic post-processing to bombard the TPU surface with CNTs to make it conductive: a poisson ratio of – 8 and a change in resistance up to 300% of strain was achieved .

Palmieri et al created a smart structure embedded a strain sensor made up of a conductive PLA to create a structure with vibration durability self-awareness [28].

As regards the modular approach several sensors have been successfully fabricated and tested: Kim et al [29] fabricated a multi axis force sensor using a custom made MWCNTs PLA and a dielectric TPU, showing a good response (a maximum resistance change of almost 4.5 %) when attached to flip-flops to detect human gait activities. Alsharari et al [30] fabricated a multilayer pressure sensor including air gaps to improve its performance taking advantage from the PVA support (melted in water after the print); they used a custom made TPU doped with carbon black (CB) filler as conductive material and they discovered a GF of 23 at 10 KPa, showing a good response when applied to a glove to detect the force applied to grasp several objects.

Singh et al [31] fabricated a ring-shaped flexible force sensors made up of commercial conductive TPU which can be easily integrated into gripper systems to obtain a direct feedback, showing a sensitivity of almost 68 $\frac{k\Omega}{mm}$ and a R^2 of 0.95 when a force ranging from 0 to 12 N was applied.

Two main aspects related to 3D printed strain gauges need to be taken into consideration: i) a direct correlation among change in resistance and temperature and ii) high resistance values obtained after the fabrication process.

As regard the first aspect, a temperature coefficient of resistance α_T $(\frac{1}{^\circ C})$ of 0.011 and 0.007 was found in [32] respectively for a commercial conductive PLA and TPU, while in [33] a value ranging from 0.03 to 0.01 was found for conductive PLA.

In particular, the coefficient of resistance α_T $(\frac{1}{^\circ C})$ is calculated as follows (eq (5)):

$$\alpha_T = \frac{R-R_0}{R_0(T-T_0)} \qquad (5)$$

Where R is the electrical resistance of the sensor (Ω) at temperature $T(^\circ C)$,and $R_0(\Omega)$ is the electrical resistance of the sensor (Ω) at temperature T_0 $(^\circ C)$.

The strong correlation resistance-temperature from one hand requires a compensation when 3D printed strain sensors are used to measure force/strain, but from the other hand paves the way to a huge exploitation of the FFF technology for the fabrication of temperature sensors.

As regards the second aspect, namely high value of electrical resistance after the manufacturing process, it might adversely affect the sensor performance due to the Joule effect, for this reason several studies have been conducted to find a way to minimize it. The optimization of the process parameters, as shown in [32] and [34] plays a key role for the reduction of the electrical resistance. An intriguing post-process used to reduce the final electrical resistance as well, is the flash ablation metallization through an high intensity pulsed light, which has been proved to increase the electric conductivity of two order of magnitudes [35][36].

Besides the fabrication of piezoresistive-based sensors, recently progress in the fabrication of sensors using FFF technology lead to i) the development of capacitive sensors used as force/pressure[16] [37] [38], liquid [39]and temperature sensors [40], ii) the usage of conductive materials for the fabrication of accelerometers [41], iii) the study of the dynamic piezoresistivity of embedded sensors [42] [43], and iv) the modelling the anisotropic electrical properties of strain gauges [44].

In conclusion, FFF technology seems to be really appealing for the fabrication of sensors (in Tab 2.1, all the cited researchers are summarized) due to several intrinsic features like the possibility to fabricate smart object, high design freedom and the reduction of the assembly and manufacturing steps. All those benefits motivated many researchers to overcome different problems like i) the lack of a huge variety of marketable conductive filament, ii) a really high correlation among electrical resistance and temperature and iii) low conductivity of the 3D printed sensors; coming up with a variety of solution aiming to push the role of FFF for the sensor fabrication to a new level.

The following chapter is organized as follows: in 2.2 the piezoresistive-based sensors fabricated by means of FFF is analyzed using a Design of Experiment (DOE) approach to reduce the electrical resistance and variability and the relationship among temperature and electrical resistance is studied. In 2.3 a one-shot load cell equipped with four embedded strain gauges is discussed. Finally, in 2.4 the capacitive based sensors fabricated by means of FFF is analyzed.

Tab. 2-1- Summary of the work cited in 2.1: MEX for the fabrication of sensors

Reference	Sensor mechanism	Conductive Material	FFF approach	GF/sensitivity
Stano et al [23]	Piezoresistive	Commercial (conductive PLA)	Monolithic	$0.008\ \frac{mV}{V\ g}$
Kim et al [24]	Piezoresistive	Custom-made (TPU + CNTs)	Monolithic	---
Leight et al [20]	Piezoresistive	Custom made (PCL+ CB)	Monolithic	---
Georgopoulou et al [25]	Piezoresistive	Custom made (SEBS + CB)	Monolithic	53
Xiang et al [26]	Piezoresistive	Custom made (TPU + CNTs + GNs)	Monolithic	140
Li et al [27]	Piezoresistive	Custom made (TPU + CNTs)	Monolithic	---
Palmieri et al [28]	Piezoresistive	Commercial (conductive PLA)	Monolithic	---
Kim et al [29]	Piezoresistive	Custom made (PLA + MWCNTs)	Modular	$\frac{2.689\ *10^{-4}}{kPa}$
Alsharari et al [30]	Piezoresistive	Custom made (TPU+ CB)	Modular	23

Singh et al [31]	Piezoresistive	Commercial (conductive TPU)	Modular	$68\ \frac{k\Omega}{mm}$
Loh et al [16]	Capacitive	Commercial (conductive TPU)	Modular	---
Schouten et al [38]	Capacitive	Commercial (conductive TPU)	Modular	---
Ozioko et al [39]	Capacitive	Commercial (conductive polyester)	Monolithic	---
Ragolia et al [40]	Capacitive	Commercial (conductive PLA)	Modular	$0.24\ \frac{pF}{^{\circ}C}$

2.2 Piezoresistive-based sensors: Design of Experiment (DoE) for electrical resistance (and variability) minimization and thermal analysis

In this study, working on 3D-printed strain gauges, process and design parameters have been investigated in order to find a set of parameters which minimize the final electrical resistance and the variability among identical strain gauges in terms of the electrical resistance. A total of 105 samples (strain gauges) were fabricated and tested. In particular, three different commercial conductive filaments have been analyzed in terms of their performance. First of all, a 2^3 factorial plan on printing parameters was conducted and afterwards, keeping unchanged the best identified printing parameters, a new factorial plan 2^2 was developed to identify the best strain gauge geometry, in order to minimize the electrical resistance and variability.

The aims of the minimization and uniformization of the electrical resistance are as follows: i) to try to decrease the electrical resistance to reduce the noise during measurements; ii) to achieve a low resistance value in order to use 3D-printed conductive traces to exploit the Joule effect, with the goal of heating polymers characterized by the shape memory effect [45] from the perspective of new emerging 4D printing [46]; iii) to reduce the variability among resistance values of the identical (both from a design and manufacturing process point of view) strain gauges, to pave the way for the mass production of sensors manufactured by inexpensive FFF technology; and iv) to reduce the variability in order to better balance four 3D-printed strain gauges connected to form a Wheatstone bridge to obtain better measurements.

After finding the best set of parameters the correlation between resistance variation in strain gauges and environmental temperature change was studied. This study has produced evidence of the relevant thermal effects on 3D-printed strain gauges (a thermal coefficient of resistance ranging from 0.007 and 0.011 $°C^{-1}$ at T_0 = 20 °C was experimentally found), suggesting a new possible application field for conductive filaments: the fabrication of 3D-printed temperature sensors.

2.2.1 Materials and methods

Three different commercial conductive filaments were studied in this investigation: i) AlfaOhm, a Polylactic acid (PLA)-based filament doped with carbon black and carbon nanotubes (CNT), which make it conductive, developed by LATI and FiloAlfa; it is characterized by a resistivity of 15 $\Omega \cdot$ cm along the layers and 20 $\Omega \cdot$ cm perpendicular to the layers; ii) Fabbrix CNT (henceforth called CNT), a PLA-based filament doped with carbon nanotubes (CNTs) and developed by Fabbrix, with a surface

electrical resistance of 10 Ω, tested in accordance with ISO D257; and iii) Ninjatek Eel (henceforth called Eel), a flexible conductive filament, consists of thermoplastic polyurethane (TPU) doped with carbon-black, produced by Ninjatek with a hardness of 90 A, tensile strength of 12 MPa, elongation at strength of 355%, and surface electrical resistance of $1.5 \cdot 10^3$, in accordance with ANSI/ESD STM 11.1. All data on the mechanical and electrical properties were taken from filament data sheets. For AlfaOhm and CNT, the available filament diameter on the market is 2.85 mm, while for Eel, it is 1.75 mm. For this reason, two different dual extruder FFF printers were used: Ultimaker S^5 was used for 2.85 mm filaments, while Raise Pro2 was employed for 1.75 mm filaments. Another notable difference between the two 3D printers is the different feeder (the mechanical system which pushes the filament to the extruder) locations: while for Ultimaker S^5, it is located at the bottom of the printer (called the bowden system) and pushes the filament through a Teflon tube up to the extruder, for Raise Pro2, the feeder is joined to the extruder (called direct system) so that the filament path employed to reach the nozzle is the minimum. The different feeder positions affect printing parameters such as the printing speed (3D printers with the bowden system are lighter and allow fast extruder movements) and retraction distance (for printers equipped by the direct system, low values of retraction are required).

The open source software Ultimaker Cura 4.4 was used to communicate with Ultimaker S^5 and set the printing parameters, while ideaMaker 3.4.2 was used for Raise Pro2. Two commercial thermoplastic polyurethane (TPU) filaments were used as non-sensitive elements: for Ultimaker S^5, TPU 95 A developed by Ultimaker ltd was used, while for Raise Pro2, TPU 90 A produced by Fabbrix was chosen. Therefore, the whole sensor was composed of a dielectric part in TPU (95 or 90 A, in accordance with the 3D printer used), equipped with an M4 hole to easily connect the sensor to a support framework for future characterization tests and a sensitive part composed of a strain gauge printed with AlfaOhm, CNT, or Eel filaments. In **Fig 2.1**, the structure of the whole sensor is shown.

To minimize and equalize the electrical resistance in 3D-printed strain gauges, the following method was used: printing process parameters and design parameters were split and separately investigated. First of all, strain gauges with fixed design parameters were manufactured by changing three different printing parameters in accordance with a 2^3 factorial plan, with three replications; from this phase, a combination of three printing parameters which ensured minimization and uniformization of the electrical resistance stood out. Afterwards, keeping the best printing parameter combination identified fixed, two different design parameters were studied following a 2^2 factorial plan with three replications. The final output of the experimental phase was a combination of process and design parameters which guaranteed the achievement of the desired objectives. It was possible to perform two consecutive factorial plans, 2^3 and 2^2, by splitting printing and design parameters, rather than a

unique 2^5 one only, because printing and design parameters are independent of each other; indeed, printing parameters do not affect design ones and vice versa. Arbitrarily, it was decided that the study would start with the printing parameter investigation (with the design parameters kept unchanged), and after this, it would be switched to a design parameter examination (with the best combination of printing parameters found in the previous phase kept fixed), but vice versa would have led to the same result.

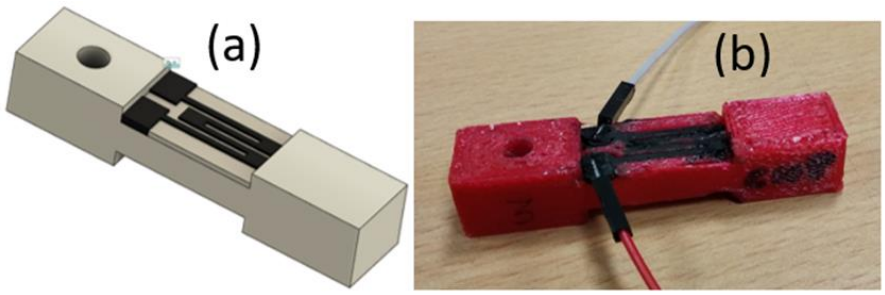

Fig. 2-1- Proposed piezoresistive sensor: a) CAD model, and b) 3D printed sample

2.2.2 DoE for Process parameters

In this section, an investigation on how the chosen printing parameters affect the electrical resistance and the variability in 3D-printed strain gauges is reported. The factorial plan 2^3, with three replications for each combination, was performed. The strain gauge geometry on which to vary the printing parameters was fixed; in particular, it was characterized by a number of tracks of 4 and an active length of 9 mm. In other terms, all experiments were performed by keeping constant D and E parameters at the low level of -1 (see section 2.3 to better understand this point).

The printing parameters analyzed in this study are the layer height, line width, and printing orientation.

The layer height is the height of the extruded filament, and it affects the total number of layers which will be printed (increasing the layer height provides a reduction of the total number of printed layers). In this study, this parameter is indicated with the letter A and two levels (respectively -1 and +1) corresponding to height values of 0.2 and 0.3 mm.

The line width feature is the width of the extruded filament. It depends on the nozzle diameter and should approximately range from –20% of the nozzle diameter up to +20%. The line width affects the number of adjacent extruded filament lines (when increasing the line width value, the number of adjacent lines will be reduced). This parameter is indicated with the letter B and the two levels, -1 and +1, respectively, are 0.33 mm, which is equal to three adjacent extruded lines, and 0.5 mm, which is equal to two adjacent extruded lines.

The layer height and line width parameters are illustrated in **Fig 2.2 a).**

Regarding the latter printing parameter, namely, the printing orientation, it refers to way in which the strain gauge is orientated relative to the build plate. This parameter is indicated with the letter C and the low level, -1, refers to the strain gauge parallel to the build plate, while the high level, +1, refers to the strain gauge perpendicular to the build plate (**Fig. 2.2(b) and (c)**).

In **Tab2.2**, the printing parameter factors and the respective levels are summarized.

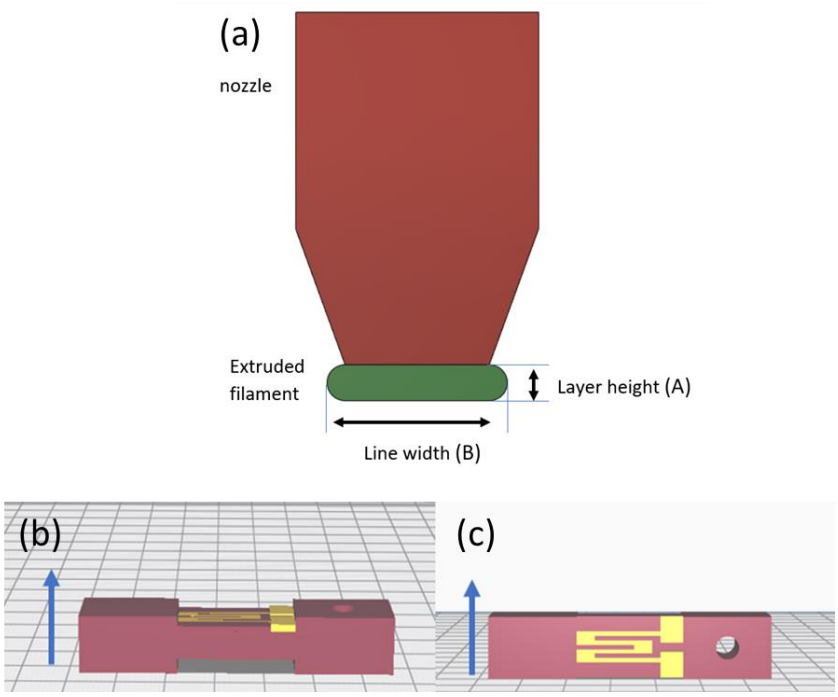

Fig. 2-2-Process parameters varied during the study: a) layer height and line width, b) printing orientation parallel to the build plate, and c) printing orientation perpendicular to the build plate

Tab. 2-2-Printing parameters factor

FACTOR	**LEVEL**	
	-1	**+1**
A (layer height)	0.2 mm	0.3 mm
B (line width)	0.33 mm	0.5 mm
C (printing orientation)	parallel	perpendicular

The process parameters, except for the layer height, line width, and printing orientation (varied in accordance with the 2^3 plan), were kept fixed for each sensor specimen during the experiments. They, starting from the suggested values provided by the filament suppliers, were changed until the best process values for each filament, both conductive than non-conductive, had been found using a trial-and-error approach. The fixed printing parameters set during all the experiments are shown in **Tab**

2.3. In particular, the identical process parameters set for each filament were as follows: i) nozzle diameter of 0.4 mm ii) build plate adhesion type set as brim; iii) infill pattern set as lines; and iv) infill density set as 100%. For the printing parameter choice, two major differences among filaments extruded by means of the bowden machine (Ultimaker S^5) and direct one (Raise Pro2) stand out: i) The Bbowden machine, because of its architecture, with the feeder located at the bottom of the 3D printer, is lighter than the direct one and for this reason, higher printing speed values were set, and ii) in the direct machine, the path of the filament from the feeder to the nozzle is very short compared to that of the bowden machine, and for this reason, for TPU 90 A (extruded with Raise Pro2), the retraction distance value is almost half that of TPU 95 A (extruded with Ultimaker S^5).

Another considerable discrepancy is the different value set for the "retraction" parameter for conductive filaments; this choice is not linked to the kind of 3D printer used, but depends on the different chemical compositions underlying conductive filaments. As a matter of fact, AlfaOhm and CNT are PLA-based filaments doped with conductive elements, which increase the brittleness of the filament, while Eel is a flexible conductive filament (TPU-based) characterized by a non-brittle behavior. Experimentally, it has been proved that for PLA-based conductive filaments, there is a high probability of filament breakage between the driving gears which push the filament to the nozzle, when retraction is enabled. On the other hand, Eel does not show any breakage issues when the retraction is enabled because of its flexible and non-brittle nature. Additionally, to reduce cross-contamination issues at the interface between conductive and non-conductive material, the prime tower parameter was enabled for all specimens. After sensor manufacturing, electrical wires were welded at the temperature of 350 °C to each pad of strain gauges, in order to use benchtop multimeters for electrical measurements (see **Fig. 2.1 b)**).

Tab. 2-3. Fixed process parameters for every material

PARAMETER	ALFAOHM	CNT	EEL	TPU 95 A	TPU 90 A
Temperature (°)	220	225	235	223	230
Printing Speed (mm/s)	20	25	22	40	25
Flow (%)	120	120	130	106	106
Retraction	disabled	disabled	enabled	enabled	enabled
Retraction Distance (mm)	---	---	4	8	4,5

In **Tab. 2.4, 2.5**, and **2.6**, the factorial plan 2^3 for the three conductive filaments is shown. The mean μ (equation (6)) and standard deviation σ (equation (7)) were calculated as follows:

$$\mu_j = \sum_{n=1}^{m} r_{j;n}, \qquad (6)$$

$$\sigma_j = \sqrt{\frac{1}{m-1}\sum_{n=1}^{m}(\mu_j - r_{j;n})^2}, \qquad (7)$$

where j indicates the jth combination, and n is the replication number with $n = 1,..,m$ and $m = 3$, so $r_{j;n}$ indicates the electrical resistance value associated with the jth combination and nth replication.

Tab. 2-4-AlfaOhm printing parameters factorial plan

AlfaOhm								
Combination	A	B	C	Replication ($k\Omega$)			μ ($k\Omega$)	σ ($k\Omega$)
				n_1	n_2	n_3		
(1)	-1	-1	-1	5.1	3.9	2.9	4	1.1
a	+1	-1	-1	2.5	2.2	3.1	2.6	0.46
b	-1	+1	-1	3.4	5.2	3	3.9	1.2
ab	+1	+1	-1	2.8	2.4	2.3	2.5	0.26
c	-1	-1	+1	3.8	6.2	4.4	4.8	1.2
ac	+1	-1	+1	2.6	3.4	2.5	2.8	0.49
bc	-1	+1	+1	3.4	6.1	4.5	4.7	1.3
abc	+1	+1	+1	2.6	3.2	2.5	2.8	0.38

Tab. 2-5- CNT printing parameters factorial plan

CNT								
Combination	A	B	C	Replication ($k\Omega$)			μ ($k\Omega$)	σ ($k\Omega$)
				n_1	n_2	n_3		
(1)	-1	-1	-1	5.4	4.	3.6	4.3	0.9
a	+1	-1	-1	2.4	2.4	2.5	2.4	0.1
b	-1	+1	-1	4	3.5	4.9	4.1	0.7
ab	+1	+1	-1	1.9	2.2	2.3	2.1	0.2
c	-1	-1	+1	4.1	6.5	5.1	5.2	1.2

ac	+1	-1	+1	2.6	2.4	2.8	2.6	0.2
bc	-1	+1	+1	6	4.6	4.9	5.2	0.7
abc	+1	+1	+1	2.7	2	2.6	2.4	0.4

Tab. 2-6- Eel printing parameters factorial plan

EEL								
Combination	A	B	C	Replication ($k\Omega$)			μ ($k\Omega$)	σ ($k\Omega$)
				n_1	n_2	n_3		
(1)	-1	-1	-1	11.3	7.2	8.3	8.9	2.1
a	+1	-1	-1	4.6	5.3	4.7	4.9	0.4
b	-1	+1	-1	10.4	8.4	7.1	8.6	1.7
ab	+1	+1	-1	4.8	4.3	2.4	3.8	1.3
c	-1	-1	+1	13.2	8.1	9.7	10.3	2.6
ac	+1	-1	+1	5.0	5.6	5.7	5.4	0.4
bc	-1	+1	+1	7.4	9.3	12.9	9.9	2.8
abc	+1	+1	+1	5.5	4.8	5.2	5.2	0.4

In **Fig. 2.3**, pareto charts of the standardized effects for each conductive material are reported, while in **Tab. 2.7**, the effects (non-standardized) and respective p-values ($\alpha = 0{,}05$) for each conductive material factor and factor combination are listed.

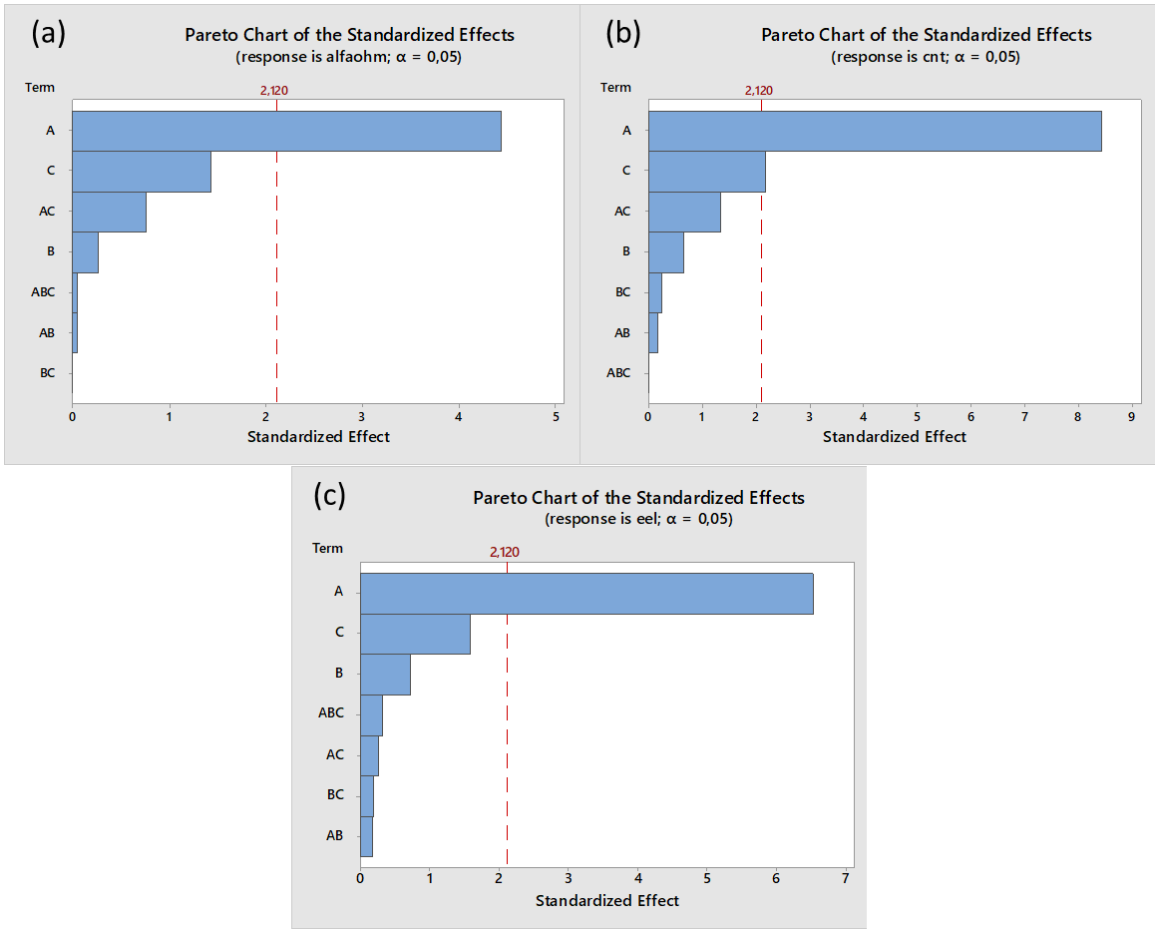

Fig. 2-3- Pareto charts of standardized effects: (a) AlfaOhm, (b) CNT, and (c) EEL

Tab. 2-7- Non standardized effects and p-value

Factor combination ↓	Factor →	**Alfaohm**		**CNT**		**EEL**	
		effect	p-value	effect	p-value	effect	p-value
A		-1.65	0	-2.317	0	-4.608	0
B		-0.1	0.792	-0.183	0.514	-0.508	0.482
C		0.53	0.171	0.6	0.044	1.125	0.131
A*B		0.017	0.965	-0.05	0.858	-0.125	0.862
A*C		-0.283	0.458	-0.367	0.201	-0.192	0.79
B*C		0	1	0.067	0.811	0.142	0.844
A*B*C		0.017	0.965	0	1	0.225	0.754

From the results of the factorial plan, several considerations can be drawn:

1) The growth of the electrical resistance affects the variability among the three strain gauges belonging to the same combination. The variability can be measured as the standard deviation of the three electrical resistance values achieved for the same combination . In particular, there is a positive correlation among resistance values and variability; indeed, when the mean electrical resistance increases, then the variability also increases. This correlation plays a key role in 3D-printed sensors because future studies on parameter optimization will lead to several simultaneous benefits due to resistance and variability minimization, such as noise reduction during measurements or the possibility to connect more strain gauges in Wheatston bridge configurations to obtain better measurements from several points of view. For AlfaOhm and CNT, the behavior in terms of the standard deviation vs. mean electrical resistance is very similar; indeed, for the four lower resistance values (combinations: $a, ab, ac,$ and abc), the standard deviation value is less than 0.5 kΩ , while for large resistance values, the standard deviation increases, reaching the maximum values of 1.3 and 1.2 kΩ for Alfa Ohm and CNT, respectively. The Eel behavior is slightly different: in terms of the lowest value of resistance (combination ab), the standard deviation is 1.3 kΩ, while for the other three lowest electrical resistance values, the standard deviation is less than 0.5 kΩ, as for AlfaOhm and CNT. This unusual behavior can be attributed to a cross-contamination problem, which is typical for multi-material printing. In the opinion of the authors, it is very probable that, during the printing, on a certain layer, a residue of TPU 90 A carried by the hot nozzle came into contact with the Eel track already deposited, reducing the electrical resistance of the strain gauge belonging to the ab combination and third replication ($n = 3$). This would explain the significative difference in resistance values for the combination ab, where there is an anomalous value of 2.4 kΩ, in contrast with 4.3 and 4.8 kΩ. To demonstrate this theory, five other Eel samples were printed in accordance with process parameter levels of the combination ab, which resulted in a measured standard deviation of 0.34 kΩ and a mean resistance value of 4.7 kΩ.

In **Fig. 2.4**, the values of standard deviation of the mean electrical resistance for each combination of the three conductive materials are reported;

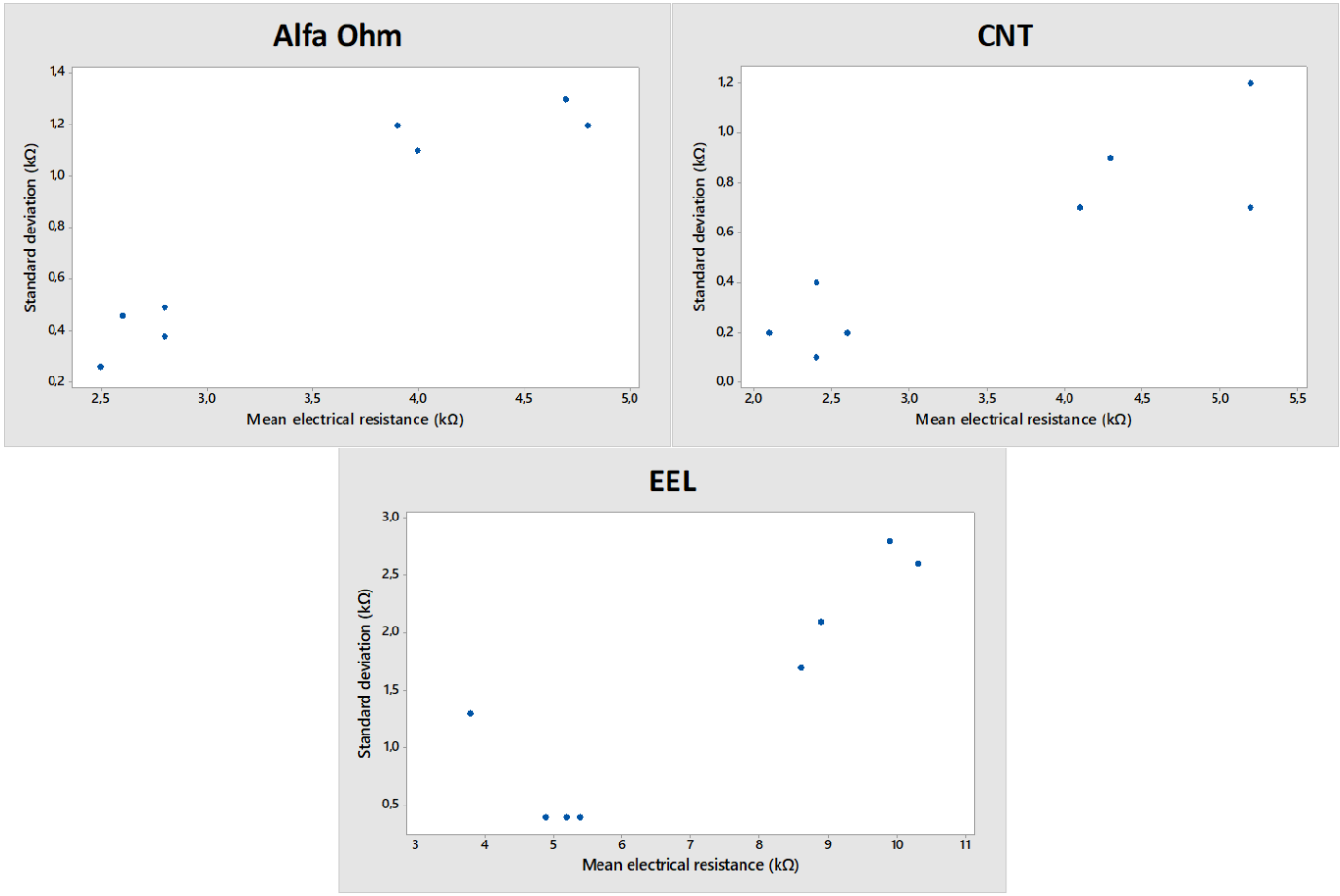

Fig. 2-4-Standard deviation vs mean electrical resistance

2) The main parameter affecting the electrical resistance, for each conductive material, is the layer height: switching from a layer height of 0.2 to 0.3 mm resulted in a greater decrease in electrical resistance in comparison to changing other parameters. Therefore, the first parameter that should be set in order to reduce the resistance (and the variability) is the layer height; in this study, a nozzle diameter of 0.4 was used, which does not allow layer height values greater than 0.3 mm, but using other diameter nozzles (for example, 1 mm), it should be possible to increase the layer height to 0.8/0.9 mm, which would entail, in accordance with the results of this study, a further reduction of the electrical resistance and variability. A possible reason why the layer height affects the electrical resistance so much is as follows: when the filament is extruded and deposited by means of the nozzle, it has a quasi-elliptical shape, and when more layers are built on each other, voids, commonly referred to as air gaps in the literature, are generated among quasi-elliptical extruded filaments of layer k and layer $k + 1$ (**Fig. 2.5**). Voids involve a reduction of electrical resistance because there are small zones in which there is no contact among extruded conductive filaments of adjacent layers, and this phenomenon is named the “welding effect” by the authors. When increasing the layer

height from 0.2 to 0.3 mm, the total number of layers that will be built decreases (in the first rows of section 2.2, the link between the layer height and number of layers is explained) from 5 to 3 (using a parallel printing orientation), so the total number of intra-layer voids decreases.

For this reason, the printing orientation is the process parameter with the second major effect for all conductive materials: when switching from a low level (parallel strain gauge orientation) to a high level (perpendicular strain gauge orientation), the electrical resistance meaningfully increases because, for a low level, the number of layers to build is less than that required for a high level.

The "welding effect" also explains why the interaction between the layer height and printing orientation causes a relevant effect in AlfaOhm and CNT (produces the third significant effect), while in Eel, this effect is marginal, but this is probably due to the anomalous resistance value found in the combination ab.

In conclusion, the resistance minimization (and variability minimization) depends on the "welding effect", which is minimized when the number of layers is reduced. The printing parameters accountable for the reduction of the layer number are the layer height (factor A) and printing orientation (factor C), so it seems clear that the optimization of these two parameters (and their interaction) leads to resistance and variability minimization.

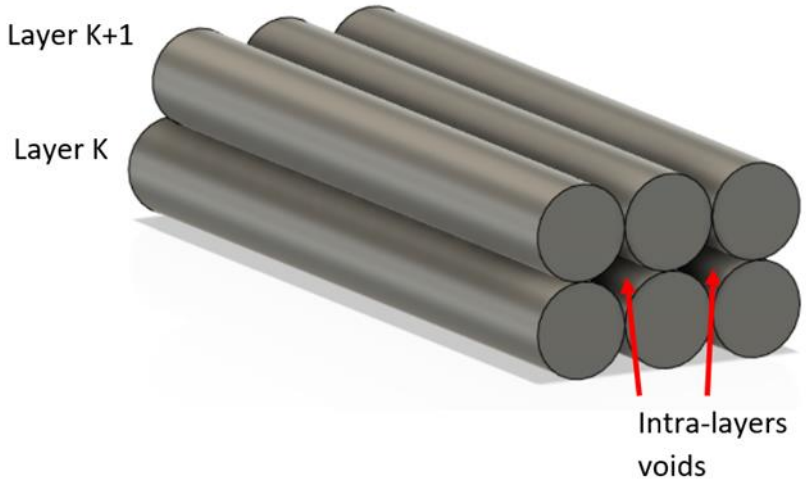

Fig. 2-5- Welding effect

3) The effect of the parameter B, namely, the line width, is not significant; indeed, voids among the extruded filaments along the same layer are very few in number and slightly affect the electrical resistance (when switching from a low to high level, the resistance increase is low). Additionally, the other parameter combinations (A*B, B*C and A*B*C) do not involve significant effects in terms of resistance minimization and variability reduction.

4) The best printing parameter combination which minimizes the electrical resistance and the variability in 3D-printed strain gauges for each conductive material is the combination ab, characterized by high levels of layer height and line width and a low level of printing orientation. Then, the process parameters set to minimize the electrical resistance and variability are a layer height equal to 0.3 mm, line width of 0.5 mm, and "parallel" printing orientation; with this process configuration, 2.5, 2.133, and 3.8 kΩ were the mean electrical resistance values obtained for AlfaOhm, CNT, and Eel, respectively.

2.2.3 DoE for Design variables

In this section, two design parameters are investigated to understand how they affect the final electrical resistance and if a correlation between them and variability exists. The printing parameters used for each conductive material in this phase were the best ones found in section 2.2: printing parameters in accordance with the combination ab (layer height = 0.3 mm, line width = 0.5 mm, and printing orientation = parallel) were set. The design parameters varied in this study are the number of tracks and active length (see **Fig.2.6**) named D and E, respectively. The low (-1) and high (+1) levels of D are 4 and 6, while for E, they are 9 mm and 15 mm. Other design parameters were kept unchanged; in particular, the distance between two adjacent tracks was 1 mm, the size of the pads (needed to weld electric wires) was 5 mm * 6 mm, and the end loops (needed to reduce transverse effects due to deformations when weights are applied) were 3 mm * 4 mm. All dimensions mentioned above refer to the x-y plane, while the height of the strain gauge was 1 mm.

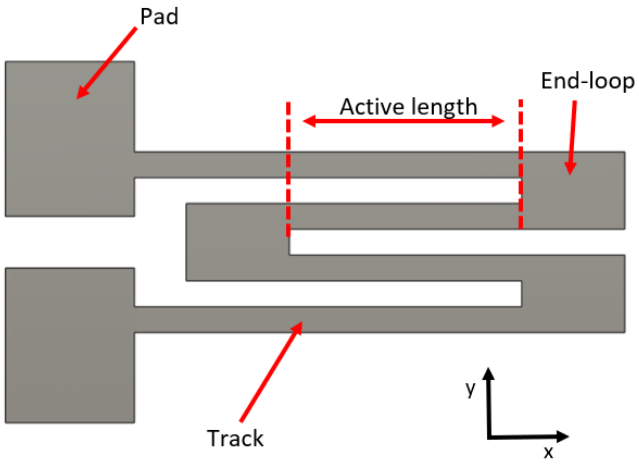

Fig. 2-6-Strain gauge design

Then, a factorial plan 2^2 with three replications was run. In **Tab. 2.8, 2.9 and 2.10**, the results for the three conductive materials are reported, while in **Fig 2.7**, pareto charts of the standardized effects are shown.

Tab. 2-8- Alfa Ohm design parameters factorial plan

AlfaOhm							
combination	D	E	Replication ($k\Omega$)			μ ($k\Omega$)	σ ($k\Omega$)
			n_1	n_2	n_3		
f	-1	-1	2.8	2.4	2.3	2.5	0.3
g	+1	-1	4.8	4.2	4.8	4.6	0.3
h	-1	+1	4.4	4.7	4.6	4.6	0.2
i	+1	+1	6.6	7.3	6.5	6.8	0.4

Tab. 2-9- CNT design parameters factorial plan

CNT							
Combination	D	E	Replication ($k\Omega$)			μ ($k\Omega$)	σ ($k\Omega$)
			n_1	n_2	n_3		
f	-1	-1	1.9	2.2	2.3	2.1	0.2
g	+1	-1	4.3	4.2	4.5	4.3	0.2
h	-1	+1	4.3	4.0	4.4	4.2	0.2
i	+1	+1	6.5	6.2	6.6	6.4	0.2

Tab. 2-10- Eel design parameters factorial plan

EEL							
Combination	D	E	Replication ($k\Omega$)			μ ($k\Omega$)	σ ($k\Omega$)
			n_1	n_2	n_3		
f	-1	-1	4.8	4.3	2.4	3.8	1.3
g	+1	-1	6.7	6.5	7.2	6.8	0.4
h	-1	+1	6.0	7.0	6.4	6.5	0.5
i	+1	+1	10.2	9.2	9.5	9.6	0.5

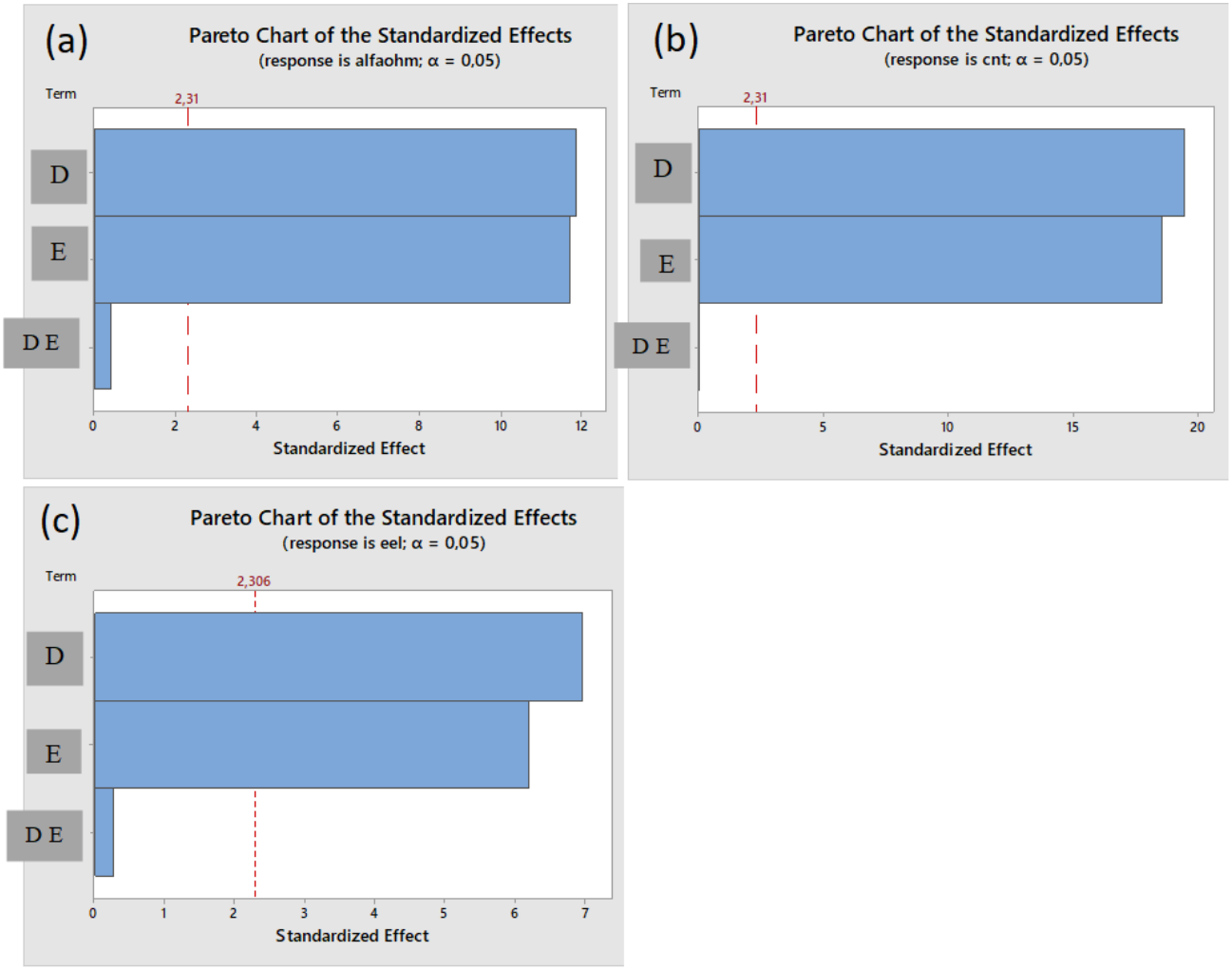

Fig. 2-7 Pareto charts of standardized effects: (a) AlfaOhm, (b) CNT, and (c) EEL.

The three samples of combination f of each analyzed conductive material were not manufactured again, because they had already been printed during the printing parameter investigation: the ab combination of printing parameters is the same as the f combination. Hence, for combination f, the same data achieved for combination ab were used.

From the data analysis of factorial plans, the following considerations stand out:

1) Unlike the previous investigation, in this case, there was no correlation among resistance minimization and variability minimization. The standard deviation for each combination of each conductive material was always less than 0.51 kΩ, except for the combination f of Eel, but this anomalous behavior, as explained in 2.2, can be explained by a cross-contamination problem. It is thus possible to affirm that the variability among strain gauges is only related to printing parameters and, in particular, to the "welding effect";

2) Parameters D and E, as shown in **Fig 2.7**, produce significant effects in terms of the final electrical resistance. When increasing the number of tracks (factor D) from 4 (low level) to 6 (high level), the electrical resistance of the strain gauge increases almost equally in comparison to increasing the active length (factor E) from 9 to 15 mm. The effect of the two design parameters analyzed in this study is very similar for all the conductive materials; to be truthful, the effect of the number of tracks is slightly more significant than that of the active length. If we increase the number of tracks and the active length, then the resistance of the strain gauges also increases, as expected, because the term l of **equation (1)**, which describes the electrical resistance law, is increased, while the other two terms (A and ρ) are left unchanged.

3) The effect of the interaction between the two design parameters does not involve any significant effect in terms of resistance minimization.

For the convenience of the reader, **Tab 2.11 and 2.12** summarize the outcome of the whole DoE in terms of the best parameters (printing and design) found and respective values of electrical resistance for each conductive filament.

Tab. 2-11- Best printing and design parameters

PARAMETER	VALUE
Layer height	0.3 mm
Line width	0.5 mm
Printing orientation	parallel
Number of tracks	4
Active length	9 mm

Tab. 2-12 Electrical resistance related to the best set of printing and design parameters at 22.5 °C.

Resistance (kΩ)			
Material / Specimen	AlfaOhm	CNT	EEL
R1	2.8	1.9	2.4
R2	2.4	2.2	4.8
R3	2.3	2.3	4.3

Mean	2.5	2.1	3.8
Standard deviation	0.26	0.21	1.3

2.2.4 Thermal analysis

The lack of scientific literature about thermal properties of this innovative class of composite materials used for the printed specimens led the authors to study the effects of temperature variation on resistance.

A first set of experiments was conducted on four specimens of two conductive materials, i.e., two CNT and two Eel materials. In particular, R1 and R2 of **Tab2.12** were considered for both CNT and Eel materials. We chose to examine the R1 specimen of Eel, although its resistance significantly differs from the mean resistance, because it could highlight interesting aspects. The experimental setup consists of the following:

i. Four GDM-8351 digital multimeters (Good Will Instruments Co., LTD), for accurate measurements of the electrical resistance;

ii. Two DS18B20 digital temperature sensors;

iii. An Arduino Nano board to acquire data from the temperature sensors;

iv. A Roboze One 3D printer, whose build plate can be heated up to 100 °C and used to control temperature variations;

v. A control program developed in LabVIEW® (by National Instruments Corp.), which allows the measurement system to be easily managed and controlled, providing real-time information about the system's state and the storage of data for post-processing.

The four specimens were placed on a flat support made of polylactic acid (PLA), as shown in **Fig 2.8**, so that they were not in direct contact with the plate of the 3D printer. Moreover, they were enclosed in a plastic box that created a sort of climatic chamber inside, in order to reduce the temperature gradients. The temperature inside the box was measured by means of the two temperature sensors, one positioned near the plate and the other at the top, in order to identify possible temperature gradients. Four benchtop multimeters were used to measure the resistance of each specimen and a control program was developed for data acquisition.

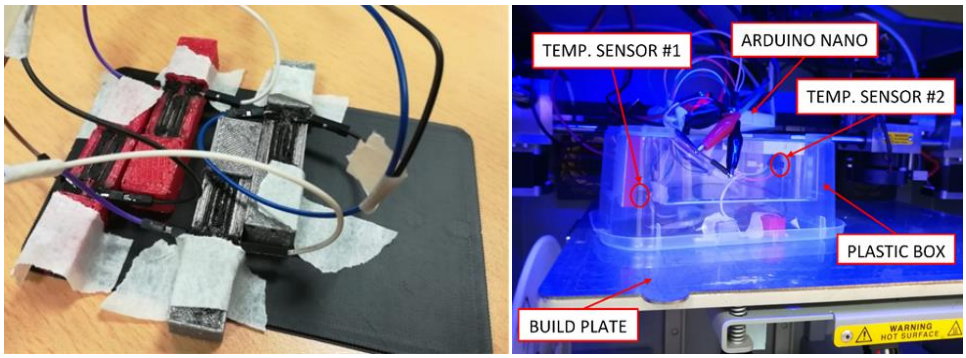

Fig. 2-8- Experimental setup for thermal characterization.

The temperature of the build plate was changed in a range of 25-50 °C, with an increment of 5 °C, for a total of six steps. For each step, a settling time was considered to assure a stable temperature inside the plastic box, within a fixed tolerance. Finally, the plastic box was placed outside the 3D printer, for a faster cooling down process. Obviously, the temperature inside the box was different form the temperature of the plate; in fact, the temperature inside the box only varied from about 18 °C to 34 °C. A temperature difference below about 0.5 °C was observed between the two sensors in stationary or varying temperature tests, which was partly due to the temperature gradients, and partly due to the sensor accuracy. Indeed, since the sensor accuracy is 0.5 °C, temperature differences up to 1 °C constitute compatible measurements. For these reasons, the mean of the temperature measured with the two sensors was considered.

Fig. 2.9 shows the behavior of the measured resistance of each specimen and the mean temperature during the experimental test. To reduce the effect of noise and quantization of the temperature measurement, a moving average of 21 samples was employed.

A positive correlation between the resistance of each specimen and the temperature could be observed. Each time the plate temperature was incremented in steps, the sensor value and resistance increase reached a steady state after a few minutes; this confirms the positive temperature coefficient (PTC) of these composite materials. The small step decreases at about 230 minutes originated when the plastic box was placed outside the 3D printer in the final part of the experiment.

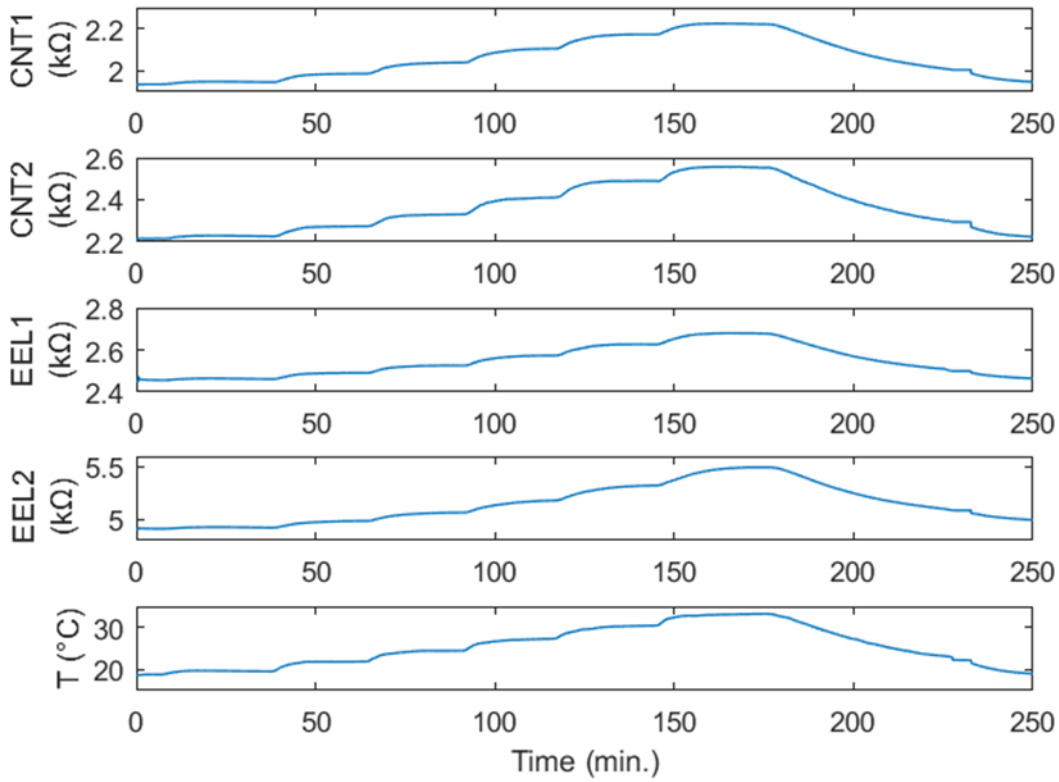

Fig. 2-9 Resistance of the specimens and temperature vs. time

To investigate the relationship between resistance and temperature, the behavior of the resistance of each specimen versus temperature was analyzed as shown in **Fig.2.10**. The presence of hysteresis in the R2 specimen of Eel can be observed. Moreover, all four specimens exhibit a high linearity in the considered temperature range. Hence, linear regression was performed, and an estimation of the temperature coefficient (TC) α_T of each material was obtained as

$$\alpha_T = \frac{R-R_0}{R_0(T-T_0)} \ (°C^{-1}), \tag{8}$$

where R is the resistance at temperature T, R_0 is the resistance at a reference temperature T_0, and α_T depends on the reference temperature considered.

Both specimens of CNT present a TC of about 0.011 $°C^{-1}$ at T_0 = 20 °C, whereas the two Eel specimens present a α_T of about 0.007 $°C^{-1}$ at T_0 = 20 °C. These values are quite high for a temperature coefficient, compared to typical values of Platinum resistance temperature sensors (RTD), which are about 0.0039 $°C^{-1}$ [47]. Moreover, the TC of CNT is of the same order of magnitude as those of commercial negative TC thermistors, which generally present a high TC from about -0.02 to -0.04 $\frac{1}{°C}$ at room temperature [48]. Therefore, also considering the high linearity of the

materials, the obtained results suggest that these materials could be exploited to realize temperature sensors.

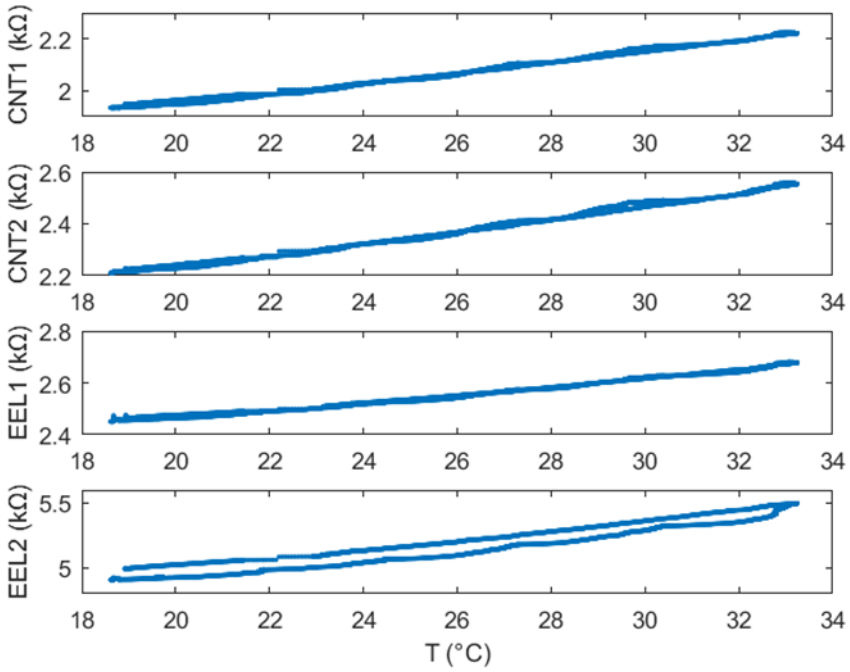

Fig. 2-10- Resistance of each specimen vs. temperature.

It is not easy to interpret these results from a chemical perspective. It should be noted that resistivity of conductive polymer composites filled with carbon (carbon black, carbon fibers, graphene or CNTs) varies greatly according to the different combinations and concentrations of polymer matrices, fillers, deposition and operation temperatures, and the outcome is not easily predictable [49]. Moreover, the precise composition of the deposed material, being a trade secret, may be unknown. Hence it is important to characterize experimentally these materials. It is believed that the main conduction mechanisms are electron hopping and electron tunneling, which lead both to a decrease of resistivity with temperature increase (negative TC); however a competing phenomenon at higher temperatures, namely the increased size of intra-bead air voids, may lead to an increase of resistivity (positive TC) [50]. It can be speculated that the results reported here (positive TC) refer to a temperature range that is, for both the examined materials, above the temperature split point between negative and positive TC.

The observed positive TC of TPU doped with carbon black is somewhat comparable with the one reported in [33] for a different polymer, namely a printed wire of PLA doped with carbon black, which exhibited a positive TC of 0.0284 $\frac{1}{°C}$ for temperature ramp up and 0.0242 $\frac{1}{°C}$ for temperature ramp down.

The observed positive TC for PLA doped with CNTs, instead, is in contrast with several works on polymer matrices (polyurethane [51], PEEK [52]) doped with CNTs, where a negative TC was reported. However, a split point at about 40 °C between negative TC and positive TC was observed in [33] for blocks printed with a graphene-PLA filament. Finally, in [50] split points between about -75 °C and 0 °C were observed for different concentrations of short carbon fibers in ultra-high molecular weight polyethylene, which is compatible with the results reported here.

2.2.5 Conclusions

In conclusion, a Design of Experiment (DoE) has been performed on three different conductive commercial materials to understand how two types of parameters (printing and design parameters) affect the electrical resistance and variability in strain gauges manufactured via Fused Filament Fabrication (FFF), which is the most common and inexpensive 3D printing technology. The following conclusions can be drawn:

- Printing parameters affect the electrical resistance and variability. In particular, from the printing parameter investigation, it could be seen that there is a positive correlation among electrical resistance and variability; indeed, with optimized printing parameters, it was possible to minimize both.
- Layer height is the main printing parameters affecting electrical resistance and variability: switching from low value (0.2 mm) to high value (0.3 mm) a great decrease of electrical resistance and variability occurs. The printing orientation parameter and the interaction among the latter and layer height cause the second and third most important effects. The authors address this behavior to welding effect (explained in 2.2.2 and shown in **Fig.2.4**) which reduces the adhesion among subsequent layers made by conductive material, generating intra-layer voids, and for this reason, an increase in electrical resistance and variability occurs.
- Design parameters affect only electrical resistance and not variability. From their investigation, expected results were achieved: when the number of tracks and the active length of strain gauges increase, then the electrical resistance also increases.
- Regardless of the conductive material used, the best results in terms of resistance and variation minimization are achieved with the following configuration: layer height = 0.3 mm; line width = 0.5 mm; printing orientation = parallel; number of tracks = 4; and active length = 9 mm.
- A thermal analysis on 3D-printed samples was carried out: the temperature coefficient of resistance was preliminarily measured in a 16 °C temperature range for four samples, obtaining values between 0.007 and 0.011 $°C^{-1}$ at T_0 = 20 °C. Obviously, further work will

consider the thermal characterization of these materials in a larger temperature range by using an industrial climatic chamber and a suitable standardized test protocol. Since the resistance of produced samples changes with the applied strain, as preliminarily shown by tests not reported here, a challenge and opportunity will be to discriminate between mechanical and thermal stresses. This has been done, for example, with optic fiber sensors, where distributed measurements of strain and temperature can be performed simultaneously. The fabrication and the characterization of a 3D printed load cell, which adopts a Wheatstone bridge configuration aimed at reducing thermal effects and measuring only applied forces, was presented by the authors in [23].

This work lays the foundation for further analysis to more deeply characterize these recent materials and their printing processes, which could find application as smart materials with temperature, force and pressure sensing capabilities in a wide range of fields, from wearable sensors to medical devices and soft robotics.

2.3 Piezoresistive-based sensors: monolithic fabrication of a load cell equipped with four embedded strain gauges

In this work, the exploitation of Fused Filament Fabrication (FFF) to manufacture a load cell using double extrusion of conductive and non-conductive commercial materials in a single-step printing cycle, is presented. A commercial thermoplastic polyurethane (TPU) was employed for the fabrication of the load cell main body, while a conductive polylactic acid was used for the fabrication of the four embedded strain gauges, which have been connected in a full Wheatstone bridge configuration. Subsequently, several tests were performed, firstly to characterize the behaviour of each strain gauge and then to characterize the load cell. The tests showed that the strain gauges are sensible to compressive and tensile deformation and that the load cell's voltage, obtained by connecting the four strain gauges in a full Wheatstone bridge, decreases as the force applied increases. In particular, a load cell sensitivity of 0.088 mV/(V· g) in a tested measurement range up to 100 g was found. This work demonstrates the potential of FFF technology in the sensor manufacturing field and that it is possible to integrate sensitive elements into non-sensitive elements without additional assembly processes by using low-cost commercial filaments and 3D printers.

2.3.1 Materials and methods

To create the sensor, two commercial materials were chosen. Polyurethane thermoplastic with a Shore A hardness of 95 (TPU95A) was used to fabricate the non-conductive parts of the load cell. It is characterized by a tensile modulus of 26 MPa and elongation at break of 580%, and it was developed by Ultimaker ltd. To create the sensitive elements, namely, the four strain gauges, we used AlfaOhm filament developed by FiloAlfa and LATI. It is a conductive PLA, characterized by a resistivity of 15 Ohm/cm along the layers and 20 Ohm/cm perpendicular to the layers (data obtained by filament data-sheet). One of the reasons why TPU95A and AlfaOhm were used is that they have similar printing temperatures. Indeed, since two different filaments are used, particular attention was paid to the choice of printing temperature in order to avoid adhesion between the two materials and cross-contamination issues. As demonstrated by Tamburrino et al [53] the adhesion strength in multi-material FFF printing depends on several factors such as infill pattern, infill density and printing orientation. The open-source software Cura 3.6.0 was chosen to slice the 3D model, to control the printer, and to set up process parameters. The 3D printer used is an Ultimaker 3, a dual-extruder FDM printer that enables the usage of two different filaments in the same printing cycle thanks to a switching system between the two nozzles.

The sensor is composed of three different elements: i) four strain gauges, ii) the load cell body, and iii) two leveling layers (see **Fig.2.11**). Each of the four strain gauges is composed of 4 tracks and a grid length of 15 mm that includes end loops 4 mm long needed to reduce stress sensitivity in the axis perpendicular to the deformation axis. The strain gauges were designed following a Design for Additive Manufacturing (DfAM) approach. Indeed, the single track's thickness is 1 mm; in this way, it is possible to print the strain gauges' tracks with only two lines of extruded conductive filament (by setting line width parameter = 0.5 mm and choosing to print strain gauges perpendicularly to the build plate) to have greater uniformity of the conductive filaments and to reduce resistance values. The single track width of 1 mm is equal to the distance between two adjacent tracks. The strain gauges are equipped with two pads, located on the same side, that are 5 mm long, 6 mm wide, and have a thickness of 1.5 mm (not 1 mm like the track thickness) to solder the electrical wires more easily. The second sensor element is the body of the load cell, which has a binocular shape, length of 96 mm, width of 14 mm, and height of 26 mm. At the opposite ends of the body, there are i) an M5 hole to connect the load cell to a supporting frame during the tests thanks to a screw and ii) an M4 hole were to place the calibrated weight. The binocular shape was chosen because, in this way when a force is applied on M4 hole (while the whole load cell is fixed to a supporting frame thanks to M5 hole) it is generated an S-shaped deformation. This kind of deformation generates positive and negative strain zones on the surface that are close to each other and this particular behavior involves a very less sensitivity to load application point comparing to single-beam load cell. In **Fig. 2.11 f)** it is shown the Finite Element Analysis (FEA) computed with Autodesk Fusion360 on the load cell body with the chosen binocular shape, it is possible to see that when a force of 100 g is applied on M4 hole it is generated an S-shaped deformation with a maximum displacement of 2.128 mm. The output signal in single-beam load cell depends on the bending moment meanwhile with the binocular design it is possible to reduce this kind of problem. The last elements are the top and bottom "leveling layers" which reproduce the strain gauges' geometry in negative; these are needed to fill the empty spaces around the strain gauges. From a manufacturing point of view, the sensor was 3D printed with the strain gauges perpendicular to the build plate, as shown in **Fig.2.12 a)**, for several reasons: i) in this way, each strain gauge is built in the same way so the resistance value of the four strain gauges should be the same or comparable; ii) this orientation choice does not involve the usage of supports; and iii) in this way, the height of the sensor on the build plate is 14 mm, while if it was printed with strain gauges parallel to the build plate, the height would be 26 mm; as a consequence, this choice decreases adhesion problems.

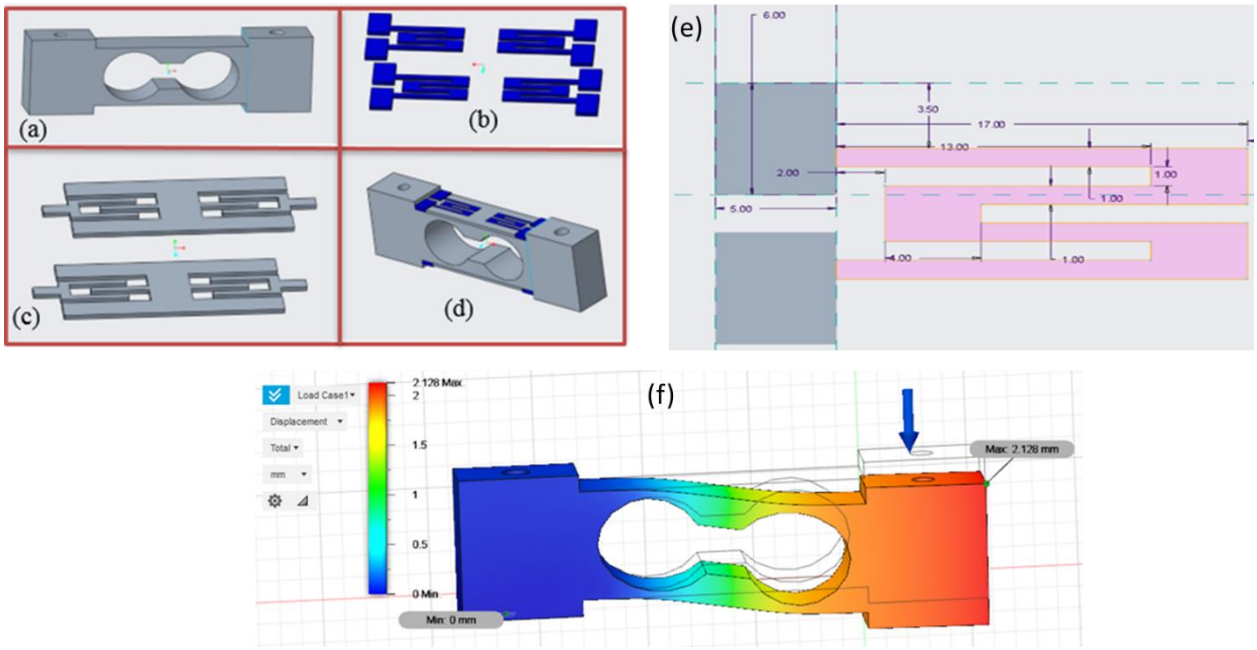

Fig. 2-11- a) main body of the load cell, b) four strain gauges, c) leveling layers, d) whole load cell with embed strain gauges, e) strain gauge dimensions (mm), and e) FEA analysis.

Moreover, to improve the adhesion between the build plate and the initial layer and to reduce the deformation problems in the bottom of the structure it was necessary to heat the build plate to 70 °C and use the brim strategy on Cura ™, which is a thin layer of materials between the build plate and the initial layers of the sensor. The diameter of each nozzle was 0.4 mm, and the most relevant process parameters, chosen on the basis of a trial-and-error approach, are shown in **Tab.2.13**. From this it is possible to note that the printing temperatures of TPU95A and AlfaOhm needed to melt the solid filament in the print head differ by only 3 °C; this ensures good adhesion between the two different materials.

The total time estimated by the slicing software was 2 hours and 11 minutes, while the total cost was 2.76 € (2.41 € for TPU 95A and 0.35€ for AlfaOhm). Another important process parameter is retraction. This was disabled for the AlfaOhm filament to avoid filament breakage during the printing process; indeed, Carbon black makes this filament much more brittle than simple PLA, and with the Ultimaker3 printer being a bowden printer, the feeder is located not above the print head but in the bottom, increasing the probability of filament breakage during printing jobs longer than one hour. After the sensor manufacturing, electric wires were soldered at the temperature of 350 °C to each pad of the strain gauges. The proposed 3D printed load cell equipped with four embedded strain gauges is shown in **Fig.2.12 b).**

Tab. 2-13- Process parameters for the load cell with embedded strain gauge fabrication.

Process parameters	**TPU95A**	**AlfaOhm**

Printing speed (mm/s)	45	20
Layer height (mm)	0.2	0.2
Line width (mm)	0.5	0.5
Infill density (%)	100	100
Infill pattern	Gyroid	Lines
Printing temperature (°)	223	220
Flow (%)	106	120
Wall line count	1	1
Retraction	ON	OFF

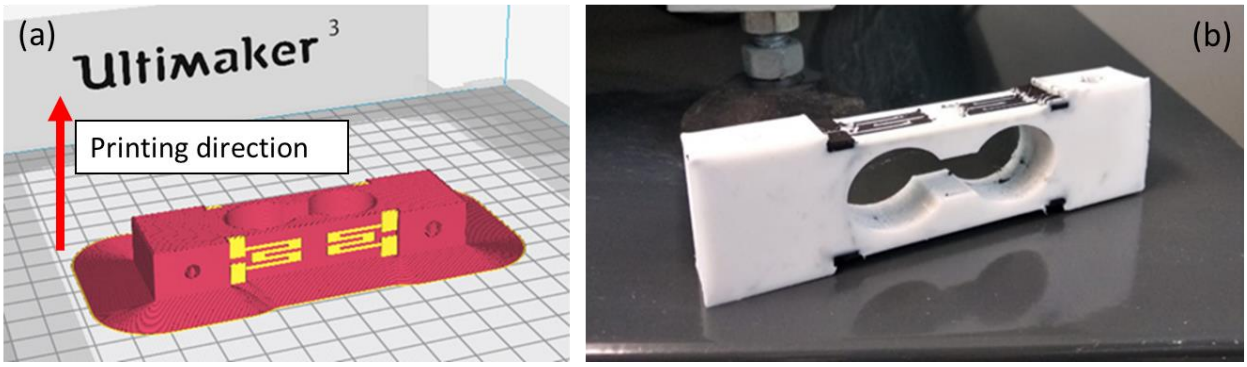

Fig. 2-12- a) load cell in the slicing software, and b) 3D printed load cell with the four embedded strain gauges.

2.3.3 Characterization

In this section, the results of the characterization of the manufactured load cell are presented. As a first step, the individual resistances of the four strain gauges of the load cell were measured for

different applied weights under loading and unloading cycles. Subsequently, the whole load cell behavior was analyzed, quantifying its hysteresis and its sensitivity to weight positioning.

The first tests were performed to investigate the strain gauges' behavior by measuring the resistance variations when the applied force was changed. The measurement setup (shown in **Fig.2.13 a)**) consisted of *i)* a support framework to fix the load cell by means of an M5 hole placed at the end of the body of the load cell and *ii)* a digital benchtop multimeter, model GDM-8351 by GW Instek, for measuring resistances. In **Fig.2.13 b)**, it is possible to see the position of each strain gauge in the load cell and the point where the force is applied. Initially, the resistance of each strain gauge was measured without any applied force, and 2.5 kΩ, 2.1 kΩ, 1.9 kΩ, and 2.1 kΩ were obtained for strain gauges A, B, C, and D, respectively. The electrical resistance among the four strain gauges is similar each other but not the same, this behavior could depend on a not uniform electrical resistance in the raw filament before being melted together with noise effects occurring during extrusion, such as vibrations, room conditions, etc.

To measure the characteristic curves of the strain gauges, four calibrated weights (10, 20, 20, and 50 g) were combined and positioned above the M4 hole in order to obtain the following final weights: 10, 30, 50, and 100 g. The procedure used to obtain the calibration points is shown in **Tab.2.14**

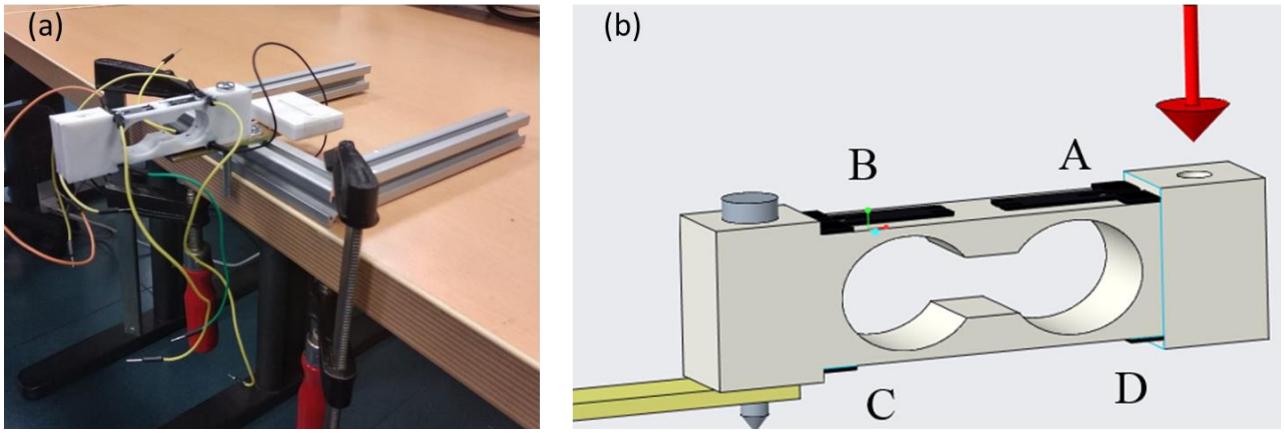

Fig. 2-13- a) Measurement setup, and b) load cell scheme

Tab. 2-14- Measurement protocol.

Weight added (+) / weight removed(-) (g)	**Total weight (g)**
---	0
(+) 10	10
(+) 20	30
(+)20	50

(+)50	100
(-) 50	50
(-) 20	30
(-) 20	10
(-) 10	0

The proposed characterization cycle consisted of the application of the selected weights in ascending (loading phase) and descending (unloading phase) order, passing through nine calibration points overall. In this way it is possible to evaluate hysteresis phenomena of the strain gauges. The procedure requires a waiting time of one minute after placing the weight before measuring the resistance value; this is because it was observed experimentally that such a delay ensures the reaching of a steady state. The relation between the applied force and change in resistance is shown in **Fig.2.14**. It is possible to highlight that for strain gauges A and C, which work in compression, the resistance decreased as the applied weight increased; meanwhile, for strain gauges B and D, which work in tension, the resistance increased when the applied weight grew. To evaluate the hysteresis of the strain gauges, the differences between the load and unload resistance values when the same weight was applied were calculated. The experimental results show that for each strain gauge the hysteresis phenomena is always present; this may be due to the viscoelastic behavior of the conductive material. In correspondence to the resistance for zero weight, the resistance values measured before loading and after unloading phases differed by 1.8, 4.2, 4, and 1.5 Ω for strain gauges A, B, C, and D, respectively. The hysteresis values for strain gauge D can be better appreciated in **Tab.2.15.**

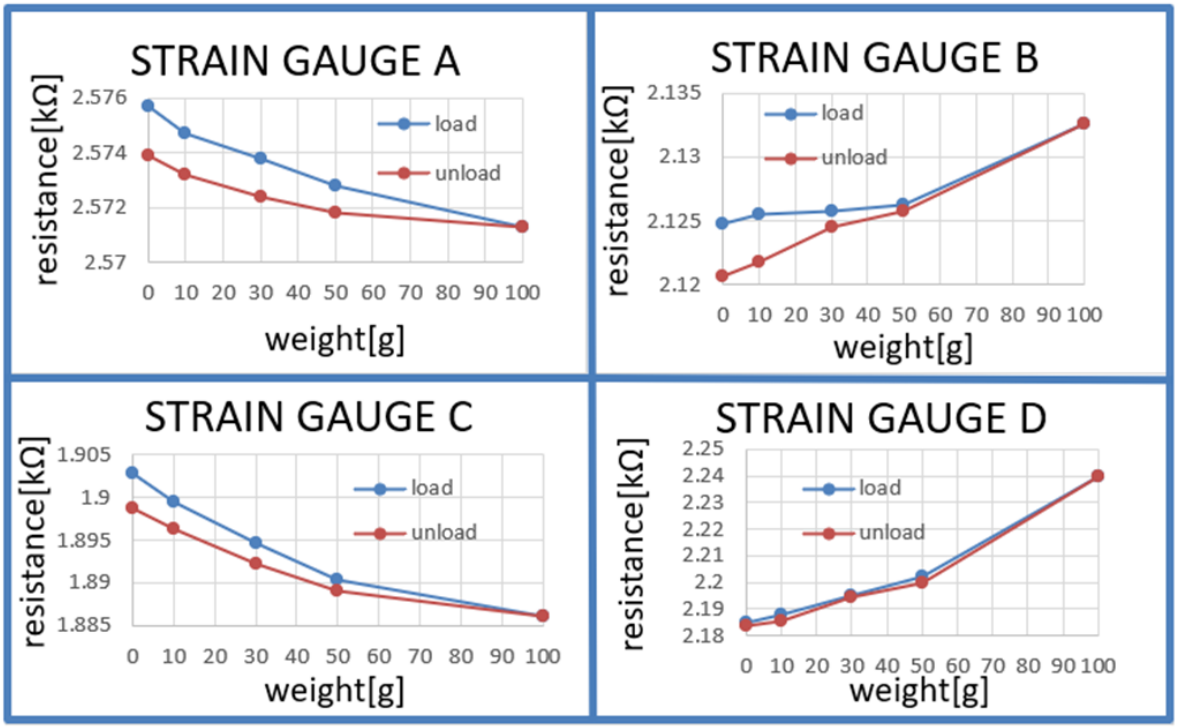

Fig. 2-14- Resistance vs. weight for each strain gauge of the load cell.

Tab. 2-15- Hysteresis for strain gauge D

Weight (g)	**Load resistance (kΩ)**	**Unload resistance (kΩ)**	**Hysteresis (Ω)**
0	2.185	2.1835	1.5
10	2.1877	2.1858	1.9
30	2.1951	2.1942	0.9
50	2.202	2.2	2
100	2.2398	2.2398	-

After carrying out the characterization of the individual strain gauges, the performance of the load cell with the four sensors connected in a full Wheatstone bridge configuration (see **Fig.2.15a)**) was evaluated. The Wheatstone bridge was powered with a supply voltage of 5 V. The test protocol was the same as that used for the strain gauge characterization, with the only difference being that the output value is not a resistance change but the output voltage of the Wheatstone bridge. When the applied weight was increased, the output voltage decreased. When no weight was applied, the voltage output was 47.7 mV; this is because the bridge is not balanced. Indeed, the strain gauges' resistance values are similar to each other but not the same. In general, the resistance mismatch between strain gauges should be minimized to reduce load cell nonlinearity and drift. The experimental results (shown in **Fig.2.15b)**)highlight that the load cell also exhibits hysteresis phenomena as indicated in **Tab.2.16**. On the other side, the bridge connection greatly reduces the effects of the nonlinearity of

individual strain gauges that was observed in **Fig.2.14**. To evaluate the input/output characteristic of the load cell, the coefficients of linear regression on experimental data were calculated by obtaining the following equation (9):

$$\hat{V}_{out}(w) = V_s \cdot (-0.088 \cdot w + 9.361) \qquad (9)$$

where w is the applied weight and V_{out}, and V_s are the output and supply voltages of the Wheatstone bridge, respectively. The offset value ($V_s \cdot 9.361$) can be reduced by performing a zeroing procedure before load cell usage. Also, the load cell is characterized by a high sensitivity of 0.088 mV/(V· g). To quantify the accuracy of the load cell liner model, the relative root-mean-square error was calculated, and a value of 19.54 % was obtained in equation (10):

$$e_V = \sqrt{\frac{1}{N}\sum_{i}^{N}\left(\frac{\hat{\mathrm{V}}_{\mathrm{out}}(w_i) - \mathrm{V}_{\mathrm{out}}(w_i)}{\mathrm{V}_{\mathrm{out}}(w_i)}\right)^2} \qquad (10)$$

where $N = 9$ is the number of calibration points, $w_1, \ldots, w_N$ are the calibration weights, and $V_{out}(w)$ and $\hat{V}_{out}(w)$ are the voltages measured and estimated by means of Equation (9), respectively.

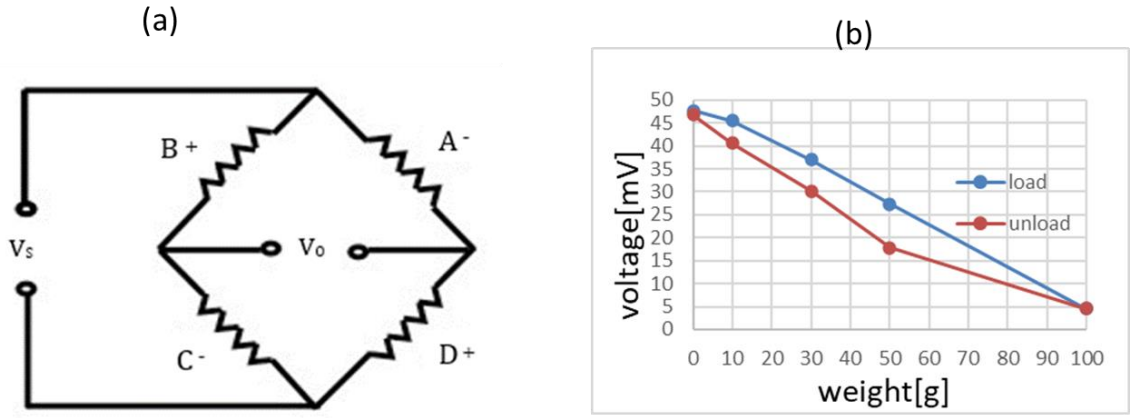

Fig. 2-15-a) Wheatstone bridge configuration where '+' indicates compression while '–' indicates tension, and b) Voltage output vs. weight for the load cell.

Tab. 2-16- Hysteresis of the load cell

Weight (g)	Load voltage(mV)	Unload voltage(mV)	Hysteresis(mV)
0	47.7	46.8	0.9
10	45.5	40.5	5

30	37	30.2	6.8
50	27.3	17.8	9.5
100	4.6	4.6	-

The experimental results listed in **Tab.2.16** highlight that the hysteresis phenomena increases in magnitude with the applied weight. After one minute from the end of the first test cycle, the same test was repeated in order to evaluate the data repeatability. To quantify the repeatability error, the output voltage difference between two measurements at the same weight and during the same phase (load or unload phase) was calculated in equation (11):

$$e_r = \left|V_{out_1} - V_{out_2}\right| \qquad (11)$$

where V_{out_1} and V_{out_2} are the output voltages of Tests 1 and 2, respectively. The results for weights 0, 10, 30, 50, and 100 g in the load and unload phases are shown in **Tab.2.17**.

Tab. 2-17- Repeatability test.

Weight (g)	**Phase**	V_{out_1} **(mV)**	V_{out_2} **(mV)**	$\mathbf{e_r}$ **(mV)**
0	load	47.7	47.5	0.2
10	load	45.5	45.8	0.3
30	load	37.0	36.2	0.8
50	load	27.3	27.5	0.3
100	load	4.6	4.3	0.3
50	unload	17.8	19.4	1.6
30	unload	30.2	30.3	0.1
10	unload	40.5	41.5	1.0
0	unload	46.8	46.5	0.3

In the performed experiments, the repeatability error was lower in the load phase except for when the applied weight was 30 g.

A new test was performed to investigate the load cell's behavior when higher weights were applied. Unlike the previous one, this test did not consist of a load and unload phase, but the test protocol

included the application of weights according to the sequence 200, 0, 150, 0, 100, 0, 50, and 0 grams; the output voltage was measured after one minute from the change of the weight, and the output voltage at the intermediate zero weights was not considered. The output voltages corresponding to the applied weights are listed in **Tab.2.18**, and they show that for weights over 100 grams, the output voltage decreases, indeed it takes negative values.

Tab. 2-18- Test using higher weights

Weight (g)	**Output Voltage (mV)**
200	−40.8
150	−21.3
100	−10
50	17.6
0	42.3

In all experimental tests, the application point of the weight was always the same (above the M4 hole of the load cell); hence, two different tests were performed to analyze how the position of the application point of the weight affected the output voltage due to a different moment arm. For this aim, a plate was printed in PLA material using the same 3D printer used to manufacture the load cell. The plate, shown in **Fig.2.16**, is composed of a circular structure with diameter of 12 mm where the calibrated weight can be placed and a rectangular structure under the circular one to fix the whole balance to the M4 hole of the load cell by means of a screw and a nut. The total printing time estimated by the slicing software was 1 hour and 12 minutes.

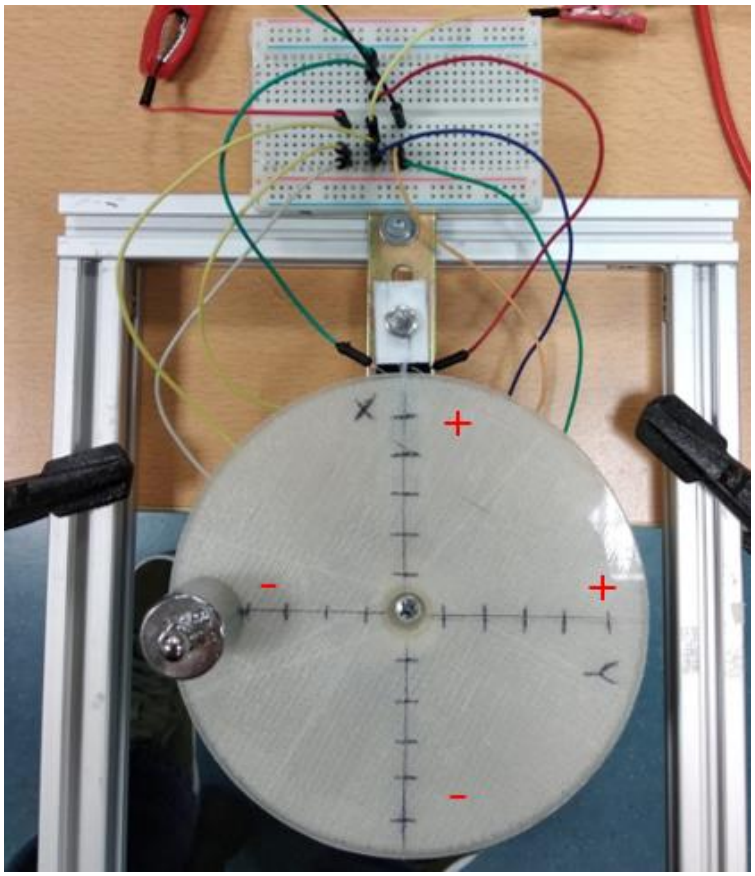

Fig. 2-16- Top view of the plate placed above the M4 hole of the load cell

x and *y* axes were drawn on the plate, centered on the screw head, with 10 mm ticks (see Fig.12). Afterwards, a test was performed to evaluate the effect of the application point on the output voltage using the 50 gram weight. The test protocol was the following (see **Tab.2.19**): the 50 g weight was placed above the origin, and after 1 minute the output voltage was measured; afterwards, the weight was moved and placed on the first notch of the *x* axis (x = 10 mm and y = 0 mm), and after 1 minute the output voltage was measured; this procedure was repeated for each tick of the *x* axis (for both positive and negative positions). The same test was repeated for the y axis (x = 0 mm). To quantify how the position of the application point of the weight affects the output signal, the error due to the weight position (e_p) was calculated as shown in equation (12):

$$e_p(x,y) = \left| \frac{v_{out}(0,0) - v_{out}(x,y)}{v_{out}(0,0)} \right| \qquad (12)$$

where $v_{out}(x,y)$ is the voltage corresponding to weight position (x,y). The results for x and y chosen in the range from −50 mm to 50 mm with step size 10 mm are shown in **Tab.2.19**.

Tab. 2-19- Application point test with a 50 g weight.

***x* axis**	***y* axis**	**V_{out} (mV)**	**e_p (%)**
0	0	–63.2	---
10	0	–60.0	5.06
20	0	–58.5	7.44
30	0	–58.0	8.23
40	0	–53.6	15.19
50	0	–49.0	22.47
–10	0	–67.0	6.01
–20	0	–68.0	7.59
–30	0	–76.3	20.73
–40	0	–86.2	36.39
–50	0	–88.9	40.66
0	10	–61.7	2.37
0	20	–60.3	4.59
0	30	–59.6	5.70
0	40	–58.8	6.96
0	50	–52.2	17.41
0	–10	–62.1	1.74
0	–20	–61.5	2.69
0	–30	–46.8	25.95
0	–40	–32.6	48.42
0	–50	–20.8	67.09

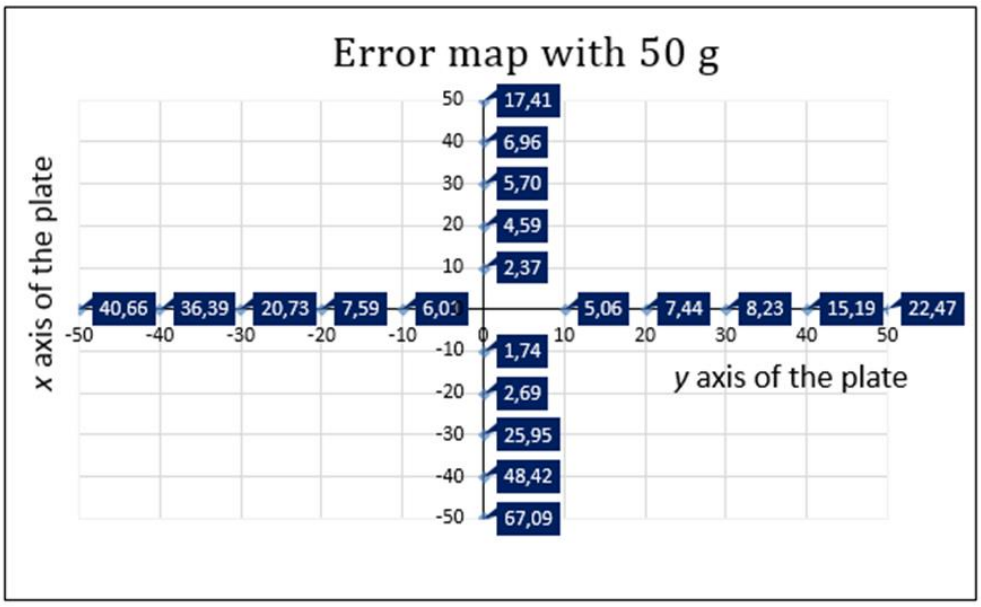

Fig. 2-17- Position error map on the x axis and y axis of the plate with a 50 g weight

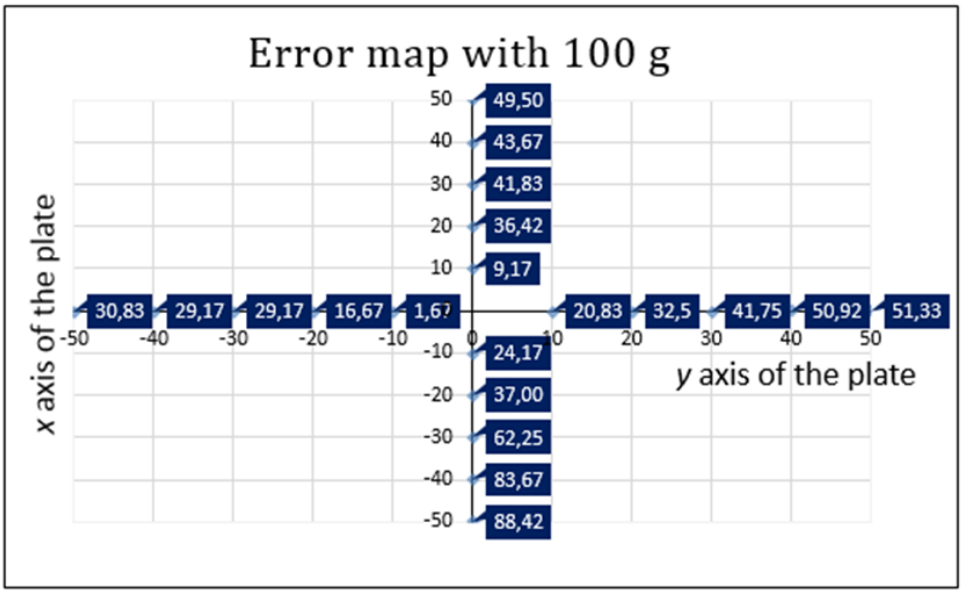

Fig. 2-18- Position error map on the x axis and y axis of the plate with a 100 g weight

Analyzing the behavior along the x axis of the plate, it is possible to note that near the origin the position errors obtained in correspondence to the positive and negative variations are comparable (i.e., for x ranging from −20 mm to 20 mm). Moving away from the origin, the position errors for the negative semi-axis are higher than for the positive semi-axis; indeed, when x = 50 mm the error is 17%, while when x = −50 mm the error is 67%. For the y axis, the behavior is like that of the x axis; indeed, near the origin, the position error is comparable between the positive and negative semi-axes, and far from the origin (above y = 30 mm and below y = −30 mm) the error grows much more in correspondence with the negative semi-axis (e.g., the errors at y = 50 mm and y = −50 mm are 22% and 40%, respectively). In **Fig.2.17** a map of the error as a function of the x- and y-axis is provided.

Moreover, for each positive value of y, the error is always lower than for the correspondent negative value. Hence, the load cell is sensible to the application point of the weight, but the behavior on the positive and negative semi-axes of x and y is not the same; indeed, far from the origin, the position error is always higher for the negative semi-axes of both x and y. The same test was repeated using a 100 g weight. The error as a function of the position of the 100 g weight is shown in **Fig.2.18**. It is possible to see that along the y axis, the behavior is opposite to that shown with the 50 g weight; indeed, in this case, for negative values of y the position error is always lower than that for positive values of y. On the other hand, along the x axis, the error is always lower for positive x compared to negative x, i.e., for $x = 50$ mm and $x = -50$ mm, the errors are 50% and 88%, respectively. Moreover, a greater asymmetry is observed between the positive and negative positions, for both the x and y axes, already near the center. For example, at $y = 10$ mm and $y = -10$ mm, the errors are 21% and 2%, respectively, while for the previous 50 g weight, the asymmetry near the center was smaller.

2.3.4 Conclusions

In this work we showed the feasibility of manufacturing a sensor with embedded conductive elements with FDM technology by using two different commercial materials (conductive and non-conductive ones) in a single printing cycle and without an assembly process by taking advantage of a dual-extruder 3D printer. Achieving process uniformity and repeatability is demanding; however, thanks to the study of better process parameters, design parameters, and printing strategies, it was possible to obtain a load cell with four embedded strain gauges having similar resistance which can be usefully connected in a full Wheatstone bridge configuration. From the characterization of the load cell, it stands out that the output voltage changes when the applied weight increases, with a sensitivity of 0.088 mV/(V· g) in a tested measurement range up to 100 g. That sensitivity is high if compared to typical aluminum-alloy load cells having the same 100g range, which reach values up to 0.03 mV/(V· g).

Even though the load cell was designed with a *beam-type* layout, which is known to minimize the effects of weight position (i.e., force momentum) on force measurement, a significant error due to position was observed; this is due to the high degree of deformation such a soft structure, made of TPU, is subjected to. On the other hand, the use of soft materials paves the way to applications such as wearable and stretchable sensors. Certainly, with new progress and discoveries in the field of conductive filaments, this new manufacturing approach will become more widespread for producing structures that have embedded force sensors and, at the same time, have the advantage of avoiding the assembly process. Future challenges will be i) the reduction of hysteresis phenomena using other

conductive materials without viscoelastic behavior ; ii) the reduction of the effect of the force application point on the output voltage by studying a new design and using other materials, such as PLA or ABS, for the body of the cell and iii) an investigation about fatigue effects on future AM-based load cells to better understand their behavior before widespread use can be realized.

2.4 Capacitive-based sensor: liquid level sensing

The aim of the present research is the one-shot Additive Manufacturing of a low-cost capacitive sensor for liquid level sensing. The Material extrusion (MeX) technology was used to fabricate the proposed sensors (composed of a flexible substrate, two conductive electrodes and a top flexible coverage) and a Design for Additive Manufacturing (DfAM) approach in conjunction with the 3D printing forces analysis was performed. Very thin conductive tracks (0.5 mm) were manufactured to obtain a sensor having a final capacitance value of 125 pF, readable by common laboratory instrumentation.

The sensor has been tested for the liquid level sensing using two different liquids, i.e., sunflower oil and distilled water, exhibiting very good sensitivity of 0.078 $\frac{pF}{mm}$ and 0.79 $\frac{pF}{mm}$**,** respectively, with high repeatability, thus obtaining sensing performances comparable with that of more expensive sensors found in literature. Moreover, the proposed sensor showed high linearity ($R^2 \geq 0.997$), which resulted in a maximum propagated level error of 1.4 mm.

The present research proves that the inexpensive MeX technology can be successfully employed for the fabrication of high-performance capacitive sensors: the sensor manufacturing cost is 0.38 € and no manual assembly tasks were performed. This study lays the foundation for the one-shot fabrication of smart structures with capacitive sensors on board, saving manufacturing time and cost.

2.4.1 Materials and methods

At the state of the art, material extrusion (MeX) technology has been unexploited for the fabrication of coplanar capacitive sensors due to the low manufacturability of conductive materials. In accordance with the coplanar capacitive sensor working mechanism (see eq. (1) and eq. (2)), the more the conductive tracks are thin and close to each other, the higher the final capacitance value is. The possibility to obtain high capacitance values readable by common measurement instrumentation is a key requirement for the fabrication of low-cost measurement circuits.

The main problem related to the additive manufacturing of thin conductive tracks has been addressed by *i)* exploiting the Design for Additive Manufacturing (DfAM) approach, and *ii)* studying the forces involved during the manufacturing process to avoid the breakage of the brittle conductive material during the fabrication.

The proposed capacitive sensor was designed to be used for liquid level sensing, and it was manufactured in a single shot 3D printing cycle: it consists of i) a flexible substrate of thermoplastic polyurethane (TPU) , ii) two coplanar electrodes made up of conductive polylactic acid (CPLA), and

iii) a top cover made up of TPU which seals off the electrodes, thus avoiding the direct contact of the electrodes with the liquid during the sensing. After the manufacturing process, the sensor covered with a top layer of TPU (henceforth called TPU-covered) is ready to be used for liquid level sensing. The overall sensor dimensions are shown in **Fig.2.19** : in particular, the substrate is 171 mm long and 55 mm wide, while its thickness is 0.4 mm; the top TPU cover is 0.3 mm thick.

The design of the electrodes is a crucial point to obtain a measurable capacitance value: on one hand thin conductive tracks really close to each other are required to obtain readable capacitance values, on the other hand technological constraints must be taken into account when conductive filaments are extruded. In accordance with [54] the capacitance of coplanar capacitive sensors is defined by the following equation (13):

$$C = Nl\varepsilon_0\varepsilon_{ea}\frac{K(\sqrt{1-k_0^2})}{K(k_0)} \qquad (13)$$

where C (pF) is the capacitance of the whole sensor, N (dimensionless) is the number of electrodes pairs, l (mm) is the length of each electrode along x-axis, ε_0 is the vacuum dielectric constant ($\frac{\text{pF}}{\text{mm}}$), ε_{ea} (dimensionless) is the effective dielectric constant of capacitive sensor in the air (further details about this parameter are well explained in [54]), and $K(k_0)$ (dimensionless) is the elliptical integral of the first kind in terms of k_0, where k_0 is defined as follows (equation (14))

$$k_0 = \frac{s}{s+2w} \qquad (14)$$

where s (mm) and w (mm) are the electrodes spacing and width, respectively. Thus, the only design parameters that can be set in order to maximize the final capacitance are N, l, s, and w .

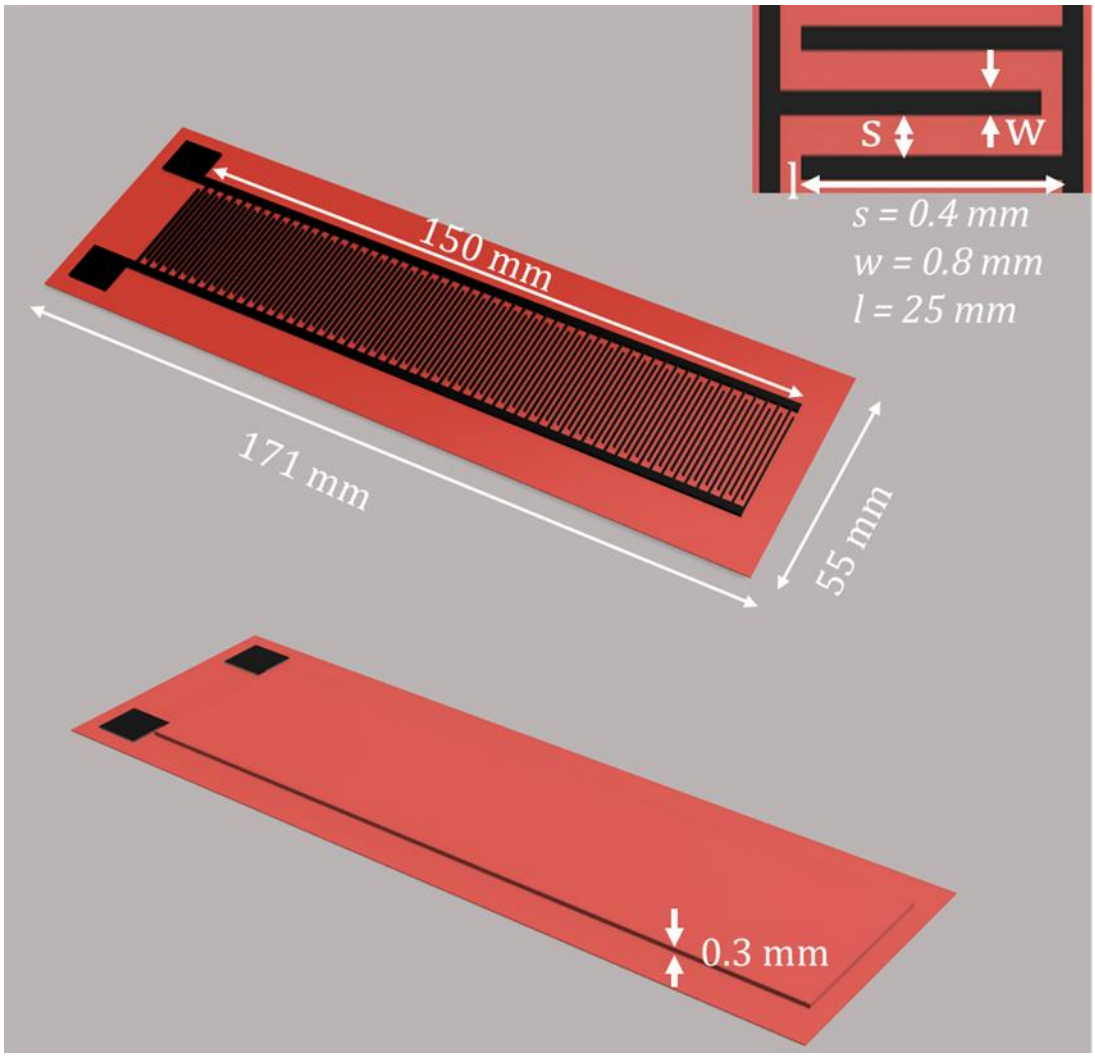

Fig. 2-19- CAD design of the proposed capacitive liquid level sensor.

As a matter of fact, the free design variables are the l parameter (length of the single electrode, as shown in **Fig. 2.19**) and the overall electrodes length, which have been arbitrarily set as 25 mm and 150 mm, respectively. Consequently, considering all the manufacturing constraints (detailed in section 2.2), it was found the best N, s and w values to maximize the final capacitance to be 57, 0.8 mm and 0.5 mm, respectively, thus obtaining a predicted capacitance of 82.7 pF from eq. (13).

The DfAM approach was used to successfully set w: considering the printing orientation (sensor flat on the build plate with the flexible substrate in contact with it), the w parameter depends on the line width process parameters, which in turn must be equal to the nozzle diameter. From equation (13), the need to minimize w stands out: the following requirement is in contrast with conductive materials processability (the bigger the nozzle, the less are the printing issues such as filament breakdown and coggled nozzle). By setting further process parameters, it has been possible to use a 0.5 mm nozzle and set $w = 0.5$ mm: it means that every conductive track will be the result of one single extruded line. Similar considerations can be drawn for the s parameter: using a trial-and-error approach it was

found that the minimum spacing between two adjacent conductive tracks allowed by the FFF machine was 0.8 mm. By setting lower values, an overlapping between adjacent conductive tracks occurred, due to the filament expansion after the extrusion: in this way, no capacitance values were measured, but only resistance ones. The electrodes thickness was arbitrarily set as 0.8 mm; however, lower values are allowed. Moreover, the sensor was equipped with two square pads (side equal to 10 mm) to weld electrical wires for the connection with the measurement instrumentation.

The sensor has been fabricated in a monolithic way, exploiting the advantages of the FFF technology. A multi-material extrusion 3D printer (Ultimaker 3, Ultimaker, Netherland) and two commercial materials were used (see **Tab. 2.20**). For TPU and CPLA, 0.8 mm and 0.5 mm nozzles were used, respectively

Tab. 2-20- Materials used for the sensor manufacturing

Material	Name	Properties	Manufacture	Sensor parts
Thermoplastic polyuretane	TPU	• Shore A hardness equal to 95 • Elongation at break equal to 580%	Ultimaker (Netherland)	• Flexible substrate • Top cover
Conductive Polylactic acid	CPLA	• Resistivity of 15 Ω · cm along the layers • Resistivity of 20 Ω · cm perpendicular to the layers	FiloAlfa (Italy)	• Electrodes • Pads

As a matter of fact, the smaller the nozzle size is, the more the level of detail is when conductive materials (generally PLA-based doped with CNTs) are used: the general advice provided by filaments suppliers regards the usage of nozzles having a diameter equal to 0.6-0.8 mm. The main problem which could occur when nozzles smaller than 0.6 mm are employed is the filament breakdown between the gears pushing it into the extruder: the doping elements (i.e., CNTs) scattered into the plastic matrix make the filament very brittle.

To overcome this issue, it becomes crucial to set the right process parameters to reduce the printing force (F_p): in this way the force between the gears and the raw filament (F_{gf}), which is responsible for the filament breakage, will be reduced as well, thus avoiding the filament breakage. Indeed, F_{gf} must be higher than F_p: in this way the gears will push the raw filament into the extruder.

$$F_{gf} \geq F_p \qquad (15)$$

In **Fig. 2.20**, a simplified model of the forces occurring during the manufacturing process, is provided (the friction among the raw filament and the teflon guiding tube has been neglected).

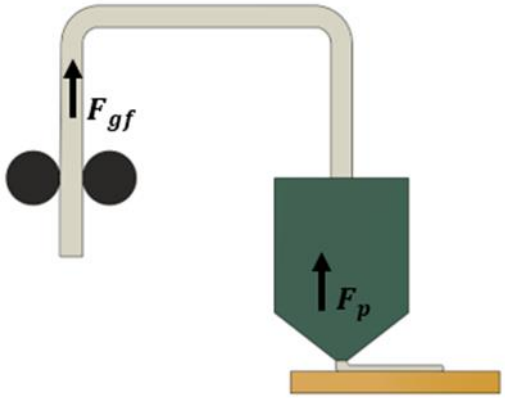

Fig. 2-20- Simplyfied sSchematic diagram of the printing forces occurring during the manufacturing process.

In accordance with [55], F_p can be calculated as the contribution of two forces:

$$F_p = F_n + F_{dep} \qquad (16)$$

where F_n is the "nozzle force" (equation (17)) and it refers to the melting process taking place inside the extruder (the extruder can be divided into 3 different regions: in each one, a pressure increment occurs), while F_{dep} is the "deposition force" referring to the interaction between just extruded filament and build plate (or previously extruded filament) taking into account the counterpressure related to melting filament downstream of the nozzle: this force has been introduced by Percoco et al [55] in 2021 and it links process parameters of the extruded filament with the classic F_n, well known in scientific literature [56]:

$$F_n = (\Delta P_1 + \Delta P_2 + \Delta P_3) A_f \qquad (17)$$

where ΔP_1, ΔP_2 and ΔP_3 is the pressure increment into the three extruder regions, while A_f is the cross-section of the filament. To better understand each term included into F_n and F_p and how they affect the total printing force F_p, the reader is addressed to [55] [57].

The nozzle geometry of this work is the same as [55] (Ultimaker nozzle), while rheological parameters for CPLA are not available in scientific literature and classic PLA ones have been used.

It has been pointed out that to reduce F_p, two parameters need to be set: printing temperature and layer height, when they increase, the total printing force decreases (see equation (18)).

$$F_p = f^{-1}(layer\ height, printing\ temperature) \quad (18)$$

It appears clear that the only way to manufacture thin conductive tracks (and reduce the total printing force) is to maximize the layer height and the printing temperature. Hence, the exploitation of the 0.5 mm nozzle for the brittle CPLA conductive filament is allowed by setting *i)* the layer height (lh) parameter equal to 0.2 mm, unlike for the classic MeX scenario where high details are reached by setting a low layer height value (i.e. 0.05 mm) [58], and *ii)* the printing temperature(T_p) equal to 230 °C, higher than the suggested printing temperature range of 190-210 °C provided by the supplier.
A 2^3-factorial plan (three repetitions) was conducted to set the best lh and T_p values: the number of printing successes for every combination (no filament breakdown and no nozzle clogging) extruding CPLA were measured. Three values of lh (0.1, 0.2 and 0.3 mm), and T_p (190, 210, and 230 °C) were studied and the best combination resulting in the maximization of the printing success was found to be lh equal to 0.2 mm, and T_p equal to 230 °C. In this way, thin conductive tracks with a width (w parameter in section 2.1) of 0.5 mm were fabricated without any filament breakdown despite a huge number (more than 20) of consecutive printed sensors.
In **Tab.2.21** the main process parameters set for both materials are summarized.

Tab. 2-21- Main process parameters set for TPU and CPLA

	TPU	**CPLA**
Nozzle size (mm)	0.8	0.4
Layer height (mm)	0.2	0.2
Printing temperature (°C)	223	225
Line width (mm)	0.8	0.5
Printing speed (mm/s)	30	25
Flow (%)	106	110

The total cost of raw materials for the TPU-covered sensor, estimated by the slicer software (Ultimaker Cura 4.6) was 0.38 €, while the manufacturing time was 41 min. **Fig. 2.21 a) and b)** show, respectively, the developed sensor during the 3D printing process and the sensor flexibility (potentially, it can be easily attached to irregular and non-conventional structures, paving the way for its exploitation in the field of wearable sensors).

The main advantage of the TPU-covered sensor, from a manufacturing standpoint, is the total absence of post-processing to seal off the electrodes: very often manual tasks, i.e. coating, strongly related to the operators' skills are employed[59], [60]. In **Fig. 2.21 c)** the TPU-covered sensor and an uncovered version (i.e., the same sensor without the top TPU cover) are shown.

Finally, to prove the additive manufacture method robustness, 10 samples of each version (see **Errore. L'origine riferimento non è stata trovata.**c) have been printed, carrying out the following conclusions: *i)* no filament breakdown occurred, and *ii)* The TPU-covered mean capacitance value was 125.5 pF with a very low standard deviation of 0.7 pF, due to a not uniform electrical resistance of the raw conductive filaments (before of being melted into the nozzle) and noise effects occurring during the printing such as vibrations, room conditions etc.

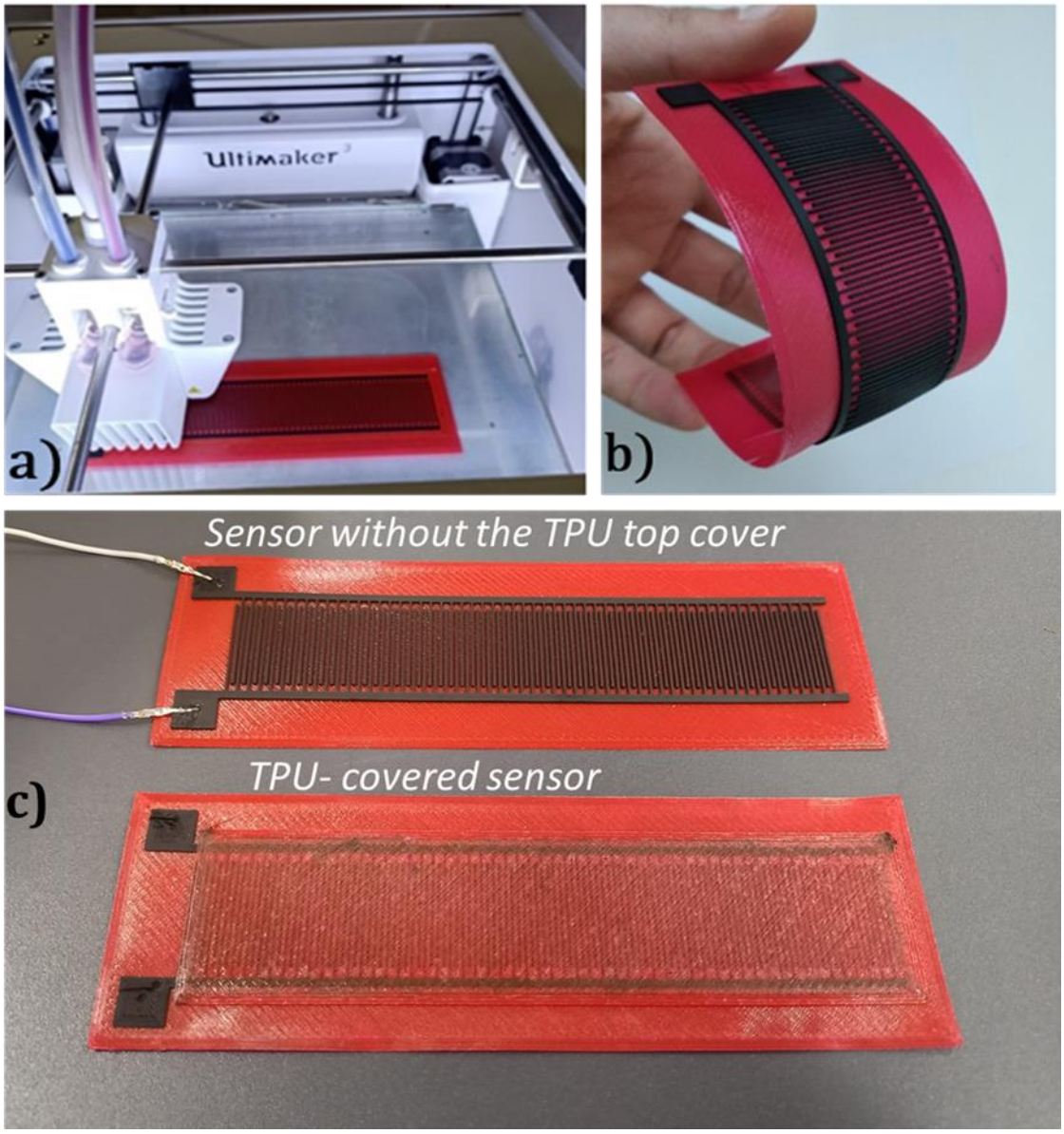

Fig. 2-21- a) Capacitive sensor during the manufacturing process, b) flexibility of the proposed sensor, and c) two versions of the sensor: "sensor without the TPU top cover", and "TPU-covered sensor".

2.4.2 Results and discussion

In this section, the TPU-covered sensor was tested for liquid level sensing. Two different liquids were used to test the sensor, i.e., distilled water and sunflower oil, and different metrological characteristics were evaluated (i.e., sensitivity, linearity, offset, and repeatability).

Moreover, the temperature was measured during the performed tests (since it affects sensor capacitance) and it was assessed to be stable (about 20 °C). A detailed analysis of the effect of temperature on the capacitance of the proposed capacitive sensors was carried out in [40], highlighting a nonlinear dependence of capacitance on temperature and obtaining a model to compensate for its effect.

The measurement setup consists of (**Fig.2 .22**):

i. a custom-made 3D printed tank, which presents a vertical channel in which it was manually injected a constant quantity of liquid by means of a syringe. The vertical channel avoids the spatter of liquid droplets on the surface of the sensors, which could lead to errors in the liquid level measurement.

ii. a 34461A digital multimeter (Keysight Technologies, Santa Rosa, California, U.S), with 6 ½ digits of resolution, for accurate measurements of capacitance in a range of 1 nF.

iii. a control program developed in LabVIEW® by National Instruments Corp., to easily manage the system, providing real-time monitoring and data storage for further processing.

iv. a digital scale with a resolution of 0.001 g to measure the amount of liquid to inject.

Before performing the experiments, a preliminary test was performed to prove the tightness of the TPU cover when immersed in two different liquids. The TPU-covered sensor was kept in a tank full of water for 48 hours and no cover degradation was observed. Afterwards, the same test was performed using sunflower oil, and no difference was observed.

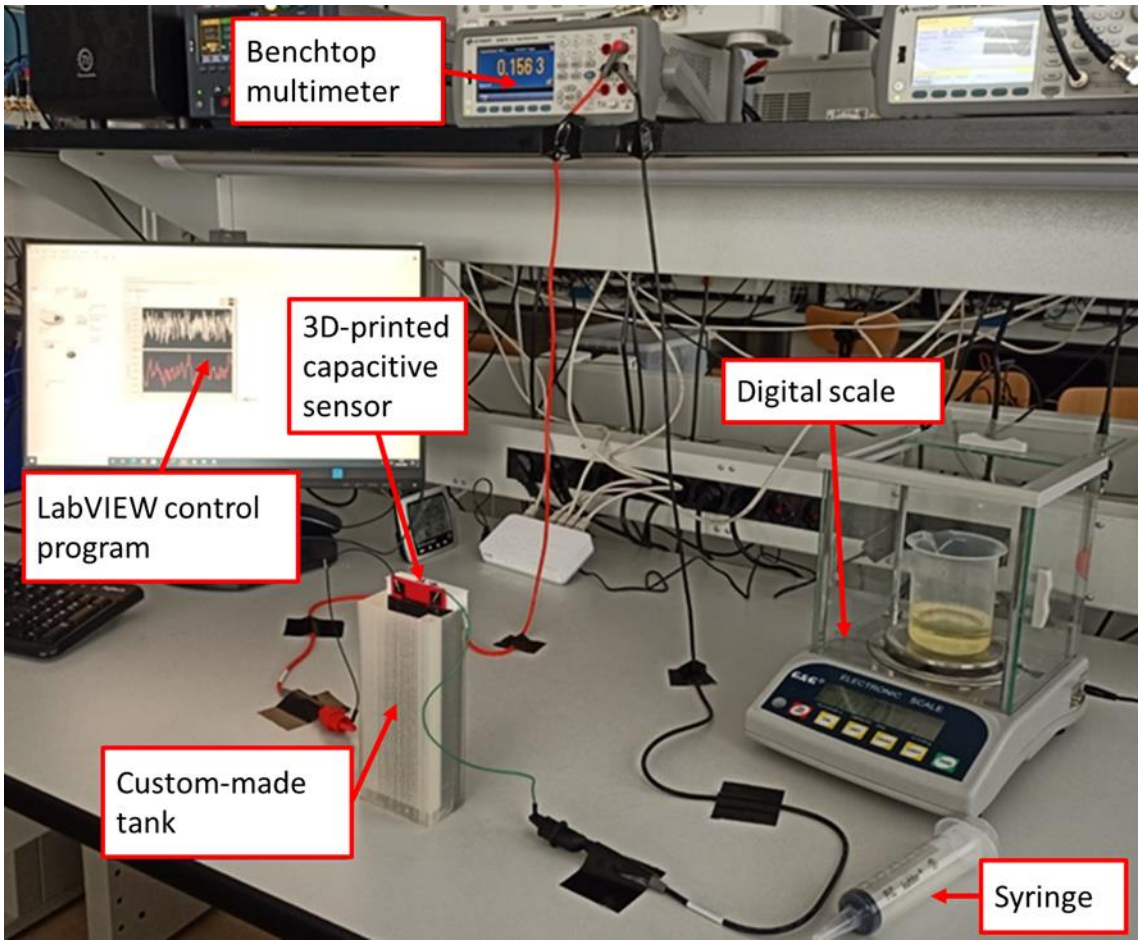

Fig. 2-22- Measurement setup

The TPU-covered was first tested for the sensing of sunflower oil level, then for distilled water level: several conclusions can be drawn, proving that its behavior is consistent with capacitive sensors described in the literature.

The following measurement protocol was used for both the liquids: the same amount of liquid, weighed by means of the high accuracy digital scale, was injected into the for a total of 5 steps: at each step, a settling time of 30 s was waited from the injection of the liquid, and the average of 20 consecutive capacitance readings was computed, in order to reduce noise. The results of test number one for the sunflower oil are shown in **Fig. 2.23**. The whole procedure has been repeated 10 times (a total of 10 test cycles) to assess the repeatability. After each cycle, a time of 4 minutes was waited, in order to manually dry the sensor and empty the tank. All tests have been performed after zeroing the offset capacitance of the multimeter and leads.

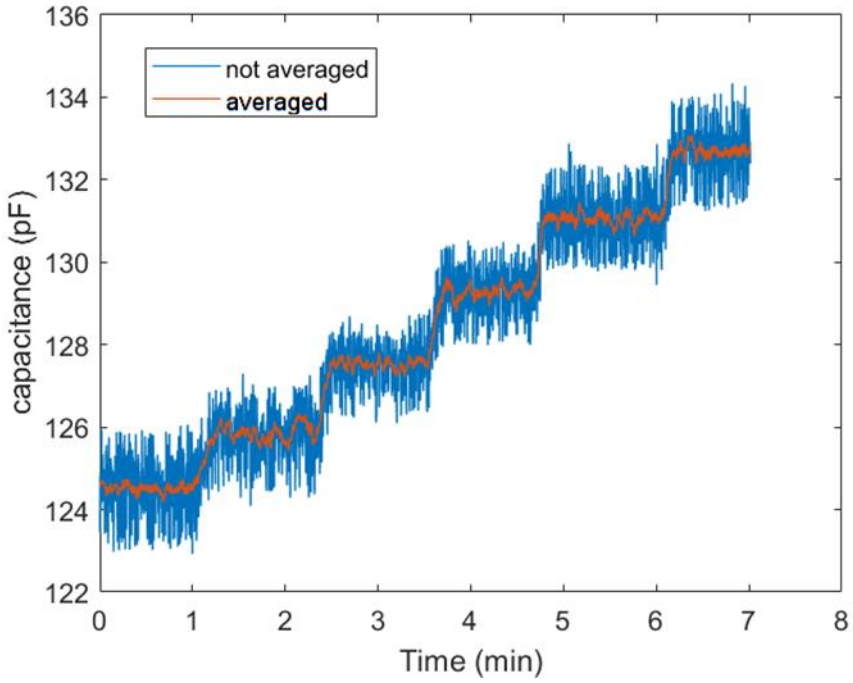

Fig. 2-23- Capacitance of the TPU-covered sensor vs time. Test 1 with sunflower oil.

Fig. 2.24 a) and b) show the results of the performed tests for the TPU-covered sensor: in particular, the offset of each curve was reduced to zero to provide a better comparison. The offsets of each curve with respect to the 1st one, are separately shown in **Fig 2.25**, for water and sunflower oil. Very high linearity of the sensitivity to the level of both liquids has been obtained, comparable to other high linearity capacitive level sensors found in the literature [54], [60], [61], with a root-mean-square error (RMSE) lower than 1.7 % of the full-scale output (FSO, calculated as the difference between the maximum and minimum of the moving averaged capacitance for each test). A maximum propagated error of 1.4 mm is obtained by dividing the nonlinearity error (RMSE) by the sensitivity of the sensor, thus ensuring the good linearity performances of the proposed sensors. The main metrological characteristics are summarized in **Tab2.22**.

The sensitivity of the sensor to oil and water is obtained by performing a linear regression on each curve and by averaging the results of the 10 performed tests. As expected, the sensitivity to sunflower oil is one order of magnitude lower than the one obtained with distilled water, since sunflower oil is characterized by different electrical properties (i.e., lower electrical conductivity and dielectric constant).

As shown in **Fig.2.25**, when sensing sunflower oil level, the offsets with respect to the 1st test shows a random distribution with a mean and standard deviation of 0.64 ± 0.16 pF. In the authors' opinion, this random offset could be due to *i)* changes in room conditions (i.e., slight temperature change), *ii)*

changes in tank conditions (after each test cycle the tank was manually cleaned up and some drops could have remained into the tank), and *iii)* slight changes in the position of connection wires.

When sensing water level, instead, the sensor presents an increasing offset for each test, spanning a range up to 14.5 pF: compared to oil sensing, the offset is meaningfully high (806 %) and it is not randomly distributed, but it is increasing. Indeed, in addition to the random variable changes, above described, in this case another important phenomenon takes place: the TPU material, of which the top cover is made up, is characterized by a water absorption value of 0.18% in accordance with the ASTM D570 test method (material data sheet). As a matter of fact, after each test cycle, a certain amount of water gets trapped into the TPU cover leading to an ever-increasing initial capacitance value (initial offset) from test cycle n to n+1, with n=1, …, 9. Instead, during oil sensing the sensor does not show increasing offset, since the employed TPU material does not provide any evidence of oil absorption, unlike for water.

Nevertheless, despite the increasing initial offset, the TPU-covered version can be employed in short-term tests by performing a zeroing procedure to compensate the offset, since the effect of water absorption seems to not affect sensing performances in the short period. The next studies will focus on the TPU-covered sensor lifespan.

However, in order to provide reliable measurements for long-duration tests, in this work a "tape-covered" version of the capacitive sensor is proposed where the conductive electrodes of the 3D printed sensor have been sealed off with adhesive tape in order to keep them isolated from the surrounding environment. The sealing process represents a further manual task, nevertheless it results easy to be performed and inexpensive: the authors present this solution as a good alternative to the TPU-covered sensor for a long-period sensor usage in water, thus overcoming the water absorption problem of the TPU cover. As for the TPU-covered sensor, also the tape-covered sensor was kept in a tank full of water for 48 hours and no cover detachment was observed. It should be said that a little amount of water is sufficient to short circuit the electrodes, thus preventing capacitance measurements; hence, the 48 hours test was necessary to assess the tightness of the adhesive tape.

The same measurement protocol was applied to the tape-covered sensor, and the results are shown in **Fig.2.24 c)**.

As for the TPU-covered sensor, high linearity is observed for the tape-covered sensor, which presents a sensitivity about 60% higher than the TPU-covered sensor: as well explained in [54], the top cover of the sensor is accountable for the different sensitivity, in fact, the main differences between the two top covers (embedded TPU cover and adhesive tape cover, respectively) are *i)* the cover thickness and *ii)* the dielectric constant of the cover material.

The obtained results are really appealing: for example, if compared to [61], the proposed TPU-covered and tape-covered sensors present a sensitivity to water level one order of magnitude higher, with the advantage that they are manufactured in a monolithic way and by using a much cheaper fabrication technology. Moreover, the proposed sensors can be directly integrated into smart structures in the same fabrication, whereas ink-jet printing technology [61] requires further assembly tasks, as well as manual procedures to isolate the electrodes from the liquid.

Finally, the tape-covered sensor presents a very low offset (1.42 ± 0.24 pF) of the same order of magnitude as the offset observed for the TPU-covered sensor when the oil was employed: as previously described, the offset is due to slight changes in room, tank and wire conditions.

To summarize, the assembly-free TPU-covered version can be employed for oil level sensing (without restrictions) and water level sensing (by applying a zeroing procedure), while the tape-covered version can be employed for water sensing without applying any zeroing procedure.

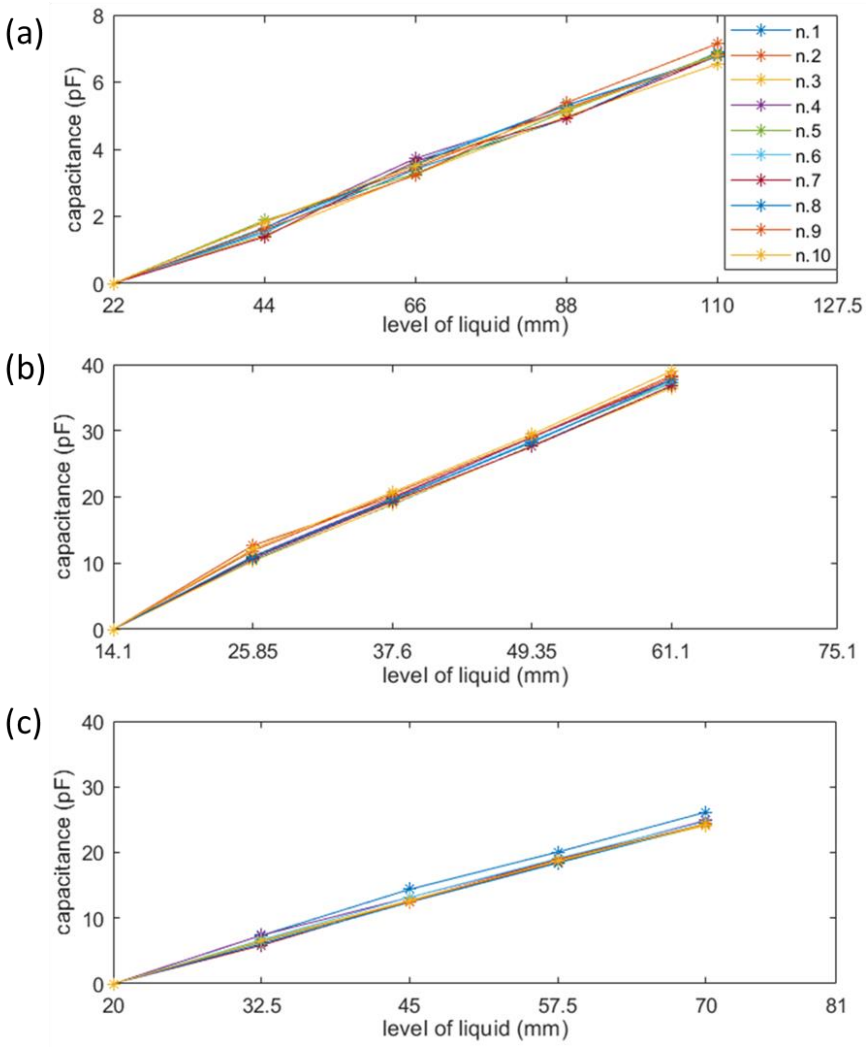

Fig. 2-24 - Capacitance vs level of liquid: a) TPU-covered in sunflower oil, b) TPU-covered in distilled water, c) tape-covered in distilled water.

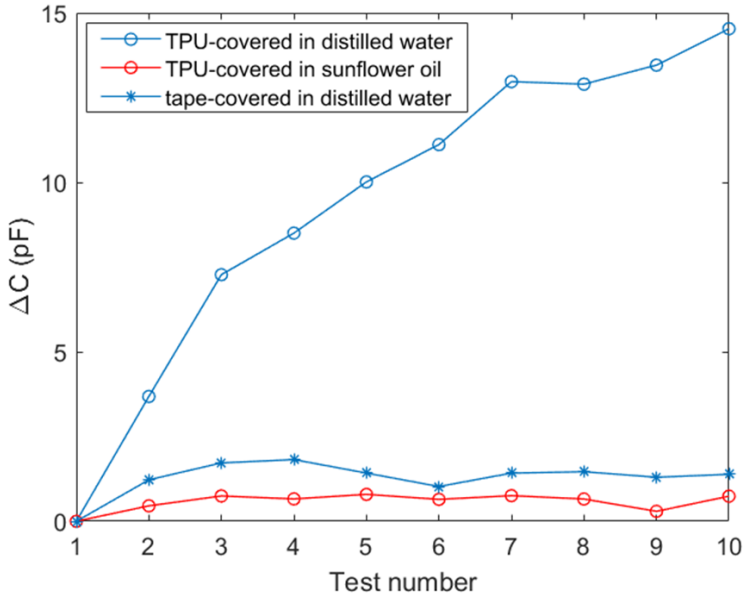

Fig. 2-25 Offset of linear regression curves with respect to the 1st one.

Tab. 2-22- Metrological characteristics of the proposed sensors. Results are expressed as mean or mean ± std. Propagated error is obtained by dividing the linearity error (RMSE) by the sensitivity of the sensor.

Liquid	**Sensor**	**Sensitivity** ($\frac{pF}{mm}$)	**Linearity**				**Offset (pF)**	**FSO (pF)**	**Comments**
			R^2	**RMSE**		**Propagated error (mm)**			
				(pF)	**(% FSO)**				
Oil	**TPU-covered**	0.078 ± 0.002	0.9977	0.109	1.6	1.4	0.64 ± 0.16	6.8	No zeroing procedure required
Water	**TPU-covered**	0.79 ± 0.01	0.9973	0.656	1.7	0.8	---	37.5	Zeroing procedure required
	Tape-covered	0.49 ± 0.01	0.9988	0.281	1.1	0.6	1.42 ± 0.24	24.6	No zeroing procedure required
	Literature [61]	0.074	0.998	---	---	---	---	---	More expensive manufacturing technology; multiple manufacturing steps

2.4.3 Conclusions

In the present research, the Material Extrusion (MeX) Additive Manufacturing (AM) technology has been employed for the fabrication of a coplanar capacitive sensor for liquid level sensing.

The Design for Additive Manufacturing (DfAM) approach, in conjunction with the printing forces analysis, has been exploited to fabricate a total of 57 conductive electrode tracks having a width of 0.5 mm and a spacing of 0.8 mm between them. In this way, a readable capacitance value of 125 pF was achieved (measurable from common measurement instrumentations). The main benefit of the proposed manufacturing approach consists of the one-shot fabrication of the whole sensor (flexible TPU substrate, conductive electrodes and top TPU cover): no assembly tasks were employed, resulting in cost and time saving (0.38 € and 40 min, respectively).

The proposed low-cost sensor has been tested for liquid level sensing: a very good sensitivity of 0.078 $\frac{\text{pF}}{\text{mm}}$ ($R^2 = 0.9977$) and 0.79 $\frac{\text{pF}}{\text{mm}}$ ($R^2 = 0.9973$) was achieved for sunflower oil and distilled water level, respectively, proving that the performances of the proposed low-cost sensor are comparable with that of more expensive sensors found in the literature. The sensor presented very high linearity, with a propagated nonlinearity error lower than 1.4 mm.

The present work aims at pushing the role of the inexpensive MeX technology for the fabrication of capacitive sensors embedded into 3D printed structures: non-conventional tanks as well as soft structures actuated by means of fluids (fluidic actuators) can be 3D printed in the same fabrication cycle alongside with the proposed capacitive sensor for liquid level detection, resulting in fabrication time and cost saving.

3. CHAPTER 3: MEX FOR SOFT ROBOTS

3.1 Introduction of the chapter

In the last two decades, soft robotics has arisen as a new emerging scientific field attracting huge interest not only in the academic world but also in industrial areas [62]. To understand the attractiveness of soft robotics, an analysis of its counterpart, traditional hard robotics, becomes crucial. Hard robots are well known for being i) very accurate, ii) able to act with high force and iii) characterized by very complex feedback systems consisting of several sensors, but at the same time they iv) can only work in a predetermined environment v) are made of discrete rigid links connected to each other: for this reason, their degrees of freedom (DoF) are finite, and as a result, they have discrete topology, vi) their degree of interaction with humans is very low, and vii) their cost is very high due to hard materials and considerable electronics. To overcome all these issues, soft robotics was developed [63].

- SOFT MATERIALS AND BIO-INSPIRATION

The use of soft materials enables the manufacture of soft robots. Soft materials are an essential requirement because they allow i) mobility of soft robots in unpredictable environments because soft materials can passively deform and adapt to the surrounding shape; ii) high impact resistance because they distribute stress over a large area; and iii) complex geometries and shapes of soft robots [64]. Some widely used terms in the soft robotics field are often misunderstood due to the lack of precise literature and continuous advances. Interesting definitions are provided by Chubb et al. [65], who describe compliance as the inverse of stiffness and softness as the inverse of hardness. Even though Young's modulus (E) refers to prismatic and cylindrical samples subjected to axial stress, it is still useful to classify materials as soft or hard. Generally, materials with $E < 10^9 Pa$ are called soft materials; the general idea is to use materials akin to natural organic materials such as fat, cartilage, and skin characterized by E ranging from 10^4 up to 10^9 Pa [66]–[68]. It is important to point out that soft materials, both biological and commercial, exhibit viscoelastic behavior, dissipating energy when a load is applied; this material characteristic has to be taken into account during soft robot design as a function of its application [69][70]. Recent advances in living materials could lead to a new era of soft hybrid robots able to interact within the human body [71]. Soft materials in conjunction with bio-inspired design give rise to soft robots with unconventional abilities such as jumping, climbing, adaptable grasping, locomotion, growth, etc. [72]. Animals and vegetables can i) perform complex movements using soft structures, ii) adapt themselves to unknown environments, and iii) modulate their stiffness; based on all of these factors, bio-inspired design is a key requirement in soft robotics

[69], [73]. Soft robots inspired by octopus [74], [75], pangolin [76], fish [77], caterpillar [78], and flower [79] are only a few examples of how nature is a powerful source of inspiration in the soft robotics field. Because of the complex geometries and movements of soft robots, the classical models widely used in hard robotics are unusable; according to [80], it is possible to split the approaches used to model robot kinematics and dynamics into three classes: black-box (based on neural networks), white-box (divided into geometry- and mechanics-based methods), and hybrid.

- APPLICATION FIELDS

Soft robots are gaining popularity thanks to the possibility of employing them in several applications. One possible application field is the exploration of unknown environments; indeed, many soft robots have been fabricated mimicking the gait principles found in nature (crawling, legged locomotion, jumping, flying, and swimming) [81].

The bio-medical field is very promising for soft robotics too [82]: soft robots can be exploited in several applications such as i) Minimally Invasive Surgery (MIS) and endoscopy [83], [84], taking advantage of recent developments in electromagnetic tracking systems for surgical navigation [85], [86], for example, Hu et al. developed a soft millimeter-scale robot able to roll into an *ex-vivo* chicken tissue [87] ; ii) drug delivery, as demonstrated by Baynojir et al [88]; iii) human body rehabilitation [89]–[92](e.g., knee, foot, hand, etc.) and assistance: a powerful example is provided by i-support devices designed to help elderly people with shower tasks [93], [94]. Another important field in which soft robotics provides several benefits compared to its hard counterpart is manipulation. Shintake et al. [95] classified soft grippers into three categories (actuation, controlled stiffness, and controlled adhesion), which were characterized by a certain degree of interaction (grasping and manipulation) with four kinds of objects (conventional, nonconventional, deformable, and flat).

- ADDITIVE MANUFACTURING

Several innovative methods have been used to manufacture soft robots. Due to the unconventional materials employed in this scientific field, overcoming the traditional manufacturing approaches becomes essential. Regarding the state of the art, the manufacturing approaches widely employed to fabricate soft robots are molding (2D and 3D molding), soft lithography, shape deposition manufacturing, and thin-film manufacturing [68-70]. In the last few years, a growing interest in additive manufacturing (AM) technologies has emerged in this scenario [71-72].

Recent developments in 3D printing of soft materials [73] such as thermoplastic polyurethane-based [74] or silicone-based [75] materials, biological-inspired materials [76], and stimulus–response materials [77-79] and the possibility of printing soft electronic devices that can also be worn [80], [81] paved the way for extensive use of AM technologies for soft robot fabrication. In this section, the role of AM technologies in the manufacturing process of soft robots is analysed; in particular,

three methods to exploit AM techniques in soft robotics are described. The general idea underlying this classification is to rank the role of these AM technologies within the entire manufacturing process leading to soft robot fabrication. The three approaches used to exploit AM technologies in soft robotics, found by analyzing the scientific literature, are rapid mold fabrication, hybrid, and total additive manufacturing. **Fig3.1** shows the three approaches as a function of the role of AM technologies in the whole manufacturing process; in particular, in rapid mold fabrication, the role of AM techniques is very marginal, in the hybrid approach the role increases but however other different manufacturing technologies are still employed in fabrication, and in total additive manufacturing the role of AM is huge; indeed, this is the only manufacturing technology employed for soft robot fabrication.

All three approaches provide several benefits due to the use of AM technologies, but only total additive manufacturing takes full advantage of AM capabilities.

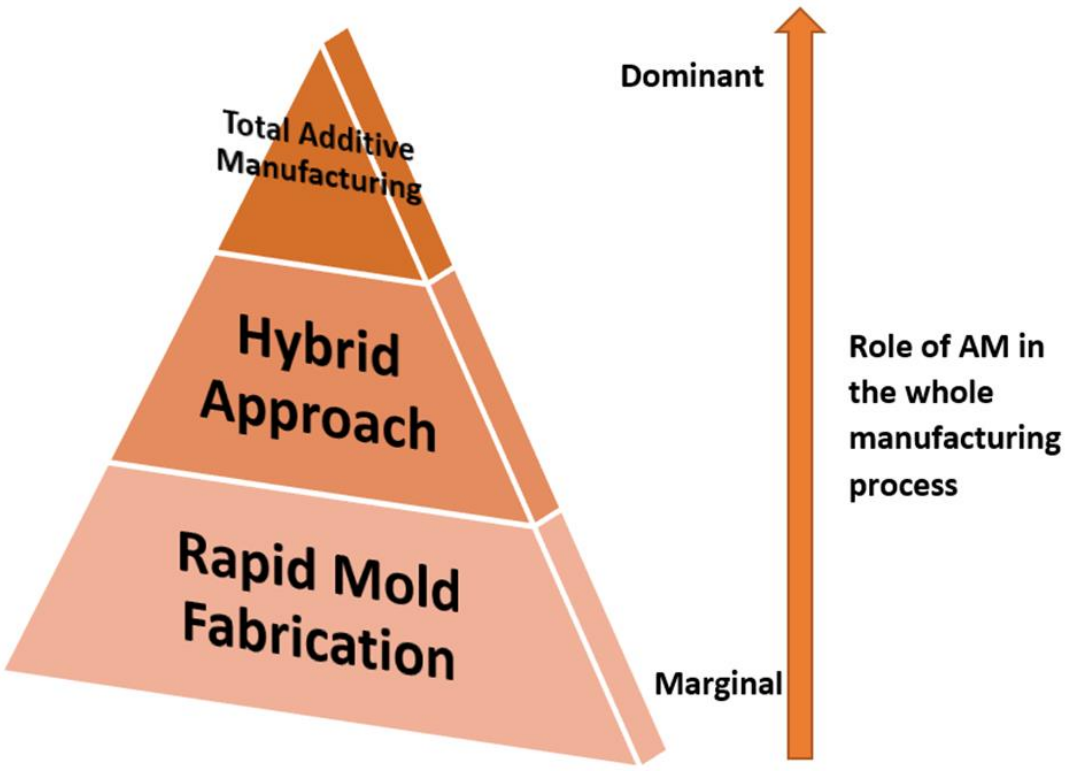

Fig. 3-1- Additive Manufacturing approaches for soft robotics: rapid mold fabrication, hybrid approach and total Additive Manufacturing.

3.2 Actuation systems in soft robotics

Actuation is the conversion of energy into mechanical work, and it can be defined as the core of the soft robot. The actuation system in soft robotics affects several points, from the movements that soft robots will be able to perform in the workspace to the required fabrication process. A wide variety of actuation systems have been employed over the years; in this section, the most common actuation systems with associated conventional manufacturing approaches are described and listed in **Tab.3.1** Some examples of actuation systems are shown in **Fig.3.2**.

- FLEXIBLE FLUIDIC ACTUATOR (FFA)

Flexible fluidic actuation (FFA) is an actuation technology that is widely employed in soft robotics because of low-cost elastomers, fast response time, and high actuation forces [35-36]. The working principle underlying FFA is the use of a fluid (gas or liquid) to obtain deformation of an elastomeric structure made up of patterned chambers connected to each other (see **Fig.3.2 a)**). Generally, compressed air is used to obtain soft robot actuation; an example is provided in [37], where the authors developed a soft robot with four legs, and when the legs were pressurized with compressed air (138 kPa), the robot was able to walk in several kinds of environments (e.g., snow-covered ground), showing benefits such as high resilience, the possibility to modulate the gait, and tolerance of large loads (8 kg). The different pattern of the chambers not only involves different movements (e.g., bending, lengthening, twisting, etc.) [38-39] but also substantial differences in stress distribution, fatigue response, exerted forces, and actuation speed [40]. All of these examples refer to air compressor actuation, but liquid-driven devices have also been developed. One of the most important is the soft glove developed in [28], consisting of several rubber chambers with fiber reinforcement; when they are hydraulically actuated, they can help people in everyday tasks, showing negligible impedance. The major advantage of using fluid (water in this case) is the portability and wearability of the devices, which is not possible with gas-driven actuation (because, usually, compressed air can be provided only by compressed air lines or portable heavy compressors): in fact, the electro-mechanical components (battery, power regulation, microcontrollers, water reservoir, hydraulic pump, and valves) have been designed to be included into a compact waist belt pack of 3.3 kg.
Figure 1 shows the main concepts related to the FFA system.

- CABLE DRIVEN ACTUATION

Cable-driven actuation is one of the easiest actuation systems used in soft robotics; this technology has long been exploited in traditional hard robotics. The general idea underlying this method is the use of DC motors to remotely pull cables anchored to soft robot bodies; in this way, several movements can be performed. This approach offers low inertia, fast response time, and the possibility to obtain high force values according to the selected motor. Another non-negligible benefit offered by cable-driven actuation concerns the control; in fact, as the DC motor is a widely known technology, it is quite easy to interact with them from an electronic point of view and create customized control systems to manage soft robot movements. Generally, this kind of actuation is often used in conjunction with other actuation technologies to increase the stiffness of the soft robot [41], such as the well-known octopus arm soft robot [14], the i-support manipulator [33], and the self-pumping soft actuator [42]. The most common cable-driven soft robots are inspired by tendons (mimicking human fingers). Xu et al. [43] developed a soft biomimetic robotic hand equipped with 10 motors, demonstrating not only good repeatability of motion of the single finger but also the possibility of teleoperation for grasping and manipulating ordinary objects. Kang et al. [44], using cable-driven actuation, designed and fabricated a wearable soft glove for people suffering from spinal cord injury; the soft glove is made of a single material and is very lightweight at 104 g, as is the box containing the motors, at only 1.14 kg. The low weight allows high wearability and suitability of the glove and the possibility to easily carry the box, which can also be placed on a desk. It is possible to classify cable-driven soft robots used to manipulate and grasp objects into two classes: contact-driven and tendon-driven [45].

- SHAPE MEMORY MATERIALS (SMMs)

Shape memory materials (SMMs) are a class of materials that can be defined as "smart" because they can be plastically deformed into temporary shapes, and after a thermal stimulus (after reaching a certain switching temperature T_s) can resume their original shape. They can repeat this cycle countless times. SMMs can be divided into two classes: shape memory alloys (SMAs) and shape memory polymers (SMPs), both characterized by the same memory effect but using different mechanisms to obtain this effect. In SMAs there is a phase change in the crystalline structure from the martensite to the austenite phase. At room temperature T_r the alloy structure is martensitic; this means that Young's modulus is low, and the alloy can be deformed by external stress. After reaching T_s, the crystalline structure switches to the austenitic phase; during the phase change, Young's modulus increases, and the original undeformed shape is recovered.

The SMP mechanism is slightly different: at room temperature, Young's modulus is high and the polymer is undeformed; when T_s is reached (in this case T_s is the polymer glass transition temperature T_g), the material's softness greatly increases and it is possible to change its shape by applying external stress. When the temperature gets back to T_r the new shape is frozen and only by reheating the material (T >T_g) can the original undeformed shape be recovered. SMA's intrinsic properties make this kind of actuation system very suitable for soft robotics [46]. For example, Lin et al. [17] to developed the GoQbot, a caterpillar-inspired soft robot, using SMA coils to improve body coordination, with the aim of performing a ballistic roll to increase the locomotion speed. She et al., using SMA as actuation technology, developed a soft hand with a grasping force of 9.7 N that was very resilient and safe for humans because of its low weight (250 g) [47]. One remarkable work in which SMP has been employed as actuation technology is the micro-gripper developed by Behl et al. [48], which is able to grasp small objects such as a penny (see **Fig 3.2b)**).

- ELECTROACTIVE POLYMERS

Electroactive polymer (EAP) is a kind of actuation system used in soft robotics that requires an electrical stimulus to work; in particular, when an electrical field is applied, EAP exhibits a change in size or shape, resulting in the actuation of the soft robot. Two classes of EAPs are employed in the soft robotics field: dielectric elastomer actuators (DEAs) [96] and ionic polymer metal composites (IPMCs). The working principle underlying the DEA is as follows: an elastomer membrane is sandwiched between two electrodes, and when high voltage is provided (generally the order of magnitude is greater than 1 kV), the electrostatic attraction force between the electrodes leads to elastomer deformation. The IPMC structure is similar to DEA, with two electrodes and a polymer membrane between them. The main difference is in the polymer composition; in this case, an ion-conducting polyelectrolyte polymer is used. When voltage is applied to the electrodes (very low voltage values compared to DEA, generally less than 5 V), the positively charged ions (cations) of the electrolyte move toward the cathode while the negatively charged ions (anions) move toward the anode. This migration involves the whole structure bending toward the positive (cathode) side. Generally, IPMCs are used for applications where low actuation forces are required [97]. Several DEA systems have been used for the manufacturing of grippers. Araromi et al. studied three gripper designs, measuring performance (bending angle and grasping force) as a function of the applied voltage, and found the best configuration for a micro-gripper weighed less than 0.65 g and was able to bend its tip 60° with a grasping force of 2.2 mN [98]. The DEA approach has been used to actuate bio-inspired soft robots able to move in water, such as fish-inspired [77] (see **Fig. 3.2 c)**) and frog-

inspired [99] robots. As shown by Lumia et al. [100], who developed an IPMC-driven micro-gripper, this actuation technology is suitable for the fabrication of grippers able to interact with and manipulate small objects (e.g., a 15 mg solder ball).

- MAGNETO AND ELECTRO RHEOLOGICAL MATERIALS (M/E-RMs)

Magneto- and electro-rheological materials are a class of materials used in soft robotics as actuation systems. They have embedded electrical or magnetic particles and can be elastomeric or fluidic materials [101]. This class of materials needs an external electric or magnetic field to work; when it is applied, they change their rheological properties. In fact, the electric or magnetic field causes an alignment of the particles with the field, leading to soft structure movements such as bending, contraction, elongation, etc. In particular, in electro-rheological materials (ERMs), the particles that respond to the electric field are polarizable particles, while in magneto-rheological materials (MRMs), the particles are ferromagnetic and are obviously susceptible to magnetic fields. The current trend in the use of M/E-RMs in soft robotics is well outlined by Manti et al. [102]: in the MRM family, the elastomeric version is widely employed because the fluidic counterpart is affected by several issues such as particle settling, sealing problems, and environmental contamination. In the ERM family, the use of the elastomeric version is less prevalent.
A very interesting aspect in MRM field is related to the possibility to program the ferromagnetic particles embedded into the soft elastomeric material by means of an external source (magnetic field) during the fabrication process in order to obtain given magnetization profiles resulting in several shape changes and consequently different kinds of allowed movements[87], [103]–[105].

- LESS USED ACTUATION SYSTEMS

In this section, other actuation systems that are historically less frequently employed in soft robotics (or, however new emerging systems) are described. Optical, humidity, pH, and chemical actuation concern soft robots made up of gels and hydrogels [106], [107], while a low melting point material (LMPM) actuation system concerns mainly alloys (embedded into the soft structure) that can switch phase from liquid to solid in response to heat for a very high number of cycles, resulting in variable stiffness soft robots [108], [109].
Soft robots made of liquid crystals (LCs) polymers and actuated by means of light-sources are gaining worldwide popularity in the last few years for the possibility to create microrobots characterized by the following advantages: adaptive motion, human-friendly interaction, and external and controllable

power supply [110], [111]. A greater example of LCs polymer-based miniaturized light-driven soft robot is the work of Zeng et al. [112], they developed a micro inching soft robot which upon visible-light excitation is capable of mimicking caterpillar locomotion on different places such as fingernails.

- HYBRID ACTUATION

Hybrid actuation systems exploit one or more actuation systems together.
An example is provided by the hydraulically amplified self-healing electrostatic (HASE) soft robots [113], [114] developed by researchers of the University of Colorado. HASE soft robots are composed of three main components: elastomeric shells, stretchable polymer-based electrodes, and a dielectric liquid. When a certain voltage is applied to electrodes, electrostatic Maxwell stress put in motion the dielectric liquid which deforms the flexible shells (by means of hydraulic pressure) resulting in a deformation of the whole soft robot. In this way, two different actuation systems are employed: EAP and FFA (in liquid-driven version).
Another example of hybrid actuation is the work of Liu et al [115] who, embedding Fe magnetic microparticles into a shape memory thermoplastic polyurethane thin-film, fabricated a novel soft robot that can be actuated in three different ways: only by means of SMP system; only by means of MRM system in elastomeric version and exploiting both methods. Several shapes (such as flower and scroll) have been designed and tested to prove the robustness of the hybrid actuation.

Tab. 3-1- Actuation systems used in soft robotics.

Name	Acronym	Subclasses
Flexible fluidic actuation	FFA	• Gas-driven • Liquid-driven
Cable-driven actuation		
Shape memory materials	SMMs	• Shape memory alloys (SMAs) • Shape memory polymers (SMPs)
Electroactive polymers	EAPs	• Dielectric elastomer actuators (DEAs) • Ionic polymer metal composites (IPMCs)

Magneto- and electro-rheological materials	M/E-RMs	• Electro-rheological materials (ERMs): elastomeric and fluid versions • Magneto-rheological materials (MRMs): elastomeric and fluidic versions
Less-used Actuation Systems	---	• Actuation systems for gels and hydrogels (optical, humidity, pH and chemical) • Actuation system for alloys (LMPMs) • Liquid crystals (LCs) polymers actuated by light sources

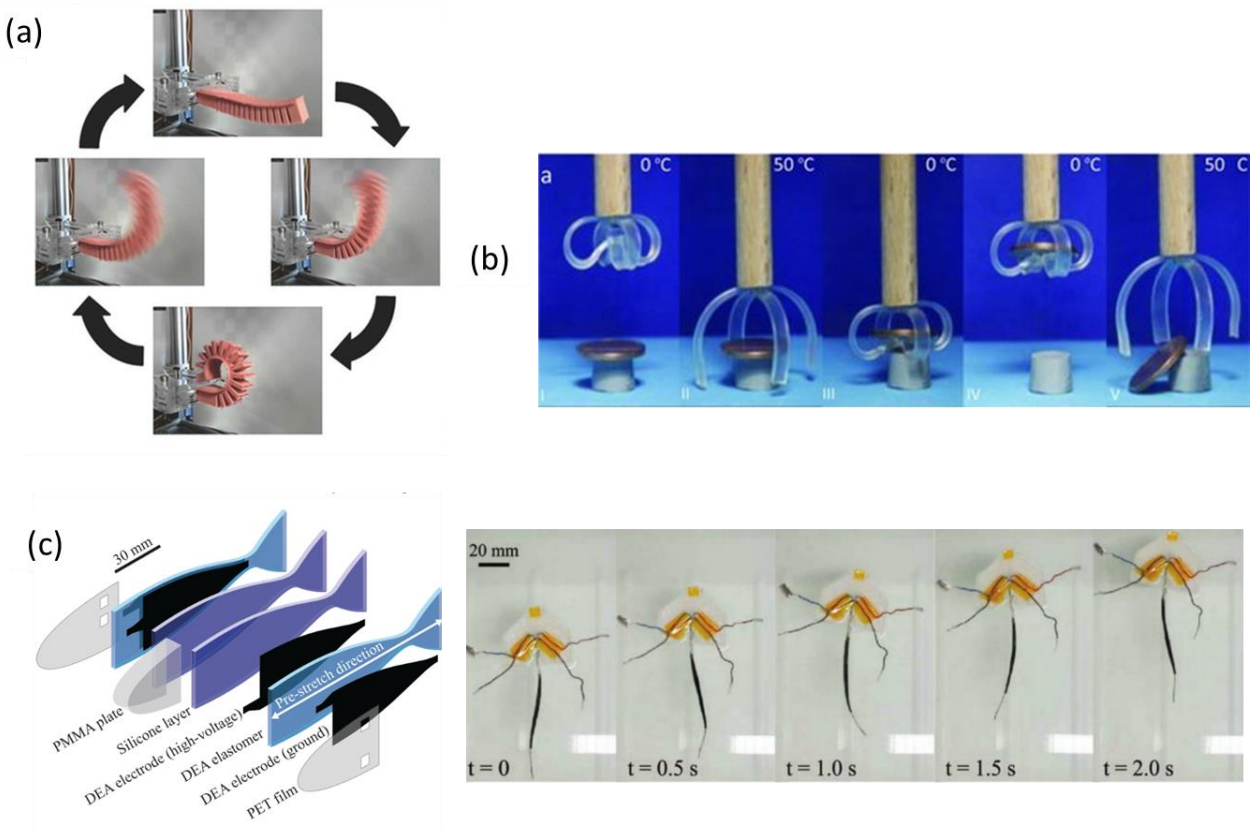

Fig. 3-2 Examples of actuation systems in soft robot: a) FFA gas-driven actuation system. Reprinted with permission from [116]*. b) micro gripper based on SMP actuation system. Reprinted with permission from* [117]*. c) fish-inspired soft robot based on DEA actuation system, able to swim in water. Reprinted with permission from* [77]

3.3 Additive manufacturing of airtight, monholitic, bending Pneunet with embedded air-connector

3.3.1 Introduction of the chapter

Air tightness is a challenging task for 3D-printed components, especially for fused filament fabrication (FFF), due to inherent issues, related to the layer-by-layer fabrication method. On the other hand, the capability of 3D print airtight cavities with complex shapes is very attractive for several emerging research fields, such as soft robotics. The present research proposes a repeatable methodology to 3D print airtight soft actuators with embedded air connectors. The FFF process has been optimized to manufacture monolithic bending PneuNets (MBPs), an emerging class of soft robots. FFF has several advantages in soft robot fabrication: (i) it is a fully automated process which does not require manual tasks as for molding, (ii) it is one of the most ubiquitous and inexpensive (FFF 3D printers costs < $200) 3D-printing technologies, and (iii) more materials can be used in the same printing cycle which allows embedding of several elements in the soft robot body. Using commercial soft filaments and a dual-extruder 3D printer, at first, a novel air connector which can be easily embedded in each soft robot, made via FFF technology with a single printing cycle, has been fabricated and tested. This new embedded air connector (EAC) prevents air leaks at the interface between pneumatic pipe and soft robot and replaces the commercial air connections, often origin of leakages in soft robots. A subsequent experimental study using four different shapes of MBPs, each equipped with EAC, showed the way in which different design configurations can affect bending performance. By focusing on the best performing shape, among the tested ones, the authors studied the relationship between bending performance and air tightness, proving how the Design for Additive Manufacturing approach is essential for advanced applications involving FFF. In particular, the relationship between chamber wall thickness and printing parameters has been analyzed, the thickness of the walls has been studied from 1.6 to 1 mm while maintaining air tightness and improving the bending angle by 76.7% under a pressure of 4 bar. It emerged that the main printing parameter affecting chamber wall air tightness is the line width that, in conjunction with the wall thickness, can ensure air tightness of the soft actuator body.

3.3.2 Leakage-free 3D printed embedded air connector

The dual-extruder 3D printer Ultimaker 3 (Ultimaker, Utrecht, the Netherlands), which enables the usage of two different filaments in the same printing cycle, has been used to manufacture the monolithic bending PneuNet (MBP). The two commercial filaments chosen were: (i) polyurethane

thermoplastic produced by Ultimaker with a shore A hardness of 95 (TPU 95A), a tensile modulus of 26 MPa, and an elongation at break of 580% and (ii) a low-friction polyurethane thermoplastic developed by BASF (Ludwigshafen, Germany) , on the market since 2019, with a shore A hardness of 80 (TPU 80A LF) and a tensile strength ranging from 17 to 22 MPa depending on the printing direction of the sample. All technical data were from filament's datasheets. TPU 95 A was used to create the male embedded air connector and to fabricate the inextensible portion of the actuator, whereas TPU 80 A LF was chosen to manufacture the extensible segment of the MBP.

The ideal material to manufacture the air connector was rigid and does neither break nor twist under high pressure (up to 7 bar). At the same time, boundary interface problems between the two materials with very different hardness values must be taken into account during the dual-extruder printing process.

A common problem with pneumatic soft robots typically occurs at the interface between the soft robot and the pneumatic system that supplies the compressed air, where recurrent air leaks may not only reduce the soft robot performance but may also pose a potential danger for the surrounding environment once high pressures are reached. This problem is often addressed through solutions that are rather complex from an assembling point of view [23], [30].

Here, an innovative 3D-printed male embedded air connector (EAC) which can be easily embed in every soft robot made with FFF technology requiring only one printing cycle has been developed. The proposed EAC ensures the total absence of any air leaks at the interface between the soft robot and the pneumatic system. Its general purpose is to mimic the commercial male air connectors (often made of steel), quickly engraftable into the female connector attached to pneumatic pipe (**Fig3.3 a)**). Since 3D-printed soft robots are made by soft materials, it has been decided to use as well a soft material for the EAC (it will be manufactured in the same printing cycle of the soft robot) in order to reduce several manufacturing problems, as explained above. The EAC was initially fabricated and tested with the same nominal size as the commercial male connector but the tests highlighted air leaks. Due to the lack of scientific literature addressing this issue, a trial and error method was applied to find the correct nominal value of the connector's diameter, increasing its value. The four external diameters of the EAC (from D_1 to D_4 in **Fig 3.3 b) and c)**) were increased in steps of 0.1 mm until the air tightness was reached. The EAC diameters needed to be designed at least 0.5 mm wider than those of the standard connectors.

Ultimaker Cura 4.4 software (Ultimaker, Utrecht, the Netherlands) was used to set the printing parameters and communicate with the 3D printer. **Tab3.2** shows the manufacturing parameters used to fabricate the EAC. Because of its circular shape, the EAC was printed with its longitudinal axis

perpendicular to the build plate (**Fig3.3 d)**) which afforded the following advantages: (i) no supports are required and (ii) the nozzle can perform circular movements to create the EAC shape.

This printing orientation also guarantees the complete absence of air leaks.

The printed EAC was inserted into the pneumatic pipe and several tests were performed to evaluate its air tightness. For each test, the EAC was submerged in a beaker filled with water to facilitate the detection of air leaks. To work safely, EAC was anchored to the beaker using a custom-made support. Each EAC underwent the following 3 tests: (i) the pressure was increased in steps of 1 bar from 0 to 7 bar (uphill phase) and then reduced again in the same manner to reach 0 bar (downhill phase), with 1 min between pressure changes. This test was repeated 10 times for each specimen; (ii) here, the pressure abruptly alternated between 0 and 7 bar, remaining for 5 s at each level and repeating these cycles 50 times; and (iii) here, the specimens were exposed to a pressure of 7 bar for a time of 15 min.

During each of the above tests, no water bubble was detected into the beaker full of water, thus demonstrating the absence of any air leaks.

The innovativeness of the EAC consists in a single-step printing cycle to embed connectors potentially in every soft robot made by FFF, reducing the use of commercial solutions, often unsuitable for pneumatic soft robots.

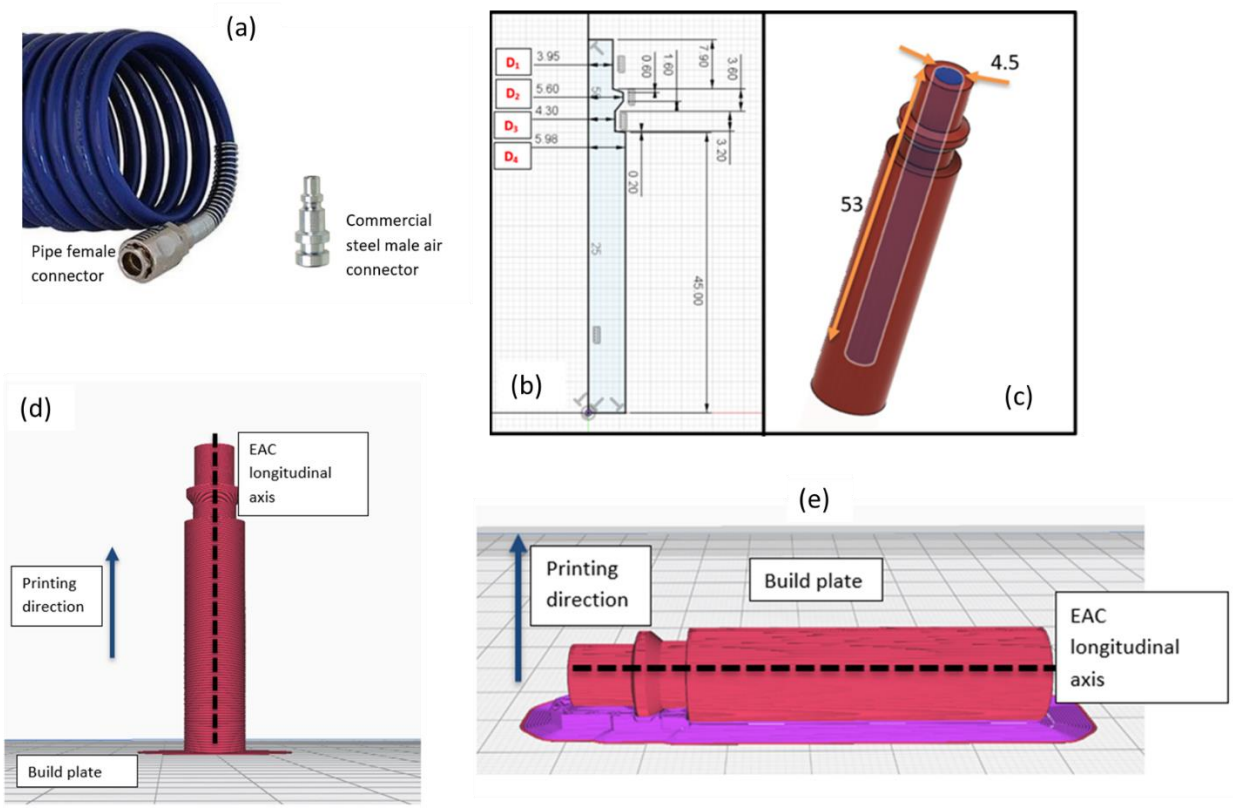

Fig. 3-3- a) Pneumatic pipe and commercial air connector, b) Revolved sketch (all dimensions are in mm), b) 3D model of the embedded air connector (EAC), c) Printing orientation (EAC axis perpendicular to the build plate), and e) Printing orientation (EAC axis parallel to the build plate).

Tab. 3-2 Printing parameters for the embedded air connector (EAC).

Parameter	Value
Nozzle diameter	0.4 mm
Printing temperature	225 °C
Printing speed	25 mm/s
Infill density	100%
Infill pattern	Circular
Retraction distance	7.5 mm
Adhesion type	Brim
Layer height	0.15 mm
Line width	0.4
Bed temperature	60 °C

One alternative printing orientation has been examined (**Fig.3.3 e)**): with this orientation (EAC longitudinal axis parallel to the build plate), supports were required during the printing process and the staircase effect affected heavily the cylindricity of the component showing a high dependence on the layer height. These two features affect the EAC's air tightness. In particular, the supports can damage the EAC when they are manually removed from the structure and thus cause air leaks. For this reason, the effect of two different kinds of materials for the supports has been studied: TPU 95 A (the same used for the EAC), which requires manual removal and polyvinyl alcohol (PVA) (Ultimaker, Utrecht, the Netherlands), a water-soluble material that does not require any manual removal.

Regarding the cylindricity, it has been decided to investigate the staircase effect on EAC air tightness. Layer heights considered in this study were 0.15 mm (the same used in the first printing orientation) and 0.05 mm, the minimum layer height allowed by the Ultimaker 3 3D printer.

Using the support material and layer height as factors and assigning two levels to each factor, a full 2^2 factorial experiment has been performed to understand the influence of these factors on air tightness and if a combination of factors that ensures the absence of air leaks exists. The response variable was the leakage (L/min) measured with the following method:

The EAC is connected to the pneumatic pipe of the compressor and a pressure P_2 of 3 bar has been reached.

The air supply is stopped and the amount of pressure reduction (indicative of an air leak) is measured, resulting in the time t_{drop} until a new pressure P_1 of 2 bar is reached.

Compressed air is resupplied and the time to reach P_2 , t_{rise}, is measured.

The amount of air leakage (q_{leak}) in L/min can then be calculated as shown in equation (19):

$$q_{leak} = Q_c * \frac{t_{rise}}{t_{rise} + t_{rop}} \quad (19)$$

where Q_c is the air flow of the compressor (180 L/min).

The software Minitab 17 was used to analyze the 2^2 factorial experiment and **Tab3.3** summarizes the nomenclature of the factors and levels.

Each EAC is characterized by a certain combination of factors and levels and was printed in triplicate (number of replication (n) of the factorial plan is 3) to account for variabilities in the manufacturing process and obtain a better estimate of the impact of factors. To reduce the effect of uncontrollable external factors related to the 3D printing process, the manufacturing of the EAC samples was completely randomized.

The amount of air leakage (q_{leak}) for each sample as well as the overall mean μ and variance σ^2 for each factor combination is shown in **Tab. 3.4**.

Tab. 3-3-Factors and levels

Factors →	**A**	**B**
Levels↓	Layer height	Support Material
-1	0.05 mm	PVA
+1	0.15 mm	TPU95A

For the combinations ab and b the variance is 11.3 and 0.29, respectively, the highest variance among the 4 combinations. Both combinations ab and b are characterized by the same level of factor B, namely the usage of TPU 95 A as support material. Manually removing the TPU 95 A supports is a critical operation that requires a high level of skill of the operator to avoid damage to the EAC which may explain the high level of variance associated to the samples using TPU 95 A support materials. In fact, for these two combinations the amount of air leakage was closely related to the support removal. Combinations (1) and a used PVA support materials and only showed low variances of 0.001 and 0.02, respectively, because no manual operations were requested to remove the supports as they are dissolved in water. **Fig. 3.4** shows an EAC specimen with PVA support.

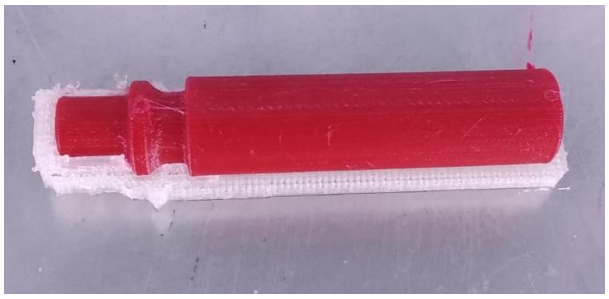

Fig. 3-4 EAC with PVA supports.

Coded Coefficients

Term	Effect	Coef	SE Coef	T-Value	P-Value	VIF
Constant		3,458	0,603	5,74	0,000	
Layer Height	5,108	2,554	0,603	4,24	0,003	1,00
Material Support	3,112	1,556	0,603	2,58	0,033	1,00
Layer Height*Material Support	1,618	0,809	0,603	1,34	0,216	1,00

Fig. 3-5- Results of the factorial plan.

Tab. 3-4- Results of the factorial plan for every combination.

Combination name	**A**	**B**	**Replicates** $[L/min]$			μ $[L/min]$	σ^2
			$(q_{leak})_1$	$(q_{leak})_2$	$(q_{leak})_3$		
(1)	-1	-1	0.17	0.11	0.19	0.157	0.001
ab	+1	+1	12.78	4.62	7.73	8.38	11.30
a	+1	-1	3.61	3.84	3.49	3.65	0.021
b	-1	+1	1.66	2.31	0.98	1.65	0.29

Several conclusions can be drawn from the data analysis, as shown in **Fig.3.5**:

1. No combination resulted in complete air tightness when the EAC was printed with its longitudinal axis parallel to build plate.
2. The main parameter affecting air leakage is layer height which indicates that switching from a layer height of 0.05mm to 0.15 mm resulted in a greater increase in air leakage than changing the support material.
3. The type of support material only has a minor effect on air leakage. Keeping the layer height constant, the variance increases by moving from PVA to TPU 95 A which is due the latter material requiring the manual removal of the support.
4. The interaction between both parameters is small in comparison to the effect of individual parameters. Also, in accordance with p-values it is possible to assert that the main effects of A and B are statistically significant and that there is no interaction among them.

5. The best solution in terms of minimizing air leakage is also the most expensive one because it requires the use of two different materials and the amount of extruded filament is larger than with other combinations (the quantity of extruded filament increases when the layer height decreases). The cost, as estimated by the slicing software, for the four combinations a, b, ab, and (1) is 0.74, 0.61, 0.58, and 0.89 €, respectively.

In conclusion, if the EAC is printed with its longitudinal axis perpendicular to the build plate results in complete air tightness. If the EAC is printed with its longitudinal axis parallel to build plate some air leakage occurs, which can be minimized to a mean value of 0.157 L/min, however, by using tailored strategies (PVA as support material and a layer height of 0.05 mm).

3.3.3 Geometry investigation for bending Pneunets

PneuNet (pneumatic network) is a class of soft actuator which can perform several movements in accordance with its design geometry. In this research the possibility of 3D printing a monolithic bending PneuNet (MBP) with the EAC directly embed into the structure (i.e., without using any commercially available air-connectors) has been investigated.

Because elements made using FFF technology are anisotropic (it is difficult to predict their behavior using methods such as Finite Element Analysis simulations), and also fabricate MBPs with this technology is inexpensive (the total cost for each MBP is less than 5 €) and automated (no manual tasks are required as for PneuNets manufactured with molding technologies) it has been decided to manufacture and empirically evaluate 4 differently shaped MBPs with the aim to find the shape that shows the best performance in terms of bending angle.

Each MBP consists of an EAC, an embedded L-junction to direct air flow to the extensible portion, an inextensible portion with a height of 3 mm, and an extensible portion equipped with several pneumatic chambers. The difference between the 4 MBPs is limited to the shape and geometry of the extensible portion (**Fig. 3.6 a),b),c) and d)**). While each MBP has the same width of 18 mm, the active bending length varies slightly to allow a finite pattern number of chambers. The active bending length (or in other terms the length of the extensible portion) for R, D, B, and S- types is 80, 76.9, 76, and 81.4 mm, respectively.

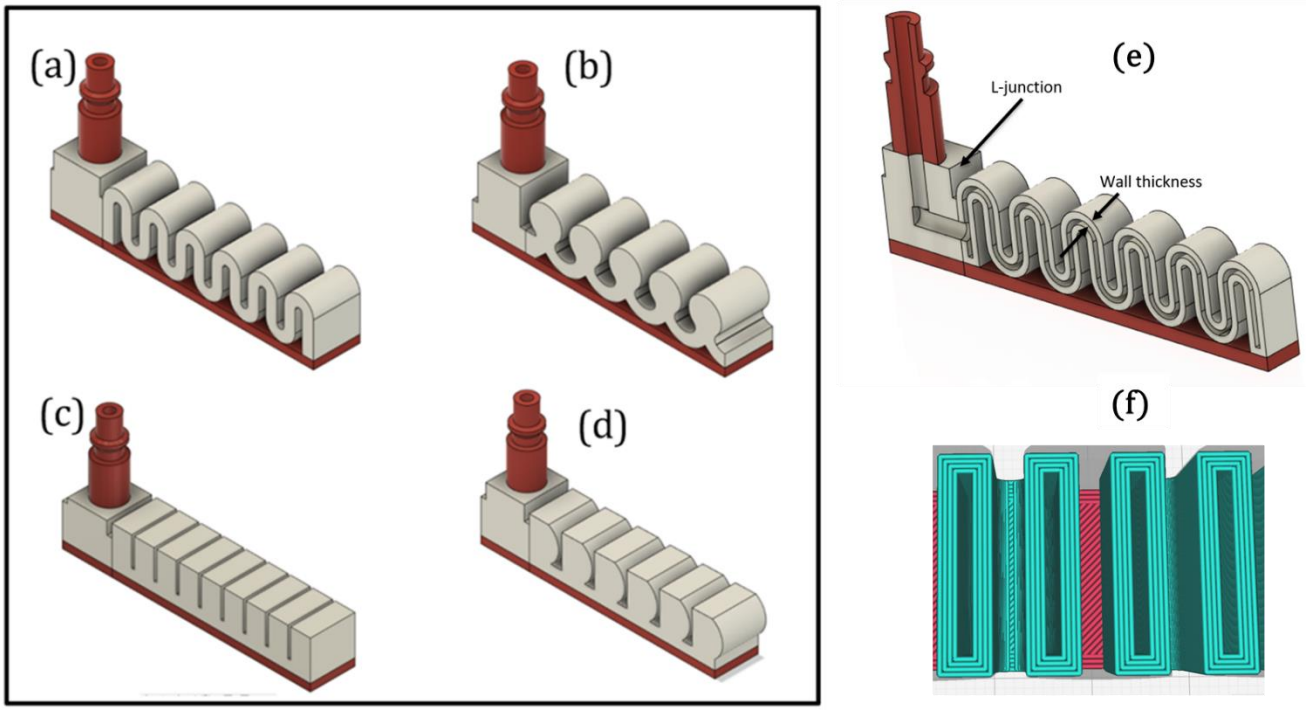

Fig. 3-6-a) S-type, b) B-type, c) R-type, d) D-type, e) Cross section of S-type, and f) top view of the S-type into the slicing software, it is possible to see the four adjacent lines of extruded materials; each one has width of 0.4 mm, which compose the 1.6 mm thickness of the chamber walls.

The proposed MBPs have been designed using the DfAM approach:

1. The EAC embedded in the soft actuator structure has been designed for printing with its longitudinal axis perpendicular to the build plate to ensure air tightness at the pneumatic pipe interface. With this design choice it is necessary to direct the air flow toward the extensible portion which is achieved through an embedded L-junction that can switch the air flow from the EAC to the pneumatic chambers (**Fig.3.6 e)**).
2. Apart from ensuring the absence of air leakage at the interface between EAC and pneumatic pipe, the authors also made sure that there is no leakage into the extensible portion. This is crucial for finding a suitable thickness of the pneumatic chambers walls. Both portions were fabricated using a nozzle diameter of 0.4 mm, for this reason in the slicing software Ultimaker Cura 4.4 the line width parameter was set to 0.4 mm. For this reason, the thickness of the pneumatic chamber walls will be a multiple of 0.4 mm. Through trial-and-error method, it has been found that the minimum chamber wall thickness to ensure air tightness is 1.6 mm. Hence the minimum number of adjacent lines of extruded filament needed to avoid air leakage is 4 (**Fig. 3.6 f)**).

The manufacturing time and cost for R, D, B and S-type estimated by slicing software were respectively 7 h 44 min, 8 h 55 min, 8 h 1min, 9 h 35 min and 4.11 €, 4.68 €, 4.23 €, 4.99 €.

Process parameters set are listed in **Tab.3.5**.

Tab. 3-5- Process parameters set for the Pneunets fabrication.

PARAMETER ↓	EAC	Inextensible portion	Extensible portion	L-junction
Material	TPU 95 A	TPU 95 A	TPU 80 A LF	TPU 80 A LF
Flow	106%	106%	120%	120%
Infill percentage	100%	100%	100%	100%
Infill pattern	CIRCULAR	ZIG-ZAG	LINES	LINES
Temperature	225 °C	225°C	240°C	240°C

After fabrication, the 4 MBPs were tested to link bending angle and tip position in 2D space to pressure input. The setup consisted of an air-compressor, a rigid frame to which the MBP was attached in front of a square millimeter grid used for the optical readings, and a Canon EOS D400 digital camera to record the tip position and bending angle (**Fig.3.7a)**).

Starting from an input pressure of 0 bar (rest condition), the pressure was increased with step of 1 bar till to reach the maximum value of 4 bar, at each pressure step one image has been captured to measure the bending angle and the tip position.

Fig.3.7 b) shows the bending angles obtained for different input pressures for the 4 different MBP shapes.

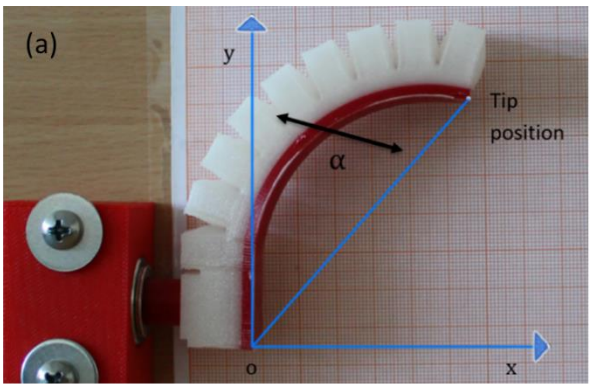

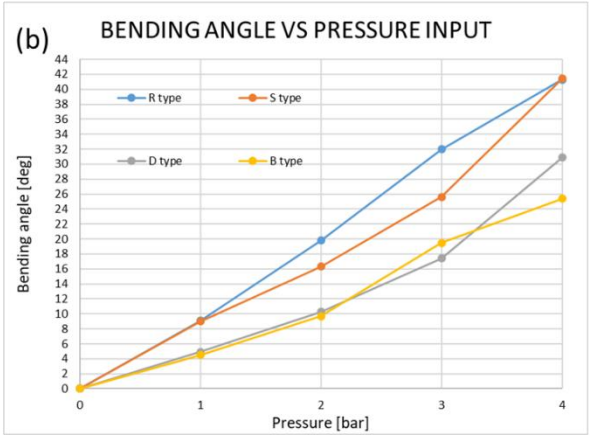

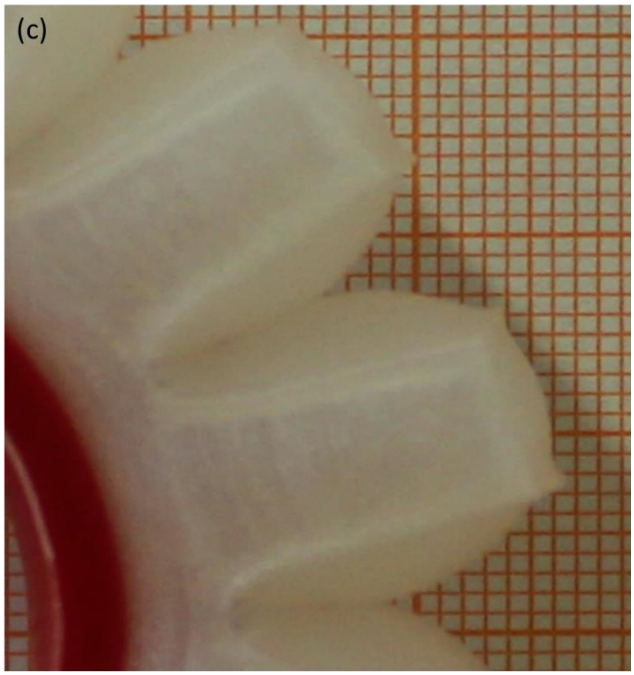

Fig. 3-7- a) Illustrating how bending angle and tip position were calculated, b) Bending angle vs. pressure for each MBP type, and c) Zoom of an R-type MBP showing its behavior when pressurized.

The R- and S-types were the most flexible and exhibited very similar bending angles and tip displacements. At 1 bar, their bending angles only differed by 0.1°. At higher pressures of 2 and 3 bar the S-type is lightly more rigid than the R-type while at 4 bar the bending angles are again very similar (41.3° for R-type and 41.4° for S-type). D- and B-type were the least flexible and had comparable bending angles between 0 and 3 bar while at 4 bar the D-type was more flexible than the B-type and, however, less flexible than both R- and S-types. Overall, the R-type thus turned out to be the best MBP as it is the most flexible between 0 to 3 bar and equally flexible at 4 bar as the S-type.
From the experimental phase, several considerations about the relationship among MBPs bending behavior and constitutive design parameters can be drawn. When pressurized, the chamber walls, aligned with the air flow (in other terms parallel to air-flow), tend to stretch and the walls perpendicular to the air flow (such as the top chamber wall) tend to expand.
Consequently, it is possible to translate this consideration in the maximization, for each pneumatic chamber, of the ratio (S) computed as shown in equation (4) being S_{par} the surface area of the walls parallel to air flow and S_{per} the surface area of the walls perpendicular to air flow:

$$\max S = \frac{S_{par}}{S_{per}} \tag{1}$$

The second most important design feature which affects the flexibility of MBPs is the close proximity of adjacent chambers. The chambers stretch their walls in the air flow direction so increasing the closeness among adjacent chambers there will be a better MBP elongation because the chambers will better push against each other. In **Fig.3.7 c)** a zoom of R-type MBP during the compressed air insufflation is shown; from this picture it is possible to graphically see the two features described above: when compressed air is insufflate the walls perpendicular to air flow expand themselves while the walls parallel to air flow stretch themselves and it involves the push of adjacent chambers resulting in the actuator bending movement.
For the same wall thickness and active bending length, the bending performance of the different MBPs mainly depended on their shapes, as a matter of fact those with maximal S ratios (see Eq.(4)) and proximity between adjacent chambers would perform best.
In conclusion, S- and R-types delivered the greatest bending angles because their designs optimize S ratio and chamber proximity. While the R-type has the closest proximity between adjacent chambers, the S-type has the highest S ratio.

3.3.4 Bending performance improvement

In accordance with scientific literature, the two main features affecting bending performance are the chambers wall thickness and the numbers of chambers. As regards the former, it has been proved both experimentally and theoretically that small values of wall thickness generate an increase in the final bending of the actuator [116], [118]. As regards the latter, it has been shown in literature, that the more are the chambers for a given length the greater is the bending[116]. In the present work, it has been decided to focus on wall thickness.

In 3.3.3, it was shown how the minimum wall thickness to guarantee air tightness was 1.6 mm, i.e., four adjacent extruded filament lines of 0.4 mm. Working on R-type, a way to reduce wall thickness but at the same time avoid any possible air leakage has been found. In this study all the design parameters, except wall thickness, have been held unchanged in order to quantify how walls thickness impact on the bending performance. Because line width parameter (in **Fig 3.8** it is possible to see the difference among 3 different line width values on the same square component) depends on nozzle size (generally this value should range from - 20% up to +20% of nozzle diameter), then it has been decided to use a nozzle diameter of 0.25 mm in order to set line width value lower than 0.4 mm in the slicing software (set to fabricate MBPs with wall thickness of 1.6 mm).

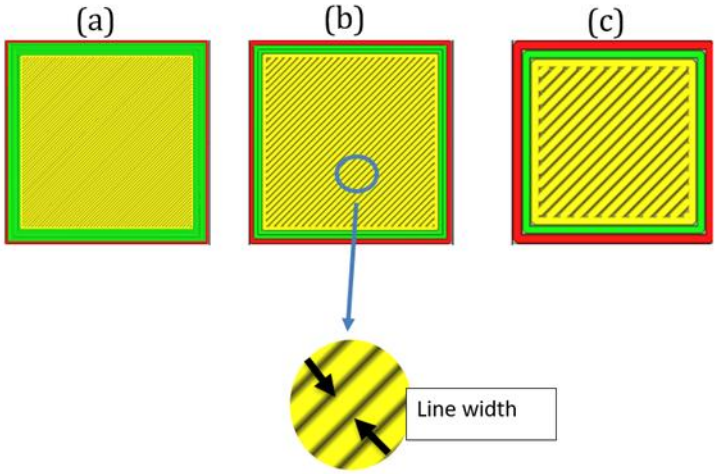

Fig. 3-8- Three different line width values: a) 0.2 mm, b) 0.4 mm, and c) 0.8 mm

In this way, a line width value of 0.2 mm in the slicing software was set and R-type wall thickness was decreased from 1.6 mm to 1 mm. These choices (nozzle diameter = 0.25 mm, line width = 0.2 mm and wall thickness= 1mm) involve 5 adjacent extruded lines. Testing this new kind of R-type, its air tightness has been proved.

The novel important feature discovered in this research is that the air tightness of MBPs manufactured via FFF technology does not depend on the wall thickness as for PneuNets fabricated by molding, but it depends on the number of adjacent extruded lines that make up the chamber wall. So, the key printing parameter that needs to be tuned to avoid air leakage is “line width”, which is related to actuator design in the following way: the wall thickness of each MBP should be equal to

line width value set in slicing software multiply for 4 or 5 times. This proves how DfAM is crucial for advanced applications involving FFF technology.

There is thus a direct correlation between “line width” printing parameter and MBP air tightness and the knowledge of this relationship is the enabling key to fabricate 3D printed soft robots with improved performance. For the 3D printer employed in this research, namely Ultimaker 3, the smallest available nozzle diameter is 0.25 mm. For other commercial dual-extruder 3D printers, nozzles with a diameter of 0.1 mm are available: it means that should be possible to fabricate soft actuators with values of wall thickness lesser than 1 mm (i.e. setting line width parameter as 0.1 mm, a wall thickness of 0.5 mm , air-tightness should be ensured).

Fig.3.9 a) and b) show the effect of the wall thickness on bending angle and tip position for R-type actuator with the two different wall thickness values: 1 mm walls R-type is far more flexible than its counterpart, i.e. the 1.6 mm walls version. In fact, the improved value of bending angle when an input pressure of 4 bar was provided was 72.9 ° against 41.3 ° of the previous version, resulting in a bending angle improvement of 76.7%

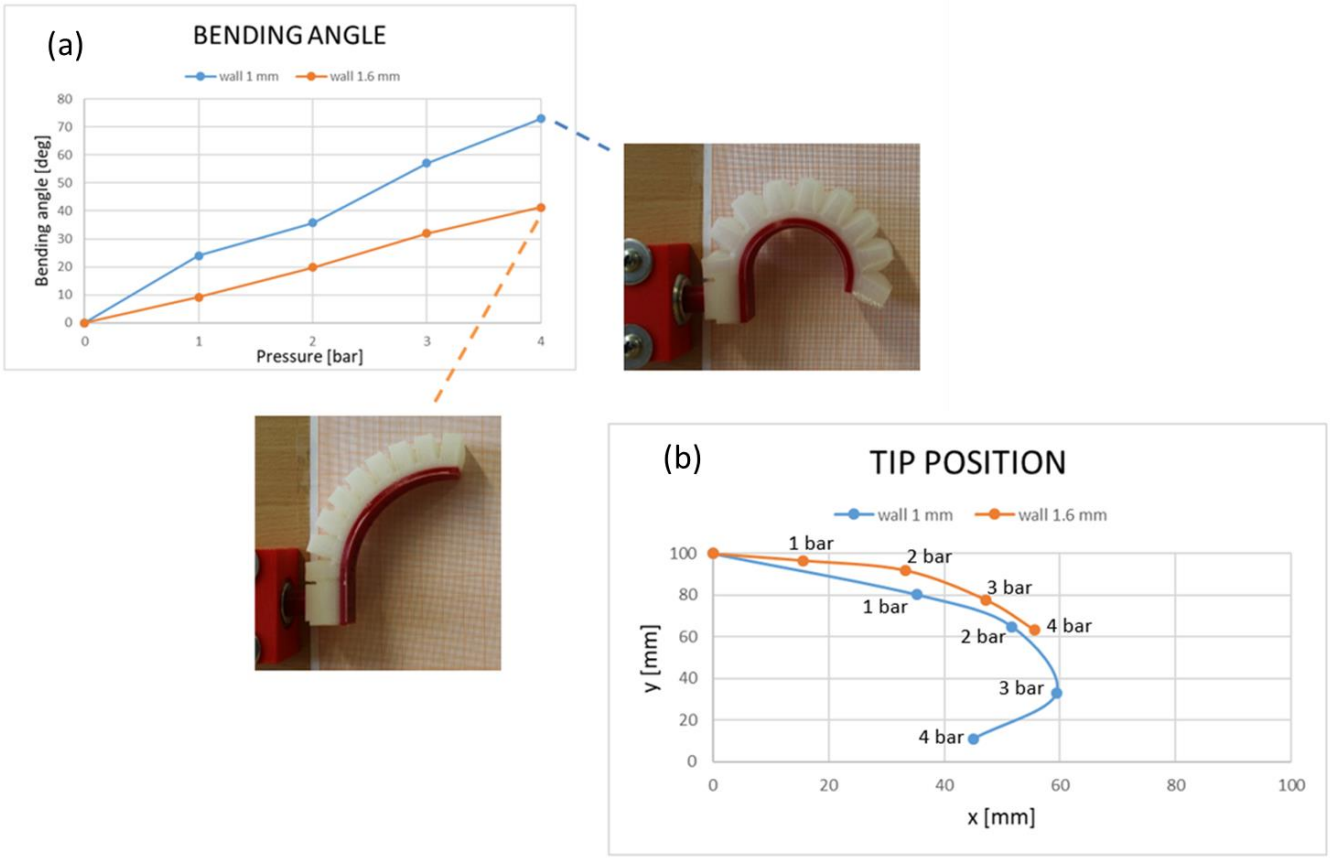

Fig. 3-9-a) Bending angle vs. input pressure for R-type with wall thickness of 1.6 and 1 mm, and b) Tip position, here it is possible to see the tip movements in the 2D space for R-type with 1.6 and 1 mm wall thickness

3.3.5 Conclusions

In this work, a new manufacturing approach for soft actuators based on the inexpensive FFF approach has been presented. A novel 3D printed air connector with the following features was developed: i) it can be easily embed in soft robots made with FFF technology as it can be manufactured in the same printing cycle as the soft robot; ii) it is completely air tight at the interface between the pneumatic pipe and the soft robot; and iii) it enables to overcome assembly problems due to the usage of marketable air connectors. Using a 2^2 factorial plan, we could show that only one printing orientation can ensure the absence of air leaks in the 3D printed air connector. By comparing four different 3D printed MBP shapes the authors found that the best performance was achieved with the R-type MBP characterized by a bending angle of 41.3 ° when a pressure of 4 bar was supplied. Also, from experimental data the authors outlined two design rules needful to better understand why some actuator shapes result more performing than others. In the shape selection phase, the minimum wall thickness able to ensure air-tightness was 1.6 mm; by using a Design for Additive Manufacturing approach (DfAM) it has been possible to reduce the minimum wall thickness up to 1mm, ensuring at the same time the total actuator air-tightness. The new improved R-type actuator results by far more flexible compared to the first version: the bending angle has been improved by 76.7 %, switching from 41.3 ° to 72.9° when a pressure of 4 bar was supplied

3.4 Additive Manufacturing of silicone structures with embedded actuators for bio-inspired soft robotic systems

3.4.1 Introduction

Recently, the fabrication of extremely soft structures capable of performing bio-inspired complex motion is a challenging task in soft robotics. On one hand, traditional manufacturing methods such as silicone molding do not allow the fabrication of complex structures; on the other hand, alternative fabrication technologies such as lithography and bioprinting of hydrogels are expensive. This research describes a unique biomimetic morphing structures obtained from a custom-made, inexpensive 3D printing setup capable of extruding silicone (Ecoflex 00-10): two process parameters, printing speed and build plate temperature were examined to study the effect on printing accuracy. Additionally, the silicone curing mechanism was investigated, and an innovative method for locally curing recently extruded silicone was proposed. The proposed 3D printing setup was used in conjunction with a cartesian pick and place robot (CPPR) to completely automate the fabrication of 7 mm thick silicone skin structures with embedded shape memory alloys actuators: these structures were fabricated monolithically without any assembly tasks and direct human intervention. Taking advantage of the possibility to 3D print bioinspired structures, three different patterns were fabricated over the silicone skin, resulting in remarkable dynamic motions: out of plane deformation (from the x-y plane to the x-z plane) was achieved for the first-time employing silicone skin, to our knowledge. This work aims to advance the role of additive manufacturing in the field of soft robotics by demonstrating all the advantages that a low-cost, custom-made silicone 3D printer can bring in terms of manufacturing soft structures, thus further paving the way for future research aimed at modeling the behavior of 3D printed bioinspired structures.

The silicone structures with embedded actuators, exhibiting motion similar to motions of animals are shown in Fig.3.10.

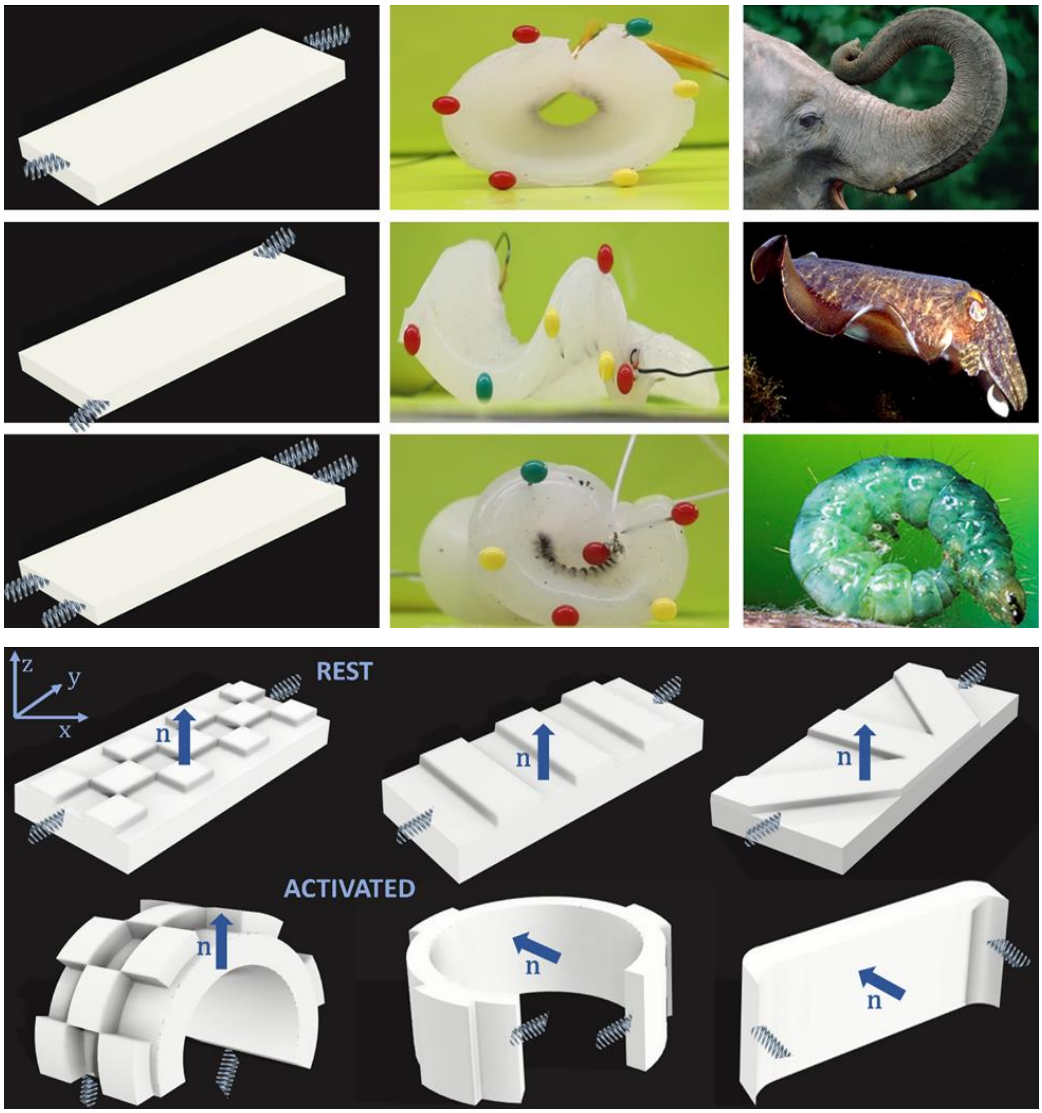

Fig. 3-10- Structures fabricated using the custom-made silicone 3D printer and motions obtained when the SMA spring actuator was activated.

3.4.2 Materials and methods

The current study demonstrated an inexpensive custom-made 3D printer based on the material extrusion technology to create extremely soft silicone structures with embedded shape memory alloys (SMAs) actuators capable of complex motions. Specifically, using the proposed setup two classes of silicone structures were fabricated: i) traditional one (proving that using the proposed fabrication setup the whole manufacturing cycle is fully automated) capable of motions recalling several animals as shown in Fig 1 a) , and ii) patterned one (silicone structures with different patterns impossible to be manufactured exploiting the traditional fabrication approach) capable of out of plane motions, as shown in Fig 1 b) An open-source 3D printer (The Maker Farm Prusa 8″ i3v kit) already used in [20] has been modified further with the addition of the following:

i) A stepper motor was installed in the machine's top section (connected to a wooden support structure).

ii) A system consisting of two gears connected to the motor shaft and a lead screw equipped with a custom made "pushing" part was assembled and connected to the lead screw to convert the stepper motor motion to a linear motion capable of pushing the syringe containing silicone material and obtaining the silicone extrusion.

iii) A syringe holder is attached to the wooden support to hold the syringe, lead screw, gears, and stepper motor.

iv) A silicone-filled syringe reservoir is connected to a plastic tube by a plastic connector (Female Luer x 1/8" hose barb adapter), which is connected to a terminal calibrated plastic nozzle via a plastic connector (Male Luer Lock 1/8" hose barb adapter).

Fig 3.11 shows the above-mentioned 3D printing setup.

Ecoflex 00-10, a dual-part silicone (part A and part B) material, was used in this research since it demonstrated excellent versatility, processing easiness and reliability while fabricating 3D printed structures and soft somatosensory actuators [119] [120]. In **Tab.3.6**, the most important characteristics of Ecoflex -10 (from material data sheet) are listed.

After pouring equal amounts of Parts A and B into the mixing container (1A:1B volume or weight ratio), they were thoroughly stirred and mixed for at least 3 minutes. The silicone was poured into a 60 mL syringe and connected to the 3D printed setup following the mixing procedure. Avoiding air entrapment and bubble formation inside the syringe is critical throughout the mixing procedure. Air bubbles were carefully removed from the syringe using vacuum degassing; otherwise, the pressure caused by the air inside the syringe could force the syringe to break.

Tab. 3-6- Silicone properties

Properties	**ECOFLEX™ 00-10**
Viscosity (Mixed)	140 $Poise$
Density	1040 Kg/m^3
Specific Gravity	1.04 g/cc
Mix Ratio (By Weight)	1A: 1B
Mix Ratio (By Volume)	1A: 1B
Elongation at Break	800%
Pot Life	30 minutes
Cure Time	4 hours
Tensile Strength	120 psi

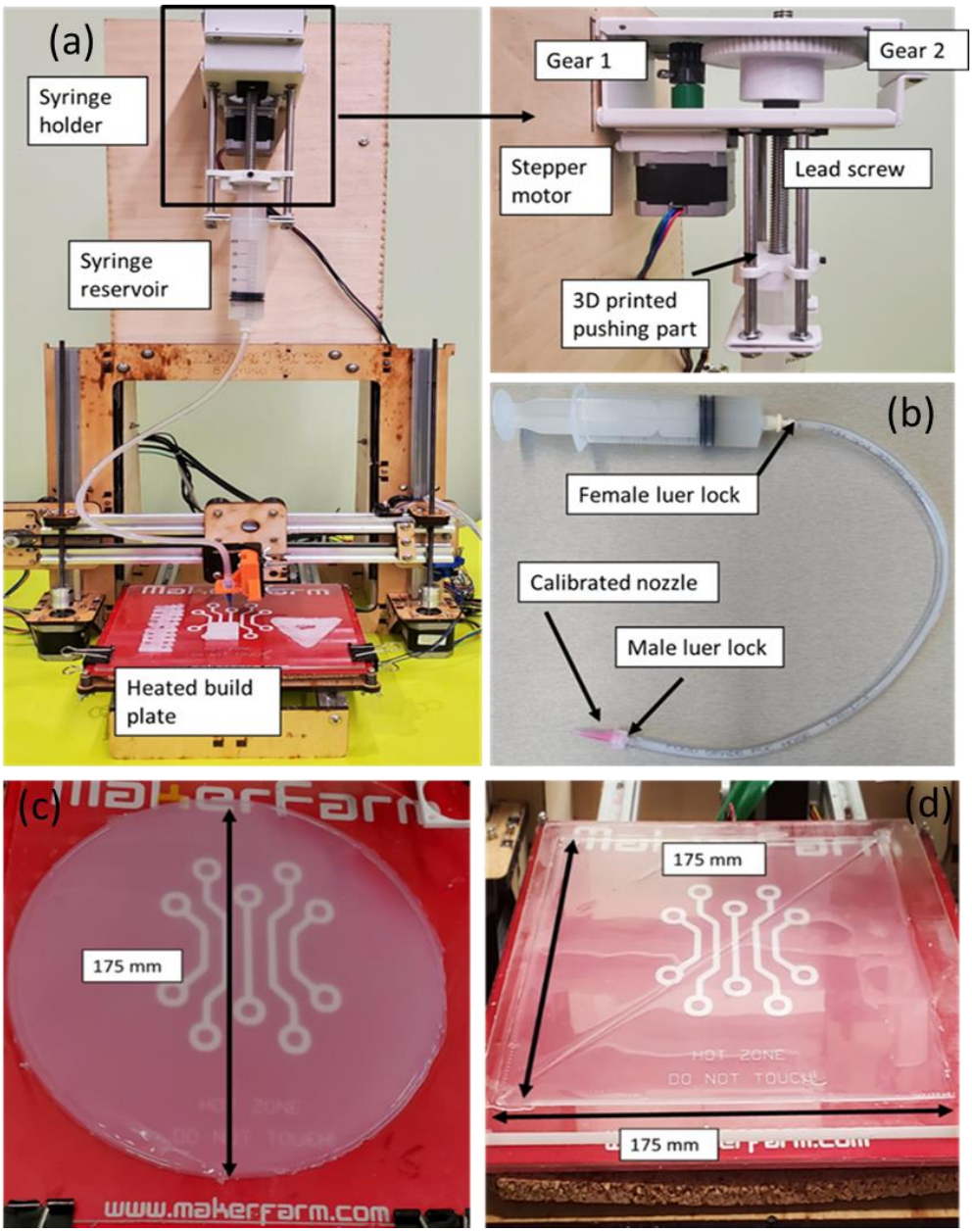

Fig. 3-11- a) Proposed custom-made 3D printing setup, b) Syringe-tube-nozzle system, c) 175 mm 3D printed circle, and e) 175 mm 3D printed square.

3.4.3 Process parameters- Literature review

Attributed to the reason that additive manufacturing of silicone structures is an emerging manufacturing technology, the scientific literature is scarce on process parameters: few studies correlating process parameters to output variables (such as mechanical properties, surface finishes, and dimensional accuracy, among others) have been conducted, in comparison to more established AM technologies such as FFF [58] and SLA [121].

The primary efforts made to correlate process parameters to printing outputs as in printing accuracy, printing force, intralayer adhesion, and mechanical properties are critically analyzed in this section: the significant process parameters, measurement units, and abbreviations are listed in **Tab.3.7.**

Tab. 3-7- Main process parameters for silicone 3D printing studied in scientific literature

Process parameter	***Measurement unit***	***Abbreviation***
Build plate temperature	$°C$	T_b
Printing speed	mm/s	S_p
Deposition Rate	mm/mm	D_r
Flow rate	mL/s	Q
Layer height	mm	h
Nozzle diameter	mm	d
(Pressure)^2	KPa	P
Raster width	mm	R_w
Curing temperature	$°C$	T_c
Compressed factor	---	X
Number of outlines	---	O
Infill angle	°	I_a

Colpani et al. [122] studied the effect of three parameters (T_b, $S_p$and D_r) on the final accuracy of silicone samples by determining the average width and variability of fabricated structures. They conducted a DoE plan and determined that i) T_b mainly affects the line width average: as T_b increases, the silicone's solidification time decreases, resulting in far less material spreading during printing and a higher degree of accuracy in the extruded structure. Furthermore, they found that the highest limit of T_b was about 100°C: above that point, they encountered nozzle obstruction. ii) The D_r linearly influences the width average value confirming that the material solidification is under control and iii) The three process parameters analyzed by the authors have no impact on the variability of the width. Plott et al. [123] studied a crucial aspect in extrusion-based silicone: the relationship among process parameters and voids (number, dimension, and effect on tensile strength). They observed that i) when X is equal to 1 and 0.97 and I_a is equal to +/- 45° and 90 °, high level of tensile strength is obtained: even though some small voids are present when X is equal to 0.97, high tensile strength was maintained because the voids were able to orient themselves along the direction of force. ii) the 0° infill specimens were found to be the worst performing in tensile strength due to the internal tangency voids. Similar considerations have been highlighted in Miriyev et al. [124] who correlated I_a to mechanical properties (and extruder silicone formulation). They discovered that maximum strain was reached when I_a is equal to 90°, while the maximum tensile force was reached by setting I_a equal to 0°.

Walker et al. [125] performed an intriguing study in which they examined the relationship between T_c and intralayer adhesion using a peeling test. This work is interesting because it analyzes intralayer adhesion in this manufacturing field for the first time. Inadequate crosslinking between layers can result in anisotropy and premature failure: this is a significant issue because this manufacturing technology is frequently used to fabricate soft robots (which are frequently actuated by compressed air) and prosthetic and rehabilitation devices with a long cycle life and the ability to withstand specific loads. The key to increasing the strength of silicone structures is to maximize the interfacial adhesion between two printed layers. In theory, when a printed layer cures, the number of cross-linkable groups available for bonding to the subsequent layer lowers. Their work results in a negative correlation between Tc and intralayer adhesion: as T_c increases, intralayer adhesion (and thus part strength) decreases. Thus, in large-scale silicone 3D printing, a trade-off must be considered: if the layers are over cured, the structure's tensile strength will be reduced, but if they are under cured, tall structures cannot be printed due to the structure collapsing.

The topic of large-scale extrusion-based silicone is extremely appealing since it has the potential to lead the way for molding replacement, resulting in an automated process that requires few human interventions and saves time and money. Plott et al. [126]established a precedent in this field by correlating process parameters to additive manufacturing forces that occur during fabrication. The ability to fabricate tall and thin structures requires an understanding of how to minimize extrusion forces. They evaluated three process parameters: $h, d,$ and Q in a parametric study, linking them to normal force (F_n) and tangential force (F_t). They determined that depending on the process parameters used, four different configurations of printing forces can occur (see **Fig. 3.12**)

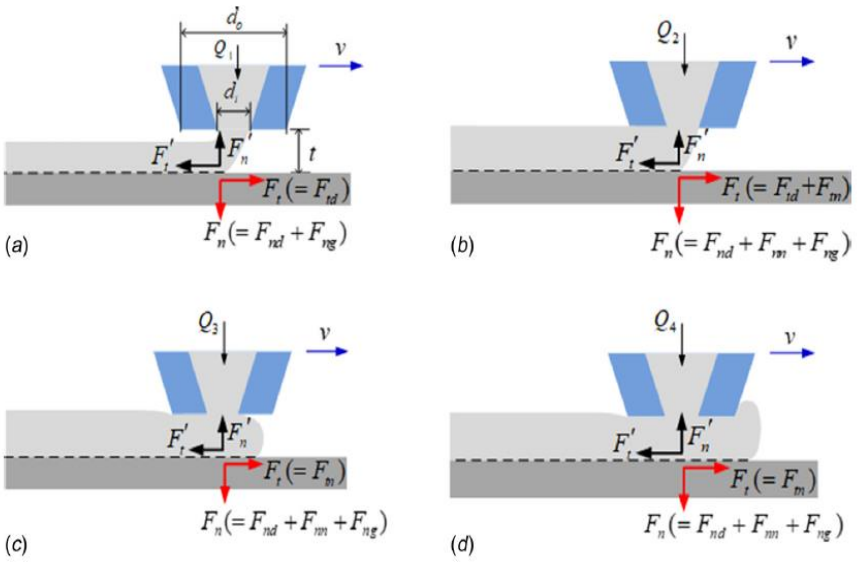

Fig. 3-12- Four different force scenario occurring when silicone is extruded in Plott et al. [126] *. From (a) to (d) Q is constantly increased leading to the four different printing scenarios explained in the text.*

They emphasized that the optimal configuration for minimizing printing forces is the one depicted in Fig.**3.12 a)**: as a matter of fact: i) F_t increases if its major component F_{tn} (tangential force caused by the nozzle dragging through the deposited silicone) increases as well, resulting in an order of magnitude increase in F_t when present, ii) F_n increases when the nozzle comes into contact with the recently extruded filament and F_{nn} (the normal force caused by the normal interaction between the nozzle and the extruded silicone) increases F_n by an order of magnitude when present, iii) to reduce the total printing force F $(F_t + F_n)$ it is necessary to reduce Q and increase h and this conclusion is consistent with the work of Percoco et al. [31], who established a relationship between the h parameter and extrusion force for FFF technology. iv) When a small nozzle (d) is used, the force-deflection ratio becomes more favorable: the force-deflection ratio also becomes less dependent on Q and t.

A summary of each cited work on silicone modeling is provided in **Tab.3.8**.

Tab. 3-8- Summary of the cited works

Reference	***Method***	***Process parameters***	***Response output variable***	***Conclusions***
[122] Colpani et al. (2019)	DoE	• T_b • S_p • D_r	• Width average(mm) • Width Variability	• T_b increases → accuracy increases • D_r increases → accuracy decreases • Process parameters don't affect width variability
[123] Plott et al. (2018)	Parametric study	• X • I_a	• Number of voids • Dimension of voids (mm) • Tensile strength (MPa)	• X =1 and I_a =+/- 45° and 90 ° → high tensile strength • X = 0.97 → voids orient themselves along the direction of force • I_a= 0 → worst tensile strength.
[124] Miriyev et al. (2019)	Parametric study	• I_a	• Strain (%) • Tensile force (N)	• I_a = 90 → maximum strain • I_a = 90 → maximum tensile force
[125] Walker et al. (2021)	Parametric study	• T_c	• Intralayer adhesion (N)	• T_c increases → intralayer adhesion decreases

[126] Plott et al. (2018)	Parametric study	• h • d • Q	• Extrusion force (F_n and F_t) (N)	• Best printing scenario to reduce extrusion force is shown in Fig S1 (a) • F_t increases when by nozzle dragging through the deposited silicone • F_n increases when the nozzle touches the recently extruded filament • Q decreases and h increases → extrusion force decreases Small d → favorable force deflection ratio occurs • Small d→ Q and h don't influence the force deflection ratio

3.4.4 Process parameters- Experimental analysis to improve the final accuracy

One of the most important relationships to study in silicone additive manufacturing is the correlation between process parameters and final part accuracy. Here in this work, two process parameters were studied: build plate temperature, henceforth T_b, (°C) and printing speed (mm/s), henceforth P_s. For each process parameters, three levels were varied: low (50 °C and 10 mm/s), medium (75 °C, and 20 mm/s) and high (100 °C and 30 mm/s).

A factorial plan with 3 repetitions was computed (see Supplementary S2 for details) printing a single layer, single line silicone bead (see **Fig.3.13 a) and b)**) and two outputs were experimentally measured: bead width and bead height. For the measurements, an optical benchtop microscope (PSM1000, Motic), equipped with a vertically positioned camera (Moticam 3+, Moticom) for photographing the magnified sample, was employed.

The most important results in terms of bead width and bead height are shown respectively in **Fig3.13 c, d**. With regards to the bead width investigation, the following conclusions can be drawn:

- For each build plate temperature, increasing the print speed (from 10 to 20 to 30 mm/s) results in a decrease in line width, resulting in a sample width value close to the theoretical value of 1.2 mm: a width of 1.8 mm, 1.61 mm, and 1.57 mm was measured for a built plate temperature of 50 °C, 75 °C, and 100 °C, respectively, when a constant print speed of 30 mm/s was set. This conclusion is particularly intriguing when compared to its FDM counterpart: for that technology, it is well known from literature [55] that there is a negative correlation between

printing speed and accuracy: in this case, the correlation is positive. To understand why this behavior occurs, it is imperative to analyze the setup and take into consideration that the flow value was constant for every experiment: the silicone inside the syringe is pushed by a mechanism activated by a stepper motor and let it flow through a PETF tube and finally into the plastic nozzle, both of which are vertically adjacent to the reservoir silicone syringe. Gravity plays a significant part in this process, as silicone is less viscous than melted plastic filaments. Even though the volumetric flow is constant for each printing speed, when a low printing speed is being used, a greater amount of silicone flows out of the nozzle due to the gravity effect. The printing speed mitigates the unwanted extra silicone generated by gravity in the following way: when the build plate temperature is set to 50 °C, 75 °C, and 100 °C, switching from the low level (10 mm/s) to the medium level (20 mm/s), the sample width is reduced by 45 %, 31 %, and 42 %, respectively. The sample width is reduced by less than 5%, 13%, and 7.6%, respectively, when the build plate temperature is 50 °C, 75 °C, and 100 °C, while the speed is increased from medium (20 mm/s) to high (30 mm/s).

- The build plate temperature produces an effect on the sample line width. The T_b affects the width of the sample in the following way when the best printing speed (namely 30 mm/s) in terms of accuracy is set: switching from 50°C to 75 °C and from 75°C to 100 °C, the sample width is reduced respectively of 10.5 % and 2.48 %. The authors explain the following results in this way: increasing the build plate temperature, the curing time of the silicone is abruptly reduced. It means that the expansion of the recently extruded silicone is reduced as well because as soon as the silicone flows out from the nozzle it got cured: this behavior is more noticeable when the build plate temperature is increased from 50 °C to 75 °C than when it increased from 75°C to 100 °C.

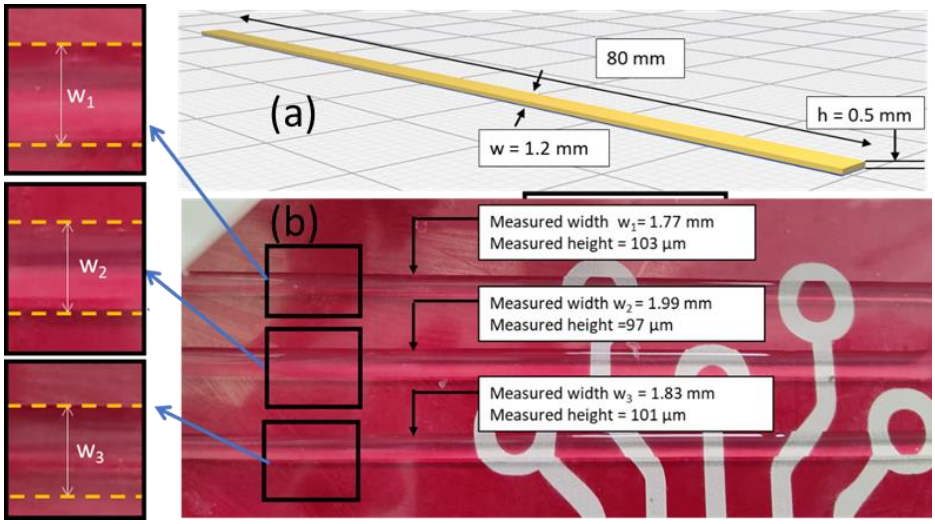

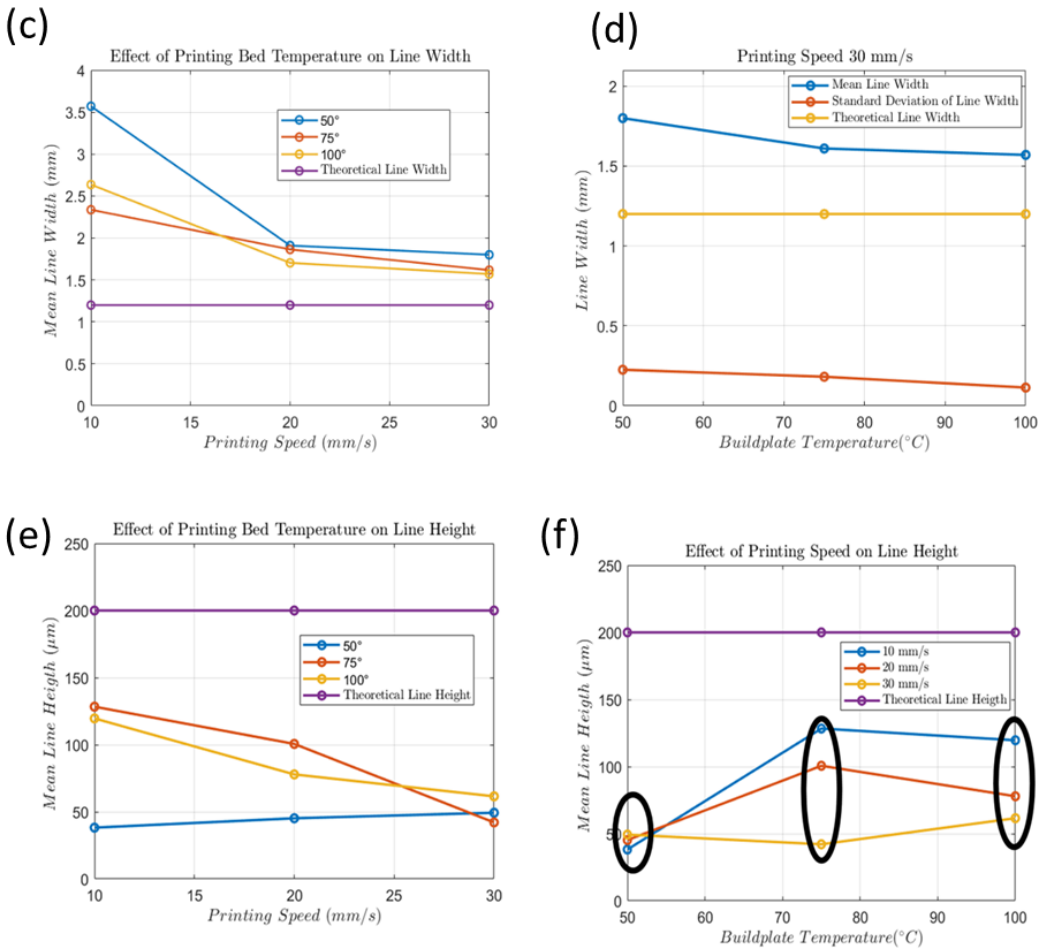

Fig. 3-13- a) 3D printed samples in the slicing software (Ultimaker Cura), b) Actual 3D printed sample manufactured setting P_s = 20 mm/s and T_b = 75 °C, c) Effect of T_b on the measured line width, d) Effect of T_b on the measured line width when Ps = 30 mm/s, e) effect of T_b on measured line height, and f) effect of P_s on the measured line height.

With regards to the sample height, the following conclusion can be pointed out (see **Fig.3.13 e), f)**).

- When the build plate temperature is set to 50 °C, the printing speed does not affect the sample height, which is nearly 50 μm (150 μm less than desired height). The authors explain the low values of layer height obtained when the build plate temperature is set to 50 °C (and the insensitivity to print speed) as follows: when the material does not receive enough heat to get instantly cured, it collapses (in fact, the line width is significantly larger when the build plate temperature is set to 50 °C), resulting in a reduction in the layer height. When the build plate temperature is 75°C and 100 °C, the printing speed produces an interesting effect: as the printing speed increases, the layer height decreases. Because the amount of silicone flowing out at 10 mm/s is more than the one at 20 mm/s, which in turn is more than the one at 30 mm/s (gravity effect) and because the build plate temperature is sufficiently high to suddenly

cure the extruded silicone, the measured layer height is greater when a low printing speed value is set. For both the build plate temperature (75°C and 100 °C), the behavior is quite similar: roughly 130 μm at 10 mm/s, 100 μm at 20 mm/s, and 50 μm at 30 mm/s.

In summary, the cross-section study yielded the following significant findings: gravity has a significant effect on the precision of silicone extrusion-based 3D printing (Ecoflex 00- 10). If the printing speed is too slow (10 mm/s), the amount of silicone that flows out of the nozzle becomes excessive, resulting in a "collapse" (bigger line width than the one set and smaller height than the one set). 20 and 30 mm/s provide a better outcome in terms of width accuracy, while only 20 mm/s provide a good result in terms of height accuracy. In terms of build plate temperature, both the medium (75 °C) and high (100 °C) values produce nearly identical results in terms of width accuracy and layer height. In conclusion, among the parameters tested, the ones that should be selected to achieve a suitable balance between width and height accuracy are: i) printing speed set at 20 mm/s and, ii) build plate temperature set at 75 °C.

The most frequently employed approach for extrusion-based additive manufacturing techniques consists of using a heated build plate to cure the extruded silicone, allowing the fabrication of layered structures. This curing approach has a significant constraint in terms of the maximum structure height: layer after layer, the heat generated by the build plate is insufficient to cure the silicone structure. As a result, the heated build plate method is unable to be utilized to fabricate the tall 3D printed structure. The current section examined the drop in heating after each layer using an infrared thermal camera at different build plate temperatures. The printed sample is depicted in **Fig.3.14 a)**, and it has a rectangular shape with a square length of 25 mm and an 8 mm in height. It was determined arbitrarily to use a 0.4 mm nozzle and a layer height of 1 mm for the slicing: in this manner, every manufactured layer correspond to 1mm. The plots with infrared images are shown in **Fig.3.14**. The experiment was performed at two different build plate temperature (55°C and 70°C): the linear regression equation (equation (20), and (21)) calculated on the experimental data is respectively,

$$T = -1.78h + 55.8 \qquad (20)$$

$$T = -1.35h + 70.9 \qquad (21)$$

Where T (°C) is temperature measured at the top of every recently extruded layer and h (mm) is the height of every layer. For both experiments, the temperature drop is quite similar: 1.78 $\frac{^{\circ}C}{mm}$ for the 55°C build plate and 1.35 $\frac{^{\circ}C}{mm}$ for the 70°C build plate, this slight drop in temperature can be attributed to room conditions; indeed, the custom-built setup is based on an open-chamber design, making it sensitive to its surrounding environment. In the experiment with the 55 °C build plate temperature,

the structure began collapsing at the 7th layer (after reaching 7 mm of height). When the temperature read from the Thermal camera reached 44 °C, it collapsed completely and the temperature at the next layer (8th layer) was 43.2 °C. **See Fig.13.4b).**

Furthermore, when 70°C was set as build plate temperature, it was not possible to create an 8 mm tall structure in this situation (not due to the structure collapsing, as was the case with the 55 °C build plate temperature), since the silicone was cured inside the tube-nozzle due to the build plate's high temperature. Around the 7th layer, the silicone began to cure; indeed, as illustrated in **Fig.13.5d)**, the final printed layer (8th) is affected by the under-extrusion problem.

To address this issue, the tube-nozzle assembly was thermally insulated using a commercially available thermal insulator spray (Loctite Insulating Spray Foam), as illustrated in **Fig.13.4 c)**. Using the new insulated tube, we fabricated taller structures: setting the build plate temperature at 70 °C, 18 mm tall structure was fabricated, finding a temperature drop of 1.51 $\frac{^{\circ}C}{mm}$. In this case, at the 18th layer when the measured temperature over the recently extruded layer was around 44 °C the structure collapsed, as expected. The advantage of the proposed approach consists of the possibility to increase the height of 3D printed silicone (Ecoflex 0010) structures from 7 mm to 17 mm.

It is important to point out that higher build plate temperature than 70 °C was found to be not suitable for the following application: when the higher temperature (from 75 °C to 100 °C) is set, the first layer gets cured too fast and adhesion between the first one and second one is not good enough involving accuracy problems. For this reason, we claim that using only the build plate temperature as heating source to cure the extruded silicone (Ecoflex 0010) the maximum height of structure that can be reached avoiding any collapse is around 17 mm (if the nozzle-tube system is thermally insulated). To overcome this issue an additional heating source was added near the calibrated nozzle, to locally cure the recently extruded silicone: in this way tall structures almost 30 mm were fabricated showing that with the proposed method, the only constraint is related to the curing process inside the syringe, after 2hr and 20 min the silicone starts getting cured.

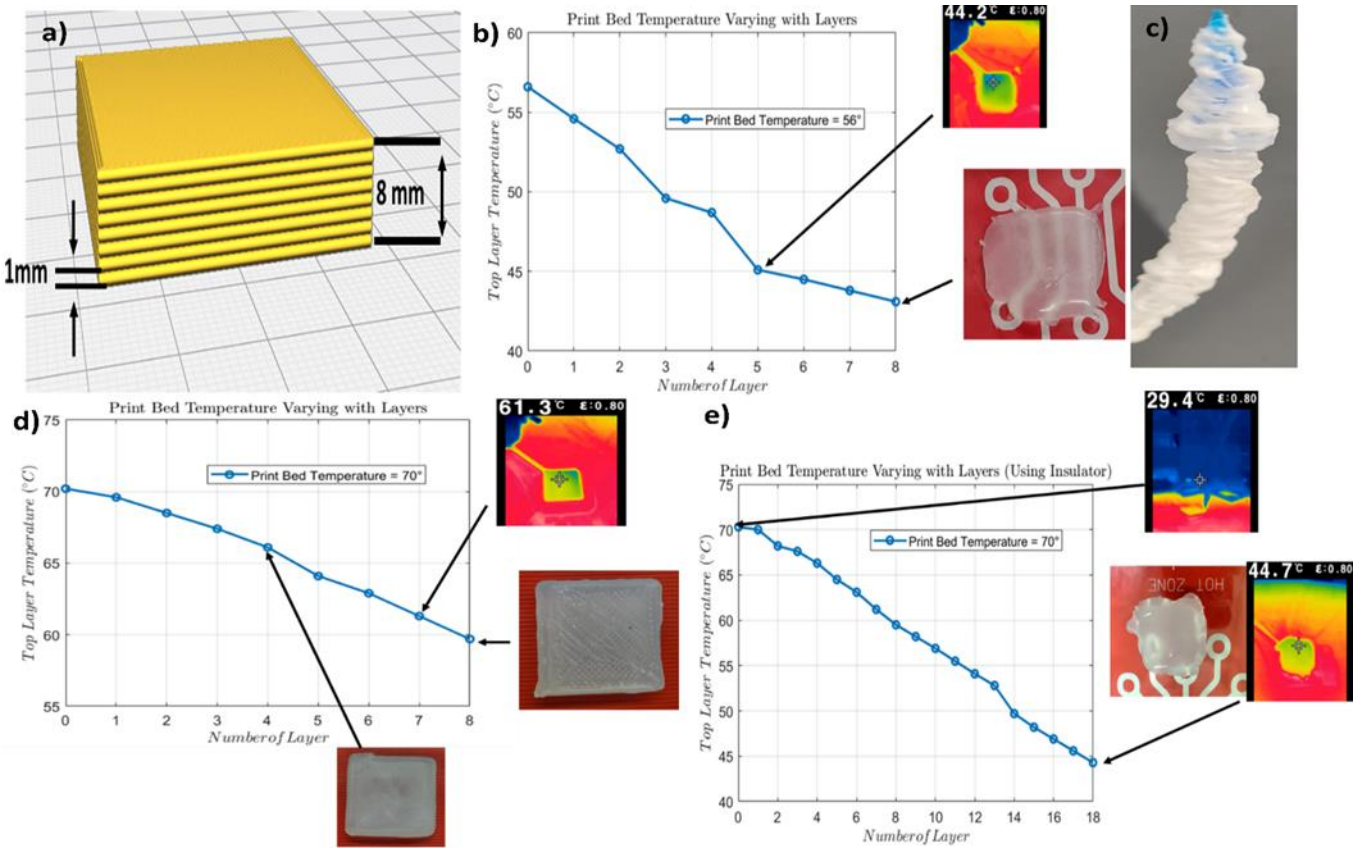

Fig. 3-14 Build plate heating study: a) 3D printed sample, b)Drop in temperature when the build plate temperature was set equal to 55 °C, c)) tube-nozzle system thermally insulated,d) Drop in temperature when the build plate temperature was set equal to 70 °C, and e) Drop in temperature when the build plate temperature was set equal to 70°C and the tube-nozzle system was insulated.

3.4.5 Application in soft robotics: silicone skin with embedded SMA

In recent years, there has been a lot of interest in the fabrication of bio-inspired soft structures with embedded actuators[127] [128] : the ability to achieve several types of movement in extremely soft elastomeric parts is appealing for various applications. In the current state of the art, silicone is poured into a mold (typically a 3D printed mold) having certain slots for the manual integration of shape memory alloy (SMA) actuators in the form of wires or springs[129]–[136].

For the first time, the whole process of fabricating a silicone skin has been automated in this research article, using the proposed 3D printer setup and a custom-made cartesian pick and place robot (CPPR). The stop and go method [137] has been employed: the silicone print has been paused through g-code instructions, the SMA spring has been placed into the manufactured channel utilizing the CPPR and, after that, the print has been resumed .**Fig.3.15 a)** shows the CPPR using two electromagnets to embed the SMA inside the 3D printed silicone structure.

SMA springs (Dynalloy, USA) were employed (see **Tab.3.9**): it is important to point out that the Austenitic Start Temperature (A_s) of the spring is equal to 90 °C, while the constant heat provided locally by the additional heating element was 50 °C, preventing the SMA activation during the manufacturing process.

Tab. 3-9- Shape Memory Alloy (SMA) spring properties

Characteristic	Value
Composition	Ni-Ti (55-45)
Overall length	110 mm
Overall thickness	3.45 mm
Single coil thickness	0.51 mm
Austenitic start temperature	90 °C
Density	6.46 g/cm^3
Specific heat	0.2 cal/g °C
Melting Point	1300 °C
Thermal Conductivity	0.18 W/cm °C
Martensite resistivity	80 μΩcm
Austenitic resistivity	100 μΩcm

Using the following approach, it is possible to automate the integration of SMA springs into 3D printed soft structures during the fabrication process: this goal has never been achieved in the scientific literature because i) the melting temperature of the filaments used in material extrusion processes is higher than A_s, and ii) silicone additive manufacturing is still in its early years. Two types of silicone skins have been manufactured: traditional and patterned, as shown in **Fig.3.15 b) and c)**. In particular, three different skins were fabricated for the traditional group: "Middle" (An SMA positioned in the middle), "Diagonal" (An SMA positioned diagonally), and "Dual" (two SMA positioned linearly); for the patterned group, a single SMA was placed at the center of each structure and three different patterns (0.4 mm tall) were fabricated for each silicone skin: "Chess", "Crown", and "Three Lines". The aim of the proposed artificial skin manufacturing is multipurpose:

- Improve the traditional manufacturing process for the artificial silicone skin by increasing the degree of automation.
- Demonstrate that the proposed 3D printing custom-made setup is capable of fabricating patterned structures that are impossible or difficult to fabricate employing traditional fabrication methods.
- Demonstrate that structures capable of performing complex motions mimicking animals can be fabricated with the proposed inexpensive setup.

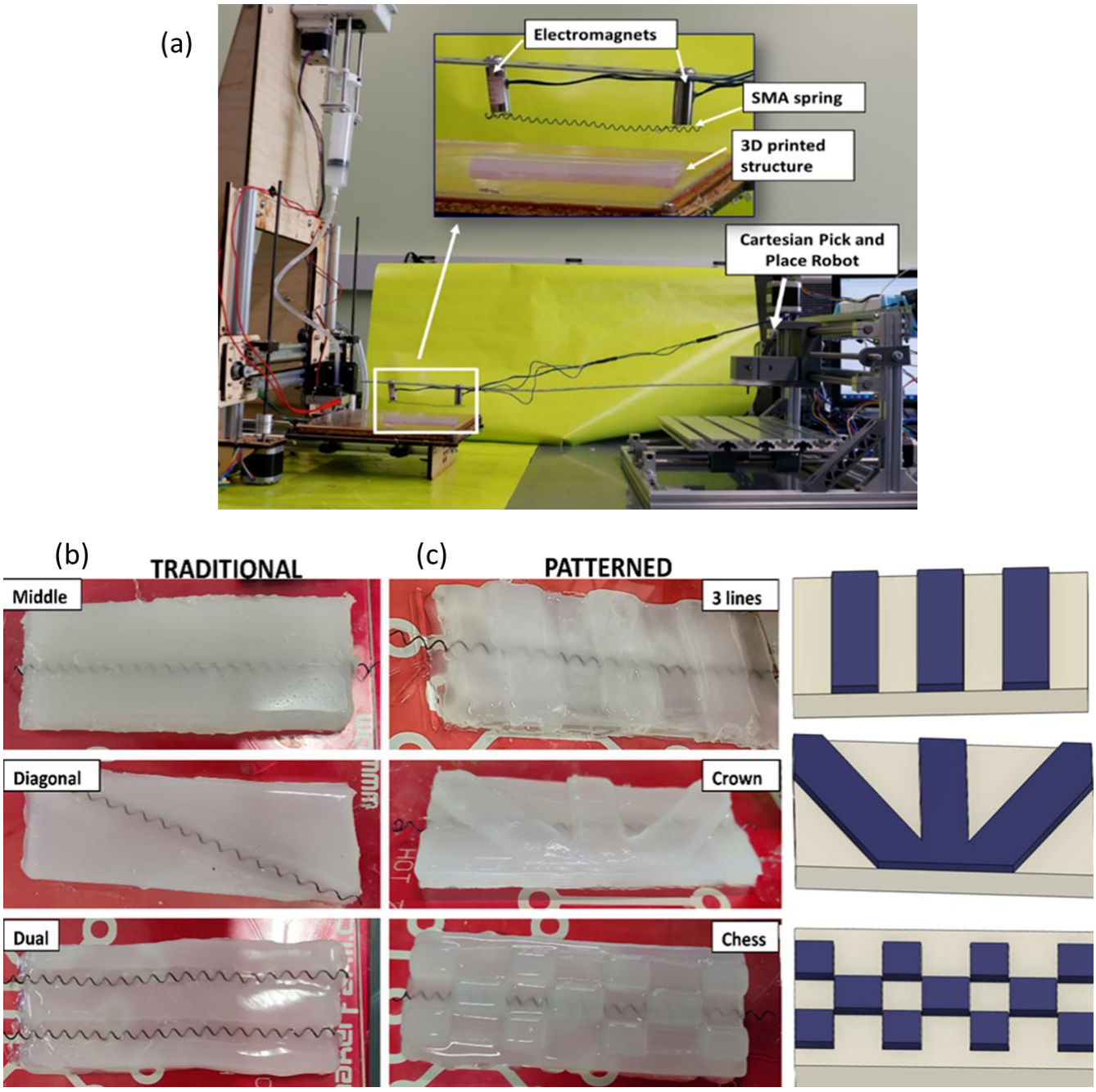

Fig. 3-15- a) CPPR used to automatically embed SMA into silicone skins, b) Traditional silicone skins, and c) Patterned silicone skins.

A digital camera (CANON EOS 400D) was used to take video of the silicone skins motions in the x-y plane, 6 markers have been placed on the side of every silicone skin and a software (Tracker) was used to analyze every video.

Three different current inputs (3A, 3.5A, and 4A) were provided to the SMA springs to examine the motions in the x-y plane for each silicone skin. The identical testing protocol was utilized for traditional and patterned silicone skins: each current input was applied for 2 seconds followed by a 20-second off period; the cycle was repeated ten times in total. Although there exist several more

sophisticated approaches to achieve a more precise activation of SMA, for the scope of this work a simple activation with direct current has been preferred to guarantee complete activation and verify the deformed shape of the silicone structure. The silicone skin characterization demonstrates that extremely high repeatability is achievable, with a standard deviation of less than 0.1 mm per point (each marker) and all graphs representing the average of ten measurements. Regarding the three silicone skins belonging to the traditional group, the increase in the applied current results in an improvement in the silicone skin motions, which mimic the animal domain: when 4A was applied, the Middle, Diagonal, and Dual (applied current to both the SMA actuators) structures recalled the elephant trunk, cuttlefish, and caterpillar behavior, respectively (see **Fig3.16 a),b),c) and d)**). **Fig.3.16 a)** shows the trajectory of the points in the skin samples at different input current to SMA, showing the final morphed shape in X and Y plane.

As regards the patterned structures, the main outcomes for each structure are here summarized:

- When 3 A is applied to the "Chess" structure, a slight deformation occurs (mostly on the left side of the structure); increasing the applied current to 3.5 A results in a completely different motion: the structure keeps contact with the base only on the left and right sides and is elevated by the base nearly 15 mm. When 4 A current is used (see **Fig. 3.17a), and b**), a similar behavior happens (left and right sides remain in contact with the base), but the central portion of the structure is elevated about 35 mm from the base.
- For the "3 lines" structure, depending on the applied current, radically different movements are accomplished: by applying 3A, a deformation mimicking the inchworm is achieved (see **Fig 3.17 a), and c)**). When 3.5 A and 4 A current is applied, an out-of-plane deformation occurs: the skin base in contact with the setup's flat base jumps from the x-y to the x-z plane. To the author's knowledge, this outcome has never been shown in silicone skin and is only achievable because of the additional pattern fabricated by employing the 3D printer. **Fig 3.17 e)** illustrates the leap dynamic (t=0 s, t=1 s, t=1.5 s, and t=2 s).
- For the “Crown” structure, no motion has been achieved at 3A; when the current was increased to 3.5 A, a bending deformation is achieved (see **Fig 3.17 a), and d)**), while at 4A an out-of-plane motion (from x-y plane to x-z plane) was achieved as shown in **Fig 3.17 d)**.

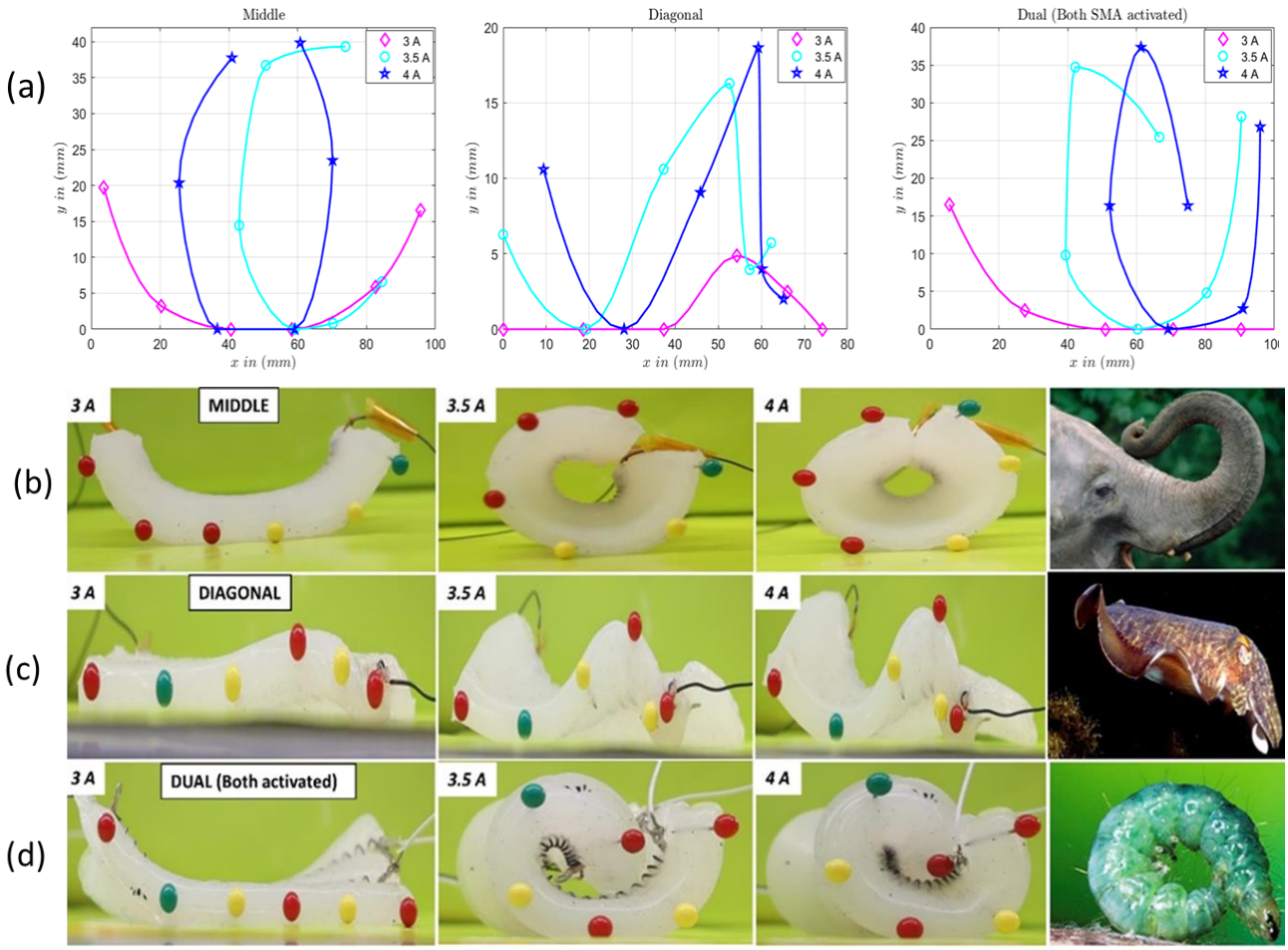

Fig. 3-16 a) Traditional flat silicone skins motions in x-y space at three different current inputs (average on 10 measurements), b) Middle structure motions at 3 different current inputs, c) Diagonal structure motions at 3 different current inputs, and d) Dual structure motions at 3 different current inputs

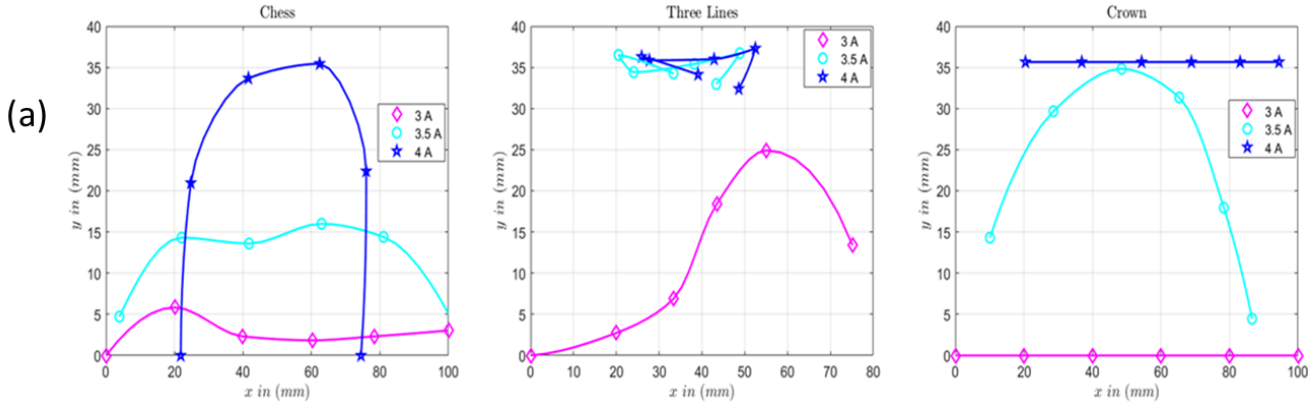

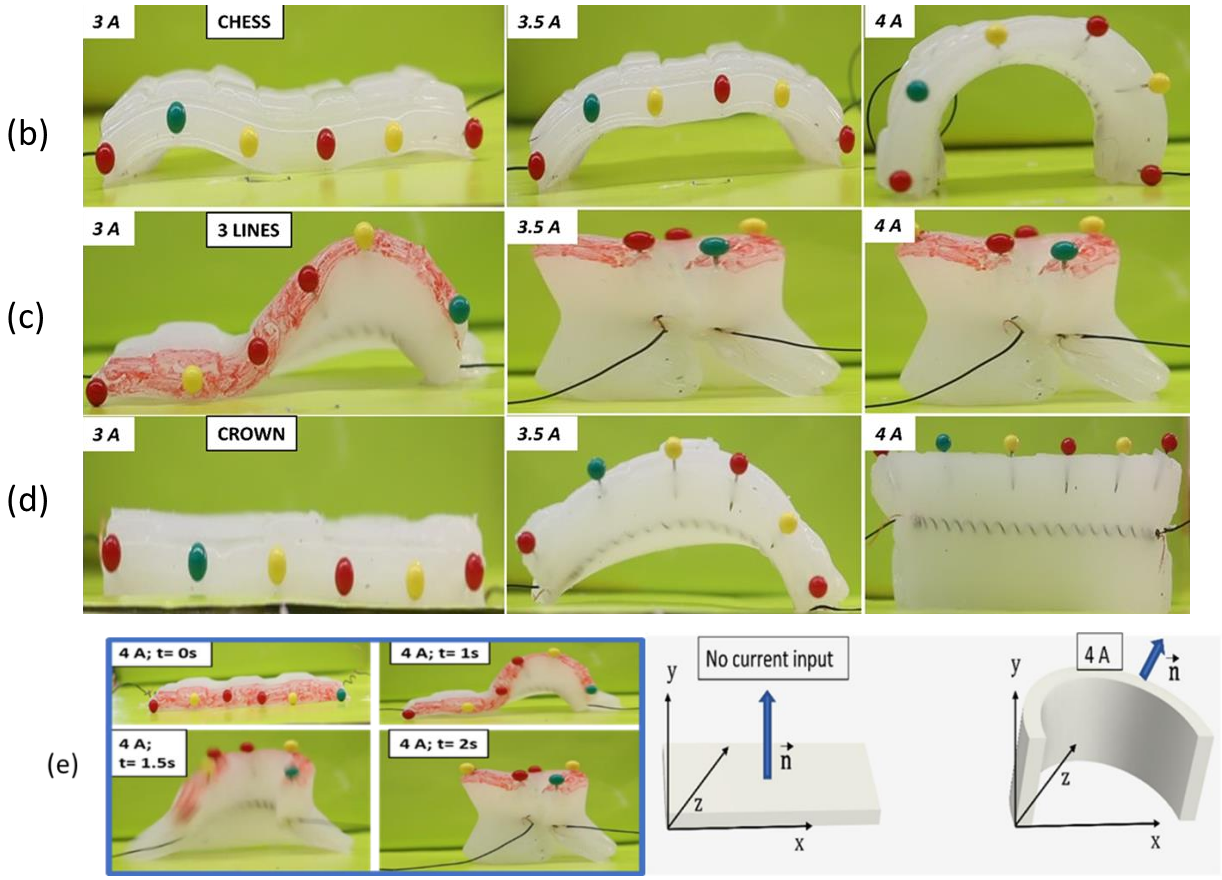

Fig. 3-17- a) Patterned silicone skins motions in x-y space at three different current inputs (average on 10 measurements), b) Chess structure motions at 3 different current inputs, c) Three lines structure motions at 3 different current inputs, and d) Crown structure motions at 3 different current inputs, e) Dynamic of the Three lines out of plane deformation.

The achieved results demonstrate how soft robotics can benefit from silicone-based material extrusion combined with a pick and place robot capable of embedding active actuators during the manufacturing process autonomously without direct human intervention; additionally, the future work will focus on mathematical modeling of patterned structures in order to predict their motions during the fabrication process. Numerous intriguing applications are feasible with the proposed 3D printed artificial skins, including soft grippers ("Middle" at 4A), walking robots ("Chess" at 4A), a soft robot capable of carrying objects ("Chess" at 3.5 A), and jumping robots ("3 lines" at 3.5 A and 4 A).

3.4.6 Conclusions

In this work, a custom-made inexpensive 3D printer capable of extruding silicone Ecoflex 00-10 through a calibrated nozzle was presented and characterized: specifically, circular, and square objects with maximum dimensions of 175 mm were fabricated. Two process parameters (printing speed and build plate temperature) were studied and correlated to the dimensional accuracy of single layer

printed beads, discovering an interesting relationship: increasing the printing speed, increases the accuracy, which is opposite behavior realized in FFF technology. The authors attribute this behavior to the gravity effect that occurs during printing: at low printing speeds, more materials flow out of the nozzle due to gravity, resulting in a decrease in accuracy. Another critical component is the silicone curing mechanism: the conventional technique of curing 3D printed silicone relied on the heat generated by the build plate, which permitted the construction of structures up to 17 mm in height (under certain conditions, such as the use of thermal insulation for the system nozzle-tube). Another curing technique employs installing an additional local heating source from the top to provide heat directly to the recently extruded silicone which results structures with a maximum height of 30 mm. Finally, the proposed custom-made 3D printer was employed to manufacture multiple types of "silicone skin" with embedded SMA actuators in a single manufacturing step autonomously without direct human intervention. The whole manufacturing process was automated using a cartesian pick and place robot that embedded the SMA using the start and stop approach. The proposed structures were tested at different current inputs and demonstrated complex motions that recalled the behavior of several animals, including an elephant trunk, cuttlefish, and caterpillar; additionally, the patterned structures demonstrated unique behavior and out-of-plane deformations. The present work paves the way for huge exploitation of silicone-based 3D printing in soft robotics, especially for the fabrication of bio-inspired structures which can potentially be fabricated monolithically, resulting in cost, fabrication time, and assembly step reductions.

3.5 Additive manufacturing for bioinspired structures: experimental study to improve the multi-material adhesion between soft and stiff materials

3.5.1 Introduction

The fabrication of bio-inspired structures has recently gained an increasing popularity: mimicking the way in which nature develops structures is a vital prerequisite in soft robotics to achieve multiple benefits. Stiff structures connected by soft joints (recalling, for instance, human bones connected by cartilage) are highly appealing: several prototypes have been manufactured and tested, demonstrating their full potential. In the present research, the material extrusion (MEX) additive manufacturing technology has been used to manufacture stiff-soft bio-inspired structures activated by shape memory alloys (SMA) actuators. First, three commercially available stiff composite plastic materials were investigated and linked to different 3D printing infills. Surprisingly, we found that the "gyroid" infill was correlated to the mechanical properties, demonstrating that it produces better results in terms of Young's modulus and Ultimate Tensile Strength (UTS) than the widely studied "lines" infill. The primary focus of the research is an experimental study aimed at improving the adhesion at the interface between stiff and soft materials using inexpensive method (i.e MEX). Three different variables that have significant effects on the interface bonding were studied :(i) the interface geometry between stiff and soft parts, (ii) the mesh overlapping process parameter, and (iii) the annealing post-treatment . By optimizing the three variables, a Young's modulus of 48.8 MPa and an UTS of 3.8 MPa were achieved, when Nylon + glass fiber (a stiff material) and thermoplastic polyurethane (a soft material) were 3D printed together. In particular, the 3.8 MPa UTS is 48 % higher than the highest adhesion between soft and stiff material (TPU and ABS) reported in literature. Finally, taking advantage of the improved stiff-soft adhesion, a bio-inspired robotic finger has been fabricated and tested using a SMA actuator, showing an enormous potential for the proposed additive manufacturing approach in realizing bioinspired systems.

3.5.2 Materials and methods

The objective of the present research is the monolithic manufacturing of bioinspired structures employing Fused Filament Fabrication (FFF) additive manufacturing technology extruding two materials with completely different material properties in the same printing cycle: a very stiff material and a soft material. The study on the adhesion mechanism between the two materials is a crucial aspect to take into consideration to create functionalized 3D printed structures activated by an external actuation system such as spring shape memory alloys. The research objective is illustrated in **Fig.3.18.**

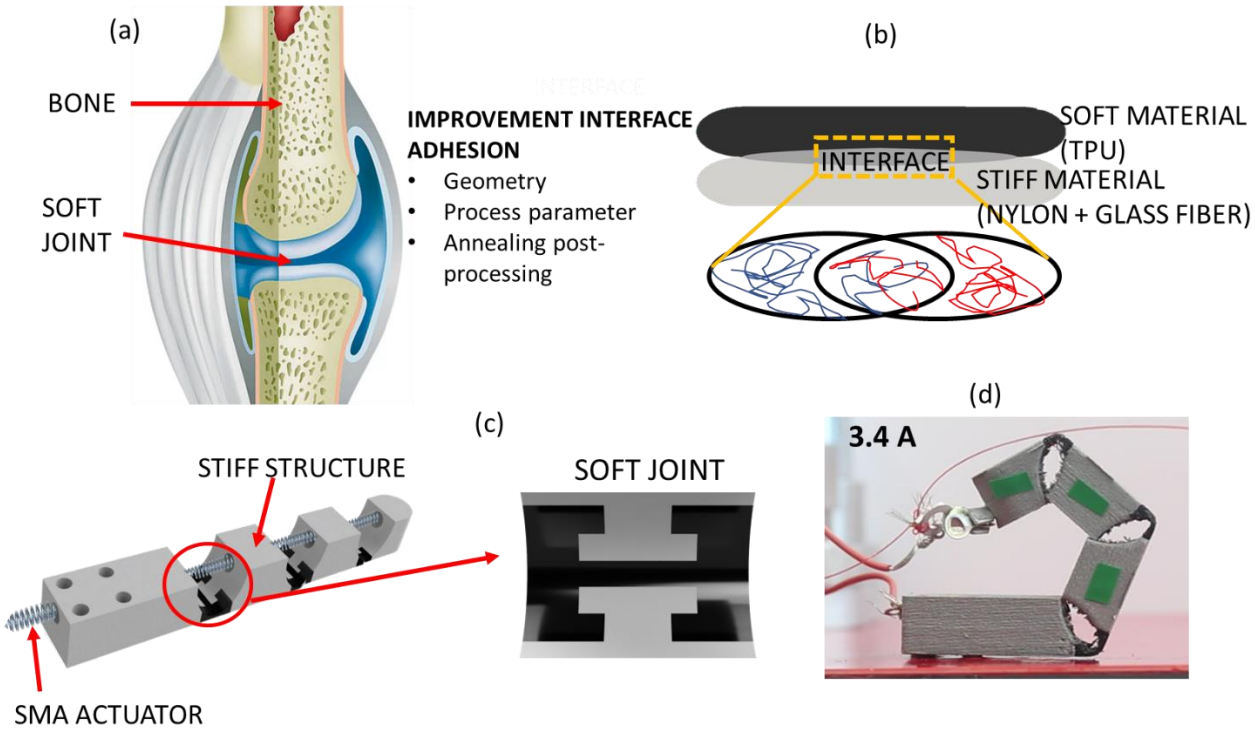

Fig. 3-18- Summary of the research and bioinspired joint: a) Human bone (example of the combination of stiff-soft materials found in nature), b) Study of the interface between stiff and soft materials, c) Main elements of the proposed stiff-soft structure, and d) Proposed finger actuated using coiled shape memory alloy actuator at 3.4 A.

A commercial-grade dual extruder 3D printer was employed throughout the whole research (Tenlog 3D) and commercial materials were used: specifically, three composite materials and a soft material were tested. The authors investigated the composite materials as stiff materials to identify the material with the best mechanical properties and they are:

- Nylon + glass fiber (GF), henceforth NGF,
- Polyethylene terephthalate glycol (PETG) + carbon fiber, henceforth PETGCF, and
- Polycarbonate (PC) + carbon fiber, henceforth PCCF

As a soft material, a commercial thermoplastic polyurethane (TPU) (Ninjaflex, Ninjatek, CA, USA) was used, which is widely recognized as one of the softest materials on the market (shore hardness equal to 85 A, elongation at break equal to 660%, and ultimate tensile strength equal to 26 MPa). After studying which composite commercially available material has the best mechanical properties in conjunction with different printing patterns, a method for improving its adhesion with the TPU soft material has been studied. An investigation was performed on three interface geometries and two parameters (a process parameter and a post-processing parameter).

In scientific literature, several studies have been conducted to correlate the mechanical properties of FFF dog bones and process parameters such as layer height, printing orientation, and printing speed. In this research, three different printing patterns were studied: lines (well known in the scientific literature for providing an increase in the mechanical properties when a 45° orientation is set), gyroid (a new infill pattern available on slicing software that has been proved to provide good results in terms of compressibility [32]), and cross 3D (a printing pattern based on the 3D fabrication of cruxes and not studied in scientific literature). All the infill patterns have been generated by the slicing software Ultimaker Cura 4.11.

3.5.3 Stiff materials study

The three composite materials (NCF, PETGCG, and PCCF) were employed, and for each material, a total of nine dog bones (3 samples for each printing pattern) were fabricated and tested under tensile loading using a universal testing machine (INSTON Inc., Model 5969, Norwood, MA). Standard ASTM D638 was utilized for the fabrication and testing of dog bones. Each material's process parameters are described in **Tab.3.10** in detail. **Fig. 3.19 a) and b)** depicts three different printing patterns and 3D-printed samples. In **Fig 3.19 c)** the obtained results in terms of Young's modulus are shown.

Tab. 3-10- Process parameters for every composite material tested.

	Layer thickness (mm)	**Top/bottom layers**	**Printing temperature (°C)**	**Build plate temperature (°C)**	**Printing speed (mm/s)**
PCCF	0.15	0/0	250	80	40
NGF	0.15	0/0	280	50	40
PETGCF	0.15	0/0	230	70	40

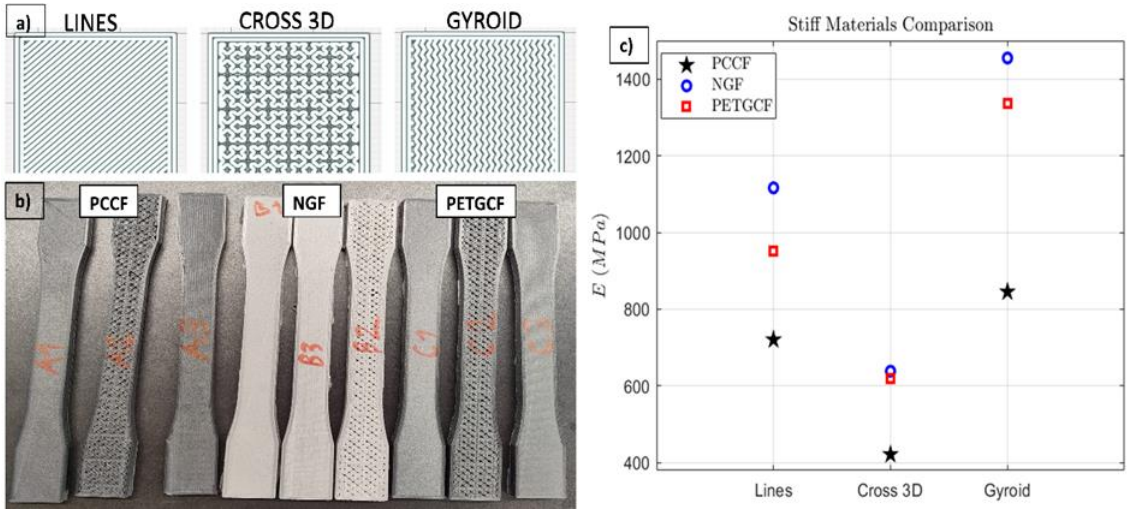

Fig. 3-19- a) Three different printing patterns, b) Manufactured dog bones using three different composite materials (PCCF= polycarbonate + carbon fiber, NGF= nylon + glass fiber, PETGCF = Polyethylene terephthalate glycol + carbon fiber), and c) Young's modulus vs infill pattern for every material obtained experimentally. The sample size is 165 mm along x-axis and 19 mm along y-axis.

In particular, considering the material composition (plastic + carbon fiber or glass fiber), a brass nozzle with a diameter of 0.6 mm was chosen; in this way, problems related to nozzle clogging have been avoided. It is noted that the use of smaller nozzles (i.e., 0.4 mm) is allowed if a particular attention is paid to the careful selection of process parameters (i.e., high extrusion temperature), nozzle material (i.e., hardened steel and ruby tip), and nozzle geometries (i.e., 50 mm long nozzle volcano version). The same nozzle diameter (0.6 mm, brass nozzle) has also been used for the extrusion of TPU, in Section 3.5.4.

The results obtained from the tensile test are summarized in **Tab.3.11**, as well as the following conclusions can be drawn:

- As a function of the printing pattern, the behavior of every material is the same: the lowest mechanical properties (E, and UTS) are obtained for the Cross-3D patter, while the highest mechanical properties are obtained for the gyroid pattern. Because of the lack in scientific literature about the effect of gyroid pattern studies, the present result might pave the way for more investigations to create mathematical models.
- Considering the gyroid pattern (the pattern with the best mechanical properties), it is evident that the NGF material has the best mechanical properties, with a Young's modulus of 1.45 GPa and a UTS of 57.48 MPa.
- The manufacturing process is robust: for each material and pattern three samples were fabricated, resulting in a standard deviation calculated on the Young's modulus less than 5%.

Tab. 3-11- Infill pattern impact on the three different stiff materials.

MATERIAL	Pattern	E (MPa)	UTS (Mpa)	Elongation at break (%)
PC+CF	Lines	720	27	0.082
	Cross 3D	421	8	0.028
	Gyroid	845	30	0.047
Nylon + GF	Lines	1116	49	0.11
	Cross 3D	622	18	0.05
	Gyroid	1455	58	0.066
PETG+ CF	Lines	952	39	0.07
	Cross 3D	620	16	0.035
	Gyroid	1335	49	0.06

In conclusion, the best composite material in terms of mechanical properties is NGF, printed using a gyroid pattern: it will be employed throughout the present research as a stiff material in conjunction with the soft TPU.

3.5.4 Stiff-soft adhesion

Several studies have been performed to improve the adhesion between two materials: in particular, Yin et al. [14] mathematically described the material strengths between two materials in multi-material FDM printing:

$$\sigma_{A/B}|_{t=t_p} = R(t)|_{t=t_p} * \sigma_A \qquad (22)$$

Where $\sigma_{A/B}$ is the interfacial bonding strength (ultimate tensile strength) between the two materials (A and B), t_p is the total printing time, $R(t)$ is the average strength ratio of the whole interface between the two materials, and σ_A is the ultimate tensile strength of the material A.
In particular, $R(t)$ can be explained as recurring to the intermolecular diffusion theory occurring at the interface between two polymers. Treating the FFF interfacial bonding as a two dimensional and grown process; considering $\boldsymbol{\Omega}$ a certain domain at the interface and that once contact of two polymers occurs, areas with inter-molecular diffusion (wetted area) are nucleated at random locations, thus the strength of domain $\boldsymbol{\Omega}$ will be the sum of all the inter-molecular diffusion initiated within $\boldsymbol{\Omega}$.
In this way, $R(t)$ can be written as follows:

$$R(t) = \int R_s(t - \tau; T(t, \vec{X}))dA(\tau, \vec{X}) \qquad (23)$$

where R_s is the strength ratio, $dA(\tau, \vec{X})$ indicates the wetted area at the position $\vec{X}$, at time τ, and A is total wetted area.

In the present research, three different adhesion geometries among the stiff and soft materials were studied: a wave geometry, a T-shape geometry, and a sandwich geometry (See **Fig 3.20 a),b) and c)**). The three geometries have been designed in accordance with the results obtained in [138]. For each geometry, two different parameters have been studied, to understand if there is a correlation between them and the mechanical properties of the dual material structures:

- A process parameter called "Mesh Overlapping", refers to the overlapping at the interface among the two parameters. Two levels of the following parameter were studied: low level (0 mm of overlapping), and high level (0.4 mm of overlapping). In Fig **3.20 e) and f)** the Mesh Overlapping parameter is depicted.
- A post-processing parameter, namely the Annealing Temperature: three levels were studied, no annealing ("As printed"), 50 °C, and 70 °C. The samples were annealed for 1 h in a furnace at the desired temperature and after they were cooled down in the air for 1 h.

A total of 54 dogbone-shaped samples were fabricated (3 repetitions for every combination) and tested, with the Young's modulus chosen as a measure of the material's adhesion (see Fig.**3.20 d) and g)**). In **Tab.3.12** the results in terms of E, and rupture zone are listed.

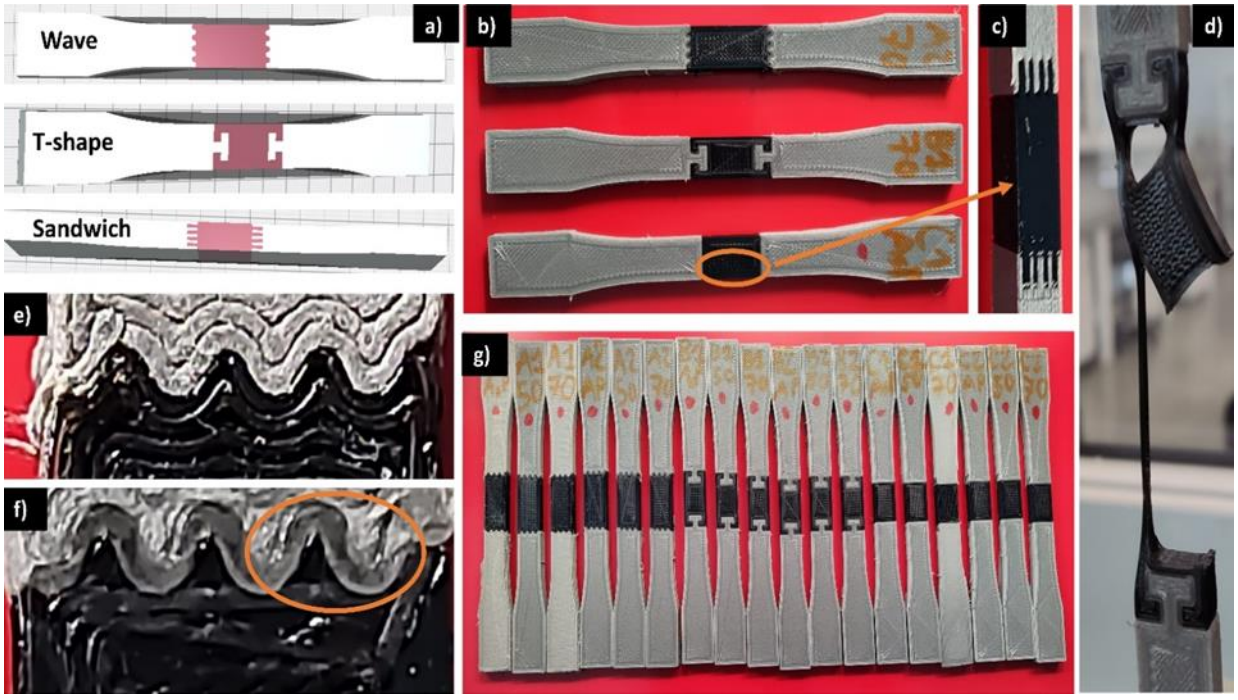

Fig. 3-20- : a) Three different adhesion mechanism (white= stiff, pink=soft), b) Manufactured dog bones with three different adhesion mechanism (grey=stiff, black= soft), c) Side view of the sandwich mechanism, d) T-shape dog bone during the tensile test, e) Mesh overlap equal to 0 mm, f) Mesh overlap equal to 0.4 mm, and g) manufactured dog bones, repetition 1.

Tab. 3-12- Results of the stiff-soft materials adhesion analysis

Sample Name	Geometry	Mesh Overlapping (mm)	Annealing Temperature (°C)	E (MPa)	Rupture
A1-AP	wave	0	As Printed	31.2	Interface
A1-50	wave	0	50	29.8	Interface
A1-70	wave	0	70	27.2	Interface
A2-AP	wave	0.4	As Printed	28.1	TPU
A2-50	wave	0.4	50	32.55	TPU
A2-70	wave	0.4	70	34.2	TPU
B1-AP	T-shape	0	As Printed	47.5	TPU
B1-50	T-shape	0	50	47.1	TPU
B1-70	T-shape	0	70	34.3	TPU
B2-AP	T-shape	0.4	As Printed	32.2	TPU
B2-50	T-shape	0.4	50	47.5	TPU
B2-70	T-shape	0.4	70	48.8	TPU
C1-AP	sandwich	0	As Printed	41.8	Interface
C1-50	sandwich	0	50	39.8	Interface
C1-70	sandwich	0	70	39.8	Interface
C2-AP	sandwich	0.4	As Printed	35.1	Interface
C2-50	sandwich	0.4	50	35.7	Interface
C2-70	sandwich	0.4	70	42.1	Interface

As shown in **Fig.3.21**, the main results can be summarized as follows:

- The annealing post-processing has a remarkable effect when the mesh overlapping parameter is set to 0.4 mm: for each geometry, switching from no annealing (as printed) to 50°C and then to 70°C increases material adhesion (increase in Young's modulus). Specifically, the E increase for the wave, T-shape, and sandwich from "As printed" to 50°C annealing is 15.91%, 47%, and 2%, while the E increase for the same geometries from "As printed" to 70°C is 21.9%, 51.6%, and 19%. The opposite behavior (reduction of E when the annealing temperature increases) occurs when the mesh overlapping parameter is set to 0 mm: in this case a reduction of E of 7%, 5% and 4.5% occurs for wave, T-shape and sandwich switching from "As printed" to 50°C, whereas switching from "As printed" to 70°C the reduction is respectively of 12.8%, 31% and 4.7%. At the state of the art, some preliminary studies have been conducted to correlate the annealing process with the mechanical properties of FFF parts, and it has been determined that the annealing process improves the mechanical properties of several materials, such as PLA and ABS. Due to a lack of scientific literature regarding the

correlation between annealing and dual materials bonding, the following results are difficult to explain: according to the authors, when the overlap parameters are set (0.4 mm), annealing increases the mechanical properties because heat facilitates intramolecular diffusion and the number of wetted areas is higher [14] (equation (22) and (23)). It is worth mentioning that the complexity of the problem is also related to the composition of the studied materials: the stiff material is a composite material made up of Nylon and glass fibers which in turn contribute to the interfacial bonding. While the obtained results are clear, their explanation from a chemical/material point of view requires more tests and examination considering multiple variables.

- For every geometry, when no annealing is performed (as printed), the best results in terms of E are obtained when the mesh overlapping was set as 0 mm. On the opposite side, after annealing at 70°C, all samples fabricated with a mesh overlapping of 0.4 mm had a higher E than the "As printed" structures fabricated with a mesh overlapping of 0 mm. Considering Table 2, E of A2-70 is higher than E of A1-AP; E of B2-70 is higher than B1-AP, and E of C2-70 is higher than E of C1-AP. In conclusion, for every geometry, the highest value of E was achieved by setting a mesh overlapping of 0.4 mm and annealing the sample at 70°C for 1 h.
- The rupture position is a powerful tool for comprehending the adhesion dynamics between the stiff and the soft material. Regarding the T-shaped sample, the geometric interlocking mechanism was robust enough to produce a rupture every time within TPU and not at the interface. For the sandwich geometry, rupture always occurred at the interface between the two materials, whereas for the wave sample, a rupture occurred within the TPU when the overlapping parameter was set to 0.4 mm and never at the interface (unlike for the case in which the mesh overlap was set to 0 mm).
- In conclusion, the best geometry and combination of process parameters for improving the adhesion between the stiff and soft material is respectively T-shape (in accordance to [138]), 0.4 mm of mesh overlapping, and 70°C of annealing. For the following configuration a UTS of 3.85 MPa was achieved, this value is 48.05% higher compared to the highest one found in the scientific literature when a combination of stiff and soft materials was extruded (Yin et al [14] obtained 2 MPa employing ABS and TPU).

Moreover, as shown in literature [139], material affinity is an important factor to consider to improve the multi-material adhesion: if two materials (stiff and soft) having similar chemical composition are jointly extruded, the following results in terms of adhesion can be improved. The development of

materials having different degrees of stiffness, but similar chemical composition will provide many benefits to the 3D printing field.

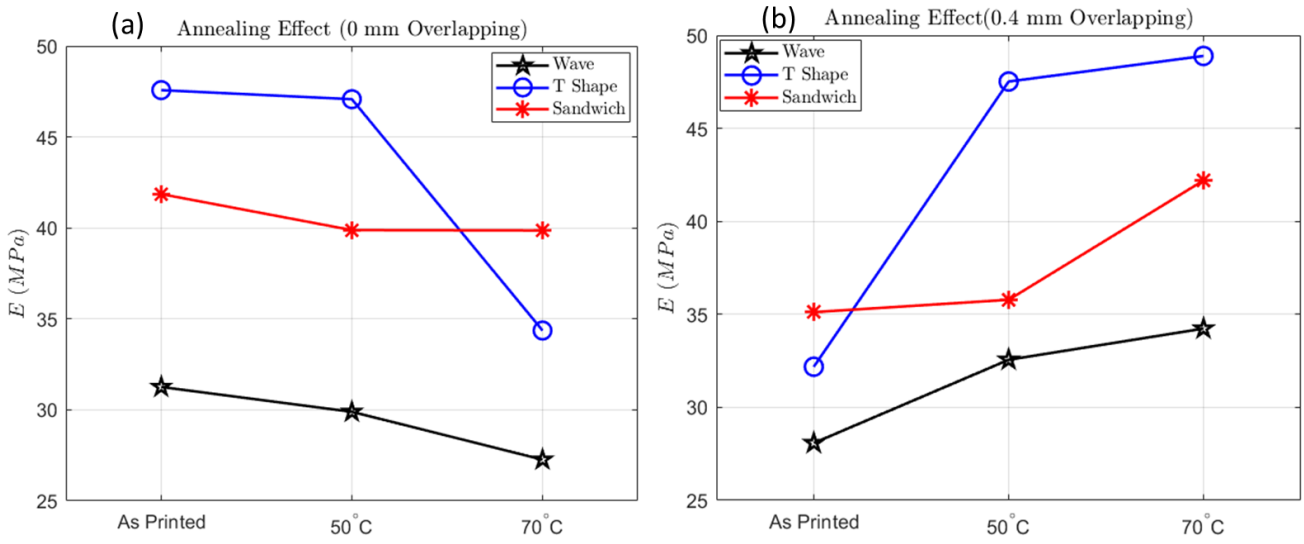

Fig. 3-21- Annealing effect on mesh overlapping a) 0 mm overlapping, and b) 0.4 mm overlapping

The outcomes of the present work can also be used as benchmark to improve the multi-material adhesion in several AM technologies able to process more materials at the same time such as material jetting [140] and hybrid AM technologies [8].

A B2 sample, the best one in terms of adhesion, was examined using a Nikon X-ray micro-computed tomography (μCT) C1 system with a scanning energy level of 65 kV at 115 μA current, and a cubic voxel size of 28.733 μm. After reconstruction from the μCT scan, the volumetric images were visualized in ORS Dragonfly software to observe and analyze the internal structure of the 3D-printed structure made of stiff-soft materials. Inspection of the volumetric images determined that the printed sample has no internal defects within the scanning resolution used. In particular, the following two observations are made (**Fig.3.22**): i) at the interface between the two materials (0.4 mm overlap), a straight region in which the two materials are completely bonded together is clearly seen, demonstrating the effectiveness of the proposed approach; and ii) after sectioning the sample, a weak adhesion in the TPU material among the external perimeters and the gyroid infill is revealed, as the gap circled in red in **Fig.3.22 d)** shows. Therefore, the future research will focus on the bonding improvement in TPU to further increase the overall mechanical properties.

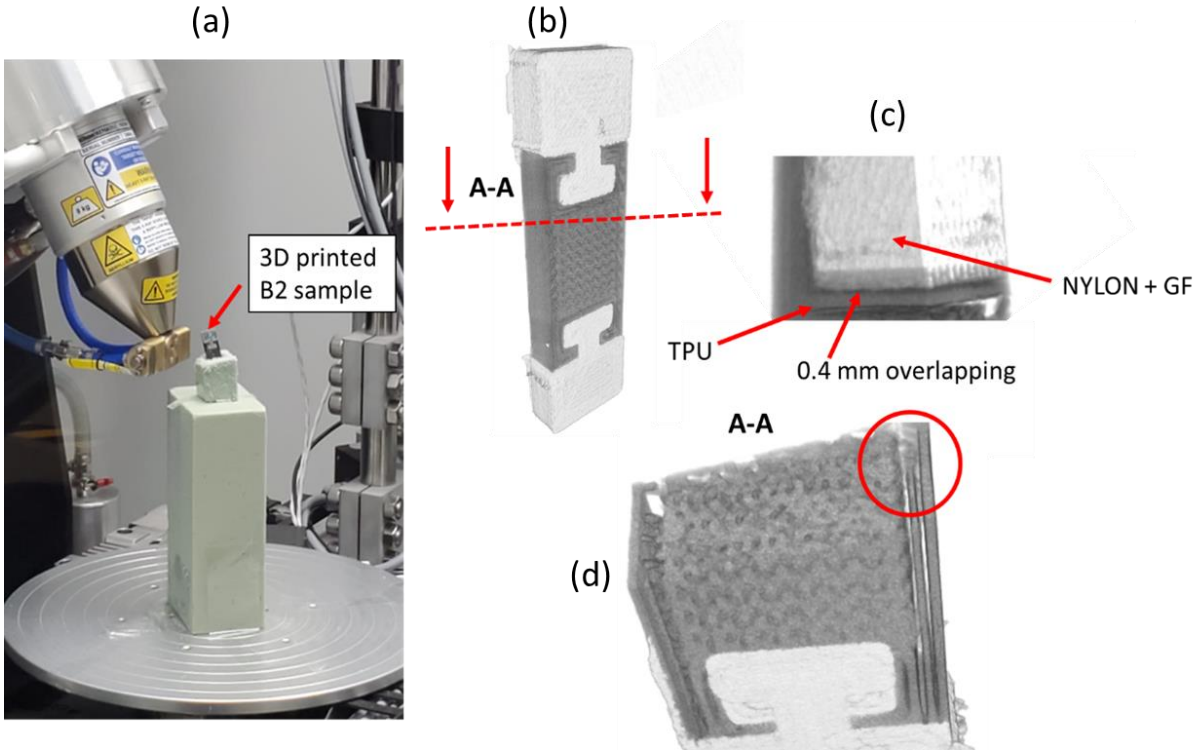

Fig. 3-22 -X-ray µCT volumetric images of the proposed sample: a) 3D printed sample scanned using the X-ray µCT apparatus, b) 3D rendering of the entire B2 sample from the µCT scan, c) closeup view showing the overlapping between the two materials, and d) 3D rendering revealing the weak wall-infill adhesion.

3.5.5 AM of soft-stiff bioinspired structures

Soft robotic, and the biomedical field in general, can benefit from the proposed manufactured approach in several ways: the fabrication of bio-inspired structures comprised of very stiff and soft materials is very appealing due to the possibility to achieve complex motions employing 3D printed structures recalling biological structures.

Setting the mesh overlap parameter equal to 0.4 mm, annealing the stiff-soft structure at 70 °C for 1 h, and using the T-shape interface geometry, a remarkable improvement at the interface was achieved (UTS of 3.8 MPa and E of 48.8 MPa), making structures manufactured in accordance with the proposed approach more reliable, improving the span life as well.

To demonstrate the potentialities of the stiff-soft (Nylon + glass fiber and TPU) additive manufacturing approach, two bio-inspired structures were designed and fabricated: a robotic finger and a multidirectional bender. For both the objects the working mechanism is the same: the joints fabricated using TPU are connected to the passive structure (made up of NGF) recurring to the T-shape interface. After the fabrication, the proposed structures were annealed for 1 h at 70 °C, to improve the interfacial adhesion in accordance with the results obtained in Section 3.5.4

It is worth mentioning that no assembly tasks were involved for the fabrication of the proposed bioinspired structures, leading significant advantages when compared to the traditional stiff-soft structure, which requires multiple assembly steps and different manufacturing technologies or expensive additive manufacturing setup [19].

The proposed finger was designed in accordance with Mutlu et al. [141], as shown in **Fig.3.23**. It has the following properties: i) it is equipped with a 4 mm hole for a shape memory alloy (SMA) actuator insertion after the annealing process, ii) made up of three TPU joints, namely MCP, DIP, and PIP, iii) it is equipped with a terminal block to fix it to the experimental setup.

The SMA actuator was provided with 3.4 A current for 2 s (in accordance with the SMA datasheet), and an off period of 20 s was set to cool the SMA down, in addition during the cooling period a deadweight of 100g was attached to the SMA crimp to fully restore its original position.

Actuation was done for 5 cycles, and it was found to be highly repeatable, among the 5 cycles the standard deviation for the MCP, DIP, and PIP joint was in the (x, y) space respectively (0.18 mm, 0.19 mm), (0.2 mm, 0.25mm), and (0.33mm, 0.29 mm). An average finger bending angle of 120° was found, and a very low standard deviation of 0.5° was calculated over 5 consecutive cycles. The proposed finger recalls human fingers not only because is it made up of stiff and soft materials but also in terms of flexibility and performed motions (see **Fig .3.23.b)**), paving the way for the fabrication of 3D printed stiff robotic hands equipped with soft joints for the biomedical field.

As regards the multidirectional bender, it was designed and fabricated to demonstrate that the proposed manufacturing approach can be applied to multiple fields, including surveillance, and walking/crawling soft robots.

The multidirectional bender is shown in **Fig.3.23 d) and e)** and it is made up of four different elements: i) stiff passive structure made up of NGF, ii) soft TPU joint connected to the stiff structure by means of the T-shape mechanism, iii) two terminal plates where the stiff structure is anchored and the SMA actuators are positioned, and iv) 8 SMA springs actuators.

The SMA actuators were placed in a square configuration and labelled from 1 to 8, as shown in **Fig.3.23 e)**. Each SMA actuator was individually activated (3.4 A for 2 s), and eight different bending motions were achieved due to the soft joint geometry, as shown in **Fig3.23 e).**

The proposed multidirectional bender is the first prototype that demonstrates how many motions a single 3D-printed object can achieve: by changing the design and connecting more benders together an extremely wide range of motions can be obtained, and several kinds of robots can be easily manufactured.

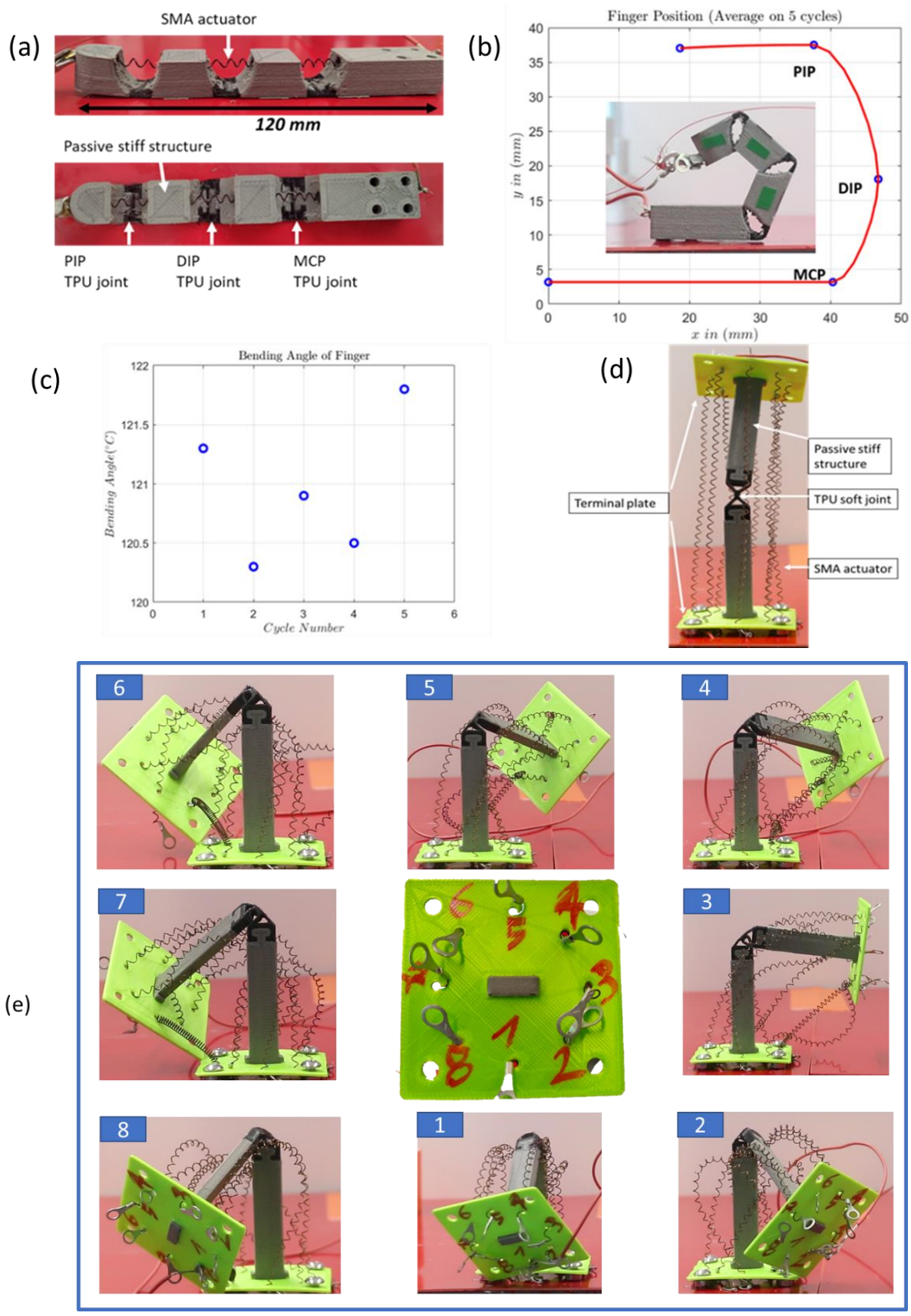

Fig. 3-23- a) Proposed finger, b) Finger position in x-y space, c) bending angle, d) proposed multidirectional bender, and e) motions performed by the bender as a function of the activated SMA.

3.5.6 Conclusions

In conclusion, the present research focuses on the multi-material extrusion of stiff-soft structures and reports a method for improving their interfacial adhesion. Using the "gyroid" infill, the Nylon + glass fiber composite material was found to be the stiffest commercially feasible material (among the three analyzed) having Young's modulus (E) of 1.4 GPa and tensile strength of 58.48 MPa. The stiff material was extruded in conjunction with a commercial soft TPU to fabricate bioinspired structures. Three different interface geometries were studied along with a process parameter (mesh overlapping) and a post-processing (annealing). The optimal combination (maximizing the Young's modulus) of the three variables was determined to be as follows: T-shape, 0.4 mm, and 70°C for 1 h. Tensile tests were performed for all the manufactured dog bones as a measure of the interface adhesion, and in the best case, E of 48.8 MPa and UTS of 3.8 MPa was achieved. In particular, the latter is 48 % higher than the highest adhesion value between soft and stiff materials available in scientific literature. Finally, a bio-inspired robotic finger actuated employing SMA actuators was fabricated and tested, mimicking very well the human finger motion. The subsequent results in terms of stiff-soft adhesion pave the way for enormous exploitation of AM material-extrusion technology for the fabrication of soft robots: humanlike biomimetic joints, such as prosthetic hand and arm-wrist systems for humanoid robots, and other biomedical applications. Moreover, future works will focus on the application of the findings on several baseline materials (such as PLA and ABS, widely used for hobbyist aims) in conjunction with soft TPU, to provide a 3D printing guideline useful at different levels, from makers to researchers.

3.6 One shot 3D printed soft device actuated using Metal filled Channels and sensed with embedded strain gauge

3.6.1 Introduction

In the present work, a fully 3D printed soft electromagnetic (EM) actuator, based on internal channels, filled with soft liquid metal (Galinstan) and equipped with an embedded strain gauge is presented, for the first time. The proposed actuator has been fabricated by taking full advantages from the multi-material extrusion (M-MEX) additive manufacturing (AM) process by employing a soft thermoplastic material and a conductive thermoplastic material in the same cycle. At the state of the art, M-MEX techniques result underexploited for the manufacturing of EM actuators: only traditional manufacturing approaches are used resulting in many assembly steps. The main features of the present work are: i) one shot fabrication, ii) smart structure equipped with sensor unit, and iii) scalability. The actuator was tested in conjunction with a commercial magnet, showing a bending angle of 22.4 ° degree (when activated at 4 A), a relative error of 0.7 % and a very high sensor sensitivity of 49.7 $\frac{\Omega}{^\circ degree}$. Two more examples, showing all the potentialities of the proposed approach, are presented: a jumping frog-inspired soft robot and a dual independent two-finger actuator. The present paper aims to push the role of Extrusion Based AM for the fabrication of EM soft robots: several advantages such as portability, no cooling systems, fast responses, and noise reduction can be achieved by exploiting the proposed actuation system if compared to the traditional and widespread actuation mechanisms (shape memory polymers, shape memory alloys, pneumatic actuation and cable-driven actuation).

3.6.2 Materials and methods

The main idea underlying the following research is the one-shot fabrication of a soft EM actuator based on internal channels (filled with Galinstan) and equipped with an embedded sensors by using M-MEX technology.

The soft EM actuator, shown in **Fig.3.24 a), b) and c)** is composed of the following parts: i) a main flexible body, ii) a flexible joint to improve the bending performance, iii) a bottom strain gauge to obtain real time feedback, and iv) a total of 9 internal channels. In particular, the latter element is crucial to exploit the Lorentz force. The channels have a square profile $(0.8 * 1.3)\ mm$ have been filled up with liquid soft Galinstan (a liquid alloy composed of 68% wt. gallium, 22%indium and 10%wt tin), well known for its good electrical performances. After the Galinstan injection, two metals

pins have been assembled over the 3D printed connection in order to hook up the electrical wires. The Galinstan has been purchased by Peguys, Israel.

The M-MEX machine Ultimaker 3 (Ultimaker, The Netherlands) in conjunction with two thermoplastic materials have been used. A soft thermoplastic polyurethane (TPU) with a shore harness of 85 A and Young's Modulus of 20MPa has been employed for the flexible parts (main body, joint and connections for the metal pins), while a conductive polylactic acid (CPLA) with a resistivity of 15 Ω · cm along the layers and 20 Ω · cm perpendicular to the layers has been employed for the sensor fabrication.

The TPU (commercial name "TPU 80A LF") and CPLA (commercial name "AlfaOhm") materials have been purchased respectively by BASF SE, Germany and FiloAlfa, Italy.

The overall actuator dimensions along x-, y-, and z-axis are $(40 * 73 * 4.7)mm$, while the strain gauge results in 6 tracks and a thickness of 0.4mm.

The main process parameters set during the manufacturing process are listed in **Tab.3.13.** Moreover, printing speed and infill percentage have been found to be crucial variables for the channels fabrication. If the channels are not fabricated properly, a Gallistan leakage could occur involving problems during the soft device actuation (impossibility to be activated). Using a trial-and-error approach it was found a printing speed of 25 mm/s and an infill percentage of 100% to ensure a solid channel structure, avoiding Gallinstan leakage.

In particular, the relationship among strain gauge extruded single layer thickness (lt) and total number of layers (tl) has been considered.

As shown in [32] the reduction of tl implies a reduction of the final strain gauge resistance and standard deviation: in this way electrical power losses will be minimized.

Being the overall strain gauge thickness (SGT) fixed to 0.4 mm, the only way to reduce tl is increasing the single extruded layer thickness (lt) in the slicing software, as shown in equation (24).

$$SGT = lt \cdot tl \qquad (24)$$

A value of lt equal to 0.2 mm was set, it means that the whole strain gauge is composed of 2 consecutive layers in order to minimize the welding effect (number of voids between adjacent extruded layers) found in [32]. Moreover, further characterizations about the CPLA viscoelastic behavior will be carried out to improve the dimensional accuracy of 3D printed sensors.

The total printing time and cost is respectively 1h37min and 3.75€.

The main advantages of the proposed manufacturing approach, compared to the main works using MEX technique to exploit the EM actuation system found in scientific literature and discussed in the introductions are:

i) The EM actuation is achieved by employing a soft metal liquid metal instead of rigid copper wires: in this way soft devices can be fabricated without recurring to rigid external elements [142][143]

ii) The EM actuation is achieved by employing a soft metal liquid metal instead of extruding thermoplastic composite materials loaded with magnetic fillers[144][145]. The main issue related to magnetic thermoplastic materials is their low processability: the magnetic fillers make the whole filament brittle and difficult to be extruded, generally problems like nozzle coggling and breakage of the filaments between the 3D printers pushing gears occur. Using the proposed manufacturing approach, all the problems above described have been overcome.

The proposed 3D printed soft EM actuator filled with soft liquid Gallinstan is shown in **Fig.3.24 d)**. The working mechanism of the used M-MEX machine (Ultimaker 3) is shown in **Fig.3.24 e)**.

Tab. 3-13- Process parameters

Process Parameter	**TPU**	**Conductive PLA**
Nozzle size (mm)	0.4	0.8
Layer thickness (mm)	0.2	0.2
Extrusion temperature (°C)	240	260
Printing speed (mm/s)	25	20
Infill percentage (%)	100(for the channels) 100(for the joint) 25(for other parts)	100

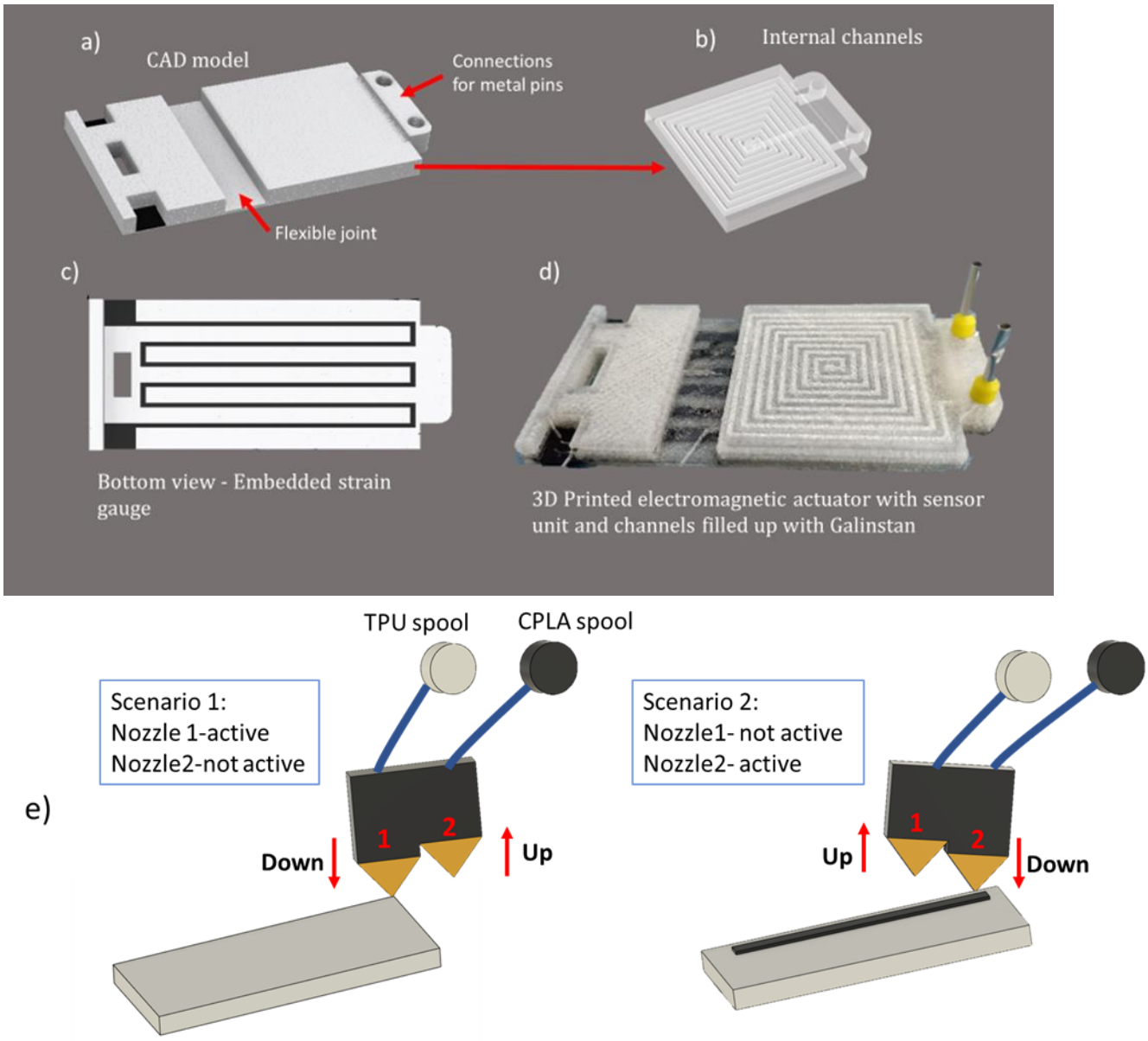

Fig. 3-24 Soft EM actuator: a) Computer Aided Design (CAD) model; b) internal channels; c) Botton view: embedded strain gauge sensor(white = TPU, black= CPLA); d) 3D Printed EM soft actuator with embedded sensor and channels filled up with Galinstan; and e) Schematic diagram depicting the basic multi-material-extrusion working mechanism of Ultimaker 3.

3.6.3 EM actuator characterization

The proposed 3D printed soft EM actuator was characterized to evaluate i) bending performance as a function of the applied current and, ii) the embedded strain gauge performance. A permanent magnet (purchased by Supermagnete.de, Germany) was used to generate a magnetic field of 1.29T.

In accordance to [146],the equilibrium Lorentz force equation shown in equation (25) is:

$$F = \frac{2M}{Z_i + Z_{i+1}} \qquad (25)$$

where Z (mm) is the distance between the permanent magnet and the channels, i is the number of the channel ($i = 1,2,..,9$), and M ($m^2 * A$) is the total magnetic moment as shown in equation (26)

$$M = \int I_i B L_i Z_i \qquad (26)$$

where B (T) is the magnetic field, I is the input current (A) and L (mm) is the length of the main channels.

Three different current inputs (2A, 3A, and 4A) were tested evaluating the final EM soft actuator bending angle: 10 cycles for every current input were performed.

The testing protocol is the following: the current is provided to the Galinstan channel for 1 s (because of the Lorentz force the EM soft actuator result in bending motion), after the current is set to 0 A for 1 s (rest time) and the actuator get backs to its initial position, subsequentially the current is provided again for 1 s, the whole cycle is repeated for 10 times.

The current input providing the best bending performance is 4A: a bending angle of 22.4 ° is obtained, resulting, respectively, 35.4% and 46.9% higher than the bending angle obtained at 3A and 2 A. The standard deviation has been calculated on 10 cycles, resulting really low for every current input (standard deviation of 0.21 ° at 2A, standard deviation of 0.16 ° at 3A, and standard deviation of 0.17 ° at 4A). See **Fig.3.25 a), b) and c)**.

When a current input of 4A is provided, a relative error (e), a good metric to evaluate the accuracy in terms of bending of the proposed actuator, was found to be 0.7 %. The low relative error makes the proposed EM soft device appealing for applications requiring high accuracy, such as biomedical and industrial devices.

The strain gauge performance has been analyzed: the best current input, namely 4A, has been provided to the EM actuator for a total of 100 consecutive cycles. The current is provided for 1 second, followed by an off period of 5 second, for a total of 100 times. Two electrical wires have been welded to the strain gauge pads and connected to the benchtop multimeter (GW Instek, GDM-8341) which in turn was connected to the laptop to collect data.

From the testing phase it stands out that the strain gauge change of resistance is characterized by two phases: an initial phase in which the change in resistance tends to grow and a second phase where it is stable (see **Fig 3.25 d)**). The authors explain the two different phases as follows: during the first phase the overall change in resistance constantly grows for the first 28 cycles because of the i) Mullin

effect, and ii) material (TPU) hysteresis. After the 28 th cycle, a stabilization in the material hysteresis and mitigation of the Mullins effect occur and the change in resistance of the embedded strain gauge result stable. In particular, the sensitivity (s) of the strain gauge throughout the second phase (stability phase) is 49.7 $\frac{\Omega}{^\circ degree}$ and R^2 is equal to 0.96. In particular, the high sensitivity allows the exploitation of the proposed EM actuator without relying on any resistance amplifier. The following results suggest that the proposed 3D printed soft EM actuators need to be trained for 28 cycles before the usage, in order to obtain consistency in the bending behavior.

It is worth mentioning that the training phase (28 cycle) mostly depends on two factors: i) size of the device (changing the size, the amount of training cycles can change), and ii) material properties: every material (even different kinds of TPU) is characterized by different viscoelastic properties, affecting the bending behavior of the EM soft device. Every soft EM device fabricated with the proposed approach needs to be initially tested to understand when the stabilization phase (in terms of consistency in the bending behavior) occur. Further works will focus on the fatigue analysis of the proposed soft EM device, paying particular attention at the interface adhesion among CPLA and TPU when the device is subject to repetitive cycles.

The embedded strain gauge has been used to obtain real-time feedback, in future it can be used to create closed control loops, improving the automation degree of the proposed EM soft actuator.

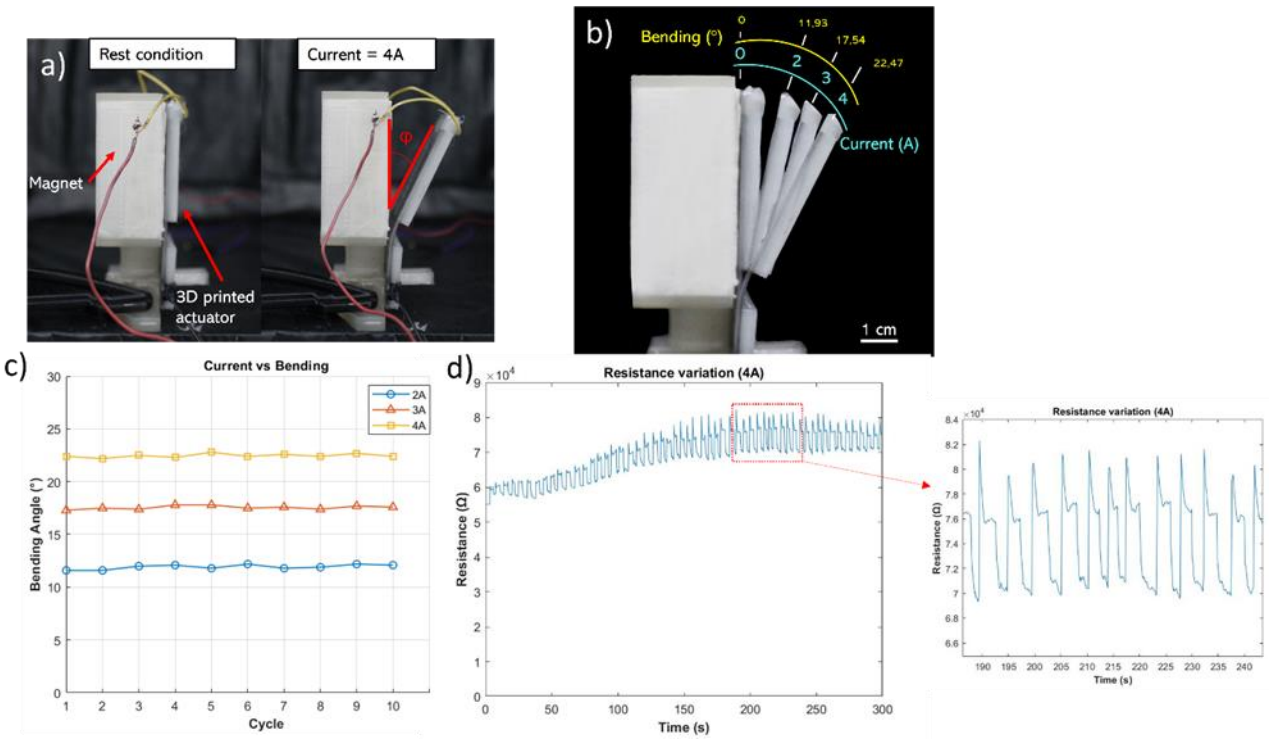

Fig. 3-25 Characterization of the EM soft actuator; a) Working principle of the soft EM actuator with current input of 4 A; b) Observed bending angle as a function of the current inputs; c) Comparison of the bending angle at the current input variation versus number of cycle; d) Embedded sensor behavior: resistance variation at 4 A current input.

3.6.4 Applications: bio-inspired frog robot and independent dual actuator (IDA)

To prove the potentialities of the proposed manufacturing approach, two different applications have been developed: a jumping bio-inspired soft frog and an independent dual actuator (IDA).

The bio-inspired jumping soft frog was used to demonstrate that the proposed EM soft device can be employed for soft robotics applications: a challenging topic concerns the fabrication of animal-based soft robots capable of crawl, jump and swim [147][77][148]

The frog-inspired soft EM robot (see **Fig.3.26 a)**)is based on a core main body equipped with internal channels filled with Galinstan (the same of the EM soft actuator shown in section 3.2) and four legs (one for each corner of the main body) designed with flexible TPU joints to improve jumping motions. TPU was used to manufacture the soft frog setting the same printing parameters listed in **Tab.3.14**.

The jumping performance of the soft EM frog have been evaluated, in terms of position in the x-,y-space and repeatability.

The soft EM frog body was placed parallel to the permanent magnet on the horizontal plane: the center of the magnet is fixed as the zero of the axis-system for each orientation. Four different orientations were tested: Nord-, Sud-, Est, and West-orientation.

The following testing protocol was used: for each orientation, one by one, a single input current of 4 A is provided to the Galinstan channel, and the soft EM frog results in jumping movement. Subsequentially, the current is set to 0 A for 10 seconds and the frog soft robot is placed at $x = 0$, and $y = 0$. The whole cycle is repeated 3 times for each orientation.

A virtual marker for each leg was used to evaluate the x- and y-position (**Fig 3.26 b)**) of the soft frog: the jumping movement is substantially repeatable, and in **Tab.3.14** the standard deviation of each leg (1 to 4), for every orientation (Nord, Sud, Est, West), is listed. The standard deviation has a random behavior: for the x-position, the standard deviation ranges from 1 mm to 5 mm and for y-position it ranges from 1 mm to 10 mm. The mean (x-; y-position) standard deviation for Nord-. Sud-. Est-. and West-orientation is respectively (3.72; 3.69) mm, (4.79; 7.53) mm, (3.14; 3.76) mm, and (3.01; 7.16) mm. The following outcomes (see **Fig.3.26 c)**) indicates that the presented EM bio-inspired soft robot can be employed as jumping robot, moreover future works will focus on the modelling, simulation, and control aspects of the jump motion.

Tab. 3-14-Jumping motion evaluation

	Orientation	Mean position		Standard deviation	
		x (mm)	y (mm)	x (mm)	y (mm)
Nord	**Leg 1**	-23.15	80.51	4.61	1.34
	Leg 2	52.36	68.17	4.34	5.91
	Leg 3	42.49	5.35	3.24	5.64
	Leg 4	-43.25	7.58	2.71	1.90
Sud	**Leg 1**	-99.73	-35.49	2.39	11.70
	Leg 2	-57.24	39.02	6.80	7.79
	Leg 3	26.21	0.470	2.56	6.03
	Leg 4	-23.86	-78.45	7.42	4.58
Est	**Leg 1**	-15.47	37.84	3.01	1.08
	Leg 2	22.56	-0.58	2.29	2.29
	Leg 3	0.14	-8.05	1.43	7.13
	Leg 4	49.89	-75.22	5.83	4.53
West	**Leg 1**	-104.02	34.56	1.39	3.23
	Leg 2	-23.51	64.64	3.38	9.27
	Leg 3	8.64	-16.98	2.74	10.87
	Leg 4	-76.22	-46.96	4.54	5.28

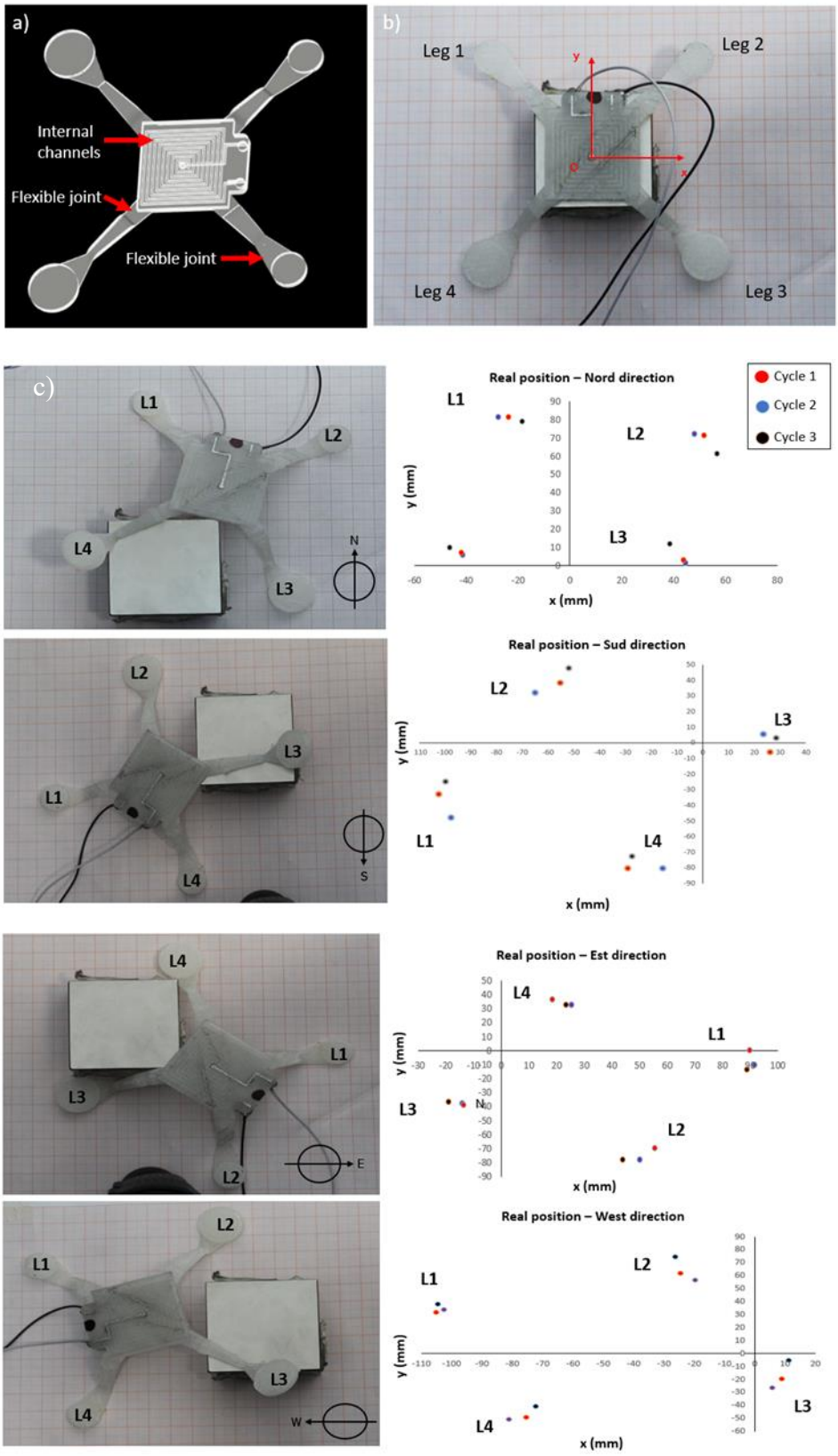

Fig. 3-26 Bio-inspired EM soft Frog: a) CAD of the soft Frog; b) Rest position (at 0 A); c) characterization of jumping motion at four different frog orientation: Nord-, Sud-, Est, West-direction.

A great advantage offered by M-MEX technique and in general by AM methods concerns the possibility to fabricate assembly-free device that can be scaled up and down [13].

To demonstrate that the proposed fabrication method is suitable for small size, non-assembly EM soft actuator, an independent dual actuator (IDA) was designed and fabricated. The EM-based IDA takes inspiration from human fingers: they are connected to the hand, and they can be activated both independently and simultaneously. The proposed IDA device (**Fig.3.27 a), and b**) is composed of two TPU fingers connected each others to a base: each finger is 50 mm long and 23 mm wide and composed of nine internal channels (which will be filled up with Galinstan after the fabrication step) and one bottom strain gauge sensor. The distance between the two fingers is 4 mm.

The possibility to selectively choose which finger will be activated is really appealing (see **Fig. 3.27 c),d), e) and f)**) and can find applications in many fields such as i) on-off switching devices for button without human intervention, and ii) swimming robot (mimicking fish fins).

Another important aspect of the proposed IDA is related to the presence of two different strain gauges (one for each finger) which provide feedbacks (change in resistance) when the fingers are activated.

The IDA device was characterized to evaluate i) bending performance and, ii) the embedded strain gauge performance: only a 4 A input current was used for the tests.

The current input has been provided for a total of 10 cycles (single cycle: current on for 1 s and off for 1 s) in three different configurations: i) only the finger 1 has been activated (**Fig 3.27 e)**), ii) only the finger 2 has been activated (**Fig 3.27 f)**), and iii) both the finger 1 and 2 have been simultaneously activated (**Fig.3.27 d)**)

A mean bending angle of 15.5 ° (standard deviation of 0.4 °), and 15.4 ° (standard deviation of 0.6 were found when only the finger 1, and the finger 2 where separately actuated.

As shown in **Fig 3.28 a) and b)**, the strain gauge sensitivity of the finger 1 when activated (finger 2 not activated) is activated is 3.67 $\frac{K\Omega}{^\circ degree}$ ($R^2 = 0.96$) while the strain gauge sensitivity of finger 2 when activated (finger 1 not activated) is 3.84 $\frac{K\Omega}{^\circ degree}$ ($R^2 = 0.93$).

The whole IDA device has been fabricated in a single step cycle resulting, respectively, in a manufacturing time and cost of 1h12min and 3,06 €: it consists of two strain gauges (CPLA material) and two soft (TPU material) bodies.

Full advantages have been taken from the M-MEX approach: a comparison is here provided with the same IDA device fabricated in a modular way (two separate soft bodies, two separate strain gauges, a connection structure). In this case the 3D printing cost is 4.57€ (1.68 € for every soft body, 0.54 € for every strain gauge and 0.13 € for the connection structure), and the manufacturing time is 2h 20 min (48 min for every soft body, 27 min for every strain gauge and 7 min for the connection structure). On top of that, four manual assembly tasks are required: assembly of the two soft bodies with the connection part (2 tasks), and assembly of the two strain gauges in the bottom part of each soft body (2 tasks). The authors assumed a total manual assembly time of 30 min for a total manufacturing cost

and time of 4.57€ and 2h 30 min. It is important to point out that the human operator cost/minute has not been considered.

The exploitation of the M-MEX approach, in this specific case, lead to a reduction in cost and time, respectively of 14.65 % and 55.2 %, proving all the potentialities of the proposed 3D printing method.

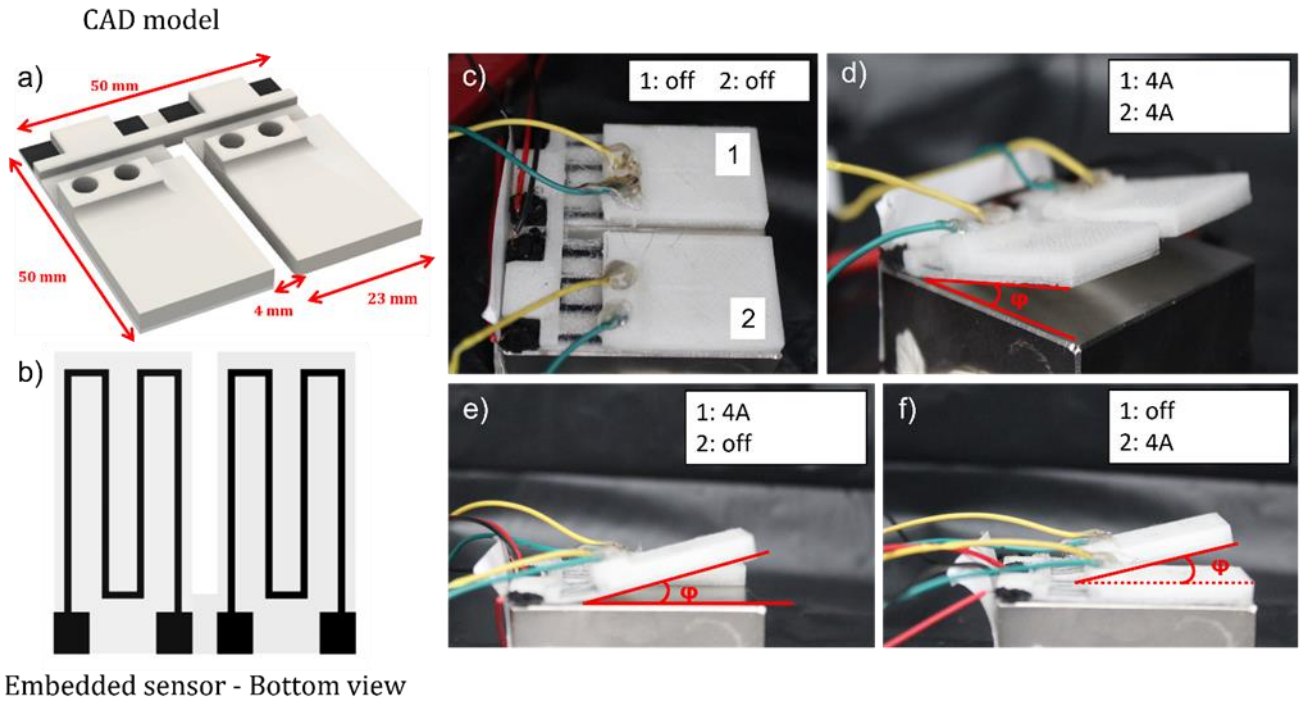

Fig. 3-27: Independent Dual soft EM Actuator (IDA) and characterization: a) CAD of the proposed IDA: b) Bottom view of the embedded strain gauge sensors; c) Zero-current input for Finger 1 and 2; d) 4A current input provided to both the fingers: bending of both the fingers; e) Bending of Finger 1: 4 A current input provided to Finger 1 and 0 A current input provided to Finger 2; f) Bending of Finger 2: 4 A current input provided to Finger 2 and 0 A current input provided to Finger 1.

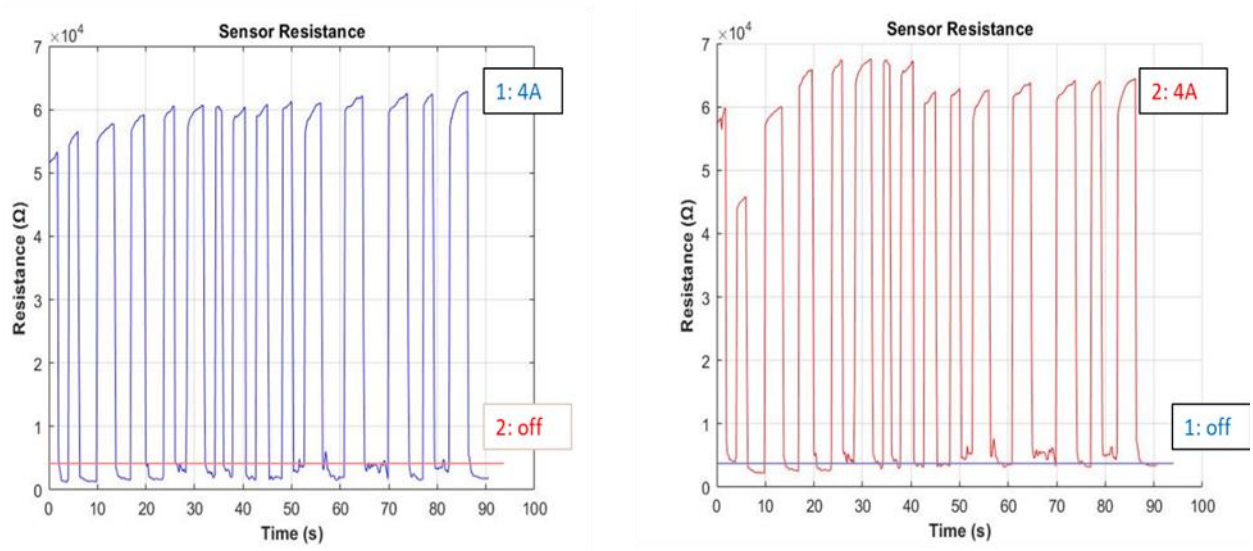

Fig. 3-28- Strain gauge characterization when the fingers are separately activated: a) Resistance variation of Finger 1; b) Resistance variation of Finger 2.

3.6.5 Conclusions

This work demonstrates the advantages offered by the multi-material extrusion (M-MEX) additive manufacturing (AM) process for the fabrication of soft electromagnetic (EM) actuators: even though this class of actuator is really appealing for soft robotic applications, it results, at the state of the art, still underexploited.

The main benefit of the proposed manufacturing approach consists in the monolithic fabrication of the soft EM device equipped with i) internal channels (filled up with liquid metal Galinstan) and ii) with an embedded strain gauge sensor. As a matter of fact, manufacturing steps and assembly tasks have been abruptly reduced making M-MEX technology suitable for the fabrication of the proposed soft EM devices.

A soft EM actuator used for bending purpose has been characterized showing a bending angle of 22.4 ° and a very low relative error of 0.7 %, while the 3D printed embedded strain gauge sensitivity was found to be 49.7 $\frac{\Omega}{^\circ degree}$. Two more examples have been presented: a soft frog-inspired EM robot and a dual finger independent actuator (IDA) equipped with two separate strain sensors. The latter, can be used for industrial application such as electromagnetic switcher. It was also proved that the usage of the M-MEX approach for the fabrication of the dual independent actuator (IDA) with embedded sensors resulted in a reduction of 14.65 % and 55.2 % in manufacturing time and cost, compared to a modular MEX approach. In conclusion, the outcomes of the present research lay the foundation for a huge exploitation of M-MEX technology (and AM technologies, in general) for the fabrication of EM devices equipped with sensors.

4. CHAPTER 4: ONE SHOT-ADDITIVE MANUFACTURING OF ROBOTIC FINGER WITH EMBEDDED SENSING AND ACTUATION

4.1 Introduction

Recently, Additive Manufacturing (AM) technologies have started gaining a lot of interest in the soft robotics and biomedical field [1], due to several intrinsic features such as the possibility to: i) employ soft materials, ii) easily create complex structures, iii) use more materials in the same manufacturing cycle, and iv) fabricate smart structures [2]–[6]. Among the different material extrusion techniques, Fused Filament Fabrication (FFF) technology, seems to fit well with soft robotics requirements: in particular, as pointed out by Shintake et al [149], several researchers focused on the study (design, optimization, simulation, fabrication, and control) of soft grippers. It is possible to classify the contribution of FFF into the soft robotic field as a function of the actuation mechanism underlying the fabricated soft robot, as follows: pneumatic actuation, shape memory polymers and tendon driven. 3D printed pneumatic actuators consist of a main body made up of soft material actuated by means of compressed air. The main body can be patterned in different ways to achieve several kinds of deformations (such as bending, twisting, elongating, and shortening). The bending actuator is the most widespread class fabricated by means of FFF [150]. Some examples of bending pneumatic actuators equipped with strain sensors (fabricated using a dual extruder machine) are provided in [25], [151], [152]. Several results have been achieved in this field such: i) a way to improve the object grasping capability, ii) the possibility to fabricate embedded air connectors [153] and iii) the possibility to obtain helicoidal motion [40]. Shape memory polymers actuator is based on phase change of the materials such that the change of Young's modulus when the switching temperature (Ts) is reached resulting in a change of material softness. FFF has been largely employed for the fabrication of structures based on this actuation method [154]–[157] proving how printing parameters (infill and pattern) affect recovery time and recovery quality [158]. A new and promising way to exploit the shape memory effect in FFF structures is the creation of structures made up of at least two parts: joints made of shape memory polymers and links made of non-shape memory material. This design choice implies several advantages: i) the time required to activate only the joint is just a couple of seconds (compared to more than 30 s to activate the whole structure), ii) it is possible to take full advantage of multi-material 3D printing, and iii) complex movements are enabled [159]–[163] [164]. Finally, tendon-driven-based FFF robots have been largely exploited over the past few years and it consists of creating structures (for example fingers) actuated utilizing cables connected to motors. In [141] a soft manipulator has been fabricated using a custom-made FFF machine enabling the bonding

strength when different materials (hard and soft) are extruded. The authors studied the best hinge geometry providing a new finger version (reducing the phalanges dimension) to improve the finger conformability around unknown objects for grasping tasks . Mohammadi *et al.* demonstrated that this approach can be used to fabricate a fully 3D printed hand (34 h for the manufacturing) costing 200 USD and characterized by at least 1 year of lifetime which can be employed as prostheses [165].

Shape memory alloys (SMAs) are a very promising class of actuators, largely employed in soft robotics to actuate soft structures: they are smart materials able to change their crystalline structure from martensite to austenite when thermally activated, leading to a change of Young's modulus. Compared to the above-mentioned actuation methods, SMAs do not require heavy systems to work such as pneumatic compressors or motors and their actuation is faster and less power-consuming than shape memory polymers. Silicone molding is the most used fabrication technique to embed SMAs into elastomeric matrices to achieve several kinds of motion such as bending and twisting [130]–[133].

Recently, AM has been used to fabricate structures activated by SMA, showing at the same time: i) all the potentialities of AM technology (capability to create complex structures, capability to obtain complex motion paths using two materials with different stiffness in the same printing cycle), and ii) a huge problem related to the manual embedding of SMAs wires after the fabrication [166], [167]

The accurate placement of SMAs into 3D printed structures is a big challenge and addressing this requirement would abruptly increase the impact of FFF in soft robots manufacturing, as a matter of fact solving this problem would i) reduce the manual tasks leading to a completely automated manufacturing process, ii) increase the accuracy of the SMAs placement and iii) allow the placement of SMAs into complex structures. Although several interesting solutions have been discovered in the field of FFF fiber reinforcement [168]–[170] and wires placement [143], they cannot be applied to SMAs integration due to the high extrusion temperature of the common FFF filaments (180 to 250 °C), far above the austenitic start temperature threshold of SMAs.

In the present work, the authors propose a flexible manufacturing approach to solve the problem of the automated SMAs placement into FFF structures, using a commercial and inexpensive (300 USD) dual extruder FFF machine and a pick and place robot. The key enabler of the present research is related to the use of a material characterized by a printing temperature (T_p) lower than the SMA austenitic starting temperature (A_s): polycaprolactone (PCL) filament (extruded temperature of 70°C) in conjunction with a SMA spring, having A_s equal to 90°C has been employed. After studying process parameters and compliance behavior of PCL, the stop and go method [171], [172] has been used to automatically embed the SMA spring during the printing process with the help of a custom made cartesian pick and place robot.

To the best of the authors' knowledge, despite huge exploitation of FFF for the fabrication of sensors (such as force [42] [15], strain [43] pressure, [16][173] and accelerometer [174][175]) and 3D printed actuators, there is a lack in the literature, concerning 3D printed structures with embedded sensors and actuation systems, fabricated in a single step manufacturing process[176]. In the present research, for the first time, an FFF-made soft robot with embedded two sensors (based on two different principles: piezoresistive and capacitive) and an actuator (SMA spring) has been manufactured in a monolithic way. To demonstrate the potentialities of this fabrication method and to take full advantage of multi-material FFF 3D printing, a soft finger was manufactured, employing 3 different materials (conductive, flexible, and the above-discussed PCL). The goal of this research is to show that, exploiting the proposed manufacturing approach (FFF + pick and place robot), it is possible to create smart active structures closing the loop between actuation and sensing without recurring to any post-process and assembly task.

4.2 Materials and methods

The main goal of the present work, shown in **Fig.4.1**, is the one-shot additive manufacturing of a soft robotic finger equipped with sensing systems (a strain gauge for the bending sensing and a capacitive force sensor for the object detection) and a SMA spring actuator. To achieve this goal, a low-cost multi material extrusion machine and a custom-made cartesian pick and place robot (to automatically embed the SMA spring) were employed. The proposed manufacturing approach aims to push the role of AM into a new dimension: structures having the capability to provide real-time feedbacks and with embedded actuation systems can be fabricated in a fully automated way without relying on assembly tasks.

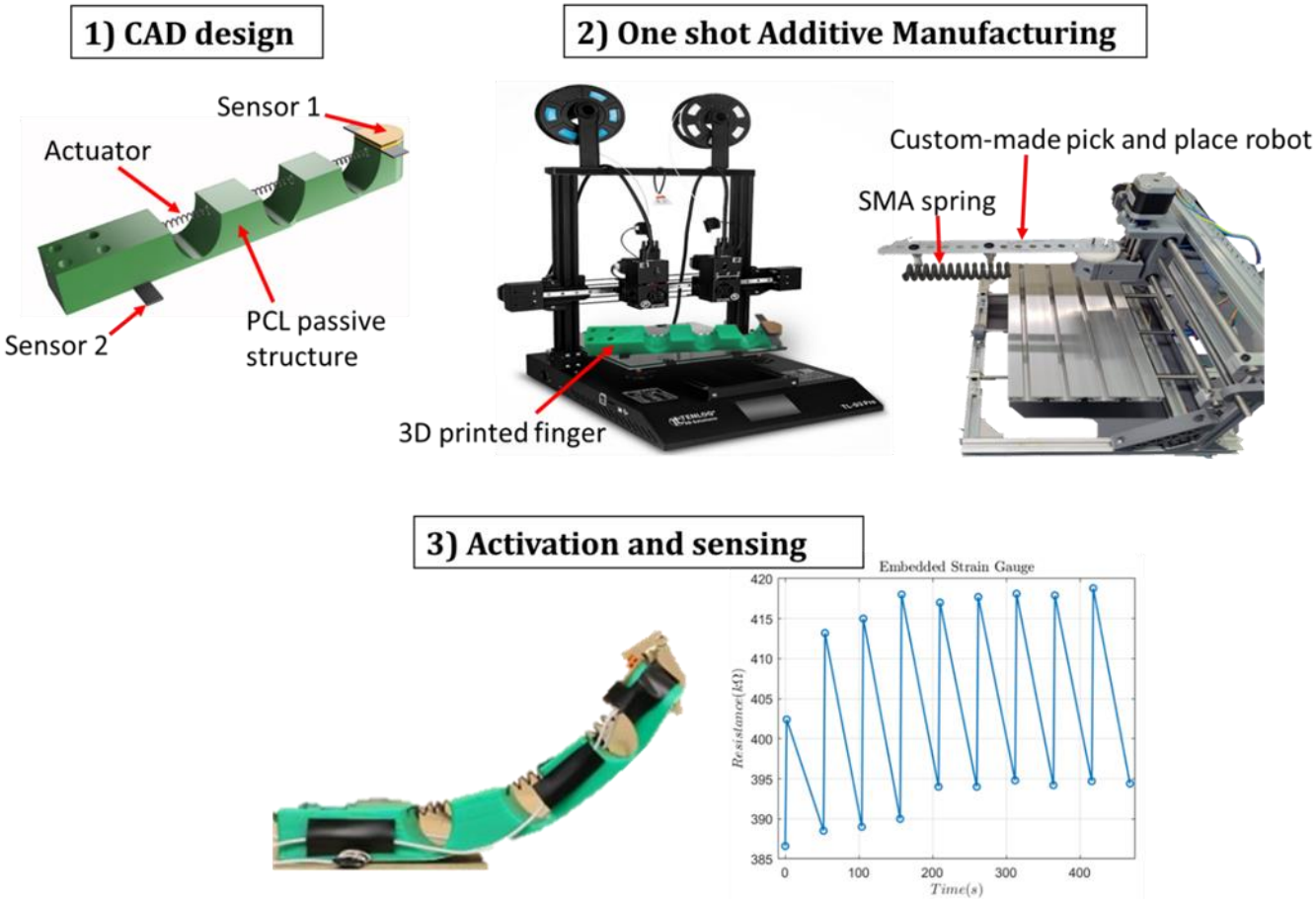

Fig. 4-1- Main goal of the proposed research: one-shot 3D printing of a smart device equipped with sensor and actuator units.

Apparently, a huge temperature incompatibility issue occurs when SMAs have to be embedded, during the fabrication process, into FFF parts: generally, flexible materials such as common thermoplastic polyurethanes (TPUs) are characterized by a printing temperature (T_p) above 220 °C, far above the A_s of Nickel-Titanium SMAs (ranging from 70 to 90 °C). The aim of automating SMA embedding into 3D printed parts motivated us to pause and restart the print after inserting the SMA using a pick and place robot. This task has been made possible by using polycaprolactone (PCL) filament: a non-conventional material, mainly used in the biomedical field for scaffold manufacturing [177]–[180] . PCL material is characterized by T_p ranging from 70 °C to 110 °C, being compatible with SMAs' A_s without affecting its thermal memory. PCL is also well-known for getting softer when locally heated up to a temperature close to T_p. This behavior will take place when the SMA will be activated through the Joule effect. PCL (eMate-PCL, eSun, China) was used in this study, while a Dynalloy Inc. SMA spring with A_s equal to 90 °C was employed.

The main process parameters to consider for our application are i) printing temperature (T_p), ii) printing speed (s), nozzle size (d) and layer height (h). Regards to T_p, the authors decided to set the minimum range as suggested by the filament manufacturer [70, 110] °C, because the need to avoid

any interaction to A_s (equal to 90°C) is a crucial requirement for the integration of SMA. As well-known from scientific literature [58], s mainly affects the printing quality (dimensional accuracy and surface roughness): with a trial and error approach, we found 15 mm/s and 10 mm/s around the corners to be the best s values to set ensuring a good printing quality.

PCL material is stiffer than classic TPU (used for the fabrication of soft robots such as fingers) but softer than PLA. The PCL structure should be easily deformable by the SMA actuators: a study on the stiffness has been conducted. To address this requirement, the relationship among d, h and weight of PCL structures was studied using a factorial plan 2^2.

From the plan, several considerations can be drawn:

- The two factors (namely d and h) affect the weight (g) of the structure while the interaction among the two factors does not affect the weight
- The way in which the two main parameters affect the weight of the PCL structures is:

  i) nozzle size: switching from a 0.4 mm to a 1 mm nozzle size, the weight increases.
  ii) layer height: switching from 0.2 mm to 0.4 mm, the weight increases.

- The residual analysis shows the consistency and robustness of the computed factorial plan.
-

In summary, the 2^2 factorial plan provides the best d and h value to set, to create a lightweight structure which is found to be 0.4 mm, and 0.2 mm respectively. The four most important process parameters for the proposed application have been analyzed and listed in **Tab.4.1.**

Tab. 4-1- Summary of process parameters for PCL

Parameter	Value	Expected advantage
Printing temperature (T_p)	70 $°C$	Avoid affecting SMA programming
Printing speed (s)	15 and 10 (near the corner) mm/s	Increase printing quality
Nozzle size (d)	0.4 mm	Reduction of weight
Layer height (h)	0.2 mm	Reduction of weight

In this section, the relationship between PCL compliance and local heating using a resistive wire is studied. To address this goal, several PCL samples with embedded resistive wire (Nichrome wire, diameter 0.5 mm) have been fabricated. The sample dimensions were 70, 35, and 10 mm in size along the x, y, and z-axis. The printing process was stopped manually to embed the resistive wire and later resumed to incorporate the resistive wire into the PCL structure (see **Fig 4.2 a) and b)**). The resistive

wire has the function to mimic the SMA actuator: it was heated up in the same range of SMA temperature (up to 110 °C) which will be used for actuation later.

The compliance of a structure is calculated as follows:

$$Cm = \frac{1}{S} \tag{27}$$

Where Cm $[mm/N]$ is the compliance and S is the stiffness, calculated as follows:

$$S = \frac{F}{d} \tag{28}$$

Where F is the applied force $[N]$ and d is the sample displacement $[mm]$.

An *ad hoc* set-up was used to evaluate the change of compliance, it consists of i) a power supply to heat up the embedded resistance, ii) a thermal imaging camera to evaluate the actual temperature of the wire, iii) a calibrated weight (2.5 N) connected to the sample (see **Fig4.2 a) and b)**), and iv) a digital camera to take pictures at each increment of temperature in order to calculate the displacement. The applied force was the same for each temperature increment and the only variable to measure was the displacement of the tip (see **Fig.4.2**), which allowed us to deduce the change in overall compliance.

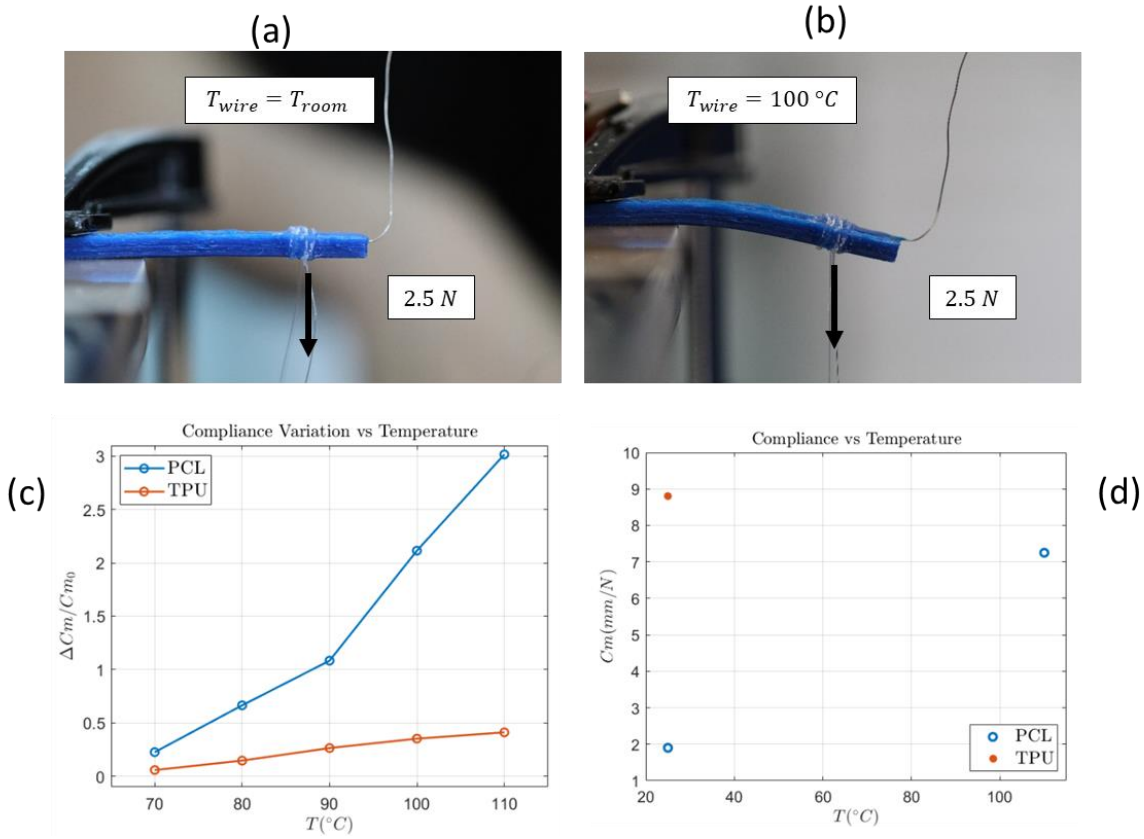

*Fig. 4-2- a) Tested sample when $T_{wire} = T_{room}$, and b) T_{wire} = 100 °C. c) $\Delta Cm/Cm0$ **vs** T for PCL and TPU, d) absolute compliance vs T for PCL and TPU.*

Starting from T_{room}, the temperature of the embedded resistive wire was incrementally increased and a picture was taken from 70 °C up to 110 °C with a step of 10 °C. Three PCL samples were analyzed, with three tests done for each sample, resulting in a statistically insignificant standard deviation. (see **Tab.4.2**).

Tab. 4-2- PCL samples: change in compliance $\Delta C_m/C_o$ vs Temperature

	Sample1 $\Delta Cm/Cm0$ *[mm/N]*		**Sample2** $\Delta Cm/Cm0$ *[mm/N]*		***Sample3*** $\Delta Cm/Cm0$ *[mm/N]*	
T [°C]	**mean**	**Std.dev**	**mean**	**Std.dev**	**mean**	**Std.dev**
70	0.229	<0.001	0.209	<0.001	0.241	<0.001
80	0.659	<0.001	0.665	<0.001	0.672	<0.001
90	1.09	0.02	0.98	0.01	1.18	0.03
100	2.05	0.04	2.12	0.03	2.17	0.06
110	2.99	0.11	3.08	0.16	2.97	0.14

A significant change in compliance ΔC_m compared to the initial compliance Cm_0 of almost 3 times occurs when the resistive wire is heated up to 110 °C (the maximum temperature that will be reached from the embedded SMA) making this material suitable for our application (see **Fig 4.2 c)**). To have a direct comparison with TPU, the same identical tests were performed on TPU showing a maximum change in compliance$\Delta Cm/Cm_0$ of 0.4 (86% less than PCL): these data refer to the mean among 3 samples for PCL and TPU. From these tests, it is possible to get a comparison in terms of absolute compliance: when PCL is locally heated up to 110 °C, the temperature that will be reached by SMA, its absolute compliance, as shown in **Fig 4.2 d)**, is almost 7 mm/N (when the resistive wire temperature is equal to T_{room}, C is less than 2 mm/N) not that far from the compliance of TPU at T_{room}(almost 9 mm/N).

In conclusion, PCL material appears to be the right candidate to match with SMA integration, not only because of its low printing temperature but also because its compliance abruptly increases when it is locally heated up, making PCL soft when SMA will be heated to be actuated.

For the current study, a shape memory alloy (SMA) spring with the following properties was used: i) T_{as} equal to 90 °C, ii) internal diameter equal to 0.51 mm, and iii) external diameter of 3.45 mm. This selection was made to obtain a higher displacement and sufficient force for flexing the finger joints. It is important to note that the printing temperature of PCL equal to 70 °C helped the integration of the SMAs, otherwise, it would have been impossible to integrate SMA with lower A_s without adversely affecting its thermomechanical behavior.

The length of the SMA spring depends on the finger dimensions (see next Section 4.3), being the finger length equal to 122 mm, an overall spring length (in its extended state, including the two terminal-crimps as well) bigger than that threshold value is required.

The length of the only SMA spring in its extended state (in its pretension state) was 92 mm: 20 mm shorter than the finger length, in fact after crimping it with terminal metal crimps, it reached 140 mm in length. The choice of the right crimp size is crucial to be perfectly embedded into the two anchor points during the manufacturing process by means of the extruded filament. With a trial-and-error approach, the right dimension of the crimp was selected.

Before embedding the SMA into the 3D printed structure, it has been characterized using a custom-made setup (detailed in [181], [182]) to determine the relationships between input and output. The following time-domain properties: applied current, voltage, displacement, temperature and force were obtained. Three different current inputs were provided (2.8 A, 3.2 A and 3.6 A) for 2 s, followed by an off period of 50 s (corresponding to a frequency of 0.02 Hz): for each current input the following protocol was applied for a total of 5 cycles. The characterization results are summarized in **Fig 4.3a) and b)**. From the SMA characterization, it stands out that the best current value to apply is 3.2 A, for the following reasons:

- By applying 3.2A input current, the SMA temperature values reached from 110 °C up to 120 °C, this range corresponds to the highest compliance in PCL material. The other two current inputs, 2.8 A and 3.6 A, provide respectively inadequate temperature to take full advantage of the PCL behavior and a too high-temperature value (around 160 °C) which would melt the PCL finger.
- The average displacement obtained providing 3.2A is 11.2 mm, while the one obtained at 3.6 A is 11.5mm: these two values are very close but using only 3.2 A it is possible to reduce the power consumption.
- The same observation can be seen with the force values: almost identical force values are reached providing 3.2A and 3.6 A. Also, in this case, providing 3.2A, the power consumption is going to be reduced.

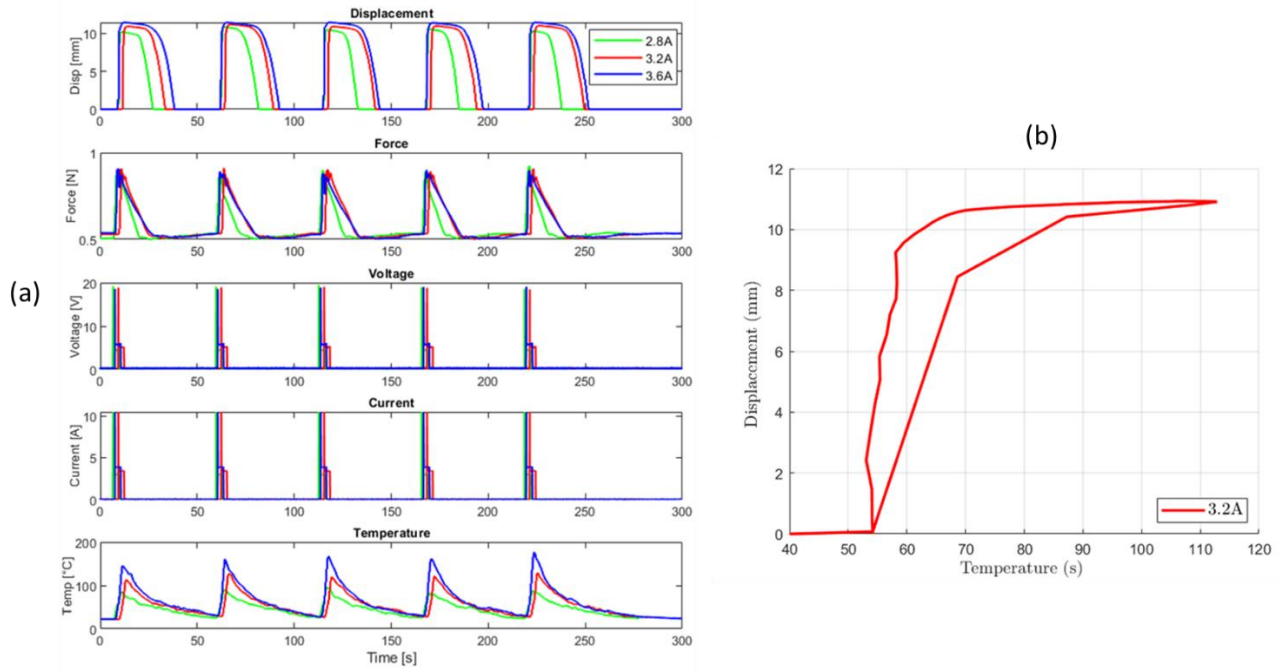

Fig. 4-3- SMA characterization of 0.51 mm wire diameter ,3.45 mm coiled diameter, 92 mm length spring: a) overall results for five consecutive cycles at different current inputs, and b) relationship temperature-displacement for the first cycle (time 0 to 13 seconds corresponding to the peak of temperature) at 3.2A.

4.3 Design and sensor analysis

4.3.1 Design of the proposed robotic finger

To prove the potentialities of the proposed manufacturing approach, a soft finger (with embedded sensors and an SMA spring actuator) was fabricated. We followed the design rules pointed out by Mutlu et al [141] for this work while using FFF based approach. They pointed out two major outcomes, summarized as follows:

i) They experimentally studied different finger joints finding the best one named "nonsymmetric elliptic".

ii) To improve the finger behavior in terms of conformability around objects, the finger design should not exactly replicate the human finger geometry: shortening the proximal phalanx length, motion mimicking real human fingers is allowed and the grasping performance is improved.

The proposed finger (see **Fig.4.4**) can be subdivided into two portions: the active finger and a terminal block equipped with 4 holes to fix the finger to a custom-made platform during the tests. The hole in which the SMA spring will be embedded during the printing process is one of the most important parts of the finger. It has been drawn with the following features: i) diameter of 3 mm (with a trial-

and-error approach, this value was found to be the best diameter to ensure a complete and full embedding of the SMA spring) and ii) above the neutral axis of the structure to provide a better bending when the SMA is activated.

The finger is equipped with two sensors which will be manufactured in the same printing cycle as the finger. At the bottom of the finger, a strain gauge sensor has been drawn which consists of two pads (15 mm x 5 mm) where electrical wires will be welded. There are 4 tracks that have an active length of 84 mm, a width of 1.2 mm, and a distance between two adjacent tracks of 1.2 mm. Also, end-loops (3.6 mm x 4 mm) were included to reduce stress sensitivity in the axis perpendicular to the deformation axis and to improve the measurement quality. The strain gauge geometry is shown in **Fig.4.4 c)**).

The second sensor is on the tip of the finger, and it is used as a force/contact sensor. The sensor is based on the capacitive principle, and it has been fabricated using the same conductive material employed for the strain gauge and a different insulator material from PCL named NinjaFlex, well known for being one of the softest commercially available filaments. More details about the two just discussed sensors are provided in the next lines.

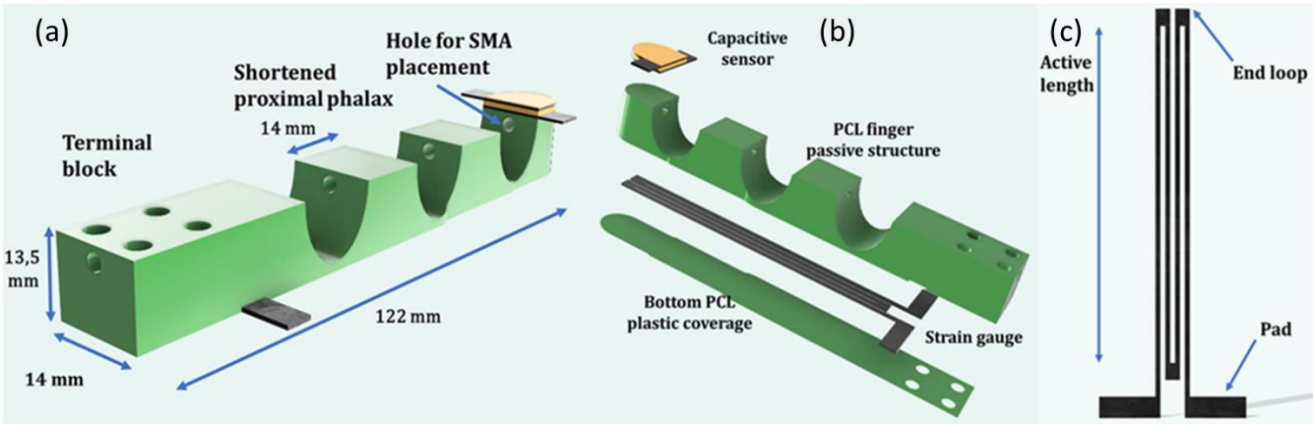

Fig. 4-4- proposed finger: a) finger dimensions, b) finger components, and c) embedded strain gauge

4.3.2 Piezoresistive strain gauge sensor and capacitive touch sensor

Here in this section, the two manufactured sensors are analyzed and studied, showing all the potentialities of the dual extruder FFF technology in the manufacturing of embedded sensors. It is important to point out that the two proposed sensors are based on two different working principles: piezoresistive (change in electrical resistance) and capacitive (change in capacitance). In this work, we are showing for the first time, to the best of the authors' knowledge, two sensors based on different principles are 3D printed and embedded in the same structure and evaluated in a fully functional robotic/ prosthetic finger.

The dimensions of the proposed strain gauge sensor are above described. The length and the width are the same as the "active finger". Exploiting the piezoresistive effect (equation 26), the strain gauge will provide a change in resistance when the finger will be actuated. The goal of embedding the strain gauge is to correlate the finger bending angle to the change of resistance and to have direct and real-time feedback.

$$R = \rho \frac{l}{A} \tag{29}$$

Where $R(\Omega)$ is the strain gauge electrical resistance, ρ $(\frac{\Omega}{mm})$ is the material resistivity (a constant value which does not depend on the geometry), l (mm) is the track length, and $A(mm^2)$ is the track surface area. When a stimulus is applied (i.e., bending, compression, tension and so on), only the $\frac{l}{A}$ ratio changes, leading to a change in the final strain gauge resistance R. FFF-based strain gauges [17] have been largely employed and several experimental and theoretical studies have been performed to improve the scientific knowledge in this field under different points of view (i.e. dynamic piezoresistivity [42], thermal effects [183] [33] and modelling of anisotropic electrical conductivity [44]).

The sensors were manufactured in a conductive thermoplastic polyurethane (CTPU), namely NinjaTek Eel, NinjaTek, USA, to address severe bending that would break conductive polylactic acid (henceforth CPLA). One of the problems related to the fabrication of resistive sensors through FFF is the high electrical resistance (low conductivity) [35] involving electrical losses: as a matter of fact, these kinds of filament are made up of a polymeric matrix doped with conductive fillers (such as carbon black, carbon nanotubes and so on). To minimize the electrical resistance, it is important to study FFF process parameters to find out a correlation between them and the increase of conductivity. So far, in scientific literature, it has been proved that layer height and printing orientation affect the final electrical resistance in 3D printed strain gauges [32]. In the present work, two more process parameters have been studied, correlating their effect to the final electrical resistance of the 3D printed samples: printing pattern P_p and printing temperature T_p.

Considering P_p, the only 3 different patterns allowed by the combination between active strain gauge width (1.2 mm) and employed nozzle size (0.4 mm) were studied. The three P_p analyzed are 3 lines (called "A"), line-zigzag-line (called "B") and only zigzag (called "C"). The idea underlying the study of the best printing pattern is to investigate if it is possible to manufacture an optimal path for the current.

Considering T_p, 2 different values were changed, 230 °C (called "X") and 240 °C (called "Y"): the minimum and the maximum value suggest by the filament manufacturer. The idea, in this case, is to

investigate if the temperature affects the final electrical resistance. The studied process parameters are listed in **Tab. 4.3**.

A manufactured plan based on a total of 3 repetitions for each combination (fabricated in a random order to reduce the impact of external factors) was followed, and two outputs were measured for each combination: i) mean final electrical resistance (using a benchtop multimeter) and ii) standard deviation. The 3D printed samples consist of a 0.4 mm substrate of TPU and the proposed strain gauge (same dimension as section 3.1). In **Fig.4.5 a) and b)**, the sample CAD model, the theoretical printing pattern generated by the slicing software (Ultimaker Cura 4.11) and the actual 3D printed tracks are shown.

Tab. 4-3- Process parameters studied for resistance minimization

Printing pattern (P_p)- **Printing temperature** (T_p)	**Name**
3 lines(P_p)	A
Line- zigzag- line(P_p)	B
Zigzag (P_p)	C
230 °C (T_p)	X
240 °C (T_p)	Y

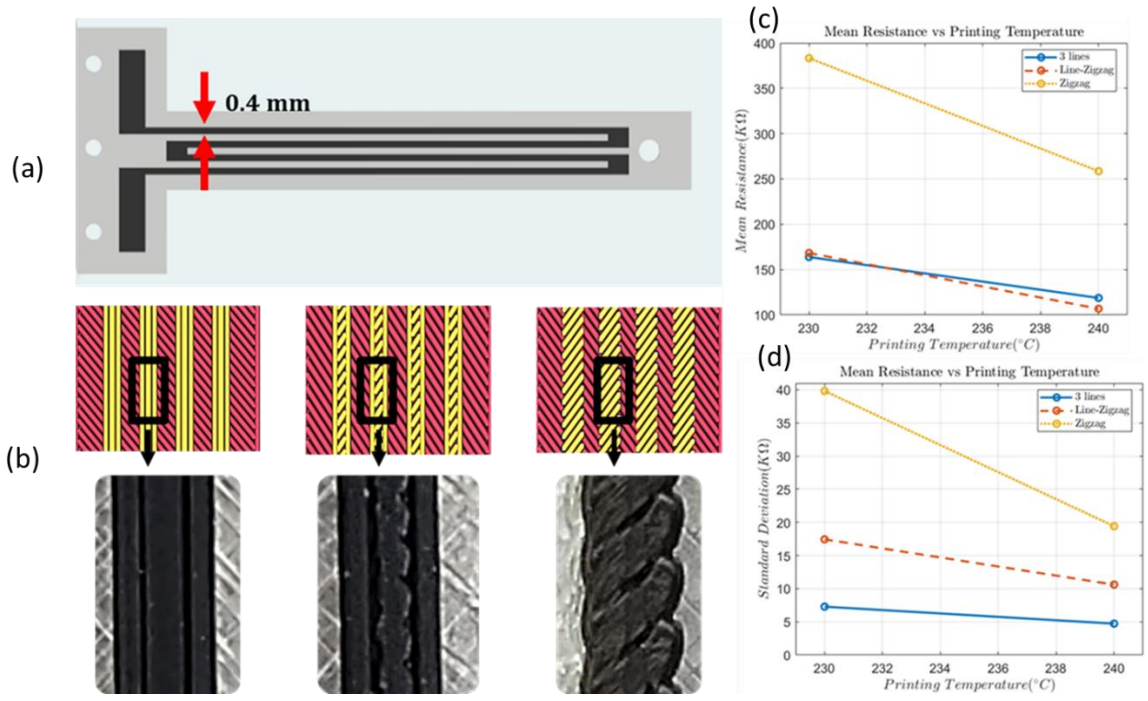

Fig. 4-5- a) CAD model of the studied strain gauge, and b) theoretical printing pattern and actual 3D printed tracks c) mean resistance vs printing temperature, and d) standard deviation vs printing temperature.

The results of the parameter investigation are shown in **Fig 4.5 c) and d)**.

From the results, the following conclusions can be drawn:

- Both the studied process parameters, statistically affect the electrical resistance of the proposed strain gauge.
- For each printing pattern, the increase of the printing temperature from 230°C up to 240 °C involves a huge decrease in the final electrical resistance respectively of 27,6 %, 36.5% and 32,1 % for A, B and C. Also, the standard deviation decreases respectively of 35.1%, 39.2% and 52.2% for A, B and C, when T_p switches from X (230 °C) to Y (240 °C). In the authors' opinion, this behavior is related to the melting process of the conductive filler (carbon black) scattered into the TPU matrix: in accordance with the percolation theory, the conductivity of conductive polymers is due to the creation of conductive network in which the electrical current can flow. Because the size of carbon black nanoparticles scattered into the TPU matrix is not uniform (the melting point of conductive fillers depends on its size[184]), increasing the printing temperature (namely the melting point of the carbon-black), the probability that more carbon black is melted increases, and also the probability to create a stronger conductive network for the current flow increases too. For this reason, for each pattern when the printing temperature increases, the mean electrical resistance and also the standard deviation (a total of 3 repetitions for each pattern) decreases (see **Fig. 4.5 d**)). For a good understanding of the percolation theory the authors suggest referring to [185]).
- At $T_p = 240\ °C$, the best printing pattern in terms of minimized electrical resistance is B (line-zigzag- line) providing a mean resistance of 106,7 $k\Omega$ and a reduction of electrical resistance of 11.9 % and 142% compared respectively to A (lines) and C (zigzag). This result can be portrayed in the following way: pattern B provides the best current path [186] compared to the other two possible patterns, resulting in low electrical resistance.

The combination of the printing pattern and printing temperature that minimizes both electrical resistance and the standard deviation is "line-zigzag-line" and "240°C", which will be used for the embedded strain gauge fabricated into the finger.

Over the tip of the finger, a capacitive sensor has been manufactured to obtain direct and real-time feedback (change in capacitance), when the tip of the finger touches objects.

The proposed capacitive sensor design is shown in **Fig 4.6a)**. It is made up of 4 main elements: a bottom electrode (0.6 mm thick), a separator layer (1 mm thick), a top electrode (0.6 mm thick) and a top plastic coverage (0.2 mm thick), for an overall thickness of 2.4 mm and the length and width are 21 mm and 14 mm.

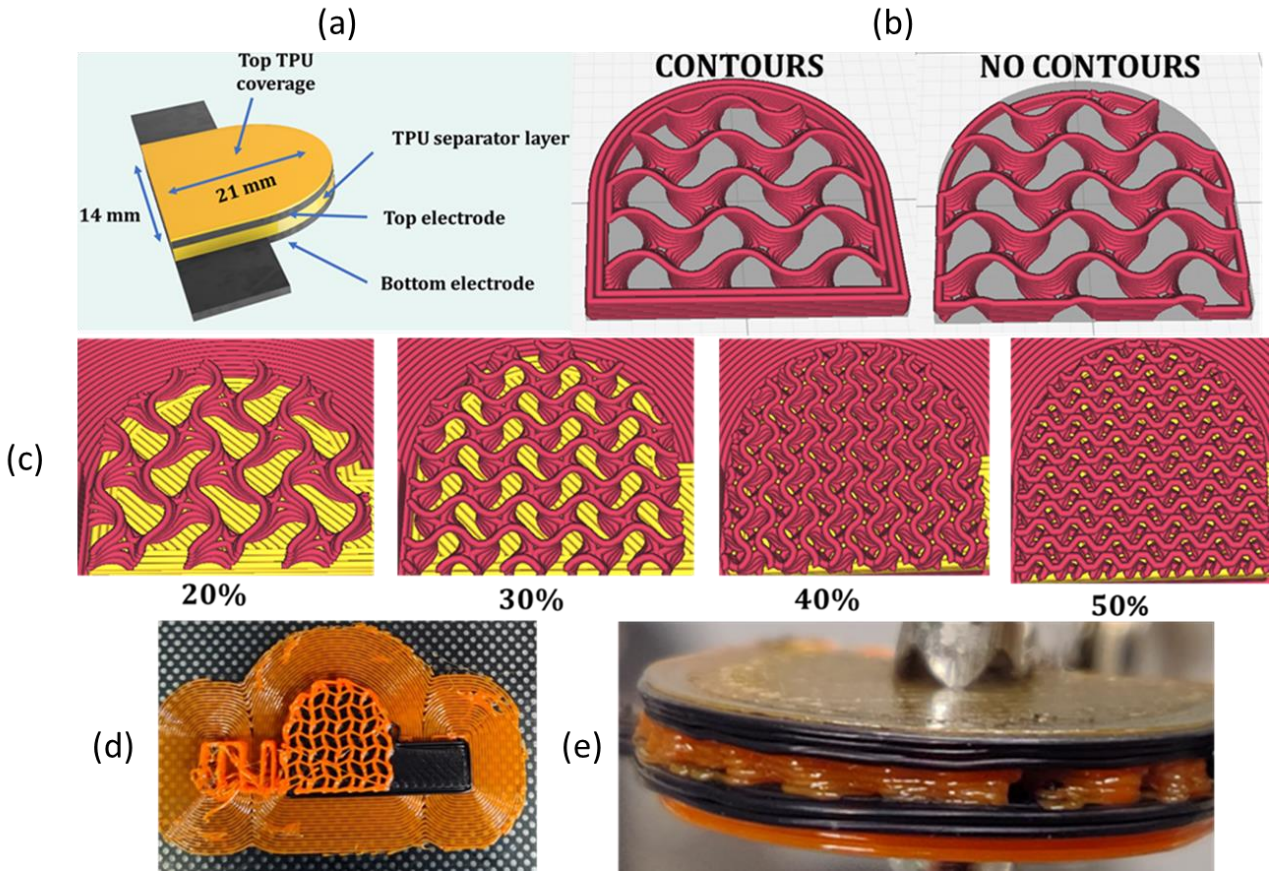

Fig. 4-6- a) Capacitive sensor b) contours vs no contours, c) different infill percentage, d) capacitive sensor during the manufacturing process, and e) magnification of the manufactured sensor, it is possible to appreciate the air gaps into the separator layer.

The equation governing the proposed sensor is:

$$C = \frac{A}{d}\,\varepsilon_0\varepsilon_s \tag{30}$$

Where C is the capacitance of the sensor (nF), A is the surface area of the electrodes (mm^2), d is the electrode distance (also known as separator layer thickness) (mm), ε_0 is the vacuum dielectric constant ($\frac{pF}{mm}$) and ε_d is the relative dielectric constant of the separator layer, in particular, the latter can be expressed as

$$\varepsilon_s = \varepsilon_{air} * \%V_{ir} + \varepsilon_e * \%V_e \tag{31}$$

Where ε_{air} is the air relative dielectric constant, ε_e is the relative elastomeric dielectric constant (pF/mm) while $\%V_{air}$ and $\%V_e$ are respectively the percentage of volume of air and elastomeric material (it is important to point out that $\varepsilon_{air} = 1$ and that $\varepsilon_e > \varepsilon_{air}$).

As well-known from scientific literature [187] [188], the separator layer needs to be a porous-based structure with air gaps due to the following reasons:

- When a force is applied, it shows more flexibility (with the same applied force, the distance among the electrodes will be greatly reduced in the case of a separator layer with air voids compared to a full separator structure) resulting in a greater capacitance change
- The percentage of the volume of air gaps ($\%V_{air}$) will be reduced under a force/pressure stimulus whereas the percentage of the volume of the elastomeric material ($\%V_e$) will increase resulting in a greater capacitance change ($\varepsilon_e > \varepsilon_{air}$).

The separator layer has been designed (Fusion 360, Autodesk) as a full structure: the porous structure (air gaps) has been generated into the slicing software (Ultimaker Cura 4.11.0) using gyroid infill (well known in the scientific literature for providing a good response when it is compressed [10]).
It is important to point out that the separator layer needs to be fabricated without any contour, otherwise the structure would be more rigid, and a huge amount of force will be required to compress the solid contours resulting in less sensor sensitivity (see **Fig 4.6 b)**). To achieve this goal, three process parameters have been successfully set: wall line count, top layer and bottom layer, respectively as 0, 0 and 0.
For the fabrication of the separator layer the TPU 85 A NinjaFlex (henceforth TPU), (NinjaTek, USA), was used due to the need to produce a separator layer as flexible as possible, to obtain a good sensor sensitivity.
As shown in **Fig.4.6 c)** four different infill percentages of the gyroid separator layer were studied: 20%, 30%, 40% and 50%. In **Fig.4.6 d)** a 3D printed sensor during the fabrication is shown. In **Fig.4.6 e)**, a magnification of the pourous separator layer is provided.
2 different conductive materials were used, conductive TPU (CTPU) and conductive PLA (CPLA), to study the best one in terms of sensor sensitivity.
After printing the capacitive sensors with different infill percentages of the separator layer and conductive material for the electrodes, the following conclusions can be drawn-

- Using CPLA and printing the separator layer setting 20% infill, 8 prints out of 10 have failed, showing manufacturing inconsistency: the separator layer act as “support structure” during the manufacturing process and being not dense enough the top electrode collapse when printed. The top electrode comes into contact with the bottom one: no capacitance values can be read (instead resistance values were read).
- Using CPLA and increasing the separator layer percentage (30%, 40% and 50%) the previous issue has been solved

- Using CTPU, it was possible to print the separator layer setting 20% infill (10 prints on 10) unlike for the CPLA. The authors justify the following behavior as follows: being CTPU made of TPU (82% TPU and 18% carbon black) the adhesion between the previous substrate (TPU) and the first electrode layer is abruptly increased if compared to CPLA.
- Increasing the infill percentage (from 20% to 50%) for both conductive materials, the capacitance value of the final sensor (after wiring, at rest) increases too because the percentage of TPU volume increases while the percentage of air volume decreases.

After connecting electrical wires to the pads, the sensors have been characterized. The measurement protocol used is the following: calibrated weights have been placed over the capacitive sensor and the capacitance value has been recorded using a digital multimeter.
In particular, the applied weight has been increased in the following way: 0, 200, 400, 800, 1000, 1500, 2000, 2500, 3000, 3500 g. A force sensor has been placed under the proposed capacitance sensor to record actual applied force values.
Results are shown in **Fig. 4.7**.

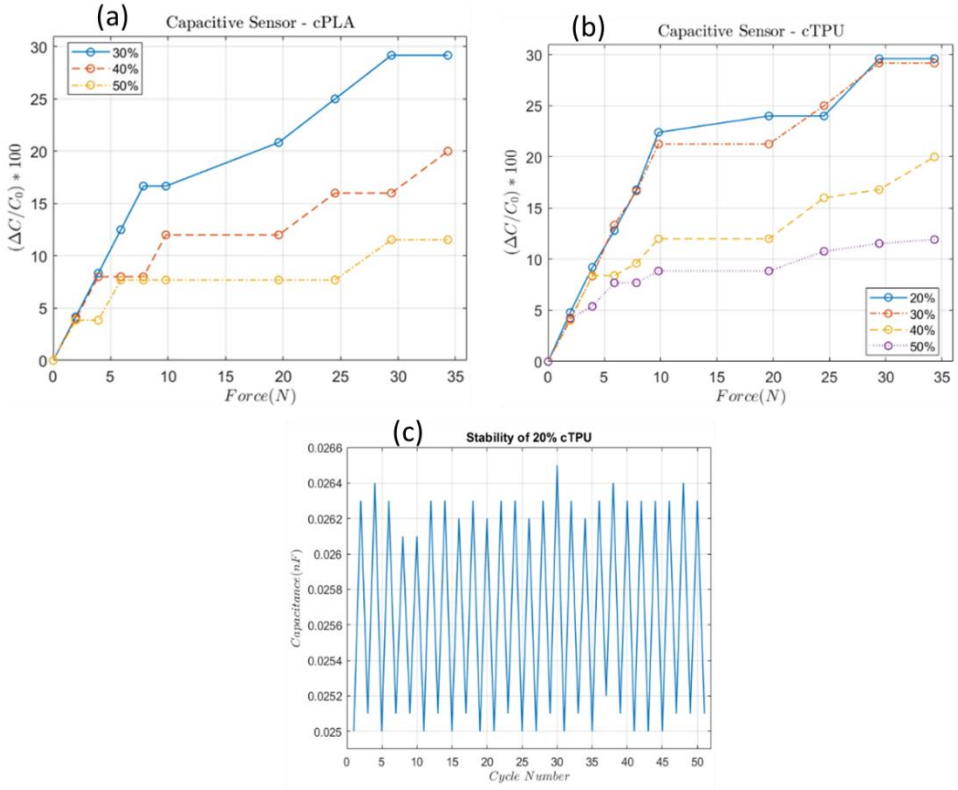

Fig. 4-7 - Capacitive sensors results a) CPLA sensitivity, b) CTPU sensitivity, and c) CTPU stability

From the characterization of the capacitive sensors, it stands out:

- Increasing the infill percentage, the performance (sensitivity) of the capacitive sensor decreases both for CTPU and CPLA.

- At the same infill percentage (30, 40 and 50%) the behavior of the CPLA and CTPU sensors is the same showing that the only reason to choose CTPU instead of CPLA is because of its composition allowing it to be 3D printed setting the separator layer at 20% infill.
- Every curve has in common an initial straight line in which the capacitance changes with a small amount of force and a second phase characterized by a sort of saturation in which a huge force is required to slightly change the capacitance (i.e., in 20%CTPU to achieve a 23% in ΔC/C0 almost 10 N are required while to switch from 23% to 25 % (2% increase) almost 15 N are required).
- CTPU 20% infill is the best sensors in terms of sensitivity, calculated as the ratio of incremental output to incremental input.

$$S = \frac{\Delta C}{\Delta F} \tag{32}$$

And it has been calculated in the linear region of the curve (from 0N to 16,6 N corresponding to 0g to 1000 g applied on the sensor) and is: $S = 0.53\ \frac{pF}{N}$, with a minimum detectable change of capacitance force of 1.9 N.

- Also, 20% infill is the best solution not only for the higher sensitivity but also because the amount of material used during the fabrication is reduced (and the time too).

One more test has been performed to evaluate the stability of the best sensor (see **Fig 4.7c)**): a 200g weight (which corresponds to the minimum force detectable from the sensor) was applied for 2 seconds, removed for 2 seconds, and applied again for the same amount of time, for a total of 50 cycles. The sensor shows high stability, and it can be used as an ON/OFF sensor to detect a minimum applied weight of 200g (force of 1.9 N).

In conclusion, although the sensitivity of the sensor is almost 2/3 order of magnitude less than the ones fabricated using traditional approaches, it can be used as ON/OFF sensors: the following advantages have been achieved using this manufacturing method-

- Only one fabrication method is involved (in the traditional approach at least 3)
- 0 assembly tasks are required (in the traditional approach at least 3)
- It is possible to create smart structures embedding the following sensor in the same printing cycle.

4.4 Additive Manufacturing

For the manufacturing of the proposed finger with the two embedded sensors and the integration of the SMA spring, a commercial low-cost (350 $) dual extruder machine based on the IDEX (independent dual extrusion) mechanism was used (Tenlog TL D3 Pro, Tenlog 3D Solutions, USA). Three different filaments were extruded from 2 nozzles: PCL (for the finger, nozzle 1), CTPU (for both the sensor's active parts, nozzle 2) ad TPU (for the separator layer and top coverage of the capacitive sensor, nozzle 1).

Several g-code modifications have been made, due to the following reasons: i) to set print temperature equal to 70 °C, ii) to stop the print at a certain layer number to embed the SMA spring and iii) to stop the print at a selected layer height to change the filament (from PCL to TPU) to print the separator layer and the top cover of the capacitive sensor.

The most important process parameters used are summarized in **Tab.4.4**: two 0.4 mm nozzles were employed, and 0.2 mm was set as layer height parameter (same value for each material).

Tab. 4-4- Process parameters used for the finger for the finger fabrication

Parameter	PCL	CTPU	TPU
Printing temperature ($°C$)	70	240	225
Line width (mm)	0.4	0.4	0.4
Printing speed ($\frac{mm}{s}$)	• 15 • 10 (near the corner)	20	25
Flow (%)	110	120	107
Retraction (mm)	4	2.5	6
Infill percentage (%)	20	100	• 20% (separator layer) • 100 (top coverage)
Infill pattern	lines	• Line-zigzag-line (strain gauge) • Line (capacitive electrodes)	lines

In the slicing software, the 3D Printer was instructed to pause immediately following a critical layer: this layer represented half of the diameter of the holes in which the SMA nickel-titanium spring would be placed. Along with this instruction, the 3D Printer was also made to maneuver its axes to present

the partial-completed print to the Cartesian Pick and Place Robot (CPPR): a custom-made machine developed as a small-form-factor alternative to larger, more industrial, and expensive versions. As it is composed of a 400x330 mm aluminum framework and 3D printed components, the design is highly modifiable and easily integrated with other machines. It is controlled with an Arduino Uno, as well as three A4988 Bipolar Stepper Motor Drivers, and utilizes a custom-written G-Code interpreter. The CPPR (see **Fig.4.8 a)**) has been able to use two electromagnets to manipulate the steel crimpled SMA actuators into the desired position. These electromagnets are simultaneously activated through an Omron relay module, which is controlled by the Arduino using G-Code over a serial connection to the host computer. This method enabled precise delivery of the SMA actuators without direct action from the user.

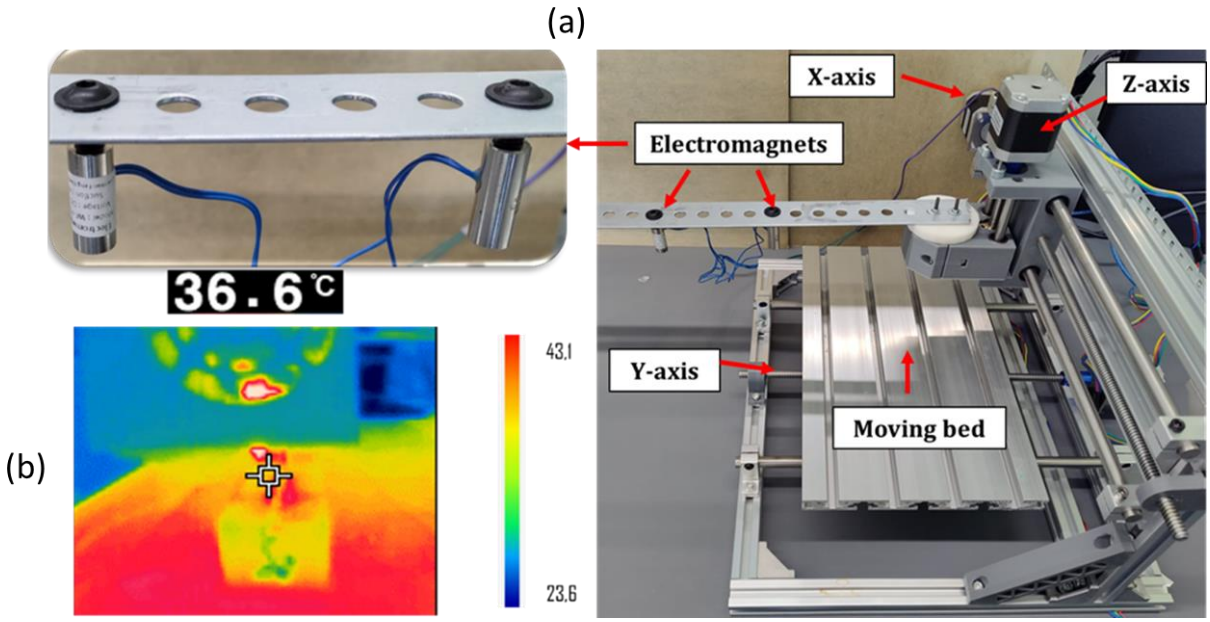

Fig. 4-8- a) Custom-made cartesian pick and place robot (CPPR) for SMA spring placement. b) Infrared image during the 3D printing process: the central marker (temperature of 36.6 °C) refers to the just extruded PCL filament over the embedded SMA spring, proving that the temperature of the filament in contact with the SMA is less than its austenitic start temperature

After placing the SMA spring, the print was resumed and the PCL filament was extruded above to spring to completely embed it into the finger: as discussed before, it is crucial that the temperature of the extruded filament above the SMA is lower than A_s to avoid SMA activation. The PCL temperature above the SMA was measured by means of infrared thermal imaging: as shown in **Fig.4.8 b)**, as soon as the filament flows out from the nozzle, due to the interaction with the air its temperature abruptly decreases from 70 °C (printing temperature) to 36.6 °C: the temperature of the just extruded PCL bead over the SMA is 36.6°C, ensuring the preservation of the SMA martensite structure and avoiding any SMA activation.

In **Fig.4.9**, the manufacturing steps and the final finger are shown.

The total cost of the proposed finger, computed by the slicing software as a function of the amount of material employed during the manufacturing process, is 1.2 $, while the total printing time was 2h and 51 min, which needs to be increased of almost 10 min to embed the SMA using the CPPR and to change material (from PCL to TPU).

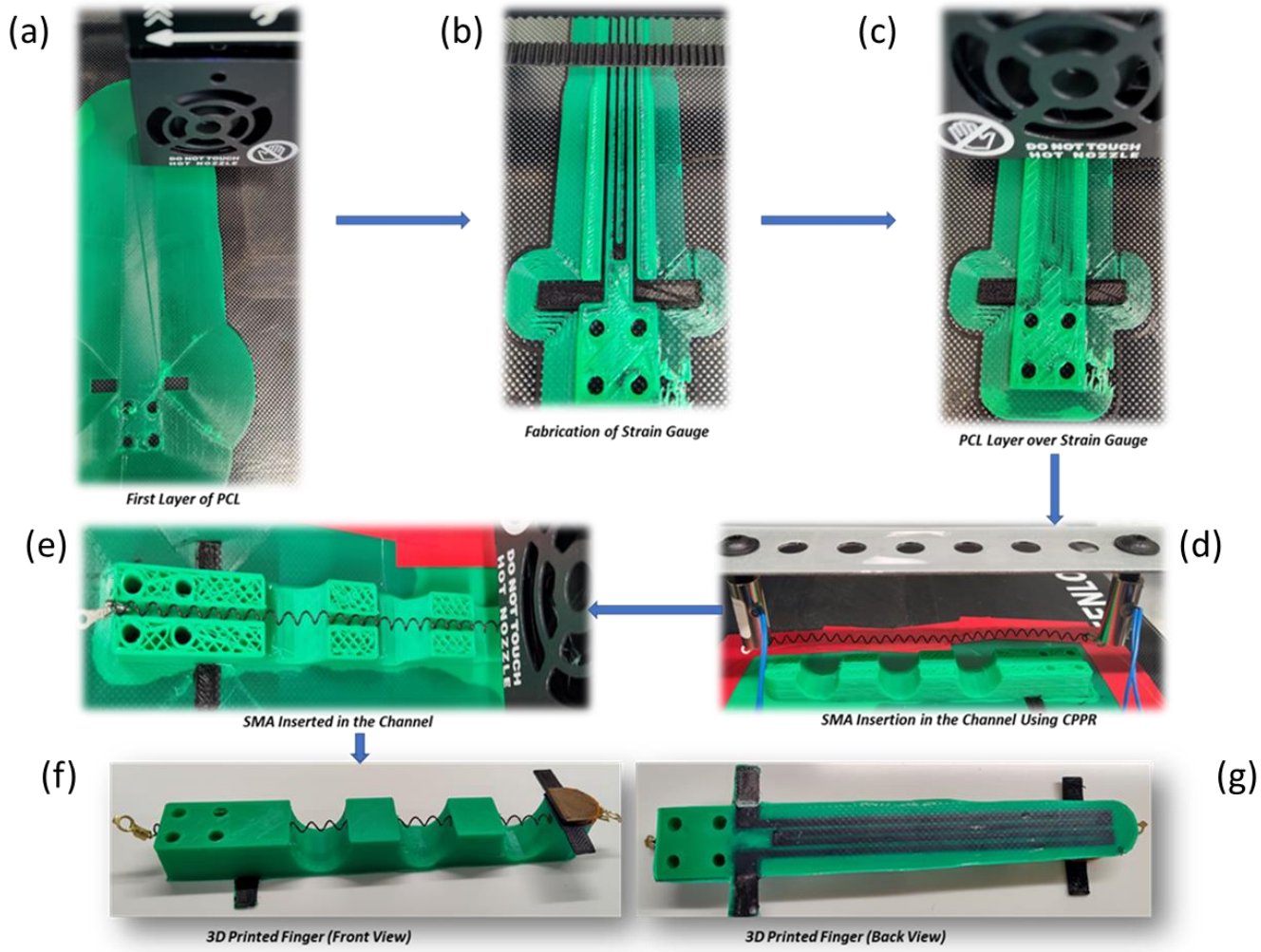

Fig. 4-9- Manufacturing process: a) first PCL layer, b) manufactured strain gauge, c) PCL coverage above the strain gauge, d) CPPR using electromagnets to insert the SMA into the channel, e) SMA into the channel, f) manufactured finger top view, and g) manufactured finger bottom view.

4.5 Characterization

The proposed finger has been characterized with several tests to evaluate: i) PCL material behavior in terms of hysteresis, ii) bending angle of the finger and its motion, iii) correlation among change in

resistance (embedded strain gauge) and bending angle, and iv) usage of the capacitive sensor as ON/OFF sensor when the finger touches objects.

For the characterization test, a custom-made setup shown in **Fig 4.10 a)** was used.

It consists of the following elements:

i) A custom-made bracket where the terminal block of the finger has been attached used screws, nuts, and bolts

ii) A digital camera (Canon EOS 70D) to take video, to calculate bending angle and joint position in the 2D space.

iii) Two digital multimeters, to take measurements of resistance and capacitance.

iv) A power supply (BK Precision 9116) to provide current input to the SMA in accordance with the desired frequency.

v) A custom-made circuit to calculate the voltage when current is provided to the SMA.

The following protocol was employed to characterize the finger: a current input of 3.2 A (chosen in accordance with the previous SMA characterization, section 4.2) was applied to the SMA for 2 s followed by a cooling time of 50 s (in that period a dead weight of 100g was applied to the finger to get it back at its rest position) for a total of 10 cycles.

Furthermore, two fingers were characterized: the one described so far (SMA spring completely embedded) and one more fabricated by embedding the SMA spring only into the two end parts (SMA partially embedded) shown in **Fig.4.10 b)**, to understand the best SMA spring position.

The bending angle and the position into the 2D space of each phalanx were measured as shown in **Fig.4.10 c).**

The results in terms of bending angle are shown in **Fig.10 d) and e)** for both versions of the finger: “SMA completely embedded” and “SMA partially embedded”, as well as the finger tracking into 2D space for the “SMA completely embedded”.

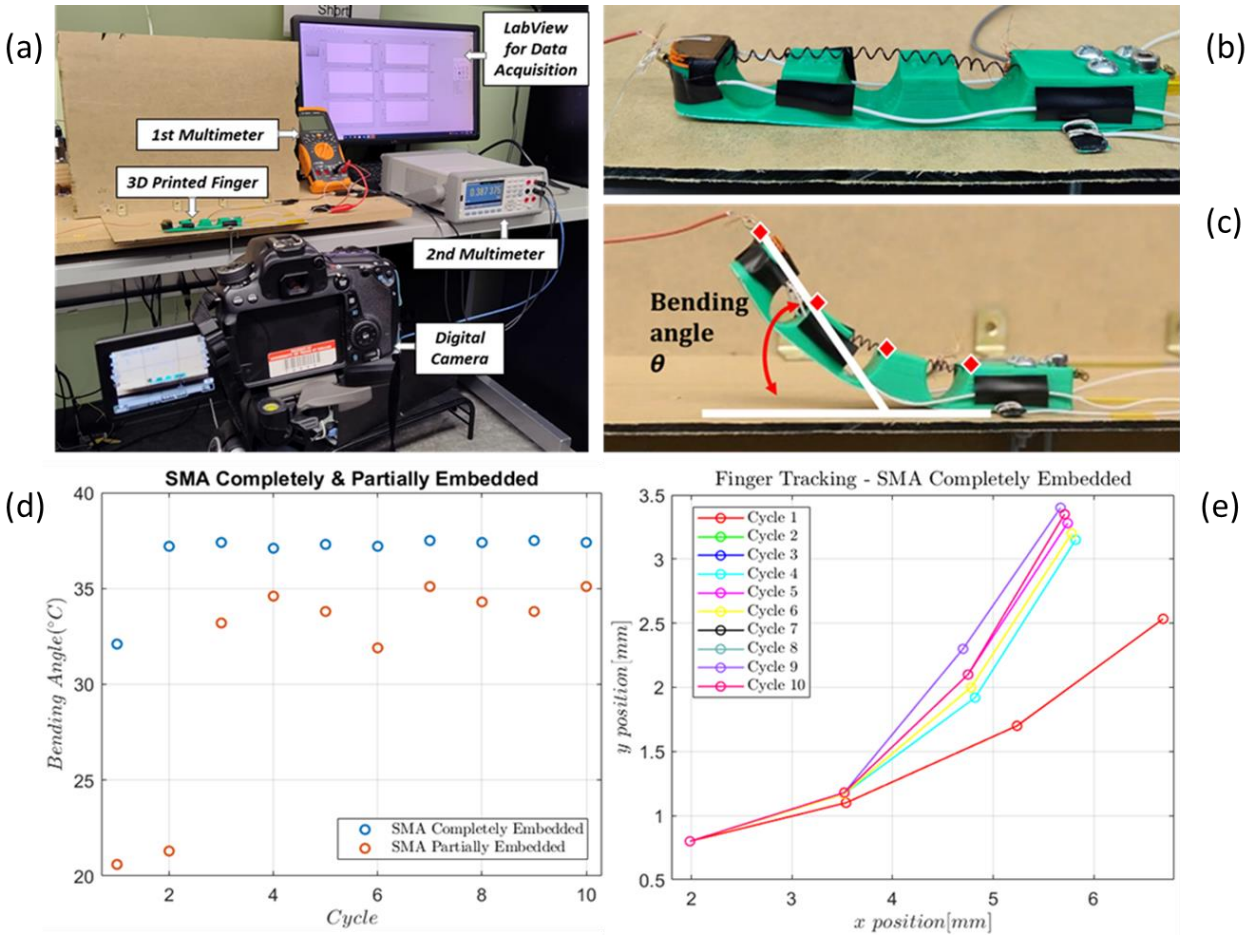

Fig. 4-10 a) Characterization setup for bending b) Finger with partially embedded SMA spring (embedded only into the two end parts) c) Bending angle and phalanx position in 2D space d) bending angle for both fingers version, e) finger tracking in 2D space for the finger with embedded SMA (several x- and y- position from cycle 2 to cycle 10 overlap each other)

The following considerations can be pointed out:

- For both configurations, the initial cycles (only cycle one for "SMA completely embedded" and cycle one and two for its counterpart) are characterized by a smaller bending angle, subsequentially the bending angle increases becoming constant in a certain range: for the "SMA completely embedded" the mean bending angle from cycle 2 to cycle 10 is 37.3° with a standard deviation of 0.13 °, for its counterpart the mean bending angle from cycle 3 to cycle 10 is 33.9 ° with a standard deviation of 0.99 °. The change in the bending angle from the first cycles to the last ones can be addressed to the Mullins effect, affecting thermoplastic materials.

- The "SMA completely embedded" version is better than its counterpart not only because the mean bending angle is 9.1 % higher but also because the standard deviation is less.

- From the finger tracking diagram, it stands out that the finger movement (the movement of each phalange) mimics very well the human finger motion, proving how the Mutlu et al [141] design rules are important to achieve this goal.

The change in bending angle has been correlated to the change of resistance provided by the embedded strain gauge: the measured data were fitted, obtaining the following linear regression equation:

$$y = 0.6748\,\alpha + 390.79 \tag{33}$$

With R^2 = 0.93

From equation (33), the sensitivity of the strain gauge is found to be 674.8 $\frac{Ohm}{°}$.

Fig.4.11 shows that for the first cycle the change in resistance is less, in accordance with a smaller bending angle, while from cycle 2 to cycle 10 the change in resistance is almost constant. Moreover, from cycle 5 up to cycle 10 the resting point is slightly higher than the one obtained for the previously cycles: this behavior is attributable to the PCL hysteresis, as a matter of fact from cycle 5 the finger does not get back in its original rest position (the bending angle between the bottom part of the finger and the support is 2,5° instead than 0°)

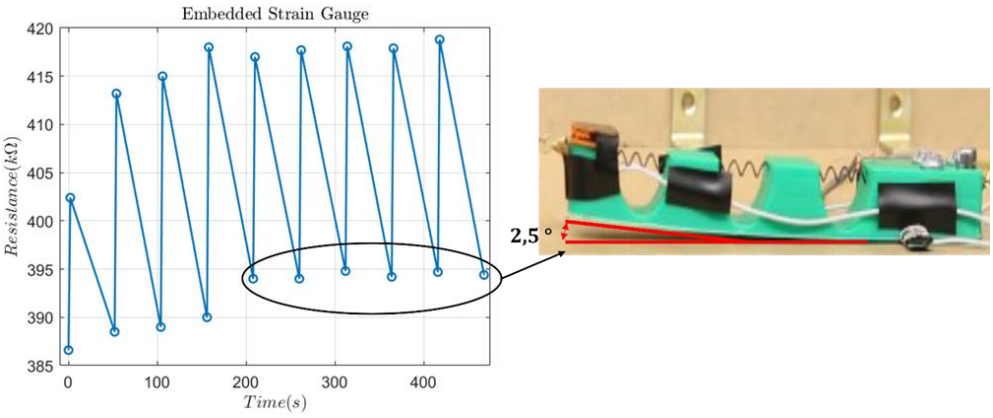

Fig. 4-11- Strain gauge characterization

The capacitive sensor (already characterized in section 4.3.2) having a sensitivity of 0.53 $\frac{pF}{N}$, has been used in conjunction with different objects (adhesive tape, calibrated weight, lollipop, glue, and coffee cup) placed randomly into the 3D space, mimicking a real scenario. As shown in **Fig.4.12** the capacitive sensor provides fast feedback as soon as it gets into contact with target objects, getting back to its initial capacitance value when the finger is no longer pushing against the object. The following result suggests that this kind of sensor can be used at least as ON/OFF sensor to provide

direct feedback about the presence/absence of objects: to achieve this aim, more characterization steps are required(for example a deep study about the interaction among the material surface of the object and the capacitive sensor). As shown in [189], the benefits due to the exploitation of force sensors over the soft finger tip are many and can potentially make these devices really appealing for the biomedical field.

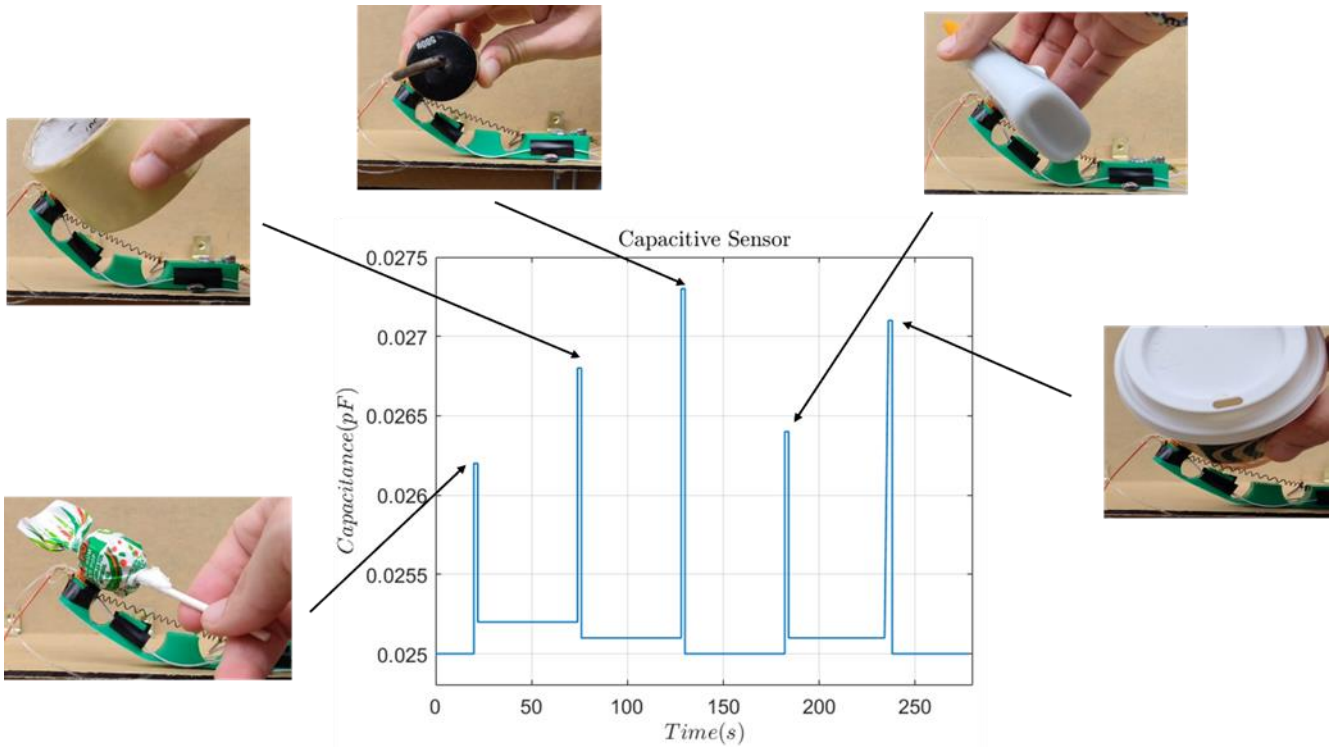

Fig. 4-12 -Capacitive sensor embedded into the finger in contact with different objects.

4.6 Conclusions

In this research, a new manufacturing approach to embedding actuators (SMA springs) into 3D printed structures has been presented: the main pillars of the proposed approach are: i) the usage of PCL material because its printing temperature is less than the austenitic start temperature of the embedded SMA, ii) the exploitation of the stop and go method to embed the SMA, and iii) the usage of a custom-made cartesian pick and place robot to reduce manual tasks and increases the placement accuracy. To take full advantage of the proposed manufactured method (based on material extrusion), a soft finger with 2 embedded 3D printed sensors (based on two different mechanisms: capacitive and piezoresistive) and an integrated SMA spring actuator was manufactured in a single shot fabrication cycle (for the first time, at the best of the author's knowledge). Furthermore, two process parameters were studied to reduce the strain gauge electrical resistance, which has been reduced by 142% compared to the worst parameters set, in order to reduce power losses during its usage. Several tests

were carried out to characterize each element of the proposed finger: i) the best current input for the activation of the SMA was found to be 3.2 A, ii) the capacitive sensor sensitivity was found to be 0.53 $\frac{pF}{N}$ and iii) the strain gauge sensitivity that was used to detect the finger bending angle, was 674.8 $\frac{Ohm}{^\circ}$. The proposed fabrication method paves the way for huge exploitation of the inexpensive FFF technology for the embedding of SMA, or other kinds of thermally activated actuators, like twisted coiled polymers (TCP), into complex FFF structures reducing human tasks and increasing placement accuracy. Moreover, several soft robots and gripper systems can be manufactured by embedding both sensing elements and actuators, resulting in assembly-free structures.

5. CHAPTER 5: DISCUSSION AND CONCLUSIONS

The aim of the present PhD thesis was to demonstrate that Material Extrusion (MEX) Additive Manufacturing (AM) technology is a suitable fabrication approach for the manufacturing of soft robots and sensor. Thanks to work done at the Interdisciplinary Additive Manufacturing (IAM) Lab, Politecnico di Bari, Italy and Humanoid Bio-Robotic and Smart materials (HBS) Lab, University of Texas at Dallas, USA, the goal of the thesis was achieved: several sensors, soft robots, and smart structures were 3D printed and characterize.

MEX technique, well known for being a low-cost technology, is very widespread both in the makers domain and research field: unique advantages can be obtained when a scientific/engineering approach is applied.

As shown in the present work, the main benefits that MEX technology can offer for the fabrication of soft robots are: i) reduction in cost and manufacturing time, ii) possibility to fabricate smart devices, iii) multi-material extrusion of stiff and soft material, iv) possibility to embed actuation systems during the fabrication, v) possibility to obtain assembly-free objects.

The usage of inexpensive commercial MEX machines allowed the development of complex solutions, such as bending actuators, stiff-soft robotic finger, capacitive and piezoresistive sensors and robotic fingers equipped with actuator and sensing units. Moreover, a low-cost custom-made machine based on the silicone-extrusion working principle was developed (250 $) to extrude material much softer than the one allowed from commercial FFF machines. It has also been shown that the usage of a cartesian pick and place robot, can increase the automation degree of the whole fabrication cycle: Shape memory alloys (SMA) spring actuators have been placed into 3D printed parts during the fabrication by taking advantage from the stop-and-go method.

Another achievement reported in the following work concerns the improvement in the multi-material adhesion when soft and stiff materials are jointly extruded: an increase of the 48% was achieved by studying several parameters (process parameters, post-processing and design parameters).

MEX-based machines are also easy to customize, generally two ways have been followed, in scientific literature: i) customization in order to monitor process parameters, and ii) customization to improve the fabrication performance. Both the approaches can bring many benefits for the fabrication of soft smart robots: new materials (i.e. magnetic materials) can be processed having the real-time full control of the process parameters.

In the author's opinion, MEX technology will be widely used over the next years for the fabrication of soft smart structures, from one hand soft robotics domain will take advantages from AM techniques

(assembly and manual tasks will be reduced), from the other hand AM will become more popular thanks to soft robotics and more widespread in industry environments for mass-production.

In conclusion, despite MEX technology has not reached a full level of maturity, it seems to be the perfect fit for the soft robotics domain: new advances in simulations, functionalized materials, stretchable electronics, and multi-extrusions machines will push MEX technology beyond the current limitations. The author envisions a bright future for Additive Manufacturing technologies (MEX technology, in particular) in the field of smart structure: when the benefits brought from soft robotics (over its counterpart) will become common knowledge, industries will extensively use Additive Manufacturing technologies, saving cost and time.

References

[1] E. Sheydaeian, O. O. Ibhadode, E. Hu, R. Pilliar, R. Kandel, and E. Toyserkani, "Additive manufacture of porous ceramic proximal interphalangeal (PIP) joint implant: design and process optimization," *Int. J. Adv. Manuf. Technol.*, vol. 115, no. 9–10, pp. 2825–2837, 2021, doi: 10.1007/s00170-021-07283-0.

[2] G. Stano and G. Percoco, "Additive manufacturing aimed to soft robots fabrication : A review," *Extrem. Mech. Lett.*, vol. 42, p. 101079, 2021, doi: 10.1016/j.eml.2020.101079.

[3] F. Schmitt, O. Piccin, L. Barbé, and B. Bayle, "Soft robots manufacturing: A review," *Front. Robot. AI*, vol. 5, no. JUN, 2018, doi: 10.3389/frobt.2018.00084.

[4] J. Z. Gul *et al.*, "3D printing for soft robotics–a review," *Sci. Technol. Adv. Mater.*, vol. 19, no. 1, pp. 243–262, 2018, doi: 10.1080/14686996.2018.1431862.

[5] T. J. Wallin, J. Pikul, and R. F. Shepherd, "3D printing of soft robotic systems," *Nat. Rev. Mater.*, vol. 3, no. June, 2018, doi: 10.1038/s41578-018-0002-2.

[6] Y. L. Yap, S. L. Sing, and W. Y. Yeong, "A review of 3D printing processes and materials for soft robotics," *Rapid Prototyp. J.*, vol. 26, no. 8, pp. 1345–1361, 2020, doi: 10.1108/RPJ-11-2019-0302.

[7] O. Byrne *et al.*, "Additive manufacture of composite soft pneumatic actuators," *Soft Robot.*, vol. 5, no. 6, pp. 726–736, 2018, doi: 10.1089/soro.2018.0030.

[8] D. J. Roach, C. M. Hamel, C. K. Dunn, M. V. Johnson, X. Kuang, and H. J. Qi, "The m4 3D printer: A multi-material multi-method additive manufacturing platform for future 3D printed structures," *Addit. Manuf.*, vol. 29, p. 100819, 2019, doi: 10.1016/j.addma.2019.100819.

[9] H. K. Yap, H. Y. Ng, and C. H. Yeow, "High-Force Soft Printable Pneumatics for Soft Robotic Applications," *Soft Robot.*, vol. 3, no. 3, pp. 144–158, 2016, doi: 10.1089/soro.2016.0030.

[10] D. W. Holmes *et al.*, "Mechanical behaviour of flexible 3D printed gyroid structures as a tuneable replacement for soft padding foam," *Addit. Manuf.*, vol. 50, no. November 2021, p. 102555, 2021, doi: 10.1016/j.addma.2021.102555.

[11] A. Hamidi and Y. Tadesse, "3D printing of very soft elastomer and sacrificial carbohydrate glass/elastomer structures for robotic applications," *Mater. Des.*, vol. 187, p. 108324, 2020, doi: 10.1016/j.matdes.2019.108324.

[12] O. D. Yirmibesoglu *et al.*, "Direct 3D printing of silicone elastomer soft robots and their performance comparison with molded counterparts," *2018 IEEE Int. Conf. Soft Robot. RoboSoft 2018*, pp. 295–302, 2018, doi: 10.1109/ROBOSOFT.2018.8404935.

[13] K. Lussenburg, A. Sakes, and P. Breedveld, "Design of non-assembly mechanisms: A state-of-the-art review," *Addit. Manuf.*, vol. 39, no. May 2020, 2021, doi: 10.1016/j.addma.2021.101846.

[14] J. Yin, C. Lu, J. Fu, Y. Huang, and Y. Zheng, "Interfacial bonding during multi-material fused deposition modeling (FDM) process due to inter-molecular diffusion," *Mater. Des.*, vol. 150, pp. 104–112, 2018, doi: 10.1016/j.matdes.2018.04.029.

[15] K. Kim, J. Park, J. hoon Suh, M. Kim, Y. Jeong, and I. Park, "3D printing of multiaxial force sensors using carbon nanotube (CNT)/thermoplastic polyurethane (TPU) filaments," *Sensors Actuators, A Phys.*, vol. 263, pp. 493–500, 2017, doi: 10.1016/j.sna.2017.07.020.

[16] L. Y. W. Loh, U. Gupta, Y. Wang, C. C. Foo, J. Zhu, and W. F. Lu, "3D Printed Metamaterial Capacitive Sensing Array for Universal Jamming Gripper and Human Joint Wearables," *Adv. Eng. Mater.*, vol. 2001082, pp. 1–9, 2021, doi: 10.1002/adem.202001082.

[17] M. Schouten, G. Wolterink, A. Dijkshoorn, D. Kosmas, S. Stramigioli, and G. Krijnen, "A Review of Extrusion-Based 3D Printing for the Fabrication of Electro- A nd Biomechanical Sensors," *IEEE Sens. J.*, vol. 21, no. 11, pp. 12900–12912, 2021, doi: 10.1109/JSEN.2020.3042436.

[18] A. Maurel, M. Haukka, E. Macdonald, L. Kivijärvi, E. Lahtinen, and H. Kim, "Version of Record : https://www.sciencedirect.com/science/article/pii/S221486042031023X Considering Lithium-ion Battery 3D-printing via Thermoplastic Material Extrusion and Polymer Powder Bed Fusion © 2020 published by Elsevier . This manuscript is made a."

[19] L. Feng, N. Xie, and J. Zhong, "Carbon nanofibers and their composites: A review of synthesizing, properties and applications," *Materials (Basel).*, vol. 7, no. 5, pp. 3919–3945, 2014, doi: 10.3390/ma7053919.

[20] S. J. Leigh, R. J. Bradley, C. P. Purssell, D. R. Billson, and D. A. Hutchins, "A Simple, Low-Cost Conductive Composite Material for 3D Printing of Electronic Sensors," *PLoS One*, vol. 7, no. 11, pp. 1–6, 2012, doi: 10.1371/journal.pone.0049365.

[21] J. F. Christ, N. Aliheidari, A. Ameli, and P. Pötschke, "3D printed highly elastic strain sensors of multiwalled carbon nanotube/thermoplastic polyurethane nanocomposites," *Mater. Des.*, vol. 131, pp. 394–401, 2017, doi: 10.1016/j.matdes.2017.06.011.

[22] H. K. Sezer and O. Eren, "FDM 3D printing of MWCNT re-inforced ABS nano-composite parts with enhanced mechanical and electrical properties," *J. Manuf. Process.*, vol. 37, no. December 2017, pp. 339–347, 2019, doi: 10.1016/j.jmapro.2018.12.004.

[23] G. Stano, A. Di Nisio, A. Lanzolla, and G. Percoco, "Additive manufacturing and characterization of a load cell with embedded strain gauges," *Precis. Eng.*, vol. 62, no. June 2019, pp. 113–120, 2020, doi: 10.1016/j.precisioneng.2019.11.019.

[24] K. Kim, J. Park, J. hoon Suh, M. Kim, Y. Jeong, and I. Park, "3D printing of multiaxial force sensors using carbon nanotube (CNT)/thermoplastic polyurethane (TPU) filaments," *Sensors Actuators, A Phys.*, vol. 263, pp. 493–500, 2017, doi: 10.1016/j.sna.2017.07.020.

[25] A. Georgopoulou, L. Egloff, B. Vanderborght, and F. Clemens, "A Sensorized Soft Pneumatic Actuator Fabricated with Extrusion-Based Additive Manufacturing," *Actuators*, vol. 10, no. 5, p. 102, 2021, doi: 10.3390/act10050102.

[26] D. Xiang *et al.*, "3D-Printed Flexible Piezoresistive Sensors for Stretching and Out-of-Plane Forces," *Macromol. Mater. Eng.*, vol. 306, no. 11, pp. 1–10, 2021, doi: 10.1002/mame.202100437.

[27] B. Li, W. Liang, L. Zhang, F. Ren, and F. Xuan, "TPU/CNTs flexible strain sensor with auxetic structure via a novel hybrid manufacturing process of fused deposition modeling 3D printing and ultrasonic cavitation-enabled treatment," *Sensors Actuators A Phys.*, vol. 340, no. February, p. 113526, 2022, doi: 10.1016/j.sna.2022.113526.

[28] M. Palmieri, J. Slavič, and F. Cianetti, "Single-process 3D-printed structures with vibration durability self-awareness," *Addit. Manuf.*, vol. 47, no. May, p. 102303, 2021, doi: 10.1016/j.addma.2021.102303.

[29] H. G. Kim, S. Hajra, D. Oh, N. Kim, and H. J. Kim, "Additive manufacturing of high-performance carbon-composites: An integrated multi-axis pressure and temperature

monitoring sensor," *Compos. Part B Eng.*, vol. 222, no. April, p. 109079, 2021, doi: 10.1016/j.compositesb.2021.109079.

[30] M. Alsharari, B. Chen, and W. Shu, "Sacrificial 3D Printing of Highly Porous, Soft Pressure Sensors," *Adv. Electron. Mater.*, vol. 8, no. 1, pp. 1–12, 2022, doi: 10.1002/aelm.202100597.

[31] D. Singh, C. Tawk, R. Mutlu, E. Sariyildiz, V. Sencadas, and G. Alici, "A 3D Printed Soft Force Sensor for Soft Haptics," *2020 3rd IEEE Int. Conf. Soft Robot. RoboSoft 2020*, pp. 458–463, 2020, doi: 10.1109/RoboSoft48309.2020.9115991.

[32] G. Stano, A. Di Nisio, A. M. Lanzolla, M. Ragolia, and G. Percoco, "Fused filament fabrication of commercial conductive filaments: experimental study on the process parameters aimed at the minimization, repeatability and thermal characterization of electrical resistance," *Int. J. Adv. Manuf. Technol.*, pp. 2971–2986, 2020, doi: 10.1007/s00170-020-06318-2.

[33] F. Daniel, N. H. Patoary, A. L. Moore, L. Weiss, and A. D. Radadia, "Temperature-dependent electrical resistance of conductive polylactic acid filament for fused deposition modeling," *Int. J. Adv. Manuf. Technol.*, vol. 99, no. 5–8, pp. 1215–1224, Nov. 2018, doi: 10.1007/s00170-018-2490-z.

[34] T. B. Palmić, J. Slavič, and M. Boltežar, "Process parameters for fff 3d-printed conductors for applications in sensors," *Sensors (Switzerland)*, vol. 20, no. 16, pp. 1–21, 2020, doi: 10.3390/s20164542.

[35] J. A. Cardenas *et al.*, "Flash ablation metallization of conductive thermoplastics," *Addit. Manuf.*, vol. 36, no. March, p. 101409, 2020, doi: 10.1016/j.addma.2020.101409.

[36] N. Lazarus, J. B. Tyler, J. A. Cardenas, B. Hanrahan, H. Tsang, and S. S. Bedair, "Direct electroless plating of conductive thermoplastics for selective metallization of 3D printed parts," *Addit. Manuf.*, vol. 55, no. February, p. 102793, 2022, doi: 10.1016/j.addma.2022.102793.

[37] C. C. Santiago *et al.*, "Erratum: 3D Printed Elastomeric Lattices with Embedded Deformation Sensing (IEEE Access (2020) 8 (41394-41402) DOI:10.1109/ACCESS.2020.2973664)," *IEEE Access*, vol. 8, p. 87184, 2020, doi: 10.1109/ACCESS.2020.2991896.

[38] M. Schouten, R. Sanders, and G. Krijnen, "3D printed flexible capacitive force sensor with a simple micro-controller based readout," *Proc. IEEE Sensors*, vol. 2017-Decem, no. 3, pp. 1–3, 2017, doi: 10.1109/ICSENS.2017.8233949.

[39] O. Ozioko, H. Nassar, and R. Dahiya, "3D Printed Interdigitated Capacitor Based Tilt Sensor," *IEEE Sens. J.*, vol. 21, no. 23, pp. 26252–26260, 2021, doi: 10.1109/JSEN.2021.3058949.

[40] M. A. Ragolia, A. M. L. Lanzolla, G. Percoco, G. Stano, and A. Di Nisio, "Thermal characterization of new 3d-printed bendable, coplanar capacitive sensors," *Sensors*, vol. 21, no. 19, 2021, doi: 10.3390/s21196324.

[41] M. Arh, J. Slavič, and M. Boltežar, "Design principles for a single-process 3d-printed accelerometer – theory and experiment," *Mech. Syst. Signal Process.*, vol. 152, 2021, doi: 10.1016/j.ymssp.2020.107475.

[42] M. Arh, J. Slavič, and M. Boltežar, "Experimental identification of the dynamic piezoresistivity of fused-filament-fabricated structures," *Addit. Manuf.*, vol. 36, no. April, p. 101493, 2020, doi: 10.1016/j.addma.2020.101493.

[43] M. Maurizi *et al.*, "Dynamic measurements using FDM 3D-printed embedded strain sensors," *Sensors (Switzerland)*, vol. 19, no. 12, pp. 1–15, 2019, doi: 10.3390/s19122661.

[44] A. Dijkshoorn, M. Schouten, S. Stramigioli, and G. Krijnen, “Modelling of anisotropic electrical conduction in layered structures 3d-printed with fused deposition modelling,” *Sensors*, vol. 21, no. 11, pp. 1–37, 2021, doi: 10.3390/s21113710.

[45] T. Pretsch, “Review on the functional determinants and durability of shape memory polymers,” *Polymers (Basel).*, vol. 2, no. 3, pp. 120–158, 2010, doi: 10.3390/polym2030120.

[46] A. Mitchell, U. Lafont, M. Hołyńska, and C. Semprimoschnig, “Additive manufacturing — A review of 4D printing and future applications,” *Addit. Manuf.*, vol. 24, pp. 606–626, 2018, doi: 10.1016/j.addma.2018.10.038.

[47] H. N. Norton, *Handbook of transducers*. Englewood Cliffs, NJ, USA: Prentice Hall, 1989.

[48] F. C. S. Luz, S. A. Pianaro, C. E. Yurk, G. Capobianco, A. J. Zara, and S. M. Tebcherani, “Construction and testing of a system for the electrical characterization of ceramic thermistors at low temperatures,” *Ceramica*, vol. 60, no. 353, pp. 96–101, 2014, doi: 10.1590/S0366-69132014000100014.

[49] A. Király and F. Ronkay, “Temperature dependence of electrical properties in conductive polymer composites,” *Polym. Test.*, vol. 43, pp. 154–162, May 2015, doi: 10.1016/j.polymertesting.2015.03.011.

[50] R. Zhang, Y. Bin, R. Chen, and M. Matsuo, “Evaluation by tunneling effect for the temperature-dependent electric conductivity of polymer-carbon fiber composites with visco-elastic properties,” *Polym. J.*, vol. 45, no. 11, pp. 1120–1134, Nov. 2013, doi: 10.1038/pj.2013.40.

[51] R. Zhang, A. Dowden, H. Deng, M. Baxendale, and T. Peijs, “Conductive network formation in the melt of carbon nanotube/thermoplastic polyurethane composite,” *Compos. Sci. Technol.*, vol. 69, no. 10, pp. 1499–1504, Aug. 2009, doi: 10.1016/j.compscitech.2008.11.039.

[52] M. Mohiuddin and S. V. Hoa, “Temperature dependent electrical conductivity of CNT-PEEK composites,” *Compos. Sci. Technol.*, vol. 72, no. 1, pp. 21–27, Dec. 2011, doi: 10.1016/j.compscitech.2011.08.018.

[53] F. Tamburrino, S. Graziosi, and M. Bordegoni, “The influence of slicing parameters on the multi-material adhesion mechanisms of FDM printed parts: an exploratory study,” *Virtual Phys. Prototyp.*, vol. 2759, 2019, doi: 10.1080/17452759.2019.1607758.

[54] Yang, “Inkjet-printed capacitive sensor for water level or quality monitoring theoretically and experimentally,” *Mater. Chem. A*, 2017, doi: 10.1039/C7TA05094A.

[55] G. Percoco, L. Arleo, G. Stano, and F. Bottiglione, “Analytical model to predict the extrusion force as a function of the layer height , in extrusion based 3D printing,” *Addit. Manuf.*, vol. 38, no. December 2020, p. 101791, 2021, doi: 10.1016/j.addma.2020.101791.

[56] A. Bellini, S. Güçeri, and M. Bertoldi, “Liquefier dynamics in fused deposition,” *J. Manuf. Sci. Eng. Trans. ASME*, vol. 126, no. 2, pp. 237–246, 2004, doi: 10.1115/1.1688377.

[57] J. Chen and D. E. Smith, “Filament rheological characterization for fused filament fabrication additive manufacturing: A low-cost approach,” *Addit. Manuf.*, vol. 47, no. March, p. 102208, 2021, doi: 10.1016/j.addma.2021.102208.

[58] A. Dey and N. Yodo, “A Systematic Survey of FDM Process Parameter Optimization and Their Influence on Part Characteristics,” *J. Manuf. Mater. Process.*, vol. 3, no. 3, p. 64, 2019, doi: 10.3390/jmmp3030064.

[59] L. E. Helseth, “Nano Energy Interdigitated electrodes based on liquid metal encapsulated in

elastomer as capacitive sensors and triboelectric nanogenerators," *Nano Energy*, vol. 50, no. April, pp. 266–272, 2018, doi: 10.1016/j.nanoen.2018.05.047.

[60] K. Chetpattananondh, T. Tapoanoi, P. Phukpattaranont, and N. Jindapetch, "Sensors and Actuators A : Physical A self-calibration water level measurement using an interdigital capacitive sensor," *Sensors Actuators A. Phys.*, vol. 209, pp. 175–182, 2014, doi: 10.1016/j.sna.2014.01.040.

[61] D. Paczesny, G. Tarapata, and R. Jachowicz, "The capacitive sensor for liquid level measurement made with ink-jet printing technology," vol. 120, pp. 731–735, 2015, doi: 10.1016/j.proeng.2015.08.776.

[62] Y. Ansari, T. Hassan, M. Manti, E. Falotico, M. Cianchetti, and C. Laschi, *Soft Robotic Technologies for Industrial Applications*, no. March 2019. 2019.

[63] G. ALICI, "Softer is Harder: What Differentiates Soft Robotics from Hard Robotics?," *MRS Adv.*, vol. 3, no. 28, pp. 1557–1568, Feb. 2018, doi: 10.1557/adv.2018.159.

[64] C. Majidi, "Soft-Matter Engineering for Soft Robotics," *Adv. Mater. Technol.*, vol. 4, no. 2, pp. 1–13, 2019, doi: 10.1002/admt.201800477.

[65] K. Chubb, D. Berry, and T. Burke, "Towards an ontology for soft robots: What is soft?," *Bioinspiration and Biomimetics*, vol. 14, no. 6, 2019, doi: 10.1088/1748-3190/ab483f.

[66] D. Rus and M. T. Tolley, "Design, fabrication and control of soft robots," *Nature*, vol. 521, no. 7553, pp. 467–475, 2015, doi: 10.1038/nature14543.

[67] C. Majidi, "Soft Robotics: A Perspective - Current Trends and Prospects for the Future," *Soft Robot.*, vol. 1, no. 1, pp. 5–11, 2014, doi: 10.1089/soro.2013.0001.

[68] N. Elango and A. A. M. Faudzi, "A review article: Investigations on soft materials for soft robot manipulations," *Int. J. Adv. Manuf. Technol.*, vol. 80, no. 5–8, pp. 1027–1037, 2015, doi: 10.1007/s00170-015-7085-3.

[69] S. Coyle, C. Majidi, P. LeDuc, and K. J. Hsia, "Bio-inspired soft robotics: Material selection, actuation, and design," *Extrem. Mech. Lett.*, vol. 22, pp. 51–59, 2018, doi: 10.1016/j.eml.2018.05.003.

[70] J. C. Case, E. L. White, and R. K. Kramer, "Soft material characterization for robotic applications," *Soft Robot.*, vol. 2, no. 2, pp. 80–87, 2015, doi: 10.1089/soro.2015.0002.

[71] C. Appiah, C. Arndt, K. Siemsen, A. Heitmann, A. Staubitz, and C. Selhuber-Unkel, "Living Materials Herald a New Era in Soft Robotics," *Adv. Mater.*, vol. 31, no. 36, 2019, doi: 10.1002/adma.201807747.

[72] C. Laschi, B. Mazzolai, and M. Cianchetti, "Soft robotics: Technologies and systems pushing the boundaries of robot abilities," *Sci. Robot.*, vol. 1, no. 1, pp. 1–12, 2016, doi: 10.1126/scirobotics.aah3690.

[73] S. Kim, C. Laschi, and B. Trimmer, "Soft robotics: A bioinspired evolution in robotics," *Trends Biotechnol.*, vol. 31, no. 5, pp. 287–294, 2013, doi: 10.1016/j.tibtech.2013.03.002.

[74] C. Laschi, M. Cianchetti, B. Mazzolai, L. Margheri, M. Follador, and P. Dario, "Soft robot arm inspired by the octopus," *Adv. Robot.*, vol. 26, no. 7, pp. 709–727, 2012, doi: 10.1163/156855312X626343.

[75] M. Calisti *et al.*, "An octopus-bioinspired solution to movement and manipulation for soft robots," *Bioinspiration and Biomimetics*, vol. 6, no. 3, 2011, doi: 10.1088/1748-

3182/6/3/036002.

[76] T. Sun, Y. Chen, T. Han, C. Jiao, B. Lian, and Y. Song, “A soft gripper with variable stiffness inspired by pangolin scales, toothed pneumatic actuator and autonomous controller,” *Robot. Comput. Integr. Manuf.*, vol. 61, no. May 2019, 2020, doi: 10.1016/j.rcim.2019.101848.

[77] J. Shintake, V. Cacucciolo, H. Shea, and D. Floreano, “Soft biomimetic fish robot made of dielectric elastomer actuators,” *Soft Robot.*, vol. 5, no. 4, pp. 466–474, 2018, doi: 10.1089/soro.2017.0062.

[78] H. T. Lin, G. G. Leisk, and B. Trimmer, “GoQBot: A caterpillar-inspired soft-bodied rolling robot,” *Bioinspiration and Biomimetics*, vol. 6, no. 2, 2011, doi: 10.1088/1748-3182/6/2/026007.

[79] E. Siéfert, E. Reyssat, J. Bico, and B. Roman, “Bio-inspired pneumatic shape-morphing elastomers,” *Nat. Mater.*, vol. 18, no. 1, pp. 24–28, 2019, doi: 10.1038/s41563-018-0219-x.

[80] A. Das and M. Nabi, “A review on Soft Robotics: Modeling, Control and Applications in Human-Robot interaction,” pp. 306–311, 2020, doi: 10.1109/icccis48478.2019.8974461.

[81] M. Calisti, G. Picardi, and C. Laschi, “Fundamentals of soft robot locomotion,” *J. R. Soc. Interface*, vol. 14, no. 130, pp. 0–2, 2017, doi: 10.1098/rsif.2017.0101.

[82] M. Cianchetti, C. Laschi, A. Menciassi, and P. Dario, “Biomedical applications of soft robotics,” *Nat. Rev. Mater.*, vol. 3, no. 6, pp. 143–153, 2018, doi: 10.1038/s41578-018-0022-y.

[83] M. W. Gifari, H. Naghibi, and S. Stramigioli, “A review on recent advances in soft surgical robots for endoscopic applications,” no. April, pp. 1–11, 2019, doi: 10.1002/rcs.2010.

[84] M. Runciman, A. Darzi, and G. P. Mylonas, “Soft Robotics in Minimally Invasive Surgery 1,” vol. 6, no. 4, 2019, doi: 10.1089/soro.2018.0136.

[85] G. Andria, F. Attivissimo, A. Di Nisio, A. Maria, and L. Lanzolla, “Assessment of Position Repeatability Error in an Surgical Navigation,” 2020.

[86] G. Andria, F. Attivissimo, A. Di Nisio, A. M. L. Lanzolla, P. Larizza, and S. Selicato, “Development and performance evaluation of an electromagnetic tracking system for surgery navigation,” *Meas. J. Int. Meas. Confed.*, vol. 148, p. 106916, 2019, doi: 10.1016/j.measurement.2019.106916.

[87] W. Hu, G. Z. Lum, M. Mastrangeli, and M. Sitti, “Small-scale soft-bodied robot with multimodal locomotion,” *Nat. Publ. Gr.*, vol. 554, no. 7690, pp. 81–85, 2018, doi: 10.1038/nature25443.

[88] E. B. Joyee and Y. Pan, “Additive manufacturing of multi-material soft robot for on-demand drug delivery applications,” *J. Manuf. Process.*, vol. 56, no. January, pp. 1178–1184, 2020, doi: 10.1016/j.jmapro.2020.03.059.

[89] P. Polygerinos, Z. Wang, K. C. Galloway, R. J. Wood, and C. J. Walsh, “Soft robotic glove for combined assistance and at-home rehabilitation,” *Rob. Auton. Syst.*, vol. 73, pp. 135–143, 2015, doi: 10.1016/j.robot.2014.08.014.

[90] C. M. Thalman, J. Hsu, L. Snyder, and P. Polygerinos, “Design of a soft ankle-foot orthosis exosuit for foot drop assistance,” *Proc. - IEEE Int. Conf. Robot. Autom.*, vol. 2019-May, pp. 8436–8442, 2019, doi: 10.1109/ICRA.2019.8794005.

[91] S. Sridar, Z. Qiao, N. Muthukrishnan, W. Zhang, and P. Polygerinos, “A soft-inflatable exosuit

for knee rehabilitation: Assisting swing phase during walking," *Front. Robot. AI*, vol. 5, no. MAY, pp. 1–9, 2018, doi: 10.3389/frobt.2018.00044.

[92] P. H. Nguyen, S. Sridar, S. Amatya, C. M. Thalman, and P. Polygerinos, "Fabric-based soft grippers capable of selective distributed bending for assistance of daily living tasks," *RoboSoft 2019 - 2019 IEEE Int. Conf. Soft Robot.*, pp. 404–409, 2019, doi: 10.1109/ROBOSOFT.2019.8722758.

[93] Y. Ansari, M. Manti, E. Falotico, Y. Mollard, M. Cianchetti, and C. Laschi, "Towards the development of a soft manipulator as an assistive robot for personal care of elderly people," *Int. J. Adv. Robot. Syst.*, vol. 14, p. 172988141668713, Apr. 2017, doi: 10.1177/1729881416687132.

[94] M. Manti, A. Pratesi, E. Falotico, M. Cianchetti, and C. Laschi, "Soft assistive robot for personal care of elderly people," in *2016 6th IEEE International Conference on Biomedical Robotics and Biomechatronics (BioRob)*, 2016, pp. 833–838, doi: 10.1109/BIOROB.2016.7523731.

[95] J. Shintake, V. Cacucciolo, D. Floreano, and H. Shea, "Soft Robotic Grippers," no. May, 2018, doi: 10.1002/adma.201707035.

[96] J. H. Youn *et al.*, "Dielectric elastomer actuator for soft robotics applications and challenges," *Appl. Sci.*, vol. 10, no. 2, 2020, doi: 10.3390/app10020640.

[97] S. I. Rich, R. J. Wood, and C. Majidi, "Untethered soft robotics," *Nat. Electron.*, vol. 1, no. 2, pp. 102–112, 2018, doi: 10.1038/s41928-018-0024-1.

[98] O. A. Araromi *et al.*, "Rollable multisegment dielectric elastomer minimum energy structures for a deployable microsatellite gripper," *IEEE/ASME Trans. Mechatronics*, vol. 20, no. 1, pp. 438–446, 2015, doi: 10.1109/TMECH.2014.2329367.

[99] Y. Tang, L. Qin, X. Li, C. M. Chew, and J. Zhu, "A frog-inspired swimming robot based on dielectric elastomer actuators," *IEEE Int. Conf. Intell. Robot. Syst.*, vol. 2017-Septe, pp. 2403–2408, 2017, doi: 10.1109/IROS.2017.8206054.

[100] R. Lumia and M. Shahinpoor, "IPMC microgripper research and development," *J. Phys. Conf. Ser.*, vol. 127, pp. 0–15, 2008, doi: 10.1088/1742-6596/127/1/012002.

[101] J. W. Sohn, G. W. Kim, and S. B. Choi, "A state-of-the-art review on robots and medical devices using smart fluids and shape memory alloys," *Appl. Sci.*, vol. 8, no. 10, 2018, doi: 10.3390/app8101928.

[102] M. Manti, V. Cacucciolo, and M. Cianchetti, "Stiffening in soft robotics: A review of the state of the art," *IEEE Robot. Autom. Mag.*, vol. 23, no. 3, pp. 93–106, 2016, doi: 10.1109/MRA.2016.2582718.

[103] J. Kim, S. E. Chung, S. Choi, H. Lee, J. Kim, and S. Kwon, "Programming magnetic anisotropy in polymeric microactuators," *Nat. Mater.*, vol. 10, no. 10, pp. 747–752, 2011, doi: 10.1038/nmat3090.

[104] Y. Kim, H. Yuk, R. Zhao, S. A. Chester, and X. Zhao, "Printing ferromagnetic domains for untethered fast-transforming soft materials," *Letters*, vol. https://do, 2018.

[105] Y. Kim, G. A. Parada, S. Liu, and X. Zhao, "Ferromagnetic soft continuum robots," vol. 7329, no. August, pp. 1–16, 2019.

[106] J. Kim, J. W. Kim, H. C. Kim, L. Zhai, H. U. Ko, and R. M. Muthoka, "Review of Soft Actuator Materials," *Int. J. Precis. Eng. Manuf.*, vol. 20, no. 12, pp. 2221–2241, 2019, doi:

10.1007/s12541-019-00255-1.

[107] Y. Yang, Y. Wu, C. Li, X. Yang, and W. Chen, “Flexible Actuators for Soft Robotics,” *Adv. Intell. Syst.*, vol. 2, no. 1, p. 1900077, 2020, doi: 10.1002/aisy.201900077.

[108] Y. Hao *et al.*, “A variable stiffness soft robotic gripper with low-melting-point alloy,” *Chinese Control Conf. CCC*, pp. 6781–6786, 2017, doi: 10.23919/ChiCC.2017.8028427.

[109] B. E. Schubert and D. Floreano, “Variable stiffness material based on rigid low-melting-point-alloy microstructures embedded in soft poly(dimethylsiloxane) (PDMS),” *RSC Adv.*, vol. 3, no. 46, pp. 24671–24679, 2013, doi: 10.1039/c3ra44412k.

[110] M. G. D. A. P. H. J. S. M. Pilz da Cunha, “Bioinspired light-driven soft robots based onliquid crystal polymers,” *Chem Soc Rev*, pp. 6568–6578, 2020, doi: 10.1039/d0cs00363h.

[111] H. Zeng, P. Wasylczyk, D. S. Wiersma, and A. Priimagi, “Light Robots : Bridging the Gap between Microrobotics and Photomechanics in Soft Materials,” vol. 1703554, pp. 1–9, 2018, doi: 10.1002/adma.201703554.

[112] H. Zeng, O. M. Wani, P. Wasylczyk, and A. Priimagi, “Light-Driven , Caterpillar-Inspired Miniature Inching Robot,” vol. 1700224, pp. 1–6, 2018, doi: 10.1002/marc.201700224.

[113] E. Acome *et al.*, “Hydraulically amplified self-healing electrostatic actuators with muscle-like performance,” vol. 65, no. January, pp. 61–65, 2018.

[114] N. Kellaris, V. G. Venkata, G. M. Smith, S. K. Mitchell, and C. Keplinger, “Peano-HASEL actuators : Muscle-mimetic , electrohydraulic transducers that linearly contract on activation,” vol. 3276, no. January, pp. 1–11, 2018.

[115] J. A. Liu, J. H. Gillen, S. R. Mishra, B. A. Evans, and J. B. Tracy, “Photothermally and magnetically controlled reconfiguration of polymer composites for soft robotics,” no. August, 2019.

[116] B. Mosadegh *et al.*, “Pneumatic networks for soft robotics that actuate rapidly,” *Adv. Funct. Mater.*, vol. 24, no. 15, pp. 2163–2170, 2014, doi: 10.1002/adfm.201303288.

[117] M. Behl, K. Kratz, J. Zotzmann, U. Nöchel, and A. Lendlein, “Reversible bidirectional shape-memory polymers,” *Adv. Mater.*, vol. 25, no. 32, pp. 4466–4469, 2013, doi: 10.1002/adma.201300880.

[118] W. Hu, R. Mutlu, W. Li, and G. Alici, “A structural optimisation method for a soft pneumatic actuator,” *Robotics*, vol. 7, no. 2, pp. 1–16, 2018, doi: 10.3390/robotics7020024.

[119] E. Luis *et al.*, “Silicone 3D Printing: Process Optimization, Product Biocompatibility, and Reliability of Silicone Meniscus Implants,” *3D Print. Addit. Manuf.*, vol. 6, no. 6, pp. 319–332, 2019, doi: 10.1089/3dp.2018.0226.

[120] A. Colpani, A. Fiorentino, and E. Ceretti, “Equipment for additive manufacturing of biocompatible silicone,” *AIP Conf. Proc.*, vol. 2113, no. July, 2019, doi: 10.1063/1.5112679.

[121] J. Khodaii and A. Rahimi, “Improving the surface roughness in stereolithography by controlling surface angle, hatch spaces, and postcuring time,” *Eng. Reports*, vol. 2, no. 6, pp. 1–16, 2020, doi: 10.1002/eng2.12193.

[122] A. Colpani, A. Fiorentino, and E. Ceretti, “Feasibility analysis and characterization of an extrusion-based AM process for a two-component and biocompatible silicone,” *J. Manuf. Process.*, vol. 49, no. April 2019, pp. 116–125, 2020, doi: 10.1016/j.jmapro.2019.11.017.

[123] J. Plott, X. Tian, and A. J. Shih, “Voids and tensile properties in extrusion-based additive manufacturing of moisture-cured silicone elastomer,” *Addit. Manuf.*, vol. 22, no. June, pp. 606–617, 2018, doi: 10.1016/j.addma.2018.06.010.

[124] A. Miriyev, B. Xia, J. C. Joseph, and H. Lipson, “Additive Manufacturing of Silicone Composites for Soft Actuation,” *3D Print. Addit. Manuf.*, vol. 6, no. 6, pp. 309–318, 2019, doi: 10.1089/3dp.2019.0116.

[125] S. Walker *et al.*, “Predicting Interfacial Layer Adhesion Strength in 3D Printable Silicone,” *Addit. Manuf.*, p. 102320, 2021, doi: 10.1016/j.addma.2021.102320.

[126] J. Plott, X. Tian, and A. Shih, “Measurement and Modeling of Forces in Extrusion-Based Additive Manufacturing of Flexible Silicone Elastomer with Thin Wall Structures,” *J. Manuf. Sci. Eng. Trans. ASME*, vol. 140, no. 9, pp. 1–11, 2018, doi: 10.1115/1.4040350.

[127] F. Ahmed *et al.*, “Decade of bio-inspired soft robots: A review,” *Smart Mater. Struct.*, no. https://doi.org/10.1088/1361-665X/ac6e15, doi: 10.1088/1361-665x/ac6e15.

[128] J. Z. Gul, B. S. Yang, Y. J. Yang, D. E. Chang, and K. H. Choi, “In situ UV curable 3D printing of multi-material tri-legged soft bot with spider mimicked multi-step forward dynamic gait,” *Smart Mater. Struct.*, vol. 25, no. 11, pp. 1–11, 2016, doi: 10.1088/0964-1726/25/11/115009.

[129] J. E. Shim, Y. J. Quan, W. Wang, H. Rodrigue, S. H. Song, and S. H. Ahn, “A smart soft actuator using a single shape memory alloy for twisting actuation,” *Smart Mater. Struct.*, vol. 24, no. 12, p. 125033, 2015, doi: 10.1088/0964-1726/24/12/125033.

[130] H. Rodrigue, W. Wang, D. R. Kim, and S. H. Ahn, “Curved shape memory alloy-based soft actuators and application to soft gripper,” *Compos. Struct.*, vol. 176, pp. 398–406, 2017, doi: 10.1016/j.compstruct.2017.05.056.

[131] J. H. Lee, Y. S. Chung, and H. Rodrigue, “Long Shape Memory Alloy Tendon-based Soft Robotic Actuators and Implementation as a Soft Gripper,” *Sci. Rep.*, vol. 9, no. 1, p. 11251, 2019, doi: 10.1038/s41598-019-47794-1.

[132] H. Rodrigue, B. Bhandari, M. W. Han, and S. H. Ahn, “A shape memory alloy-based soft morphing actuator capable of pure twisting motion,” *J. Intell. Mater. Syst. Struct.*, vol. 26, no. 9, pp. 1071–1078, 2015, doi: 10.1177/1045389X14536008.

[133] H. Rodrigue, W. Wang, B. Bhandari, M. W. Han, and S. H. Ahn, “SMA-based smart soft composite structure capable of multiple modes of actuation,” *Compos. Part B Eng.*, vol. 82, pp. 152–158, 2015, doi: 10.1016/j.compositesb.2015.08.020.

[134] A. Tomar and Y. Tadesse, “Multi-layer robot skin with embedded sensors and muscles,” *Electroact. Polym. Actuators Devices 2016*, vol. 9798, no. April 2016, p. 979809, 2016, doi: 10.1117/12.2219625.

[135] Y. Almubarak and Y. Tadesse, “Twisted and coiled polymer (TCP) muscles embedded in silicone elastomer for use in soft robot,” *Int. J. Intell. Robot. Appl.*, vol. 1, no. 3, pp. 352–368, 2017, doi: 10.1007/s41315-017-0022-x.

[136] Y. Tadesse, D. Hong, and S. Priya, “Twelve degree of freedom baby humanoid head using shape memory alloy actuators,” *J. Mech. Robot.*, vol. 3, no. 1, pp. 1–18, 2011, doi: 10.1115/1.4003005.

[137] N. A. Meisel, A. M. Elliott, and C. B. Williams, “A procedure for creating actuated joints via embedding shape memory alloys in PolyJet 3D printing,” *J. Intell. Mater. Syst. Struct.*, vol. 26, no. 12, pp. 1498–1512, 2015, doi: 10.1177/1045389X14544144.

[138] M. Ribeiro, O. Sousa Carneiro, and A. Ferreira da Silva, “Interface geometries in 3D multi-material prints by fused filament fabrication,” *Rapid Prototyp. J.*, vol. 25, no. 1, pp. 38–46, 2019, doi: 10.1108/RPJ-05-2017-0107.

[139] L. R. Lopes, A. F. Silva, and O. S. Carneiro, “Multi-material 3D printing: The relevance of materials affinity on the boundary interface performance,” *Addit. Manuf.*, vol. 23, no. March, pp. 45–52, 2018, doi: 10.1016/j.addma.2018.06.027.

[140] J. Mueller, D. Courty, M. Spielhofer, R. Spolenak, and K. Shea, “Mechanical Properties of Interfaces in Inkjet 3D Printed Single- and Multi-Material Parts,” *3D Print. Addit. Manuf.*, vol. 4, no. 4, pp. 193–199, 2017, doi: 10.1089/3dp.2017.0038.

[141] R. Mutlu, G. Alici, M. In het Panhuis, and G. M. Spinks, “3D Printed Flexure Hinges for Soft Monolithic Prosthetic Fingers,” *Soft Robot.*, vol. 3, no. 3, pp. 120–133, 2016, doi: 10.1089/soro.2016.0026.

[142] M. Saari, B. Cox, E. Richer, P. S. Krueger, and A. L. Cohen, “Fiber encapsulation additive manufacturing: An enabling technology for 3D printing of electromechanical devices and robotic components,” *3D Print. Addit. Manuf.*, vol. 2, no. 1, pp. 32–39, 2015, doi: 10.1089/3dp.2015.0003.

[143] C. Kim, C. Sullivan, A. Hillstrom, and R. Wicker, “Intermittent Embedding of Wire into 3D Prints for Wireless Power Transfer,” *Int. J. Precis. Eng. Manuf.*, vol. 22, no. 5, pp. 919–931, 2021, doi: 10.1007/s12541-021-00508-y.

[144] A. P. Taylor, C. Velez Cuervo, D. P. Arnold, and L. F. Velasquez-Garcia, “Fully 3D-printed, monolithic, mini magnetic actuators for low-cost, compact systems,” *J. Microelectromechanical Syst.*, vol. 28, no. 3, pp. 481–493, 2019, doi: 10.1109/JMEMS.2019.2910215.

[145] X. Cao, S. Xuan, S. Sun, Z. Xu, J. Li, and X. Gong, “3D Printing Magnetic Actuators for Biomimetic Applications,” *ACS Appl. Mater. Interfaces*, vol. 13, no. 25, pp. 30127–30136, 2021, doi: 10.1021/acsami.1c08252.

[146] G. Mao *et al.*, “Soft electromagnetic actuators,” *Sci. Adv.*, vol. 6, no. 26, 2020, doi: 10.1126/sciadv.abc0251.

[147] A. Hamidi, Y. Almubarak, Y. M. Rupawat, J. Warren, and Y. Tadesse, “Poly-Saora robotic jellyfish: swimming underwater by twisted and coiled polymer actuators,” *Smart Mater. Struct.*, vol. 29, no. 4, 2020, doi: 10.1088/1361-665X/ab7738.

[148] A. M. Soomro *et al.*, “Fully 3D printed multi-material soft bio-inspired frog for underwater synchronous swimming,” *Int. J. Mech. Sci.*, vol. 210, no. July, p. 106725, 2021, doi: 10.1016/j.ijmecsci.2021.106725.

[149] J. Shintake, V. Cacucciolo, D. Floreano, and H. Shea, “Soft Robotic Grippers,” *Adv. Mater.*, vol. 30, no. 29, 2018, doi: 10.1002/adma.201707035.

[150] A. Zolfagharian, M. A. P. Mahmud, S. Gharaie, M. Bodaghi, A. Z. Kouzani, and A. Kaynak, “3D/4D-printed bending-type soft pneumatic actuators: fabrication, modelling, and control,” *Virtual Phys. Prototyp.*, vol. 15, no. 4, pp. 373–402, 2020, doi: 10.1080/17452759.2020.1795209.

[151] K. Elgeneidy, G. Neumann, M. Jackson, and N. Lohse, “Directly printable flexible strain sensors for bending and contact feedback of soft actuators,” *Front. Robot. AI*, vol. 5, no. FEB, pp. 1–14, 2018, doi: 10.3389/frobt.2018.00002.

[152] Y. Yang and Y. Chen, “Innovative Design of Embedded Pressure and Position Sensors for Soft Actuators,” vol. 00, no. 00, pp. 1–9, 2017.

[153] G. Stano, L. Arleo, and G. Percoco, “Additive Manufacturing for Soft Robotics : Design and Fabrication of Airtight , Monolithic Bending PneuNets with Embedded Air Connectors,” no. i, pp. 1–18, 2020, doi: 10.3390/mi11050485.

[154] S. Valvez, P. N. B. Reis, L. Susmel, and F. Berto, “Fused filament fabrication-4d-printed shape memory polymers: A review,” *Polymers (Basel).*, vol. 13, no. 5, pp. 1–25, 2021, doi: 10.3390/polym13050701.

[155] G. Ehrmann and A. Ehrmann, “3D printing of shape memory polymers,” *J. Appl. Polym. Sci.*, vol. 138, no. 34, pp. 1–11, 2021, doi: 10.1002/app.50847.

[156] X. Huang, M. Panahi-Sarmad, K. Dong, R. Li, T. Chen, and X. Xiao, “Tracing evolutions in electro-activated shape memory polymer composites with 4D printing strategies: A systematic review,” *Compos. Part A Appl. Sci. Manuf.*, vol. 147, no. March, p. 106444, 2021, doi: 10.1016/j.compositesa.2021.106444.

[157] I. T. Garces and C. Ayranci, “Advances in additive manufacturing of shape memory polymer composites,” *Rapid Prototyp. J.*, vol. 27, no. 2, pp. 379–398, 2021, doi: 10.1108/RPJ-07-2020-0174.

[158] S. Nam and E. Pei, “The influence of shape changing behaviors from 4D printing through material extrusion print patterns and infill densities,” *Materials (Basel).*, vol. 13, no. 17, 2020, doi: 10.3390/MA13173754.

[159] W. Wang and S. H. Ahn, “Shape Memory Alloy-Based Soft Gripper with Variable Stiffness for Compliant and Effective Grasping,” *Soft Robot.*, vol. 4, no. 4, pp. 379–389, 2017, doi: 10.1089/soro.2016.0081.

[160] Y. Mao, K. Yu, M. S. Isakov, J. Wu, M. L. Dunn, and H. Jerry Qi, “Sequential Self-Folding Structures by 3D Printed Digital Shape Memory Polymers,” *Sci. Rep.*, vol. 5, pp. 1–12, 2015, doi: 10.1038/srep13616.

[161] Q. Ge, C. K. Dunn, H. J. Qi, and M. L. Dunn, “Active origami by 4D printing,” *Smart Mater. Struct.*, vol. 23, no. 9, 2014, doi: 10.1088/0964-1726/23/9/094007.

[162] M. Al-Rubaiai, T. Pinto, C. Qian, and X. Tan, “Soft actuators with stiffness and shape modulation using 3D-printed conductive polylactic acid material,” *Soft Robot.*, vol. 6, no. 3, pp. 318–332, 2019, doi: 10.1089/soro.2018.0056.

[163] S. Yamamura and E. Iwase, “Hybrid hinge structure with elastic hinge on self-folding of 4D printing using a fused deposition modeling 3D printer,” *Mater. Des.*, vol. 203, p. 109605, 2021, doi: 10.1016/j.matdes.2021.109605.

[164] M. Al-Rubaiai, T. Pinto, C. Qian, and X. Tan, “Soft actuators with stiffness and shape modulation using 3D-printed conductive polylactic acid material,” *Soft Robot.*, vol. 6, no. 3, pp. 318–332, 2019, doi: 10.1089/soro.2018.0056.

[165] A. Mohammadi *et al.*, “A practical 3D-printed soft robotic prosthetic hand with multi-articulating capabilities,” *PLoS One*, vol. 15, no. 5, pp. 1–23, 2020, doi: 10.1371/journal.pone.0232766.

[166] S. Akbari, A. H. Sakhaei, S. Panjwani, K. Kowsari, and Q. Ge, “Shape memory alloy based 3D printed composite actuators with variable stiffness and large reversible deformation,” *Sensors Actuators, A Phys.*, vol. 321, 2021, doi: 10.1016/j.sna.2021.112598.

[167] S. Akbari, A. H. Sakhaei, S. Panjwani, K. Kowsari, A. Serjourei, and Q. Ge, "Multimaterial 3D Printed Soft Actuators Powered by Shape Memory Alloy Wires," *Sensors Actuators, A Phys.*, vol. 290, pp. 177–189, 2019, doi: 10.1016/j.sna.2019.03.015.

[168] S. M. F. Kabir, K. Mathur, and A. F. M. Seyam, "A critical review on 3D printed continuous fiber-reinforced composites: History, mechanism, materials and properties," *Compos. Struct.*, vol. 232, no. September 2019, p. 111476, 2020, doi: 10.1016/j.compstruct.2019.111476.

[169] J. G. Díaz-Rodríguez, A. D. Pertúz-Comas, and O. A. González-Estrada, "Mechanical properties for long fibre reinforced fused deposition manufactured composites," *Compos. Part B Eng.*, vol. 211, no. October 2020, 2021, doi: 10.1016/j.compositesb.2021.108657.

[170] P. Zhuo, S. Li, I. A. Ashcroft, and A. I. Jones, "Material extrusion additive manufacturing of continuous fibre reinforced polymer matrix composites: A review and outlook," *Compos. Part B Eng.*, vol. 224, no. May 2020, p. 109143, 2021, doi: 10.1016/j.compositesb.2021.109143.

[171] D. Espalin, D. W. Muse, E. MacDonald, and R. B. Wicker, "3D Printing multifunctionality: Structures with electronics," *Int. J. Adv. Manuf. Technol.*, vol. 72, no. 5–8, pp. 963–978, 2014, doi: 10.1007/s00170-014-5717-7.

[172] E. MacDonald *et al.*, "3D printing for the rapid prototyping of structural electronics," *IEEE Access*, vol. 2, pp. 234–242, 2014, doi: 10.1109/ACCESS.2014.2311810.

[173] M. Alsharari, B. Chen, and W. Shu, "Sacrificial 3D Printing of Highly Porous, Soft Pressure Sensors," *Adv. Electron. Mater.*, vol. 2100597, pp. 1–12, 2021, doi: 10.1002/aelm.202100597.

[174] M. Arh and J. Slavič, "Single-Process 3D-Printed Triaxial Accelerometer," vol. 2101321, pp. 1–7, 2021, doi: 10.1002/admt.202101321.

[175] Arh, Slavič, and Boltežar, "Design principles for a single-process 3d-printed accelerometer – theory and experiment," vol. 152, 2021, doi: 10.1016/j.ymssp.2020.107475.

[176] C. B. Lee and J. A. Tarbutton, "Polyvinylidene fluoride (PVDF) direct printing for sensors and actuators," *Int. J. Adv. Manuf. Technol.*, vol. 104, no. 5–8, pp. 3155–3162, 2019, doi: 10.1007/s00170-019-04275-z.

[177] E. Ceretti, P. Ginestra, P. I. Neto, A. Fiorentino, and J. V. L. Da Silva, "Multi-layered Scaffolds Production via Fused Deposition Modeling (FDM) Using an Open Source 3D Printer: Process Parameters Optimization for Dimensional Accuracy and Design Reproducibility," *Procedia CIRP*, vol. 65, pp. 13–18, 2017, doi: 10.1016/j.procir.2017.04.042.

[178] Z. Meng *et al.*, "Design and additive manufacturing of flexible polycaprolactone scaffolds with highly-tunable mechanical properties for soft tissue engineering," *Mater. Des.*, vol. 189, p. 108508, 2020, doi: 10.1016/j.matdes.2020.108508.

[179] F. Liu *et al.*, "Structural Evolution of PCL during Melt Extrusion 3D Printing," *Macromol. Mater. Eng.*, vol. 303, no. 2, pp. 1–6, 2018, doi: 10.1002/mame.201700494.

[180] J. Lee, J. Walker, S. Natarajan, and S. Yi, "Prediction of geometric characteristics in polycaprolactone (PCL) scaffolds produced by extrusion-based additive manufacturing technique for tissue engineering," *Rapid Prototyp. J.*, vol. 26, no. 2, pp. 238–248, 2020, doi: 10.1108/RPJ-08-2018-0219.

[181] E. Deng and Y. Tadesse, "A soft 3d-printed robotic hand actuated by coiled sma," *Actuators*, vol. 10, no. 1, pp. 1–24, 2021, doi: 10.3390/act10010006.

[182] A. Hamidi, Y. Almubarak, and Y. Tadesse, "Multidirectional 3D-printed functionally graded modular joint actuated by TCPFL muscles for soft robots," *Bio-Design Manuf.*, vol. 2, no. 4,

pp. 256–268, 2019, doi: 10.1007/s42242-019-00055-6.

[183] S. W. Kwok *et al.*, "Electrically conductive filament for 3D-printed circuits and sensors," *Appl. Mater. Today*, vol. 9, pp. 167–175, 2017, doi: 10.1016/j.apmt.2017.07.001.

[184] S. K. Gupta, M. Talati, and P. K. Jha, "Shape and Size Dependent Melting Point Temperature of Nanoparticles," *Mater. Sci. Forum*, vol. 570, pp. 132–137, 2008, doi: 10.4028/www.scientific.net/MSF.570.132.

[185] N. A. Mohd Radzuan, A. B. Sulong, and J. Sahari, "A review of electrical conductivity models for conductive polymer composite," *Int. J. Hydrogen Energy*, vol. 42, no. 14, pp. 9262–9273, 2017, doi: 10.1016/j.ijhydene.2016.03.045.

[186] I. Tirado-Garcia *et al.*, "Conductive 3D printed PLA composites: On the interplay of mechanical, electrical and thermal behaviours," *Compos. Struct.*, vol. 265, no. December 2020, p. 113744, 2021, doi: 10.1016/j.compstruct.2021.113744.

[187] R. Li *et al.*, "Research progress of flexible capacitive pressure sensor for sensitivity enhancement approaches," *Sensors Actuators, A Phys.*, vol. 321, p. 112425, 2021, doi: 10.1016/j.sna.2020.112425.

[188] O. Atalay, A. Atalay, J. Gafford, and C. Walsh, "A Highly Sensitive Capacitive-Based Soft Pressure Sensor Based on a Conductive Fabric and a Microporous Dielectric Layer," *Adv. Mater. Technol.*, vol. 3, no. 1, pp. 1–8, 2018, doi: 10.1002/admt.201700237.

[189] P. Tripicchio, S. D'Avella, C. A. Avizzano, F. Di Pasquale, and P. Velha, "On the integration of FBG sensing technology into robotic grippers," *Int. J. Adv. Manuf. Technol.*, vol. 111, no. 3–4, pp. 1173–1185, 2020, doi: 10.1007/s00170-020-06142-8.

LIST OF FIGURES

LIST OF TABLES